DESIGN AND ADVANCED MANUFACTURING OF POLYISOBUTYLENE-BASED FUNCTIONAL ELASTOMERS AND THEIR OPTICAL NANOCOMPOSITES

A Dissertation

Presented to
The Graduate Faculty of The University of Akron

In Partial Fulfillment
of the Requirements for the Degree
Doctor of Philosophy

Naifu Shen
August 2025

DESIGN AND ADVANCED MANUFACTURING OF POLYISOBUTYLENE-BASED FUNCTIONAL ELASTOMERS AND THEIR OPTICAL NANOCOMPOSITES

Naifu Shen

Dissertation

Approved:

Advisor
Dr. Weinan Xu

Committee Member
Dr. Kevin Cavicchi

Committee Member
Dr. Fardin Tayebeh Khabaz

Committee Member
Dr. Bi-min Zhang Newby

Committee Member
Dr. Yu Zhu

Accepted:

Interim Director of SPSPE
Dr. Mark Soucek

Dean of the College
Dr. Craig Menzemer

Interim Dean, Graduate School
Dr. Gwyneth Price

Date

ABSTRACT

Polyisobutylene (PIB) is a type of elastomer with a unique combination of physical properties such as high elasticity, excellent chemical stability, low permeability to gases and liquids, and high biocompatibility. Despite its widespread use in tires, coatings, and adhesives, more advanced applications of PIB in electronics, optics, and biomedicine have not been fully explored. It is critical to integrate PIB with other advanced materials in order to achieve physical properties enhancement and new functionalities for those applications.

To this purpose, in this research we systematically investigated new materials and composites based on PIB as well as their advanced applications in 3D printing and flexible optical devices. In the first study, we studied the structure-property relationship of a series of PIB-based polyurethanes with the purpose of establishing extrusion-based 3D printing as a new processing method for them. In the second study, we designed and synthesized PIB-based polymer ligands for perovskite quantum dots (QDs) to enhance their stability and enable their selective interaction with a polymer matrix. We also demonstrated flexible optical nanocomposites based on the integration of PIB-ligand functionalized QDs with polystyrene-b-polyisobutylene-b-polystyrene (SIBS) elastomer. In the third study, we achieved specific ionic interactions between perovskite QDs and partially sulfonated SIBS through electrostatic interaction between the metal ions on QD surface and sulfonate groups in the polymer matrix. Such ionic interactions enable precise control of the spatial distribution of QDs in the polymer matrix as well as optical properties tuning.

Throughout this research, new knowledge on the design, preparation, characterization and applications of PIB-based materials and nanocomposites is generated. The demonstration of extrusion-based 3D printing strategy for PIB-based thermoplastic elastomers enables their broader applications in rapid prototyping, biofabrication and tissue engineering. The functionalization of perovskite QDs with PIB-based ligands and integrating them with SIBS elastomer will have promising applications for soft optical and optoelectronic devices.

DEDICATION

To my dearest parents and sister.

ACKNOWLEDGEMENT

I would like to express my most sincere gratitude to all who have contributed to this dissertation.

First and foremost, I am deeply grateful to my advisor, Dr. Weinan Xu, for his patience, support, and expert guidance throughout my PhD journey. Dr. Xu's mentorship has been instrumental in shaping my academic path. Thanks to Dr. Xu, I can learn from his precious academic experience and have a better understanding of how to conduct systematical academic research from abstract method design to specific instrument maintenance, which significantly contributes to the development of my professional skills. Moreover, I extend my heartfelt appreciation to Dr. Xu for the opportunities he generously provided, making it possible for me to present my research at various conferences as well as stay abreast of cutting-edge developments in academic fields. I will always cherish the shared experiences of our memorable group picnics organized by Dr. Xu.

I would like to express my sincere gratitude to Dr. Joseph P Kenndey for his invaluable support and collaboration contributing to the work of polyisobutylene polyurethane synthesis, providing the access to equipment and supplies in his lab. I would like to express my gratitude to Tejal Deodhar, Chinnapatch Tantisuwanno, and Yen-Ming Tseng who kindly and unreservedly trained me with the synthetical techniques involved in PIB-PU synthesis. I also would like to express my sincere gratitude to Dr. James Eagan and his student Arsalaan Nisar Pathan for their collaboration, invaluable support and critical insights for this work.

Additionally, I would like to extend my gratitude to Dr. Yitong Dong and his student Chenjia Mi from the University of Oklahoma for their collaboration contributing to the BCP-perovskite QDs nanocomposite research. It would not have been possible for me to even begin this project without their invaluable guidance and the resources they generously provided. I am grateful to my friend Cheng-Han Tsai for his unquestionable contribution to this work, especially zwitterion synthesis training and support throughout the study. I am grateful to Dr. Thein Kyu for allowing me access to instruments and supplies in his lab.

I would like to express my gratitude to my committee members: Dr. Bi-min Zhang Newby, Dr. Fardin Tayebeh Khabaz, Dr. Kevin Cavicchi, and Dr. Yu Zhu who kindly provided their insightful comments and guidance towards the further completion of this PhD research. I would also like to acknowledge the people who have mentored me in various instruments and techniques: Dr. Jiansheng Feng, Dr. Nancy Concepcion, Dr. Lingyan Li

Special thanks to my lab mates Jinyu Bu, Muxuan yang, Pratik Kasbe, Shan Liu, Xun Liu for their patience and helping hands throughout my PhD journey. Their company made my time at the University of Akron special and unforgettable. Last but certainly not least, I would like to thank my family for their unwavering support in encouraging me to pursue graduate studies abroad and myself for not giving up

TABLE OF CONTENTS

Page

LIST OF TABLES

Table Page

LIST OF FIGURES

Figure Page

LIST OF SYMBOLS AND ABBREVIATIONS

(Boc)2O	di-tert-butyl decarbonate
AFM	atomic force microscope
BCC	body centered cubic
BCP	block copolymer
BDO	1,4-butanediol
BPO	benzoyl peroxide
°C	degree Celsius
$CsPbBr_3$	cesium lead bromide
DBTDL	dibutyltin dilaurate
DMA	dynamic mechanical analysis
DMF	dimethylformamide
DSC	differential scanning calorimetry
ε	interaction energy between A and B monomers
f	volume fraction
FA+	formamidinium cation
FDM	fused deposition modeling
FFT	fast fourier transform
GISAXS	grazing incidence small angle X–ray scattering
H-PIB-PU	high molecular weight polyisobutylene-polyurethane
hPU	hard polyurethane
k_B	boltzmann constant
LARP	ligand assisted reprecipitation
LED	light-emitting diodes
L-PIB-PU	low molecular weight polyisobutylene-polyurethane
MA	maleic anhydride
MA+	methylammonium cation
MDI	methylene diphenyl diisocyanate
MH-*b*-PI-*b*-MH	maltoheptaose-*block*-polyisoprene-*block*-maltoheptaose
MHP	metal halide perovskite
MW	molecular weight
N	degree of polymerization
NCs	nanocrystals

NPs	nanoparticles
NWs	nanowires
ODT	order-disorder transition
P	packing parameter
P(S-b-EB-b-MMA)	poly(styrene-b-ethylene-co-1-butene-b-methyl methacrylate)
PAA-*b*-P3HT	poly(acrylic acid)-block-poly(3-hexylthiophene)
PBMA	poly(*n*-Butyl methacrylate)
PCE	power conversion efficiency
PCL	polycaprolactone
PDMS	polydimethylsiloxane
PEG	polyethylene glycol
PEG-(PCGMA-co-PGMA)-PDEA	Poly(ethylene glycol)-block-poly(glycerol monomethacrylate-co-poly(glycerol monomethacrylate)-block-poly(2-(diethylamino)ethyl methacrylate)
PEO-b-P(DEA-stat-TMSPMA)	poly(ethylene oxide)-block-poly[2-(diethylamino)ethyl methacrylate-stat-3-(trimethoxysilyl)propyl methacrylate]
PFOEMA	poly(perfluorooctyl)ethyl methacrylate)
PH	potential of hydrogen
PHEMA	poly(2-hydroxyethyl methacrylate
PHEMA-b-PMMA	poly(2-hydroxyethyl methacrylate)-block-poly(methyl methacrylate)
PIB-PU	polyisobutylene-polyurethane
PL	photoluminescence
PLQY	photoluminescence quantum yield
PMPC	poly(2-methacryloyloxyethyl phosphorylcholine)
POEGMA	poly(poly(ethylene glycol) monomethyl ether methacrylate)
PPO	polyphenylene oxide
PS	polystyrene
PSBMA	poly(sulfobetaine methacrylate)
PS-b-P2VP	polystyrene-block-poly(2-vinylpyridine)
PS-b-P4VP	polystyrene-block-poly(4-vinylpyridine)
PS-*b*-PEO	poly(styrene-block-ethylene oxide)
PS-b-PI	polystyene-b-polyisoprene
PS-b-PMMA	polystyrene-block-poly(methyl methacrylate)
PSC	perovskite solar cell
PTFE	polytetrafluoroethylene
QDs	quantum dots
RAFT	reversible-addition-fragmentation chain-transfer polymerization
SAXS	small angle X–ray scattering

SBS	poly(styrene-block-butadiene-block-styrene)
SCMF	self-consistent mean-field
SEBS	poly(styrene-b-ethylene-butylene-b-styrene)
SEM	scanning electron microscopy
SIBS	poly(styrene-block-isobutylene-block-styrene)
SIS	polystyrene-polyisoprene-polystyrene
s-SIBS	sulfonated poly(styrene-block-isobutylene-block-styrene)
T	temperature
Tg	glass transition temperature
TGA	thermogravimetric analysis
THF	tetrahydrofuran
TICG	theoretically informed coarse-grained
TPA	thermoplastic polyamide elastomers
TPC	thermoplastic polyester elastomers
TPE	thermoplastic elastomer
TPO	thermoplastic polyolefins
TPS	thermoplastic styrenic elastomers
TPU	thermoplastic polyurethane
TPV	thermoplastic vulcanizates
TPZ	miscellaneous category thermoplastic elastomer
UV-vis	ultraviolet–visible spectrophotometry
XPS	X-ray photoelectron spectroscopy
Z	number of nearest neighboring monomers in a copolymer
ν	volume
χ	Flory-Huggins interaction parameter
a_o	head group optimal area
l_c	length of the solvophobic segment

CHAPTER I

INTRODUCTION

1.1 Block copolymers (BCPs) and their phase behaviors

1.1.1 Microphase separation transition of bulk block copolymer

Block copolymer is a specific class of copolymers where the repeating units from two or more chemically distinct monomers are assembled not in alternating or random patterns but in a way that discrete homogeneous segments are connected by covalent bonds. The morphology of ordered microdomains with characteristic length scale of 5~50nm is one of the distinguishing features for BCPs. Such molecular level precision is important and compatible for nanolithography application[1]. In contrast to the binary mixing of two homopolymers, which leads to macroscopic phase separation, block copolymer (BCP) must adopt extended configurations to separate dissimilar A and B blocks. This stretching is a result of the covalent linkages at the A-B interfaces, resulting in a deviation from their original coiled states. The chain stretching, indicative of chain elasticity, produces an entropic contribution that counteracts the driving force for separation, thereby constraining the phase separation to mesoscopic dimensions.

For a diblock copolymer system consisting of A and B monomers[2,3], the thermodynamics of microphase separation transition process are determined by the volume fraction (f) and the product of Flory-Huggins interaction parameters (χ_{AB}) and the polymerization degree (N) called segregation strength based on random-phase approximation. The Florry-Huggin's interaction parameter, χ_{AB} which can be calculated by the following equation:

$$\chi_{AB} = \frac{Z}{k_B T}\left[\varepsilon_{AB} - \frac{1}{2}(\varepsilon_{AA} + \varepsilon_{BB})\right]$$

Z is the number of nearest neighboring monomers in a copolymer, k_B is the Boltzman constant, $k_B T$ is the thermal energy unit, and ε_{AB} is the interaction energy between A and B monomers. Positive χ_{AB} indicates repulsive interaction between A and B monomers and negative χ_{AB} indicates a tendency towards mixing. Without strong interactions including hydrogen bonding or ionic interaction, χ_{AB} is usually positive, small, and varies inversely with temperature. Such temperature dependence can be described by the equation: $\chi = \mathrm{A} + \frac{B}{T}$ where A and B account for entropic and enthalpic contributions respectively[4]. When the segregation strength (χN) reached above a critical value (χN=10, the weak segregation limit), the free energy of BCP system changes from entropic dominated (disordered state) to unfavored mixing enthalpy terms dominated, leading to overcoming entropic penalty and the ordered state with stretched polymer chain configurations. The morphological evolution of microphase separated diblock copolymer was predicted by self-consistent mean-field (SCMF) theory[5–7] and experimentally confirmed[8]. At fixed sufficiently large segregation strength, the increase in the volume fraction of one phase alters the microdomains from body centered spheres, to hexagonally packed cylinders, gyroids, lamellae, and following reverse morphologies[9]. The existence of perforated lamellae[10] observed in the phase portrait of PS-b-PI revealed the discrepancy between theory and experiment. On the other hand, the composition fluctuation near the weakly first-order ODT curve makes it possible that direct transition from disordered phase to other ordered phases, indicating the limitation of the self-consistent mean-field theory and the importance of relating theory to reality. And several more ordered morphologies at equilibrium were found in later studies including dodecagonal quasi-crystal[11], Frank-Kasper σ phase[12], etc. for di-block copolymer systems.

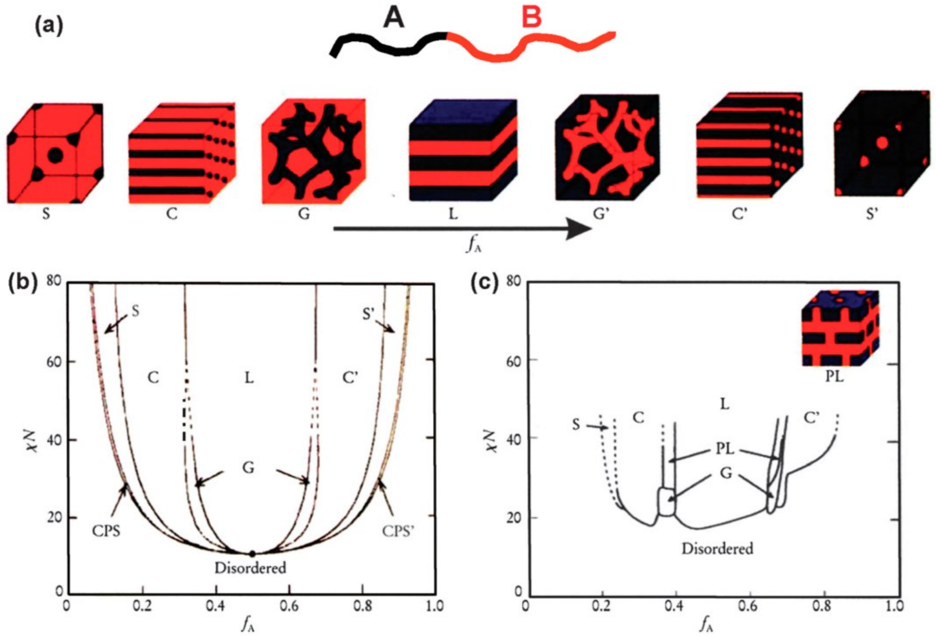

Figure 1: (a) schematic of equilibrium morphologies of AB diblock copolymer in bulk. (b) phase diagram of the AB type diblock copolymer simulated based on self-consistent mean-field theory. Close-packed spheres (CPS) spherical (S), cylindrical (C), gyroid (G) and lamellar (L). (c) experimental portrait of PS-B-PI. Perforated layers (PL). Reproduced with permission from ref.13.

When the phase behavior analysis moves from di-block BCP systems to tri-block BCP systems, there is a dramatic expansion both in affecting parameters and the number of equilibrium phases. Not only the in total three interaction parameters need to be considered[14–16], but also the sequences of the three segments can determine the morphology[17]. The real-space implementation of self-consistent mean-field theory was widely adapted for the ordered phase prediction. A series of morphological combinations of lamellae, cylinders and spheres including lamellae-cylinder combination phase, cylinder-ring combination phase, and lamellae-spheres combination phase were demonstrated using P(S-b-EB-b-MMA) triblock copolymers[18,19] with different volume fractions which were in agreement with simulation. Tang[20] concluded that when the segregation strength and overall polymerization degree for the three component are comparable, the most stable lamellae morphology would be formed. With asymmetric segregation strengths, the triblock copolymer would adapt into three possible ordered morphologies: lamellae morphologies with beads either inside one lamellae layer or at the interface, and hexagonal phase with beads at the interface.

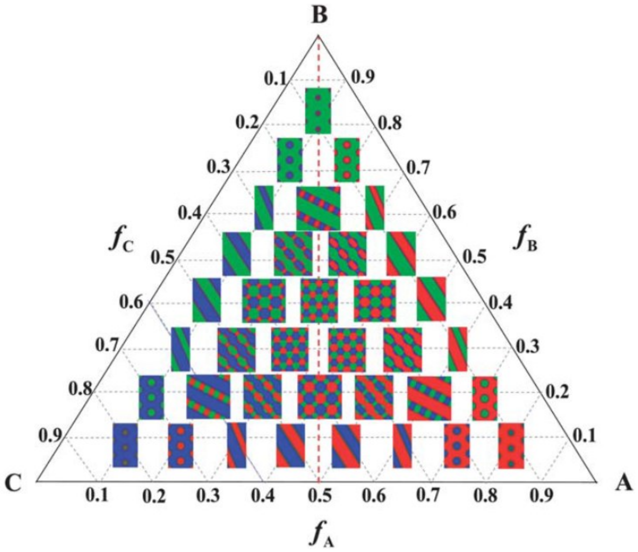

Figure 2: The triangular phase diagram of ABC triblock copolymer simulated by self-consistent mean-field theory. Reproduced with permission from ref.14.

1.1.2 Phase behaviors of BCP film

Aside from bulk BCPs or undiluted BCP melts, BCPs are also often deployed as thin films depending on the applications. Thus, the understanding and manipulation of BCP thin film microscale structures were necessary and had been also extensively investigated. To achieve periodic patterns with long range order, film thickness[21,22] is one of the crucial parameters which can significantly alter the segments arrangement and subsequent morphology. PS-b-PMMA[23] was subjected to 170 ℃ annealing temperature above the bulk order-to-disorder transition temperature after spin-coating on silicon substrate to study the effect of initial thickness. The interaction between the substrate and segments from the BCP was elucidated in this study as follows: (1) Due to the preferential attraction between substrate and one block, the ordering of copolymer chains proceeded from the substrate side and the PS blocks with lower surface energy face towards the air-BCP interface. (2) When the film thickness is below half of the interlamellar spacing (7nm in this study), the film formed discontinuous spinodal morphology in the thickness range of 0~3.5nm with a slow kinetic and transited into a different morphology where cylindrical holes or so-called islands were distributed across the film in the 3.5~7nm thickness range. (3) Entropically induced autophobic behavior and resulting spinodal pattern on a brush layer morphology were observed when film thickness was 7~19nm. Specifically, the “brush” layer of 7nm thickness contacting the substrate composed of dense copolymers with highly stretched configurations, generating interfacial tension with polymer melt above and undergoing a time dependent dewetting process. (4) When the film thickness increased to 19~35nm, there were random holes distributed on the PS-b-PMMA film. (5) When film thickness was larger than 35nm, a stable BCP film with smooth surface was observed.

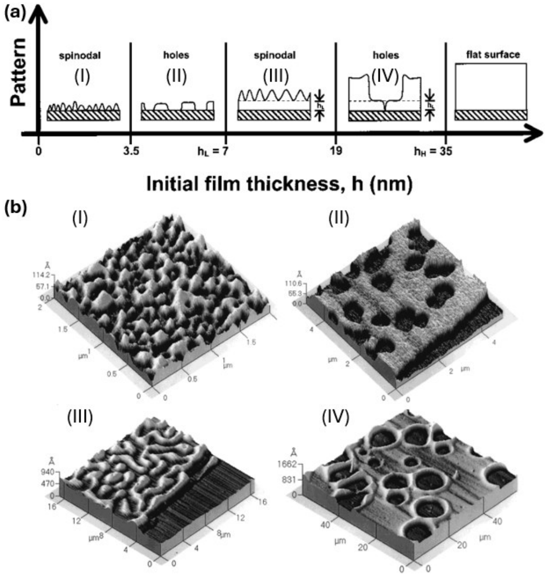

Figure 3: (a) Schematic of morphological evolution with increasing thickness. (b) Corresponding spinodal, hole, spinodal on brush layer, and holes morphologies of PS-b-PMMA thin film on silicon substrate. Reproduced with permission from ref.23

In the film fabrication process either by film blowing extrusion[24], solution casting, or spin-coating, the BCP morphology is kinetically trapped with defects due to fast cooling or rapid solvent evaporation. Thermal annealing and solvent annealing are the two most common methods to orient the microdomains in the BCP film and reduce surface defect density. For thermal annealing, the BCP film is heated above the glass transition temperatures of all segments resulting in chain mobility increase and ordered morphology. Furthermore, temperature gradient or “zone annealing condition” is crucial for thermal annealing treatment to generate micropatterns over a large area. PS-b-PI thin film with nearly perfect single grain lamellar feature was prepared by applying sharp temperature gradient as well as a small moving rate along the z-axis[25,26]. It was concluded that grain nucleation is favored along the z-axis during the annealing process where lamellae growth was continued by adding new lamella to existing lamella with its normal parallel to the temperature gradient direction. Compared with surface-induced ordering, the direction of the temperature gradient was confirmed as a dominating parameter[27]. It was evidenced by a demonstration where hcp PS-b-PI film was subjected to zone annealing with a tilted substrate angle of 45°. It was found out that the (1 0 0) planes were perpendicular to the temperature gradient, meaning the columnar grain growth was separated from the glass surface induced ordering.

In addition to temperature treatment only, introducing selective solvent vapor during the annealing process can dramatically alter the morphology of microdomains in BCPs. To decouple from the effects of oxygen and moisture, the solvent annealing is conducted in a sealed chamber in inert gas atmosphere connected with one or multiple pipelines to which saturated solvent vapor is purged and the vapor pressure is controlled by a separate nitrogen stream[28]. One major difference between solvent annealing and thermal annealing is that solvent annealing operation temperature is generally far below the glass transition temperature. Solvent molecules time dependently diffuse into BCP have several impacts including increased volume, reduction in the effective interaction parameter[28], changed film boundary condition and swollen polymer chains with enhanced chain mobility for reorganization. And the ordering process takes place during the drying step and propagates from the free surface to the substrate related to solvent concentration gradient[29]. The selectivity or the strength of attraction between solvent molecules and BCP segments is a key parameter in determining the final thin film morphology. The solvent annealing behavior of PS-b-PMMA was investigated by its exposure to non-selective THF, PS selective CS_2 vapor, and PMMA selective acetone. It was observed that the selective attraction of PMMA-acetone pairs caused an uprising of swelled PMMA block and a hexagonal packed PMMA array was induced at high swelling ratio[30]. Computational simulation of solvent annealing process was investigated based on symmetric PS-b-P2VP[31] with 40k Mw for each segment. In this study, a modified theoretically informed coarse-grained (TICG) model was adapted for the solvent annealing process description. Specifically, an additional generalized energy functional expansion was introduced in the model up to third order so the absorption-evaporation of a solvent in BCP can be calculated. And the time evolution of microphase separation and chain mobility was described based on solvent concentration. It was proposed that a well-ordered morphology can be achieved by a two-step evaporation procedure. In the simulation, the BCP film was set to firstly swollen at high vapor pressure so the effect of spin-coating can be decoupled, then target swelling ratio was met by removing a fraction of the solvent. After the two-step treatment, the simulation described a perpendicular oriented lamellae morphology with little defects in the fixed-size simulation box.

In addition to generating BCP film with reduced defect density, solvent annealing was demonstrated based on poly(2-hydroxyethyl methacrylate)-block-poly(methyl methacrylate) (PHEMA-b-PMMA)[32] to induce the morphology transition where four different morphologies can be tuned from single initial BCP and kinetically trapped as the final state by fast evaporation. All the experiments were conducted at 25°C, 1 atm pressure to investigate the effect of varying annealing time as well as the mixing ratio of methanol (good solvent for PHEMA) and THF (good solvent for PMMA). Lamellae with perpendicular orientation, cylinder, gyroid, and sphere like morphologies were realized. When the BCP film was treated with 80/20 (v/v) THF/methanol mixed solvent, the orientation of the lamellae changed from perpendicular to parallel to the substrate. When the methanol volume fraction increased to 50%, the ordering of PHEMA-b-PMMA was proved to be time dependent. For a 45min annealing time, the BCP formed a BCC sphere morphology with (1 1 0) planes parallel to the substrate. On the other hand, during the long-term annealing process, the spherical morphology gradually was found to transit into a thermodynamically stable gyroid morphology with (2 1 1) planes parallel to the substrate. When methanol volume fraction increased to 80%, the original lamellae morphology turned into a perpendicular orienting hexagonally packed cylinder morphology.

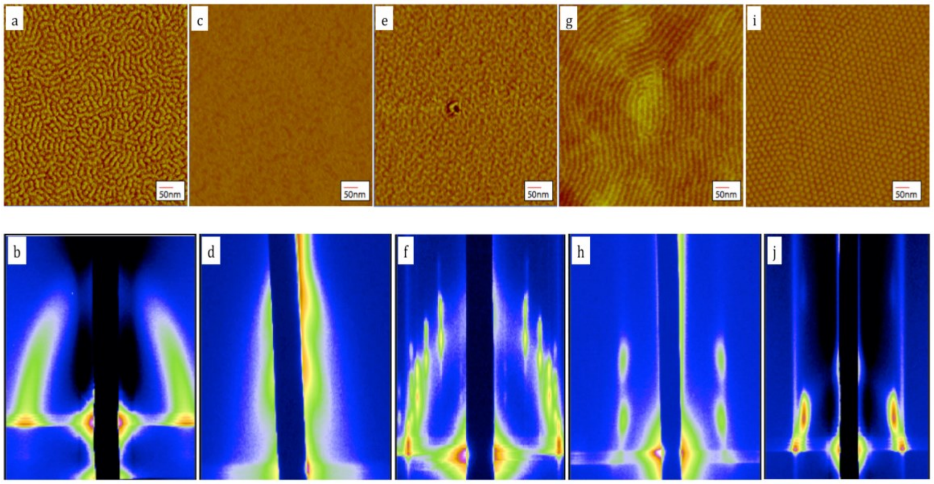

Figure 4: AFM images and corresponding grazing incidence small angle X–ray scattering (GISAXS) results for PHEMA-b-PMMA films with different solvent annealing parameters. The film morphologies were trapped by fast drying (a, b) Perpendicular lamellae. (c, d) Parallel lamellae. (e, f) Gyroid. (g, h) Parallel cylinders. (i, j) BCC spheres. Reproduced with permission from ref.32.

Aside from solvent, external forces such as shearing can also provide chain mobility for morphology reorganization. In Kang's work[33], macroscopic nanopattern template for polarization-dependent plasmonic extinction application was demonstrated with PS-b-P4VP and PS-b-PMMA. The large area polymer orientation at room temperature was realized by a swollen PDMS pad placed on top of the BCP film where constant pressure and shear rate in the lateral direction were applied for anisotropic alignment. After plasma etching, well defined grooved nanochannels with ~19nm width and ~5nm depth was used as the template for Au nanorods incorporation. This study provided a feasible method for macro-scale template fabrication and can be used in scenarios where heat sensitive functional groups were incorporated in BCP film. On the other hand, temperature gradient-induced shearing was exploited for nano template fabrication^{34}. In Singh's work, PS-b-P2VP with lamellae morphology was subjected to a high shear stress for large area aligned gold nanowire fabrication. In detail, the shearing force was generated by the local thermal expansion and contraction of top PDMS elastomer indued by the cold zone annealing treatment. And it was transmitted to PS-b-P2VP layer by the sandwiching high molecular weight PMMA films serving as the neutral protective layers to generate nanochannels along the shearing direction. As a result, nanopatterns with 7nm spacing were realized and subsequently used as critical-dimension template to generate ordered gold NWs-SiO_2 NPs hybrid structures after ion infiltration and dry etching.

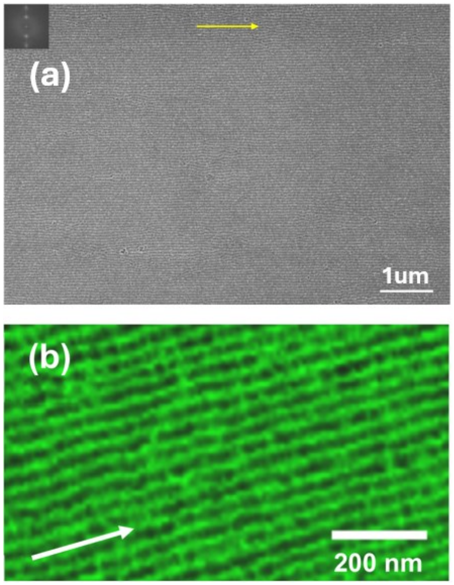

Figure 5: (a) Macroscopic aligned shear-induced PS-b-P4VP film under SEM, the inset image corresponds to the FFT image. The scale bar is 1 micrometer. Reproduced with permission from ref. 33. (b) AFM phase images of oriented lamellar PS-b-P2VP film induced by cold zone annealing. The scale bar is 200nm. Reproduced with permission from ref.34. The arrows in (a, b) indicate the shearing direction.

1.1.3 Self-assembly morphologies of BCPs in solution

For a BCP solution, when the BCP concentration increases above the critical micelle concentration (CMC), the polymer chains will aggregate into a diverse range of microstructures based on constituent block architecture. The amphiphilic BCPs would assemble together and adopt into a core-shell structure, leading to a reduction of surface energy as well as the aggregation-induced entropic loss. A dimensionless packing parameter P can be used to estimate micelle morphology. [35]

$$P = \frac{v}{a_o l_c}$$

Where v is the volume for solvophobic segments, a_o corresponds to the head group optimal area, and l_c is the length of the solvophobic segments. Generally, P=1/3 and P=1/2 are the two critical values indicating if spherical, rod-like micelle, or larger vesicle morphology is favored. (Figure 6)

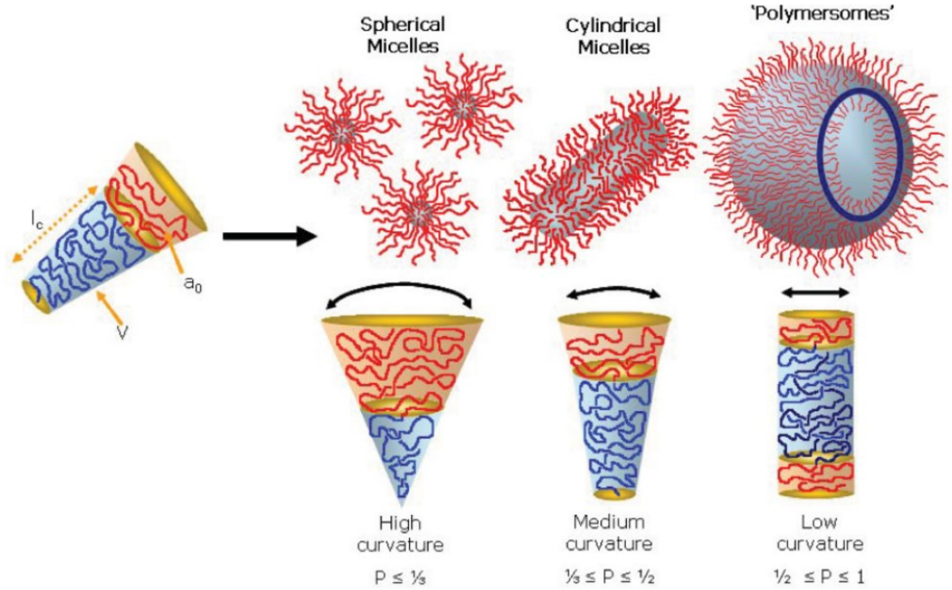

Figure 6: Different pack parameters result in molecular curvatures and corresponding self-assembled structures including spherical micelles, rods, and vesicles. Reproduced with permission from ref. 35

BCP micelles and vesicles were considered as counterparts for small molecule liposomes in biomedical field including actives delivery (drug[36], gene[37], enzyme[38], etc.), *in vivo* tissue imaging[39], and nanoreactor[40] applications. Compared with small molecule aggregation, the advantages of BCP self-assembly are more durable with enhanced mechanical properties, tunable permeability, and stimuli responsibility by surface decoration. For example, Jiang[41] *et al.* demonstrated the micellization and inner shell cross-linking of a triblock PEG-(PCGMA-co-PGMA)-PDEA where UV-curable cinnamate double bonds were introduced by partial esterification reaction. The swelling of micelle was induced by the pronation of EDA core at acid PH thus the reversible micelle deswelling can also be achieved when exposed to NaOH, indicating its PH responsibility. Du[42] *et al.* on the other hand demonstrated the BCP vesicles with tunable permeability consisting of PEO-b-P(DEA-stat-TMSPMA). Higher cross-linking degree caused lower wall permeability and prevented complete dissociation. And the tertiary amine groups in PDEA block resulted in PH-dependent permeability which was evidenced by the much slower self-quenching of fluorescent rhodamine B dye in alkaline solution.

1.2 Thermoplastic elastomers

Thermoplastic elastomer is a class of multi-phased materials possessing combined properties of thermoplastic elastomer and thermoset rubber. They demonstrate mechanical properties comparable to those of vulcanized rubber at service temperature without filler reinforcement, cross-linking agent, nor compromising ease of processing at elevated temperatures. According to ISO 18064, thermoplastic elastomers are classified into seven distinct categories based on their bonding characteristics and chemical composition. These categories include thermoplastic polyamide elastomers (TPA), copolyesters (TPC), polyolefins (TPO), styrenics (TPS), polyurethanes (TPU), vulcanizates (TPV), and a miscellaneous category (TPZ) for thermoplastic elastomers that do not fall within the aforementioned classifications.

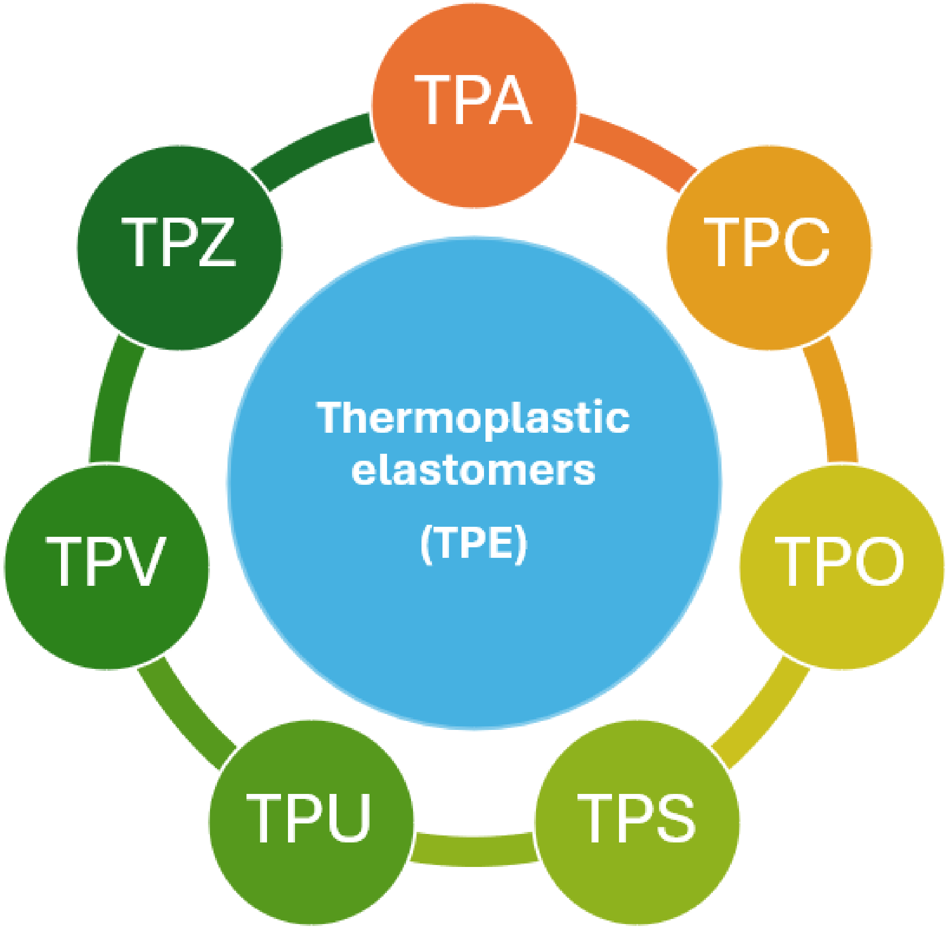

Figure 7: Classification of thermoplastic elastomers according to ISO 18064.

In block copolymer based TPEs, which constitute the majority of TPEs, segments with a higher Tg form the glassy phase and its corresponding chain entanglements serve as physical cross-linking joints, contributing to mechanical strength, while the elastomeric phase imparts elasticity, flexibility, and toughness to the material.[43] The advancement of living anionic polymerization[44] has enabled the synthesis of ABA triblock copolymers with precise molecular weight control and a narrow molecular weight distribution within a short production cycle. When integrated with high-throughput manufacturing techniques such as melt extrusion and injection molding, thermoplastic elastomers, particularly styrenic block copolymers, have been widely utilized across diverse applications, including footwear[45], automotive components[46], adhesives[47], asphalt modification[48], and biomedical devices[49], etc. For instances, Costa et al.[50] developed a wearable strain sensor incorporating poly(styrene-b-ethylene-butylene-b-styrene) SEBS and different graphene-based fillers, exhibiting a highly sensitive piezoresistive response. The sensor demonstrated a gauge factor ranging from 10 to 120 for strains up to 10%, highlighting its potential for applications in monitoring smart electronics.

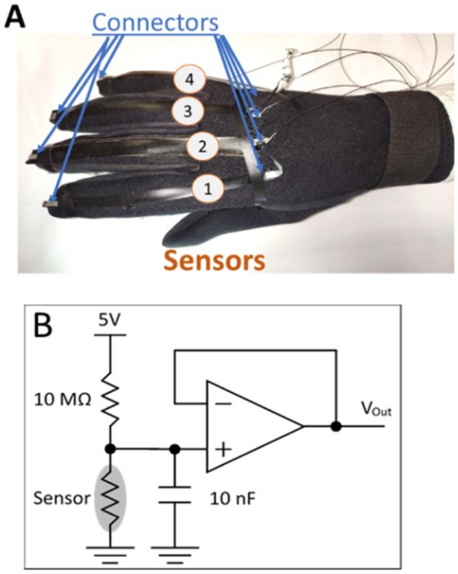

Figure 8: (a) Prototype wearable strain sensor glove with fixed SEBS/rGO stripes. (b) Schematic of signal detecting circuit for the SEBS/rGO sensor. Reproduced with permission from ref. 50.

Quaternized poly(styrene-b-butadiene-b-styrene) (SBS) has been investigated as an anion exchange membrane for fuel cell applications.[51] The presence of a hydrophobic and mechanically robust polystyrene block enhances the membrane's mechanical strength while minimizing its swelling ratio. Furthermore, the double bonds in the polybutadiene segments provide reactive sites for potential cross-linking, which was proposed to mitigate the degradation of grafted quaternary ammonium groups and thus improves the membrane's stability under alkaline conditions.

Aside from styrenic block copolymer, TPU is another common applied TPE wihch known for its high abrasion resistance.[52] When the sft segement is made of polyisobutylene, its application can be extended into biomedical field. Cozzens[53] et al. concluded that PIB-based TPU exhibited superior resistance to long-term metal ion oxidative degradation. Specifically, after 12-week immersion in 20% hydrogen peroxide solution, no surface cracking was found under SEM, and the material exhibited minimal loss in molecular weight and mechanical properties. This exceptional stability is attributed to the nonpolar and oxidative stable nature of PIB.

1.3 Additive manufacturing

Additive manufacturing or 3D printing is a recent development of material processing technique capable of constructing sophisticated shapes without a mold or material subtraction such as milling. A typical 3D printing process can be summarized into 4 steps: (1) A target standard tessellation language model is generated by computer-aided design or scanning a real object. (2) G-code containing information of each cross-section layer was converted based on the digital model using slicing software based on predefined printing parameters. (3) Printed objects are constructed through the sequential deposition of the selected building material, following the G-code instructions in a layer-by-layer pattern. (4) Optional post-printing processing for the finished part. Depending on the printer design, a diverse range of materials, including ceramics[54], metals[55], and polymers[56], can be processed through 3D printing. Among various 3D printing techniques, fused deposition modeling (FDM) is regarded as the most widely adopted method due to its simplicity, cost-effectiveness, high processing speed and its ability to fabricate hybrid structures by incorporating multiple materials simultaneously[57]. During this 3D printing process, the filament-based feedstock is directed into the printhead, where it is heated to reduce its viscosity, facilitating extrusion and ensuring proper deposition. The liquified polymer is deposited on the substrate controlled by G-code, undergoing solidification and enabling the cohesive bonding of adjacent layers to form the final structure.

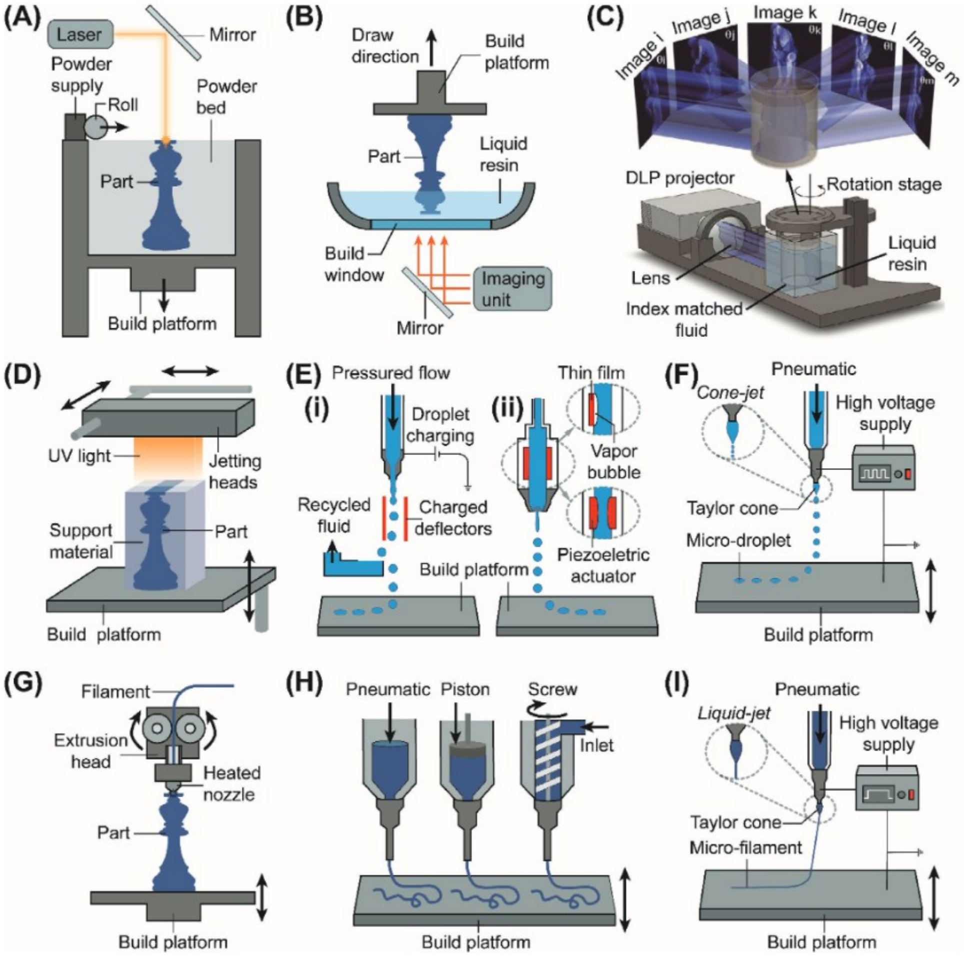

Figure 9: Schematics for different additive manufacturing techniques: (a) Selective laser sintering. (b) Digital light processing. (c) Computed axial lithography. (d),(e): inkjet printing, (i) continuous mode, (ii) drop-on-demand mode. (f) E-jet printing. (g) Fused

deposition modeling. (h) Direct ink writing. (l) Electrohydrodynamic direct-writing. Reproduced with permission from ref. 58.

Additionally, shape memory effects can be achieved when the involving material can have response to external stimuli. Cheng et al.[59] demonstrated the fabrication of a personalized elbow protector prototype using a U-PLA-PCL linear unsaturated copolymer with dual-shape memory capabilities. Specifically, the polylactic acid phase accounts for part's mechanical strength and printability, while the polycaprolactone phase, characterized by its high crystallinity, functions as the "switching segments" responsible for shape memory behavior. Additionally, in-situ UV cross-linking enhances the interlayer bonding strength, further improving part durability.

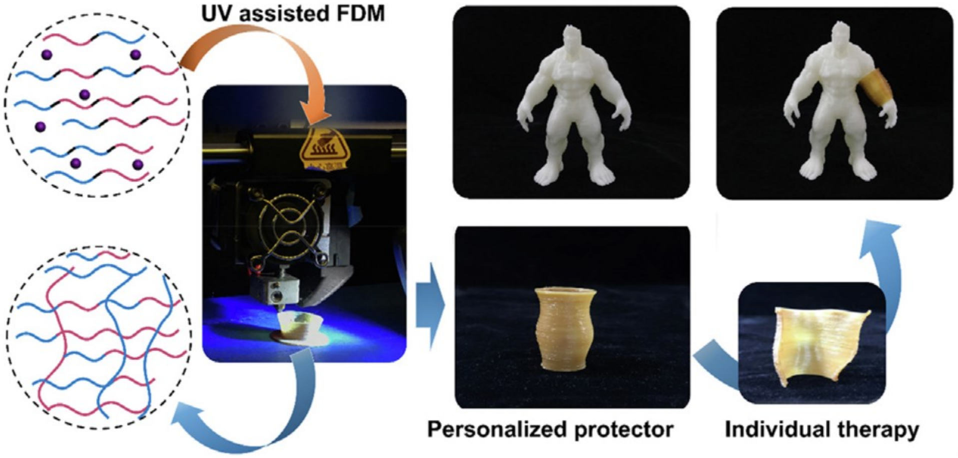

Figure 10: The schematic of personized protector realized by the shape changing behavior of PLA-PCL block copolymer after UV-assisted 4D FDM printing. Reproduced with permission from ref. 59.

In most additive manufacturing techniques, feedstock materials are deposited pointwise and the whole structure is formed in a layer-by-layer fashion. This layered approach often results in anisotropic mechanical properties, which may negatively affect the overall mechanical performance of the printed object. To address this limitation, volumetric printing techniques has been developed, enabling the simultaneous fabrication of an entire 3D structure in a single step. This approach eliminates interfacial weaknesses between layers and thus leads to more uniform mechanical properties. Regehly et al.[60] combined intersecting light beams of different wavelengths and dual-color photoinitiator to achive fast and precise volume production of cross-linked photoresin.

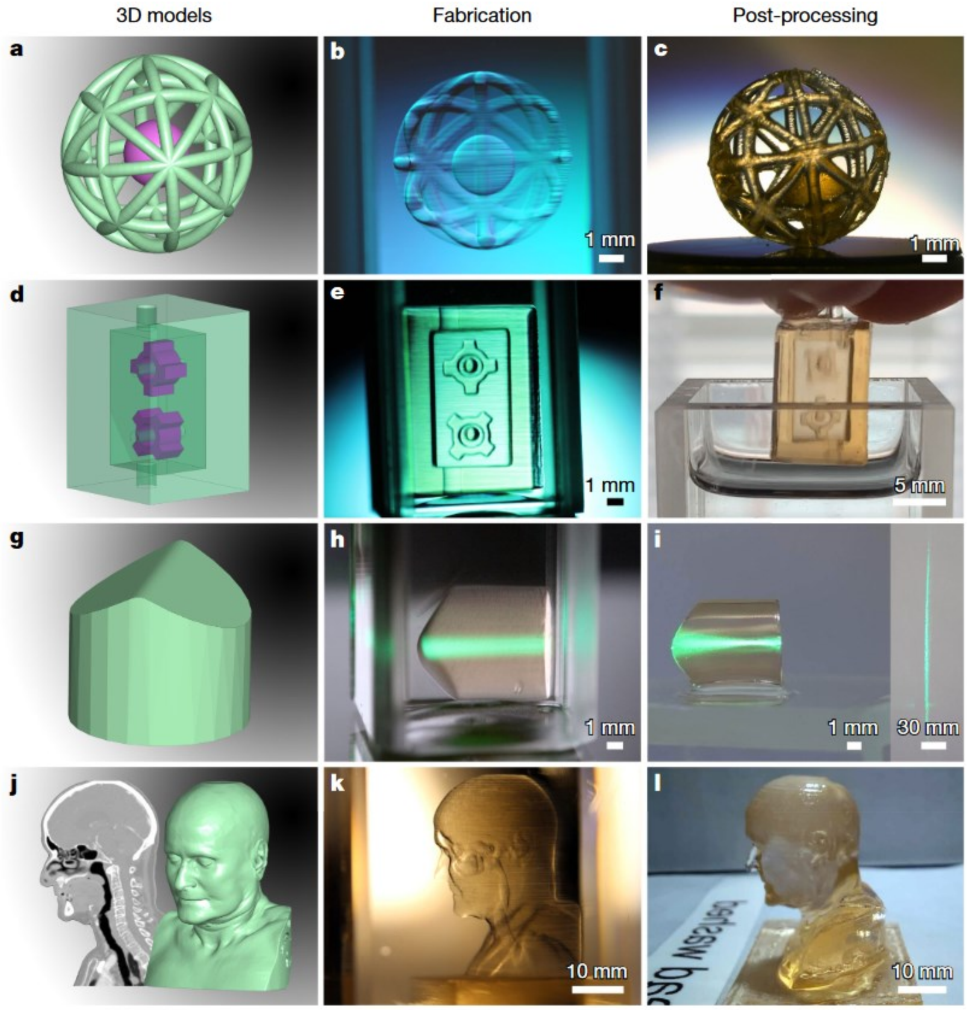

Figure 11: (a, d, g, j) Digital models. (b, e, h, k) Printed objects during the printing process: spherical cage with free-floating ball, encapsulated flow cell with rotary wheels, aspherical powell lens, and anatomical model, respectively. (c, f, i, l) objects after subsequent isopropanol washing, UV curing and thermal treatment. Reproduced with permission from ref. 60.

1.4 Metal halide perovskite (MHP) quantum dots (QDs)

Perovskites, or more specifically, metal halide perovskites (MHPs), are a type of semiconducting materials with unique optical and electronic properties.[61,62] They have been at the forefront of photovoltaics and optoelectronics research due to their efficient optical absorption and emission in the visible range.[63,64] MHPs generally have a ABX_3 crystalline structure where the organic or inorganic cations (such as MA: $CH_3NH_3^+$, FA: $CH(NH_2)_2^+$, or Cs^+) occupy the voids (A sites) created by eight corner-sharing BX_6 (B is bivalent cation and X is halide anion) octahedron.[64,65]

MHPs possess direct or indirect bandgaps and high joint density of states, they generally have more efficient light-absorbing capability compared with conventional semiconductors. The tunable bandgap via halide exchange reaction and exciton dissociation through radiative recombination enable their light-emitting capabilities with a wide color gamut. Another advantage of MHPs as a semiconductor is their intrinsic defect tolerance[66]. Mid-gap trap states due to interstitial or antisite defects are difficult to form in MHPs due to the large formation energy. Vacancy defects with low formation energy only create shallow trap states near the bandgap edges,[67] which cannot dramatically alter the perovskite's electronic structure. The efficient photoelectric conversion and efficient charge transport property of MHPs also make them suitable for photocatalytic applications.

MHPs can be synthesized and used in bulk state or in the form of nanoparticles and quantum dots (QDs). Compared to their bulk crystal counterpart, perovskite QDs have a discrete, size-dependent bandgap structure[68] due to the quantum confinement effect. A blueshift in the emission spectrum will take place as the size of QDs gets smaller towards free electron’s de Broglie wavelength.[69] Due to the restricted electron and hole wavefunction, a sharp DOS appears and leads to narrow optical emission as well as high color purity. Moreover, perovskite QDs can reach near-unity PL quantum yield with highly tunable emission colors[70–72]. Therefore, perovskite QDs are more and more used for next-generation display and optoelectronic applications.

Bulk halide perovskite is often deposited as thin films using a solution-based one-step procedure where the crystal growth is controlled by antisolvent-dripping[73] or Lewis acid-base adduct formation.[74] Perovskite QDs are usually synthesized by hot injection method,[75] or ligand assisted reprecipitation (LARP).[76] The LARP method is usually conducted by dissolving the perovskite precursors and organic ligands in a nonpolar solvent, followed by dropwise injecting into a vigorously stirring bad solvent. All-inorganic perovskite QDs are usually synthesized by the hot-injection method, for instance, Cs-oleate hot solution is injected into halide precursors. The majority of the QDs formation takes place within a few seconds after the fast injection and thus size control of QDs is achieved by varying the reaction temperature or incorporating alkylammonium halide during the synthesis.[77]

1.4 Fabrication of BCP-QDs optical materials

Despite the advantages and desirable properties of perovskites and their nanostructures, there are two main limitations that constrain their broader applications. Firstly, MHPs generally have limited stability and are vulnerable to many environmental factors, including moisture, certain solvents, oxygen, and heat.[78–80] Perovskite QDs with high surface areas are more susceptible to the effects of the environment. Secondly, direct patterning of solid perovskite materials with photolithography-based techniques is not feasible due to the poor stability of perovskite under moisture, solvents, and dry etching.[81] The lack of efficient nanopatterning methods prevents their further development and applications.[82] Other nanopatterning techniques such as direct laser writing and focused ion beam milling have been explored for perovskites,[83,84] but those methods are time-consuming, costly, and difficult to scale up.

The integration of perovskite nanostructures with block copolymers provides a very promising approach to address those two challenges.[85–87] By designing the molecular structure and properties, BCPs have the potential to improve the stability of perovskite nanostructures by encapsulating them in a highly stable and soft matrix.[88] On the other hand, the microphase-separated BCP matrix makes it possible to achieve molecular-level control of the alignment and assembly of perovskite nanostructures.[89–91] There is important recent progress in this specific topic of integrating perovskite with BCPs for the creation of soft functional optical materials and devices. This Highlight article aims to summarize those recent advancements in a logical and concise manner based on the versatile roles of BCPs in such hybrid optical materials.

We identified the following major categories of perovskite-BCP hybrid structures based on the different roles of BCP in the system. First, the microphase-separated morphology of BCP provides an efficient method of nanopatterning of perovskite materials. This can be further divided into two methods: in situ formation of perovskite nanocrystals (NCs) from their precursors inside BCP template; or the directed assembly of perovskite NCs inside the BCP matrix. Second, BCP micelles or star-shaped BCP act as the template for perovskite crystallization and form hybrid nanostructures. Third, BCP acts as the macromolecular ligands for perovskite NCs during its solution synthesis. Fourth, BCP encapsulation of perovskite NCs into hierarchical composite particles. Fifth, BCP is blended with perovskite and forms bulk composite films.

1.4.1 BCP as nanopattern template for perovskites

Nanopatterning of perovskites is critical for their advanced applications in optics and photonic devices. Due to the capability to form well-defined microphase-separated morphology of BCPs in nanometer scale, they provide a scalable and low-cost approach for nanopatterning of perovskite. This can potentially be achieved via two different approaches: (1) in situ formation of perovskite nanocrystals from their precursors within the BCP template; (2) directed assembly of perovskite nanocrystals within the microphase-separated BCP matrix.

In situ formation of perovskite NCs within BCP template: In order to achieve the in-situ formation of perovskite NCs within BCP template, at least one of the blocks on BCP needs to have favorable or preferential interaction with perovskite precursors. The most common approach is by selecting BCPs with functional groups such as pyridine ring, carbonyl, or carboxyl group that can have electrostatic or Lewis acid–base interaction with the cationic ions on perovskites or their precursors. The accumulation of perovskite precursors around selective blocks of BCP and their subsequent crystallization enables the generation of spatially defined perovskite NCs.

For instance, the precursor solution (MABr and $PbBr_2$) of methylammonium lead halide ($MAPbX_3$, X = Br^-, I^-) perovskite was mixed with poly(styrene)-*block*-poly(2-

vinylpyridine) (PS-*b*-P2VP),[92] and the mixture was spin-coated on a substrate. The obtained thin hybrid films showed well-defined patterns including cylinders, lamellae, and cylindrical mesh, with controlled domain size (40–72 nm). The hybrid structures showed enhanced exciton recombination and longer exciton lifetime due to the reduced crystal size as well as the passivating effect of the P2VP phase that reduced surface defects on the perovskite. Excellent heat and moisture resistance of such hybrid structures was also demonstrated. In another report by the same group,[93] the nanopatterned hybrid structures composed of $MAPbBr_3$ perovskite and PS-*b*-P2VP were used as the main component for artificial photonic synapses or photoreceptor cells for information storage and learning applications. The microphase-separated morphology and the $MAPbBr_3$ density were spatially tuned to stimulate the rod and cone cells distribution in the visual perception system.

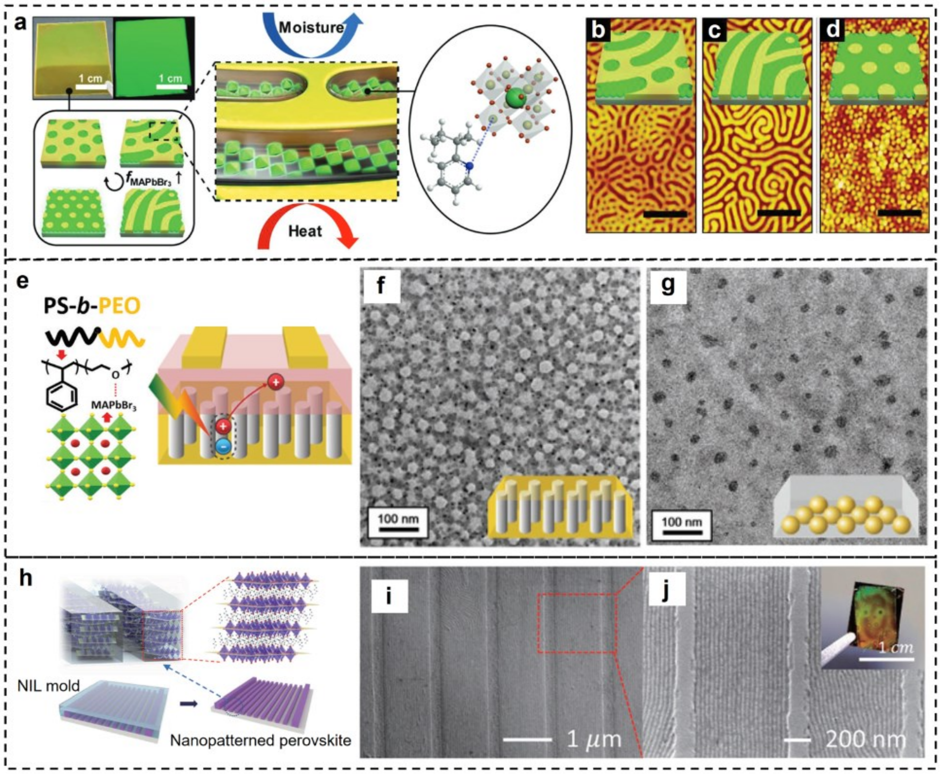

Figure 12: (a) Schematic of the fabrication of nanostructured perovskite thin films templated with PS-*b*-P2VP self-assembly. (b)–(d) AFM images of the PS-*b*-P2VP/$MAPbBr_3$ nanostructured films (Mn = 125 kg mol^{-1}, f_{P2VP}= 0.32) with (b) 40%, (c) 60%, and (d) 100% $MAPbBr_3$. The scale bars are 500 nm. Reproduced with permission from ref.92. (e) Schematic of the Lewis acid–base interaction between PS-*b*-PEO and $MAPbBr_3$ perovskite, and the charge transfer process in the BCP/$MAPbBr_3$ composite films in the photomemory device. (f)–(g) TEM images of (f) symmetric PS-*b*-PEO/$MAPbBr_3$ and (g) asymmetric BCP/$MAPbBr_3$ composite films after solvent vapor annealing. Reproduced with permission from ref.93. (h) Schematic of the fabrication of nanopatterned 2D perovskites by NIL with a PS-*b*-PDMS derived mold. (i)–(j) SEM images of the BA_2PbBr_4 nanopatterns produced by this method. Reproduced with permission from ref. 94.

Using a similar strategy, perovskite precursors (MABr and $PbBr_2$) were mixed with polystyrene-*block*-poly(ethylene oxide) (PS-*b*-PEO) copolymers to form hybrid thin films[94], and well-defined spatial pattern of the perovskite nanocrystals was achieved. The chelation between the lead ion and PEO segment promoted the anti-solvent functionalities of the hybrid films. Such perovskite/PS-*b*-PEO hybrid films were used as photoactive floating gate to elucidate the effect of morphology on the photo-responsive characteristics of photomemory. In another report,[95] they used a similar method to fabricate quasi-2D $FAPbBr_3$/PS-*b*-PEO hybrid films and used them as photoactive floating gate for flash photomemory devices with high performance.

In another recent study,[87] Ruddlesden–Popper perovskites/BCP hybrid structures were prepared by mixing the precursors of phenylethylene methylammonium lead bromide ($PEA_2MA_{n-1}Pb_nBr_{2n+1}$, n= 2, 3) and PS-*b*-PEO, followed by thermal annealing and crystallization. The perovskite crystals were geometrically confined within the microphase segregated BCP nanopatterns, the interaction between the Pb^{2+} ions of perovskite and the oxygen atoms of PEO in BCP resulted in both enhanced phase purity and ordered crystallization. Hung *et al.* demonstrated stretchable photonic device fabrication based on triblock copolymer maltoheptaose-*block*-polyisoprene-*block*-maltoheptaose (MH-*b*-PI-*b*-MH),[90] which provided a spatially confined environment for the crystallization of cesium lead halide ($CsPbX_3$) perovskite NCs. Such selective distribution was attributed to the coordination between the hydroxyl groups of the MH segment and the Pb^{2+} ions in the perovskite precursor. In another recent report,[96] PS-*b*-P2VP was assembled into alternating in-plane lamellae structure and showed structural color. By synthesizing $CsPbX_3$ or $MAPbX_3$ NCs inside the BCP via a two-step solution process, dual mode structure color and photoluminescent were demonstrated, which enabled encryption and decryption of sophisticated information.

On the other hand, the microphase-separated morphology of BCP can be used as the template for nanoimprinting lithography, which provides another method of nanopatterning of perovskites. For instance, PS-*b*-PDMS was self-assembled on a pre-patterned Si substrate to form well-defined nanopatterns with PDMS cylinders (thickness ≈30 nm) embedded in the PS matrix,[94] and the BCP pattern was then used for the fabrication of nanopatterned PDMS stamps . Subsequent nanoimprinting of the precursor film of a 2D perovskite ($A'_2MA_{n-1}Pb_nX_{3n+1}$, A′ = BA, PEA, X = Br, I) using the PDMS stamp resulted in well-defined 1D patterns of those 2D perovskites. Such nanopatterned 2D perovskites showed enhanced photoluminescence (PL) quantum yields (about four times higher) than those of the corresponding control flat films. In another report,[97] nanoimprinting guided self-assembly was conducted to fabricate nanopatterned hybrid perovskite structures. The two-step method consisted of spin-coating a mixture of the $MAPbBr_3$ precursors and PS-*b*-P2VP on the substrate followed by nanoimprinting. The P2VP block passivated the QDs surface through Lewis acid–base interaction and the nanopatterning provided local-field enhancement induced by Mie resonance, both contributing to the enhanced photoluminescence and stability.

Directed assembly of perovskite NCs with BCP matrix: The second approach to achieving nanopatterning of perovskites with BCP is through the directed assembly of perovskite NCs within the BCP matrix. In order to achieve precise control of the internal structure and interfaces in the perovskite–BCP composites, a selective block of the BCP needs to have preferential interaction with the organic or polymeric ligands on perovskite NC surface. In our recent work,[98] we designed and synthesized polyisobutylene (PIB)-based polymer ligands for $CsPbBr_3$ QDs, and based on the strong and selective interactions between the polymer ligands and polystyrene-*b*-polyisobutylene-*b*-polystyrene (SIBS) copolymer, a series of functional nanocomposites were prepared and their structure–

property relationship was elucidated. We discovered that the chemical compatibility of the polymer ligands and copolymer matrix is the key to achieve precise control of the distribution of perovskite QDs inside the soft matrix and prevent aggregation. Moreover, the PIB-based ligands on perovskite QDs and the incorporation of p-QDs inside the PIB domain of SIBS copolymer can substantially enhance the PL stability due to the high impermeability and chemical stability of PIB. Such QDs/SIBS composites have excellent flexibility, stretchability and photoluminescent properties, which can potentially be used for flexible optoelectronics, optical storage, and displays.

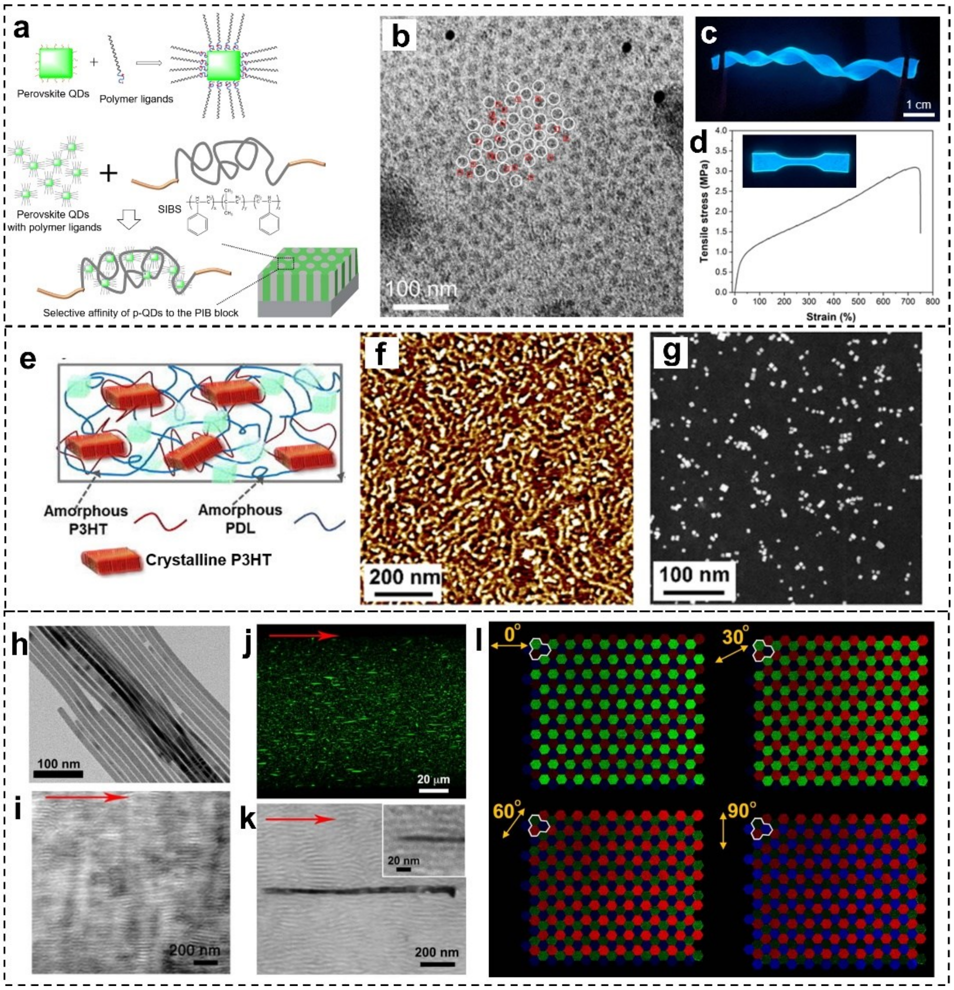

Figure 13: (a) Schematic of the selective interaction between PIB-ligand functionalized $CsPbBr_3$ QDs and SIBS. (b) Representative TEM image shows the spatial distribution of QDs, which are preferentially located at PIB domains. (c) Photo of the QDs/SIBS composites with excellent flexibility and photoluminescence. (d) Stress-strain curves of the QDs/SIBS composite. Reproduced with permission from ref.92. (e) Schematic illustration of the composite composed of PDL-b-P3HT-b-PDL copolymer and perovskite QDs. (f-g) AFM phase image and TEM image of the nanocomposites composed of fibers-like morphology of P3HT and uniformed distributed QDs. Reproduced with permission from ref.99. (h) TEM image of $CsPbBr_3$ perovskite nanowires. (i) TEM image of the SIS polymer filament. (j) Intensity projection of z-stack fluorescence confocal image of the printed nanowire-SIS hybrid filament. (k) TEM image of the printed nanowire-SIS composite filament. (l) Optical images of printed pixel arrays showing polarization-dependent emission multiplexing. Reproduced with permission from ref.100.

Conjugated triblock copolymer with soft poly(d-decanolactone) (PDL) block and hard poly(3-hexylthiophene) (P3HT) block were integrated with $CsPbBr_3$ QDs to form hybrid structures.[99] By selective solvent treatment and tuning PDL branch number, the P3HT blocks showed fiber-like crystalline structure that led to improved self-aggregation of perovskite QDs, increased grain size, and optimized interfaces between P3HT and perovskite QDs. The PDL blocks also provided mechanical flexibility, making it possible for a stretchable photosynaptic transistor that operated with ultralow energy consumption.

Spatial control or alignment of perovskite nanostructures inside a BCP matrix can also be achieved by extrusion-based 3D printing. For instance, Zhou *et al.*[100] demonstrated 3D printing with nanocomposites composed of $CsPbX_3$ nanowires and polystyrene-polyisoprene-polystyrene block copolymer (SIS) block copolymer. Alignment of perovskite nanowires in the soft matrix can be achieved with different printing paths. Such alignment resulted in soft optical materials with highly anisotropic and polarized absorption and emission. Optical devices based on such nanocomposites including optical storage and full-color displays were also demonstrated.

1.4.2 BCP micelles/stars as template for the synthesis of perovskite NCs

Besides the capability to self-assemble into microphase-separated morphology in the solid state, another interesting feature of BCP is that they can assemble into micelles of different geometries in selective solvents. For instance, amphiphilic BCPs with hydrophilic and hydrophobic blocks tend to assemble into spherical micelles consisting of a hydrophobic core and hydrophilic shell in aqueous solution to minimize the interfacial free energy. Such micelles can be used as the template or nanoreactor for perovskite NCs synthesis.[101]

For instance, PS-*b*-P2VP micelles were used as the template for $MAPbX_3$ NCs synthesis.[102] Due to the encapsulation by polymer shell, the perovskite NCs showed enhanced stability against water degradation and halide ion migration. Thin films comprising these NCs exhibited a more than 15-fold increase in lifespan in comparison to pristine NCs in ambient conditions and had good stability even when immersed in water. In a follow-up study,[103] $MAPbBr_3$ perovskite QDs were synthesized using PS-*b*-P2VP micelles as nanoreactor and the length of PS block on Förster resonance energy transfer (FRET) efficiency was studied. Longer PS block resulted in higher stability but hindered the dipole–dipole interaction between the QDs acceptor and 2D $CsPbBr_3$ nanoplatelets donors. It was also demonstrated that the combination of BCP micelle and organic ligands during perovskite NCs formation process led to enhanced optical stability.[104] The organic ligand helped to passivate the QDs surface inside the micelles and excessive ligands formed a lamellar bilayer structure surrounding the micellar-encapsulated perovskite QDs.

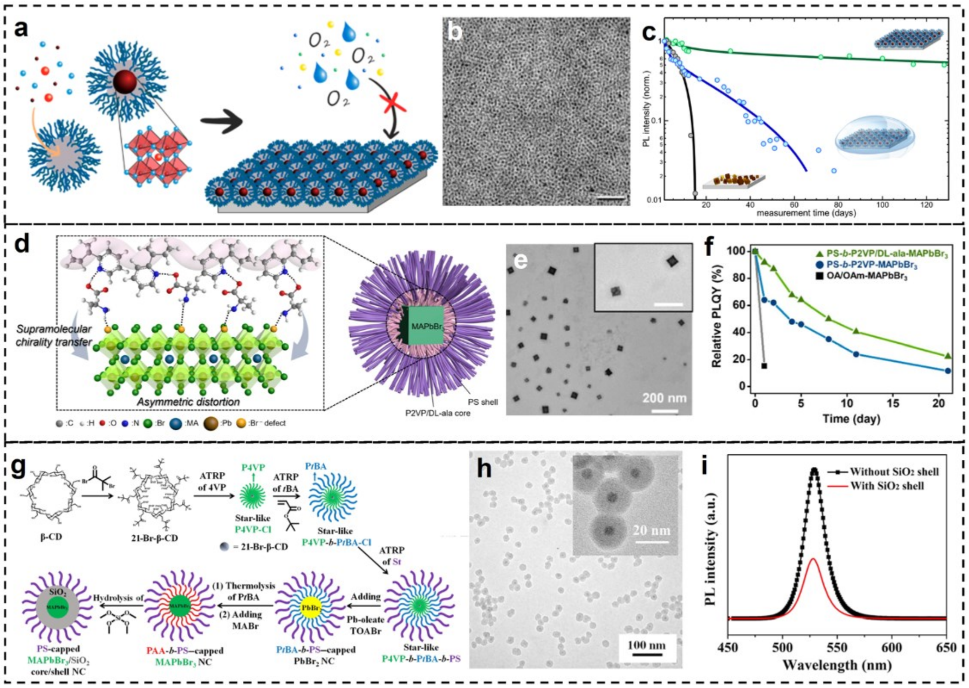

Figure 14: (a) Schematic representation of the preparation of perovskite NCs from PS-*b*-P2VP copolymer micelles and their enhanced stability. (b) TEM image of the prepared $MAPbX_3$ NCs. (c) Temporal development of PL intensity of the hybrid perovskite NC films in ambient conditions and under water, compared with pristine regular MAPI NCs. Reproduced with permission from ref.102. (d) Structure of the chiral PS-*b*-P2VP/DL-ala BCP micelle encapsulated $MAPbBr_3$ NCs. (e) TEM image of the prepared $MAPbBr_3$ NCs. (f) Thermal stabilities of the PS-*b*-P2VP/DL-ala micelle-encapsulated $MAPbBr_3$ NCs (green). The OA/OAm-capped $MAPbBr_3$ NCs (black) and the PS-*b*-P2VP micelle-encapsulated $MAPbBr_3$ NCs (blue) were used as controls. Reproduced with permission from ref.105. (g) Stepwise representation of the synthetic route to PS-capped $MAPbBr_3/SiO_2$ core/shell NCs. (h) TEM images of PEO-capped $MAPbBr_3/SiO_2$ core/shell NCs. (i) PL spectra of $MAPbBr_3$ core NC before and after the SiO_2 shell coating dispersed in toluene. Reproduced with permission from ref.106.

Using a similar strategy, POSS-PMMA-*b*-PDMAEMA (POSS: polyhedral oligomeric silsesquioxane, PDMAEMA: poly 2-(dimethylamino)ethyl methacrylate) copolymer micelles were used for the preparation of $CsPbBr_3$ QDs.[107] The hydrophobic POSS and PMMA blocks provided excellent barrier properties against moisture and led to enhanced stability of the perovskite NCs. Beyond simple spherical or cubic shapes, perovskite NCs with other shapes can also be synthesized by the block copolymer micelle template method. For instance, nanoplates and rod-like $MAPbBr_3$ NCs were demonstrated by controlling the PS-*b*-P2VP block copolymer micelles formation and their disassembly.[108]

Chiral perovskite NCs were also synthesized by using block copolymer inverse micelles as the template. PS-*b*-P2VP was mixed with racemic DL-alanine (DL-ala) through hydrogen bonding and then used as the template for $MAPbBr_3$ NC synthesis.[105] The selective occupation of perovskite precursors within chiral micellar cores resulted in chirality transfer to the electronic states of the perovskite NCs, which led to a high chiroptical response with an anisotropy factor of -2.0×10^{-4}. The surface encapsulation also led to enhanced PL stability. In another report,[109] $CsPbX_3$ and $FAPbX_3$ NCs were synthesized from PAA-*b*-PS micelle as the template. Functional additive organic molecules were also incorporated into the hybrid structure to enhance the nanocrystal stability against polar solvents and high flux irradiation. Halide exchange process of the hybrid perovskite NCs was possible when the PS block was swollen in a good solvent.

Besides spherical micelles formed by self-assembly of BCP, star-like BCPs have a similar morphology but chemically bonded structure, which can also be used as the molecular template for perovskite QDs synthesis and functionalization. For instance, by using sequential atom transfer radical polymerization (ATRP), star-like P4VP-*b*-P*t*BA-*b*-PS BCPs were synthesized and used as the templates for $MaPbBr_3$ NC synthesis in the P4VP core region.[106] Subsequent thermolysis of PtBA and hydrolysis of tetramethyl orthosilicate resulted in the formation of SiO_2 shell on the surface of $MAPbBr_3$ NC. The size and shell thickness of such hybrid perovskites NCs can be tuned. Such hybrid perovskites NCs showed enhanced PL stability due to the passivation effects of the SiO_2 shell and chemically-bonded polymer ligands on the surface.

Using a similar strategy, $CsPbBr_3$ QDs were synthesized by using star-like PS-*b*-PAA as the nanoreactors.[110] In addition, hollow perovskite NCs with a PS core were also prepared with star-like PS-*b*-PAA-*b*-PS as the template.[111] The presence of the PS core caused a blue shift of PL spectra which can be adjusted by controlling the PS core size. In another report,[112] star-like PAA-*b*-P3HT BCP was used as the template for $CsPbBr_3$ QDs synthesis. The Lewis acid–base interaction between P3HT ligands and the QDs resulted in efficient charge carrier separation compared with the physical mixture of P3HT and perovskite QDs. Similarly, star-like PHEMA-*g*-(PAA-*b*-PS) block copolymers were used as the template for preparation of $CsPbBr_3$ QDs,[113] which showed enhanced stability against UV, moisture, heat, and water, due to permanently ligated hydrophobic PS on the surface.

1.4.3 BCP as macromolecular ligands for perovskite NCs

BCPs can also be used as the macromolecular ligands for perovskite NCs, which have the effect of enhanced stability and dispersion in different solvents. Compared with conventional short organic ligands for perovskite NCs, the polymeric ligands have more flexibility in chemical composition and introduce new functionalities. For instance, PS-*b*-PAA was introduced during the formation of $CsPbBr_3$ QDs,[114] and the amphiphilic copolymers acted as ligands for the perovskite QDs. Enhanced stability and photoluminescence quantum yields were achieved compared with conventional QDs with short organic ligands.

In another study,[115] PS-*b*-PEO copolymer was used as the polymer ligands for $MAPbBr_3$ QDs synthesis. Such perovskite QDs can be dispersed well individually or self-assembled into well-defined vesicular nanostructures with high photoluminescence quantum yields. The high stability in water enabled its application in cell imaging. PBMA-*b*-PSBMA and PBMA-*b*-PMPC (PBMA: poly(*n*-Butyl methacrylate), PSBMA: poly(sulfobetaine methacrylate), PMPC: poly(2-methacryloyloxyethyl phosphorylcholine)) zwitterionic copolymers were used as polymer ligands during $CsPbX_3$ NCs synthesis.[116] The prepared perovskite NCs with BCP ligands were found to disperse and maintain their fluorescence in a range of polar organic solvents and enable direct integration into optically transparent nanocomposite thin films with high perovskite content.

Perovskite NCs with other geometries can also be synthesized with BCP as the polymeric ligands. For instance, PS-*b*-P4VP was used as the polymer ligands for $CsPbBr_3$ nanowires.[117] The surface-modified nanowires showed enhanced photoluminescent emission and good colloidal stability against water. Such nanowires were further assembled into highly aligned monolayer by the Langmuir–Blodgett technique and exhibited anisotropic optical properties.

Furthermore, the BCP ligands can also be used as the intermediate for the synthesis of inorganic shell on the surface of perovskite NCs. For instance, He *et al.* demonstrated the synthesis of perovskite nanosheets protected by TiO_2 shell and hydrophobic PMMA brushes.[118] Specifically, PMMA-*b*-PAA chains were anchored onto the nanosheet surface as multidentate ligands by a ligand exchange process. Then, *in situ* hydrolysis of mixed titanium butoxide was catalyzed by a trace amount of moisture and the -COOH groups of the PAA segments, generating a layer of TiO_2 precisely on the perovskite surface with PAA blocks. The dual-shelled perovskite showed excellent stability against moisture, polar solvents, aliphatic amine, *etc*.

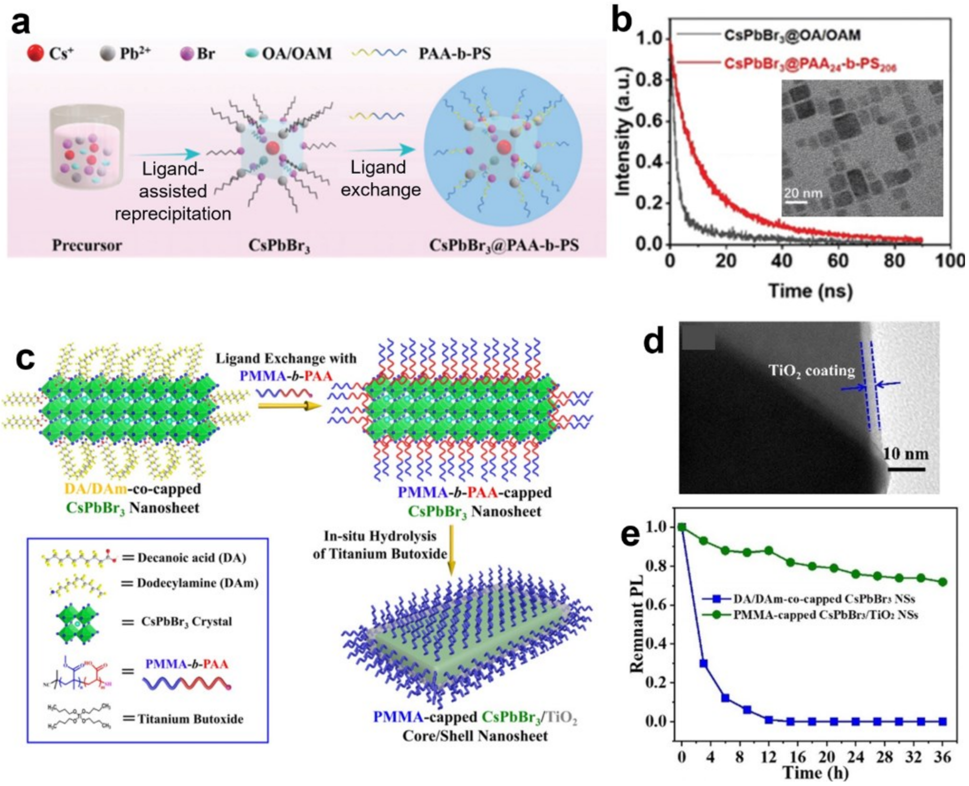

Figure 15: (a) Schematic of the process for the formation of $CsPbBr_3$@PAA-*b*-PS structure. (b) Time-resolved PL of the NCs with copolymer ligands and short organic ligands. Inset is the TEM image of the NCs with copolymer ligands. Reproduced with permission from ref.114. (c) Schematic illustration of crafting $CsPbBr_3/TiO_2$ core/shell NS with chemically bonded PMMA ligands *via* a two-step process. (d) TEM image of the PMMA-capped $CsPbBr_3/TiO_2$ core/shell NSs. (e) PL thermal stability of the PMMA-capped $CsPbBr_3/TiO_2$ NS and its control sample at 70 °C. Reproduced with permission from ref.118.

1.4.4 BCP encapsulation of perovskite NCs into composite particles

When BCPs and perovskite NCs are placed in a selective solvent or the BCP is polymerized with the presence of perovskite NCs, it is possible to form composite particles with a BCP shell or matrix and multiple perovskite NCs encapsulated in the interior. For instance, $CsPbBr_3$ NCs were encapsulated in polymer capsules made of PS-*b*-PAA copolymers by using selective solvents.[119] Such copolymer capsule encapsulated perovskite NCs showed an high photoluminescence quantum yield (~60%) that was preserved over two years in water. Such capsules can be used as photoluminescent probes for cell imaging at a very low dose so that no significant cell toxicity was found.

Perovskite QDs can be used as both luminescence centers and photocatalysts to prepare organic–inorganic nanohybrid assemblies. For instance, Shi *et al.*[120] used perfluorooctanoic acid-modified $CsPbBr_3$ QDs as the photocatalyst to induce *in situ* self-assembly of POEGMA-*b*-PFOEMA (POEGMA: poly(poly(ethylene glycol) monomethyl ether methacrylate), PFOEMA: poly(perfluorooctyl)ethyl methacrylate) nanoparticles by RAFT polymerization in which the POEGMA worked as the macro chain transfer agent and the FOEMA as the monomer. Modulation of the block length led to the transition from nanorods to spindle-like nano-assemblies and these hybrid nanoparticles showed high fluorescence and enhanced stability.

In another report, $CsPbBr_3$ QDs were encapsulated by PEG-*b*-PCL (PCL: polycaprolactone) copolymers and the hybrid structures showed improved water stability and biocompatibility,[121] Such structures were used for H_2S gas sensing due to the quenching effect of H_2S to the PL intensity of perovskite QDs. Similarly, Colloidal $CsPbBr_3$ QDs were encapsulated by amphiphilic PEO-PPO-PEO triblock copolymer,[122] such hybrid nanospheres showed good water dispersity and stable photoluminescence.

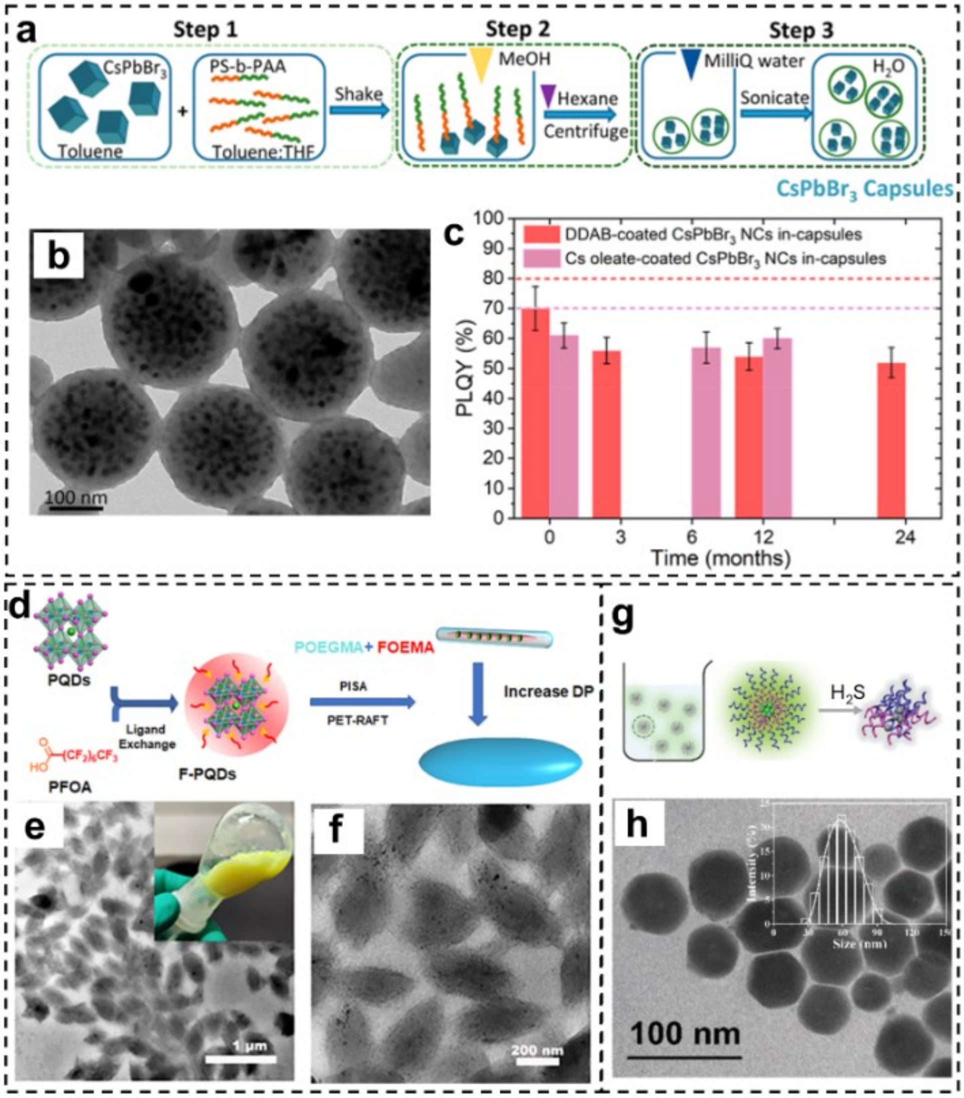

Figure 16: (a) Schematic illustration of the process for the fabrication of the copolymer capsules embedding the CsPbBr$_3$ NCs. (b) TEM image of the capsules with CsPbBr$_3$ NCs inside. (c) PLQY tracking of capsules dispersed in water over months. Reproduced with permission from ref.119. (d) Schematic of the ligand exchange strategy of PQDs and the PISA process based on PET-RAFT polymerization. (e) and (f) TEM images of the hybrid particles with CsPbBr$_3$ QDs embedded inside. Reproduced with permission from ref.120. (g) Schematic of the preparation of polymer micelles encapsulated QDs and the H$_2$S-responsive behavior. (h) TEM image of the hybrid structures. Reproduced with permission from ref.121.

1.4.5 BCP/perovskite bulk composite films

When BCP is introduced during the fabrication/crystallization of bulk perovskite films, it is possible to form BCP/perovskite bulk composite films when there is strong and/or selective interaction between BCP and crystalline perovskite. Conjugated BCP can be mixed with perovskite precursors to prepare hybrid semiconductors for high-performance solar cell fabrication. For instance, Sun *et al.* integrated PBDB-T-*b*-PTY6 with lead halide perovskites into bulk heterointerfaces for solar cell devices.[123] The incorporation of BCP did not obviously change the crystalline structure of the perovskites because it was mainly located at the surface and grain boundaries. The BCP efficiently passivated the grain boundaries and resulted in smooth and uniform hybrid organic/perovskite film, which facilitated the carriers extracting and transporting process. Moreover, the hydrophobic PBDB-T-*b*-PTY6 also acted as a barrier for moisture invasion, providing enhanced operational and storage stability.

In another report, Zong *et al.* incorporated PEO-PPO-PEO with perovskite precursors to fabricate hybrid $MAPbI_3$ perovskite films for solar cell devices.[124] The triblock copolymer acted as heterogeneous nucleation sites during the perovskite crystallization process, as a result, smaller grain size and fewer surface defects are detected, which led to solar cells with improved performance and environmental stability. Similarly, PEO-PPO-PEO was integrated with $MA_{0.7}FA_{0.3}PbI_3$ and the hybrid film was used to fabricate solar cells.[125] The copolymer preferentially located at the grain boundaries and suppressed the decomposition of the organic species. The hydrophobic PPO block also acted as the moisture barrier and increased the device stability. Li *et al.* used a two-step spin-coating process with $PbAc_2 \cdot 3H_2O$ as the lead source and PS-*b*-P2VP to fabricate hybrid perovskite films with enhanced stability.[126] The $PbAc_2 \cdot 3H_2O$ was selected for its larger molecular volume, which could alleviate the volume expansion during the perovskite crystallization process, resulting in a dense and uniform film with higher PLQY.

The integration of soft copolymers with perovskite into bulk composites also enables the fabrication of flexible optical or photonic devices. For instance, PU-PDMS copolymers containing Lewis-base functional groups and elastomer chains were introduced into MHP perovskites.[127] The soft copolymers have multiple effects including controlled crystal growth, defect passivation, protection against moisture, mechanical energy dissipation, and self-recoverability. Solar cell devices with the hybrid perovskite films showed enhanced operational stability against illumination and elevated temperature.

Stretchable luminescent nanocomposites with MHP emitters were fabricated by a two-step process.[128] P2VP-*b*-PDMS copolymer was first introduced to the crystallization process of $PEA_2(FAPbBr_3)_2PbBr_4$, and then the hybrid material was added to a PDMS matrix and cured. The BCP promoted the crystallization of the MHP as nanocrystals with an average diameter of 5.9 nm. Moreover, the copolymer enabled uniform dispersion of the perovskite NCs in the PDMS matrix, so that the nanocomposites showed stable PL emission upon repetitive stretching, and excellent environmental stability. Similarly, SEBS was used as the polymer matrix for $CsPbBr_3$ QDs, and such nanocomposites showed enhanced PL stability against water and oxygen.[85] The alkyl chains in the SEBS created a more compatible QDs-polymer interface due to the similar chemical structure with the organic ligands on QDs. Polyfluorene-*block*-poly(*n*-Butyl acrylate) (PF-*b*-PBA) copolymer was blended with $CsPbBr_3$ NCs,[129] and the composite was used to fabricate composite fiber using electrospinning. The conjugated PF block served as the donor in the double fluorescence combination so the color of the electrospun structures can be conveniently varied by changing the BCP/QDs ratio. The soft PBA block, on the other hand, enabled good stretchability of the composite fibers.

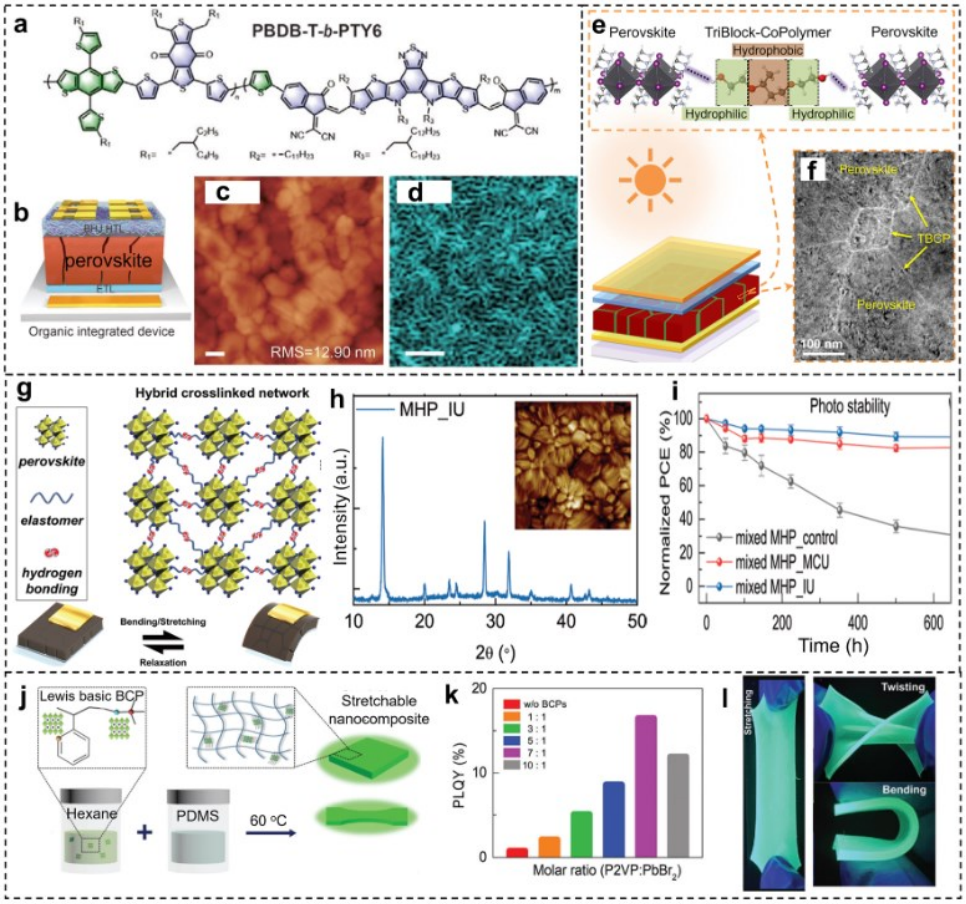

Figure 17: (a) Chemical structure of the conjugated BCP used for forming hybrid perovskite structures. (b) Solar cell device with the BCP/perovskite heterointerfaces. (c) and (d) AFM image and confocal PL mapping of the hybrid perovskite film. Scale bars are 100 nm. Reproduced with permission from ref.123. (e) Schematic of the interaction between PEO-PPO-PEO copolymer and $MAPbI_3$ perovskite, as well as the solar cell device. (f) TEM image of the hybrid $MAPbI_3$ perovskite film. Reproduced with permission from ref.124. (g) Schematic illustration of hybrid network composed of MHP and PU-PDMS copolymer and its energy-dissipation and self-recovery mechanism. (h) XRD spectrum of the hybrid MPH film with PU-PDMS copolymer, inset is the AFM image of the sample. (i) PCE evolution of solar cell devices with time under light illumination (90 ± 10 mW cm^{-2}). Reproduced with permission from ref.127. (j) Schematic of the sequential fabrication process for the stretchable composites composed of $PEA_2(FAPbBr_3)_2PbBr_4$ NPs with P2VP-*b*-PDMS and PDMS matrix. (k) PL quantum yield of the perovskite composites fabricated with different ratios of the copolymer and PbBr2 precursor. (l) Photos of the composites under stretching, twisting, and bending. Reproduced with permission from ref.128.

1.5 Applications of perovskite-BCP hybrid structures

1.5.1 Solar cells

The fundamental structure of a perovskite solar cell consists of metal anode, hole transport layer, light-absorbing perovskite layer, electron transport layer and transparent cathode.[130] Typically, the perovskite layer is in polycrystalline form fabricated by solution-based procedures,[131] which has inevitable defects ranging from point defects to grain boundaries that negatively affect the charge transport property of solar cells.[132,133] Generally, grain boundaries are most susceptible to degradation as they can trap impurities including solvent and moisture during perovskite thin film processing. The dangling bonds along the grain boundaries also lead to diffusion of small molecules and ions. The integration of BCPs during perovskite layer fabrication has been utilized to address this issue.

The incorporation of BCP can enhance the operational stability of the perovskite layer in solar cells. This has been demonstrated by perovskite solar cells (PSC) with a perovskite layer mixed with PEO-*b*-PPO-*b*-PEO,[124,125] which showed over 20% power conversion efficiency (PCE). The hydrophilic PEO blocks interact with unbonded cations of the perovskite and thus build a network functionalizing all grain boundaries throughout the thin film. This network composed of hydrophilic PEO and hydrophobic PPO simultaneously passivates surface defects and repels moisture. PSC with hybrid PU-PDMS/perovskite layer showed PCE of 22.6% and enhanced operational stability.[127] An energy dissipation network was formed by PU-PDMS due to the intermolecular hydrogen bonds, making the solar cell more resistant to mechanical stress. The reversable nature of hydrogen bond reformation leads to self-healing effect so that cracks can be repaired at elevated temperature. BCPs can also participate in the carrier transfer process beyond acting as passivating and encapsulating agents. For instance, PSC with a PBDB-T-*b*-PTY6/perovskite heterointerface achieved a high power conversion efficiency (PCE) of 24.1%.[123] This improvement was attributed to an additional energy cascade, reflecting a type II energy level alignment introduced by the conjugated and hydrophobic BCP, which facilitates exciton dissociation while preventing moisture diffusion.

The full potential of using BCP-perovskite nanocomposite as the active layer for solar cells has not been achieved yet and there is still much room for improvement. Conjuated BCPs with both donor and acceptor behavior that can also form vertically aligned channel with perovskite NCs inside such channels present an ideal active layer for solar cells. Such a structure would enable almost flawless charge transport in combination with efficient charge separation at the perovskite NCs.[134] Experimental demonstration of such a structure has not been reported yet. What's more, bandgap alignment of the BCP-perovskite nanocomposite with other components of the solar cels is critical to avoid back energy transfer and maximize light absorption.[135]

1.5.2 LED

The working principle of a light-emitting diode is the radiative recombination of injected electrons and holes. LEDs have an identical device structure as solar cell since they both involve the excitation and recombination of electron–hole pairs in a semiconductor but utilizing the material in a reverse manner.[136,137] Perovskites, especially their QDs, are being extensively studied for next-generation LEDs.[138,139] Perovskite–BCP hybrid structures have been investigated for LED applications due to the potential to eliminate surface defects and protect ionic perovskite from the external environment. PS-*b*-PAA is one of the frequently used BCP for this purpose.[110,111,114] Color tuning of perovskite–BCP LEDs can be achieved by either halide anion exchange reaction[109] or changing the perovskite QDs/polymer ratios.[129] Specifically, anion exchange can be achieved by exposing the PS-*b*-PAA encapsulated perovskite QDs in a selective solvent such as toluene, so that the swollen PS chains allows the ion diffusion and halide exchange. The incorporation of BCPs with a conjugated block can also lead to color tuning without halide exchange reaction. For instance, polyfluorene blocks on a BCP not only exhibit hole transport properties but also function as blue-emitting moieties. By leveraging the double fluorescence combination, the emission color of the perovskite–BCP composite can be adjusted by varying the ratios of QDs to BCP.

Beyond their role of encapsulation and passivation of perovskite crystals, the long-range order achieved from microphase separation of BCPs can potentially lead to alignment of perovskite NCs for optimized charge transport in LED devices.[86] For instance, if one block of the BCP form vertical cylinders with high density of aligned perovskite NCs inside, such composite structure would be ideal active layer or a color-conversion layer for LED. In such a case, the nanoconfinement leads to enhanced electronic coupling between perovskite NCs and avoids charge transport imbalance, the BCP channels also prevent electrical decoupling from occurring within or between perovskite NCs.[140]

Moreover, BCPs are known to be able to form photonic crystal structures because of the well-defined microphase separated morphology and the refractive index difference between the blocks. Such tunable photonic band gaps and structural colors of BCP matrices can also be utilized to further increase the functionality and optical performance of BCP-perovskite nanocomposites in LED applications, although this remains to be experimentally demonstrated.

1.5.3 Photodetector

Perovskite as a photoactive material can generate electron–hole pairs when excited by incident light of proper wavelength, so that it can be readily used for photodetection. By incorporating BCP in the perovskite layer, enhanced device stability or anisotropic photodetection induced by nanopatterning can be achieved[94,97] Amphiphilic BCPs are particularly suitable for this purpose as they can passivate the perovskite surface through hydrogen bonding or other interactions, and at the same time, provide hydrophobic protection layer against small molecules.[141] The combination of nanoimprinting and BCP lithography led to the fabrication of sub-30 nm 1D nanopatterns of 2D perovskites over a large area with anisotropic photocurrent generation. Furthermore, the tunable microphase-separated morphology of BCP/perovskite hybrid structures can also be used for artificial visual reception. For instance, a retina-inspired phototransistor based on PS-*b*-P2VP/$MAPbBr_3$ as the photoactive material was demonstrated,[93] the density gradient of perovskite NCs with tunable optical properties emulates the distribution of rod and cone cells in the human retina.

1.5.4 Chemical and physical sensors

Due to the fluorescence quenching effect of many chemicals and biomolecules to perovskites, the perovskite–BCP hybrid structures can also be used for sensing applications. For instance, sensing of H_2S in physiological conditions was demonstrated by hybrid structures with $CsPbBr_3$ QDs encapsulated by PEG-*b*-PCL.[121] Dopamine can also be detected by perovskite-copolymer microspheres due to the fluorescent quenching of perovskite by dopamine in its oxidized state.[142] Temperature sensing by perovskite–BCP hybrid structure has also been reported.[143] Hydrogen bonding between 2D perovskite and PEO-*b*-PPO-*b*-PEO resulted in stripping of organic cations from perovskite and a bleached phase, while the increased temperature can break the hydrogen bonding and recover the colored state. For those applications, in order to have highly consistent sensing performance and long-term stability, it is critical to carefully engineer the BCP-perovskite interface to enable the structural stability of perovskite NCs and easy accessibility to target molecules.

1.5.5 Bioimaging

By encapsulating perovskite NCs with amphiphilic BCPs, the hybrid nanostructures can diffuse into the cytoplasm of living cells and enable fluorescent bioimaging.[119] The cytotoxicity effect can be reduced by using a low dosage of perovskite NCs.[115] For instance, $CsPbBr_3$ NCs encapsulated by PS-*b*-PAA showed long-term stability in physiological conditions. They can be used for cell imaging at a does as low as 0.3 μg_{Pb} mL^{-1}, which is well below the toxicity threshold for Pb and Cs ions. But it is noted that lead-containing perovskites still pose serious concern in terms of their use in biomedicine.[144] Lead-free perovskites with Cu^{2+}, Sn^{2+}, Bi^{+} or other ions will be better options to be integrated with biocompatible BCPs for biomedical applications.

CHAPTER II

RESEARCH GOALS AND OVERVIEW

2.2 Research goals

The key objectives of this dissertation are as follows:

1. This study seeks to enhance the physical properties and introduce novel functionalities to polyisobutylene-based elastomers through integration with advanced manufacturing techniques including 3D printing and flexible optical nanocomposites fabrication.

2. This research aims to advance the understanding of the design, synthesis, characterization, and application of polyisobutylene (PIB)-based elastomers and nanocomposites, with a particular focus on molecular engineering and elucidation of structure–property relationships, exploring their potential in emerging applications beyond traditional uses in tires, coatings, and adhesives.

For our first study: additive manufacturing of PIB-based polyurethane and its composite with hard polyurethane, we have employed specific objectives as follows:

1. Achieve high quality FDM 3D printing of flexible PIB-PU based elastomers with tunable mechanical properties tailored for different application scenarios.

2. Fabrication of PIB-PU elastomers that retain their inherent excellent chemical resistance after the 3D printing process

3. Exploration and elucidation of the effects of hard polyurethane incorporation, PIB-PU molecular weight on printed samples' mechanical performance.

The hypotheses for the first study are as follows:

1. Hard polyurethanes (hPU) synthesized via random copolymerization of methylene diphenyl diisocyanate (MDI) and 1,4-butanediol (BDO), as used in PIB-PU synthesis, can be compatibly incorporated into the PIB-PU matrix.

2. Incorporation of hPU is expected to enhance the hardness of the resulting PIB-PU/hPU composite beyond the critical threshold required for successful FDM 3D printing. This enhancement allows for the use of PIB-PU with lower molecular weight, thereby simplifying its synthesis without compromising printability

3. Interlayer adhesion and cross-sectional quality of the 3D printed structures can be significantly improved by blending a suitable proportion of low molecular weight PIB-PU with high molecular weight PIB-PU. This is attributed to the enhanced chain mobility of shorter polymer chains, which promotes interlayer diffusion and entanglement, leading to improved mechanical integrity across layer boundaries.

For our second study: designed polymer ligands for perovskite quantum dots and their block copolymer nanocomposites, we have employed specific objectives as follows:

1. Achieve the design and fabrication of functionalized perovskite QDs with PIB-based surface ligand.

2. Fabrication of flexible optical material made from BCP-perovskite QDs nanocomposite with enhanced photoluminescence stability in ambient conditions

3. Achieve perovskite QDs preferential distribution and alignment through interaction between PIB based surface ligand and PIB phase in SIBS matrix.

The hypotheses for the second study are as follows:

1. Zwitterionic PIB ligands can strongly interact with the ionic surfaces of perovskite QDs via Lewis acid–base interactions, thereby enabling effective grafting of protective PIB ligands onto the QD surfaces through a ligand exchange process.

2. The combined presence of PIB ligands and the SIBS matrix is hypothesized to provide effective encapsulation of perovskite QDs, thereby enhancing their photoluminescence stability under exposure to polar solvents or ambient environment.

3. Selective localization of perovskite QDs within the PIB phase of the SIBS block copolymer matrix can be achieved following ligand exchange, owing to the compatibility between the PIB-functionalized QD surface and the PIB domains of the matrix

For our third study: partially sulfonated poly(styrene-b-isobutylene-b-styrene) incorporated with perovskite quantum dots towards stabilized soft optical material, we have employed specific objectives as follows:

1. Fabrication of flexible BCP-perovskite QDs nanocomposite with enhanced PL stability under ambient conditions.

2. Achieve selective perovskite QDs distribution within the PS phase of SIBS matrix through preferential interaction between perovskite QDs and functionalized PS.

3. To investigate and elucidate the influence of sulfonation degree, SIBS composition, and the BCP-to-QD ratio on the photoluminescence stability of the nanocomposite, with the goal of identifying an optimal formulation.

The hypotheses for the third study are as follows:

1. Electrostatic interactions between grafted sulfonic acid groups and the surface of perovskite QDs can lead to effective defect passivation, thereby enhancing the photoluminescence (PL) performance of the nanocomposite.

2. Partially sulfonated SIBS can be processed in nonpolar solvents, and due to Lewis acid–base interactions, perovskite QDs will selectively localize within the polystyrene phase of the BCP matrix.

3. An increased degree of sulfonation in s-SIBS is hypothesized to improve the PL stability of the resulting nanocomposites under ambient environmental conditions

2.3 Organization and Composition of dissertation

Chapter I presents a comprehensive literature review on the unique properties of block copolymers and their advanced applications. This chapter establishes the foundational context and highlights the scientific relevance of this PhD research.

Chapter II outlines the goals and specific objectives of the research presented in this dissertation. It also provides an overview of the dissertation's structure as well as brief descriptions corresponding to each chapter.

Chapter III covers the study of achieve novel 3D printing of flexible PIB-PU based material with excellent chemical stability. Two independently non-printable components hPU and L-PIB-PU resulted in a printable hybrid with tunable mechanical performance. H-PIB-PU can be directly 3D printed and its mechanical performance can be further enhanced through L-PIB-PU incorporation.

Chapter IV details the synthesis of a zwitterionic PIB ligand and the fabrication of an elastic BCP–perovskite QD nanocomposite with enhanced photoluminescence (PL) stability. The compatibility between PIB-functionalized QDs and the SIBS matrix enables selective distribution and alignment of QDs, imparting additional functionality to the composite.

Chapter V presents the design and fabrication of stabilized, flexible BCP–perovskite QDs nanocomposites through BCP matrix modification. Sulfonic acid groups grafted onto the PS segments of the block copolymer effectively passivate surface defects and contribute to the preferential distribution of perovskite QDs.

Chapter VI includes general conclusions for the three specific studies in the dissertation and outlines future directions.

CHAPTER III

ADDITIVE MANUFACTURING OF PIB-BASED POLYURETHANE AND ITS HYBRID MATERIALS

Abstract

Polyisobutylene-based thermoplastic elastomers can be rendered suitable for 3D printing through the incorporation of chemically compatible rigid thermoplastics, This strategy has been validated in our previous studies, where poly(styrene-b-isobutylene-b-styrene) (SIBS) was successfully processed via fused deposition modeling (FDM) printing by blending with rigid homopolymers such as polystyrene (PS)[145] or poly(phenylene oxide) (PPO)[146], demonstrating the feasibility of enhancing printability through molecular engineering. In this study, the 3D printing of polyisobutylene based thermoplastic polyurethane (PIB-PU) was demonstrated with the addition of hard polyurethane while neither the PIB-PU with lower molecular weight, L-PIB-PU(MW=50 kDa), nor the hard polyurethane (hPU) poly(di-p-phenyl diisocyanate-co-1,4-Butanediol) can be independently 3D printed by extrusion-based FDM method. To further enhance the mechanical properties of the feedstock material, an alternative approach involving an increase in the molecular weight of the PIB-PU was employed, resulting in successful 3D printing using high molecular weight H-PIB-PU (MW=100kDa). By systematically varying the blend ratios of low- and high-molecular weight PIB-PUs, as well as the ratios of L-PIB-PU to hPU, the mechanical performances of the resulting blends were evaluated. Processing parameters were subsequently optimized to enable effective FDM 3D printing

of these PIB-based formulations. Comprehensive characterization, including analysis of internal morphology, thermal and mechanical properties, as well as chemical stability, was performed to validate the printing quality and elucidate the structure–property relationships of L-PIB-PU/hPU blends and H-PIB-PU formulations.

3.1 Introduction

Thermoplastic polyurethane (TPU) is a well-established material recognized for its broad applicability across industrial and consumer sectors, primarily due to its highly tunable chemical composition. Owing to its versatility, TPU has been extensively utilized in coatings, adhesives, sealants[147], and has also garnered significant attention for emerging applications in the biomedical field[148]. Briefly, polyol, diisocyanate, and chain extender are the three major components involved in TPU synthesis. The reaction between the diisocyanate and the low-molecular-weight chain extender yields rigid, polar hard segments characterized by a high concentration of urethane linkages. These hard segments exhibit strong intermolecular hydrogen bonding, wherein the N–H groups of the urethane moieties act as proton donors and interact with oxygen atoms present in both the hard segments (urethane carbonyl oxygens) and soft segments (ether or ester oxygens)[149]. These hydrogen bonding interactions contribute to the mechanical reinforcement of TPU. In contrast, the soft segments, formed from the reaction between the polyol and diisocyanate, contain a lower concentration of urethane linkages, resulting in enhanced flexibility. These segments are primarily responsible for the elastomeric behavior of TPU, as well as its thermal stability[150] and chemical resistance. In commercial applications, the soft segments in TPU are commonly derived from polyether[151,152], polyester[153,154], or polycarbonate[155,156] based polyols.

Although commercial thermoplastic polyurethanes (TPUs) exhibit sufficient stability during fabrication and under ambient environmental conditions, several studies have reported limitations in their long-term biostability against *in vivo* oxidation and hydrolysis[157–160]. In polyester-based TPUs, the unprotected ester groups within the soft segment are particularly susceptible to hydrolysis, which is often accelerated through an autocatalytic mechanism[160]. Specifically, each chain scission event generates a carboxylic acid, which in turn catalyzes further degradation. Subsequent hydrolysis of the ester cleaves the macromolecule, and in the presence of mechanical flexion, microcracks would develop on the surface, compromising TPU's mechanical integrity. Similarly, polyether-based TPUs are also vulnerable to *in vivo* degradation, as the ether linkages can undergo oxidation to form ester groups, initiating subsequent degradation pathways[158,159,161]. In response to these challenges, various strategies have been explored to enhance the biostability of TPUs. These included the use of more hydrolytically stable polycarbonate-based soft segments[162], plasma grafted PTFE protective coating[163], the incorporation of polydimethylsiloxane (PDMS) either through surface grafting[164] or as part of the soft segment[165]. However, despite these efforts, *in vivo* biodegradation was delayed but remains inevitable due to factors such as compliance mismatch or oxygen permeation.

PIB-based TPEs exhibit a range of distinctive characteristics attributable to their composition. These include biocompatibility[49], oxidative-hydrolytic stability[166], and low permeability[167], largely owing to the inert polyisobutylene soft segments that form a protective continuous matrix. The inert nature of PIB derives from its fully saturated backbone, characterized by a pattern of alternating secondary and quaternary carbon atoms. This structural arrangement was proposed to impart exceptional chemical resistance to PIB[49,168]. An illustrative example is SIBS, a block copolymer comprising rigid polystyrene (PS) segments and flexible PIB segments, which finds application in biomedical fields[169] such as drug-eluting stents[170]. Here, the inert PIB phase was leveraged for its beneficial properties. Similarly, PIB-based thermoplastic polyurethane, featuring a 70% PIB continuous matrix, demonstrated excellent biocompatibility. This was evidenced by negligible calcification, reduced protein absorption, and minimized cell attachment when compared to commercially available medical-grade silicone-based polyurethane[171,172]. Such findings revealed the potential of PIB-based materials in biomedical applications including synthetic heart valves, artificial blood vessels, etc.

In this study, we demonstrated the successful FDM printing of PIB-based TPU, which was not previously reported in the literature, providing a new possibility for customizable biomaterial. To render PIB-based TPU suitable for filament extrusion and subsequent FDM processing, two strategies were employed: (1) blending with a compatible hard polyurethane (hPU), and (2) increasing the molecular weight of the PIB-based TPU. The mechanical properties of the PIB-PU/hPU blends were found to be tunable by adjusting the hPU content. And by mixing different molecular weight PIB-PUs at proper ratio, the hybrid polyurethane blend exhibited better mechanical performance due to enhanced interlayer adhesion. Materials prepared using both approaches exhibited superior chemical resistance when compared to commercial TPU. To optimize the FDM printing process, the quality of printed structures, rheological behavior, and thermal properties were systematically evaluated using scanning electron microscopy (SEM), capillary rheometer, differential scanning calorimetry (DSC), and thermogravimetric analysis (TGA).

3.2 Materials and experimental section

Materials: Methylene diphenyl diisocyanate (MDI), 1,4-butanediol (BDO), toluene, dimethylformamide (DMF), dibutyltin dilaurate (DBTDL), nitric acid (70%) were purchased from Sigma-Aldrich and used as received. Sulfuric acid (98%) was purchased from VWR chemicals and used as received. Tetrahydrofuran (THF) was purchased from Fisher Scientific.

Polyisobutylene-polyurethane synthesis: PIB-diol (3217g/mol, 80.5% functionality) was measured in a two-neck round bottom flask and dried under vacuum at 60°C for overnight. The amount of BDO and MDI were calculated based on two equations to generate PIB-PU with 70wt% soft segment proportion:

$$0.7 = \frac{m_{PIB-diol}}{m_{PIB-diol} + m_{BDO} + m_{MDI}}$$

$$\frac{1}{3217} \times 0.805 + \frac{m_{BDO}}{90.12} = \frac{m_{MDI}}{250.25}$$

The weight of PIB-diol was measured after drying process. Target amount of distilled THF was transferred by syringe equipped with a cannula to get a PIB-diol solution of 0.3g/ml concentration, followed by MDI powder addition. The flask was vacuumed and purged with nitrogen for 3 times to create an inert and moisture free atmosphere. The solution containing PIB-diol and MDI was heated at 65 °C with stirring until all solid contents were fully dissolved. The reaction was initiated by the addition of DBTDL in THF (5mg/ml) solution based on the initiator-MDI mass ratio of $1:10^4$, the reaction was continued for 1hour before the chain extension step. After 1hr, the chain extender BDO was slowly added into the flask and the solution was kept stirring for 4 hours. The viscos solution was cooled to room temperature and diluted by THF followed by subsequent transfer to a PTFE mold. The transparent PIB-PU film was obtained by air drying in film hood overnight and subsequent vacuum drying at 40 °C for 24 hours.

Poly (di-p-phenyl diisocyanate-co-1,4-Butanediol) synthesis: The hard polyurethane was synthesized using a similar method as PIB-PU synthesis procedure except the absence of PIB-diol addition. 13.26g of MDI and 6.74g of BDO were measured and transferred in a round bottom flask, followed by vacuum and nitrogen purge for 3 times. 30ml of DMF was added into flask and a fully dissolved solution was obtained by stirring at 65°C. The reaction was initiated by DBTDL solution addition and quenched by methanol after 3hours. The hPU product was precipitated in excessive methanol at 30:1 methanol/DMF volume ratio. The solid hPU powder was collected by vacuum filtration and vacuum drying at room temperature for overnight.

Filament fabrication: L-PIB-PU was blended with different weight percentage of its hard polyurethane (hPU) varying from 10wt% to 30wt%. The sample names show their composition information. For instance, PIB-PU/hPU(70/30) means the blend consists of 70wt% PIB-PU and 30wt% hPU. Due to the solubility difference between PIB-PU and its hard segment, the mixing cannot be achieved by solution mixing. Instead, a desktop twin-screw extruder (Thermo Haake) was used to produce melt blended PIB-PU/hPU. The two ingredients, PIB-PU and hPU, were heated at 190°C to fully disperse the hard polyurethane according to DSC results and mixed at 40rpm for 5mins while the chamber was purged with nitrogen. The mixture was collected and used as the feed material for filament production done by a capillary rheometer with a die (L/D ratio=24:1, 1.75mm inner diameter) at 160°C. Filaments were cooled in air and collected. For H-PIB-PU, it was cut into small pieces and directly extruded into filament by the capillary rheometer at 170°C.

Fused deposition modeling printing: Filaments of PIB-PU/hPU and high molecular weight PIB-PU blends were used for FDM 3D printing by a commercial 3D printer (Wanhao Duplicator i3) equipped with a modified printing head (Flexion Extruder). 3D models were built using SolidWorks software and corresponding G-codes were processed by CURA slicing software. The printing parameters are summarized as follows: printing temperature:180°C, nozzle diameter: 0.8mm, build substrate temperature: 60°C, printing speed: 0.2mm/s, infill overlap: 10%, layer height: 0.2mm.

Characterization: Scanning electron microscopy (SEM) was conducted using a JEOL-7401 FE-SEM at 5 kV or 10 kV accelerating voltage. Hardness was determined with a Shore A Digital hardness tester (Gain Express Holdings Ltd) according to ISO 868-1986. The rheological behavior was investigated by a capillary rheometer (Rosand RH2000) at 180 °C and the shear rate range was set as 10-800 s^{-1}. A die with L/D ratio of 24:1 and 1mm inner diameter was incorporated for the test. Thermal stability was studied by thermogravimetric analysis (TGA) (TA Instruments Q500) under nitrogen purge(40ml/min). The temperature range was from room temperature to 550 °C, at a heating rate of 20°C/min. Dynamic mechanical analysis (DMA) (TA Q800) was used to characterize sample’s viscoelastic behavior in the -100 °C to 200 °C range. The heating rate was set as 5°C/min. Samples were oscillated at 0.1% strain amplitude at 1 Hz frequency.

Differential scanning calorimetry (DSC) (TA Q200) was used to study the transition temperature change and predict processing temperatures for PIB-PU and its mixtures. The temperature range was set as -85℃ to 250℃ with a heating/cooling rate of 10℃/min. The nitrogen flow rate was set as 40ml/min. Tensile tests were conducted with an Instron 5567 Tensile Tester according to ISO-37 standard. Gel Permeation Chromatography (GPC) was carried out using the TOSOH EcoSec GPC 8320 system equipped with a Quad detector with two 17393 TSKgel columns (7.8 mm ID x 30 cm, 13 μm) and one 17367-TSKgel Guard Column (7.5 mm ID x 7.5 cm, 13 μm). Inhibitor-free HPLC grade Tetrahydrofuran (THF) was used as the eluent at a flow rate of 1 mL/min at 40 °C.

3.3 Results and discussion

In this study, we presented the synthesis of PIB-PU elastomers with molecular weights of 50 kDa and 100 kDa, hard polyurethane synthesis and corresponding hybrid composites fabrication. Our investigations affirmed that these PIB-PU hybrids exhibited adjustable stress-strain characteristics depending on their composition. Additionally, the inclusion of hard polyurethane did not compromise the excellent chemical resistance of the hybrid material, indicating its inert properties and potential application as the barrier material in devices intended for human skin contact. On the other hand, we demonstrated the FDM 3D printing of this flexible PIB-based elastomer, which was not previously documented in literature.

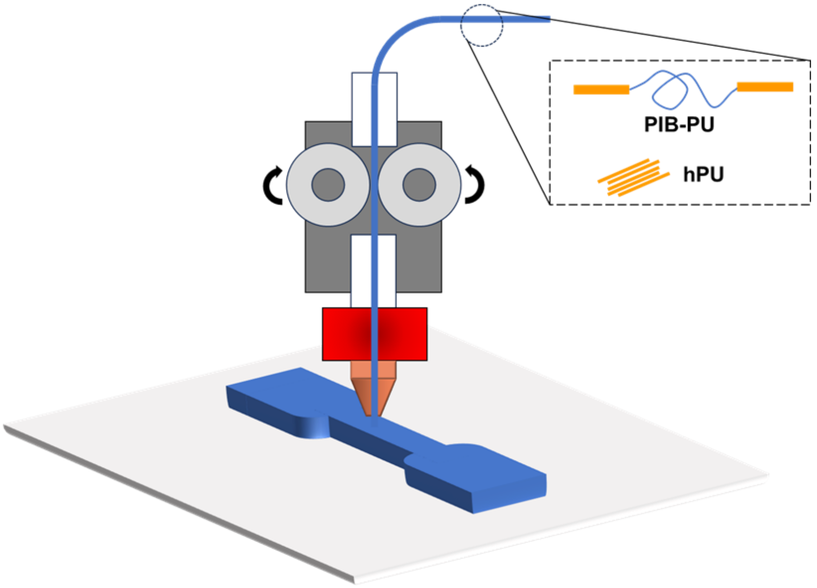

Figure 18: Schematic of FDM 3D printing with flexible PIB-PU based filament.

Mechanical, rheological, and thermal properties of PIB-PU: The hardness characteristics of the feedstock material exert substantial influence over both printability and print quality. Conventionally employed polymers for filament production predominantly comprise rigid thermoplastics, notably polyamide, polylactic acid, polyvinyl alcohol, and polyether ether ketone (among others) [173]. However, the successful application of FDM 3D printing techniques to flexible materials such as TPEs remains challenging.

Based on our previous study[145,146], the lower hardness limit required for FDM type 3D printing with continuous melt extrusion and stacking was found to be 55 HA. Table 1 summarizes the shore A hardness information of PIB-PUs and L-PIB-PU/hPU blends. It was observed that, in the absence of any reinforcement, polyisobutylene-based polyurethane with a molecular weight of 50 kDa lacked sufficient mechanical robustness, resulting in failure to achieve continuous melt extrusion during the FDM 3D printing process. This behavior was further supported by the corresponding hardness measurement mentioned in Table 1. With the incorporation of the hard polyurethane through compounding, the modulus of the hybrid composite was expected to increase, which is discussed in subsequent section. This enhancement in mechanical stiffness would reduce deformation and buckling under the strain imposed by the guiding screw during filament feeding, thereby facilitating smoother filament transfer and continuous melt extrusion. As a result, successful FDM 3D printing was achieved. A 10wt% incorporation of the hPU increased the material hardness from 48 HA to 74 HA, which surpassed the critical threshold of 55 HA and was comparable to that of 100 kDa PIB-PU. However, this was achieved with significantly reduced synthetic complexity, highlighting the advantage of this approach in terms of simplicity and processability. When the hPU content increased to 20wt% and 30wt%, the change in corresponding shore A hardness was not as significant as that of 10wt% hPU sample, leading to a final hardness of 78 HA and 82 HA, respectively. The observed nonlinear enhancement in hardness can be attributed to the inherent characteristics of the shore hardness scale. Ideally, this scale compresses an extensive range of material Young's modulus, spanning from zero to infinity, into a finite scale of 0 to 100.[174] Consequently, as additional hPU was incorporated into the system by different amounts, there were smaller increases on the Shore hardness scale.

Table 1: Shore A hardness summary of different PIB-PUs.

	Shore A hardness (HA)
L-PIB-PU	48
L-PIB-PU/hPU (90/10)	74
L-PIB-PU/hPU (80/20)	78
L-PIB-PU/hPU (70/30)	82
H-PIB-PU	74

To evaluate the effect of the hard polyurethane on the thermal stability of the material, thermogravimetric analysis was performed over a temperature range of 25 °C to 550 °C. This range was selected to ensure the capture of the complete thermal degradation profile of the material. In Figure 19a, the pristine hPU underwent relatively rapid thermal degradation compared to the PIB-PUs. This behavior is attributed to barrier property of PIB matrix; in PIB-PUs, the thermally unstable hard segments are embedded and shielded by the PIB matrix, which enhanced their thermal resistance. As a result, the degradation onset temperature (T_{95}) and the temperature corresponding to the maximum degradation rate of the unprotected hPU (207.5 °C and 330.5 °C, respectively) were notably lower than those of, for example, L-PIB-PU (328.5 °C and 437.4 °C, respectively). When comparing the thermal degradation behaviors of pristine L-PIB-PU and the L-PIB-PU/hPU (80/20) hybrid, an earlier onset of thermal degradation and an increase in the residual mass were observed, evidenced by a 21°C decrease in onset temperature and an increase of final weight percent from 3.15% to 7.8%. It indicated that part of hPU was not embedded in the PIB matrix so the degradation behavior of the hybrid possessed some feature from hPU. But this particular unprotected hPU not always have negative impact on sample performance, for instance, the exposed hPU was melted at printing temperature (180°C) before the onset of thermal degradation, it helped the material extrusion process during printing. For H-PIB-PU, its T95 was found to be 297°C which is far higher away from the printing temperature, so it is expected that no H-PIB-PU was degraded during the printing process.

The rheological properties of the feedstock material, particularly its shear viscosity at the target processing temperature, are critical parameters governing the continuity and adequacy of material flow in extrusion-based 3D printing techniques. To evaluate the rheological behavior of PIB-PU based material, a capillary rheometer was employed due to its instrumental configuration similarity to the FDM printer's printhead, specifically in terms of its heating chamber and extrusion die. Lower shear viscosity is beneficial as the filament extrusion through the printhead can be facilitated, which leads to potentially fewer defects and consequently enhanced printing quality. To assess the adequacy of material extrusion, shear viscosities at a shear rate of 20 s^{-1} were selected for comparison according to our previous study[145]. This value closely approximated the shear conditions experienced near the nozzle during the 3D printing process. As shown in Figure 19b, it can be observed that all PIB-PU based samples exhibited typical shear thinning behavior when exposed to increasing shearing rate. The incorporation of 30 wt% hPU filler resulted in a substantial reduction in material's shear viscosity at 20 $s^{-1}$from 4807 Pa·s to 1358 Pa·s. In general, the dispersion of solid fillers within an elastomer matrix leads to an increase in the composite's melt viscosity. This effect arises from a reduction in the volume fraction of the deformable polymer phase, restricted mobility of the polymer chains, and interfacial interactions or binding effects between the polymer and the filler surfaces[175]. However, this behavior assumes that the incorporated filler remains in the solid state without undergoing any solid–liquid transition. In our case, the pronounced decrease in viscosity was attributed to the rheological measurements being conducted at 180 °C, a temperature chosen to approximate the 3D printing conditions and which exceeded the onset crystallization temperature of the hPU. Consequently, the hPU component entered a partially molten state, substantially reducing the overall viscosity of the composite due to increased molecular mobility and the presence of a more deformable phase. And as mentioned in previous TGA analysis, a small part of hPU was not embedded in the PIB-PU matrix and thus was expected to lubricate the melt extrusion during testing.

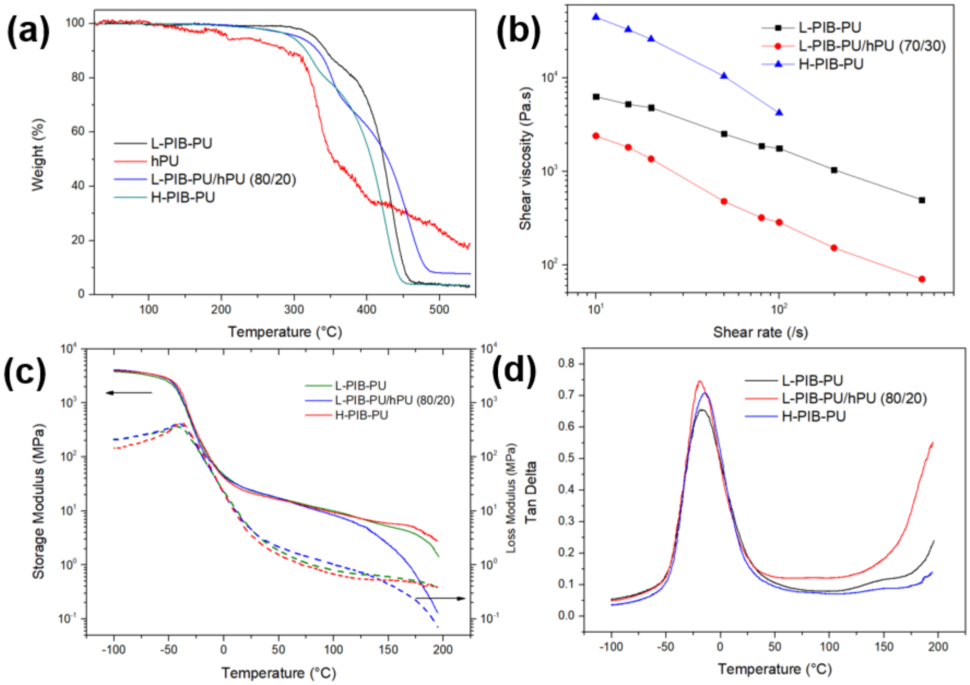

Figure 19: (a) TGA curves of L-PIB-PU, hPU, L-PIB-PU/hPU blends, and H-PIB-PU. (b) Shear viscosity versus shear rate for L-PIB-PU and L-PIB-PU/hPU blend measured by a capillary rheometer. (c) Storage modulus(G') and loss modulus(G") as a function of temperature for PIB-PUs and PIB-PU/hPU blend. (d) Damping (tan delta) of the test samples as a function of temperature.

Table 2: Summary of PIB-PU characteristic thermal degradation temperatures

Sample name	$T_{95\%}$ (°C)	Max weight loss rate temp (°C)
L-PIB-PU	328.4	437.4
hPU	207.5	330.5
PIB-PU hPU (70/30)	317.0	439.0
PIB-PU hPU (80/20)	307.4	454.9
PIB-PU hPU (90/10)	307.0	432.8
H-PIB-PU	297.2	424.5

To investigate the effect of molecular weight and hPU incropoartion on material's viscoelastic behavior, dynamic mechanical analysis was performed on L-PIB-PU, H-PIB-

PU, L-PIB-PU/hPU(80/20) samples. As shown in Figure 19c, there is a more rapid decrease in storage modulus comparing L-PIB-PU/hPU and pristine L-PIB-PU. Which can also attributed to the thermal transition of the hard polyurethane. As summarized in Figure 19d, PIB-PUs with different molecular weights both exhibited a low transition temperature at approximately –19 °C, consistent with values reported in previous literature[176]. This transition was attributed to the soft segment phase. Notably, the observed glass transition temperature of PIB-PUs was significantly higher than that of the homopolymer polyisobutylene[177] (–73 °C), indicating substantial phase mixing between the hard segments (HS) and soft segments (SS). This hypothesis was further supported by the presence of a single tan delta peak. Similar observation was reported in the work of Wei et al.[178] The effect of hPU incorporation was also evident in the higher temperature region as discussed previously, since tan delta was calculated as the ratio of loss modulus to storage modulus. So the hybrid PIB-PU/hPU exhibited a higher tan delta value compared with pristine PIB-PU sample.

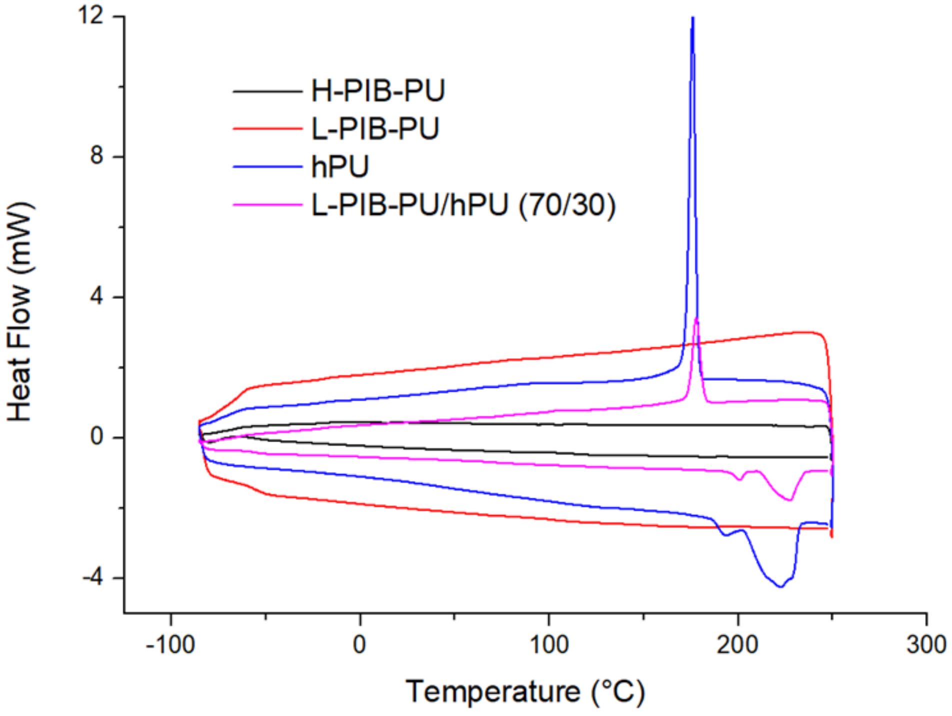

Figure 20: differential scanning calorimetry curves of H-PIB-PU, L-PIB-PU, hPU, and L-PIB-PU/hPU blends.

To elucidate the thermal transition behaviors of PIB-PU based materials, differential scanning calorimetry was conducted for PIB-PUs, hPU and L-PIB-PU/hPU(70/30). The hPU sample exhibited a pronounced exothermic peak at 175 °C, corresponding to its crystallization temperature. Additionally, a broad endothermic peak was observed in the 180–230 °C range, which was attributed to the melting process of the hard polyurethane and the influence of its molecular weight distribution. As shown in Figure 20, such characteristic thermal behavior was maintained when hPU was blended with L-PIB-PU. The crystallization peak was shifted to 178°C and the main melting peak shifted from 223°C to 227°C. In contrast, only the endothermic peak for glass transition were presented for pristine H-PIB-PU and L-PIB-PU samples.

FDM 3D printing: To demonstrate PIB-PU based elastomers can be applied in customizable part fabrication, dog bones and infilled cubic structures were 3D printed using flexible filaments. The printing quality of these 3D printed objects was primarily assessed under microscope, as exhibited in Figure 21. There were no visible defects or infill pattern distortion observed. Both 3D printed H-PIB-PU and L-PIB-PU/Hpu objects showed good shape fidelity. The dog bone specimens were subsequently subjected to tensile testing to investigate their stress–strain behavior.

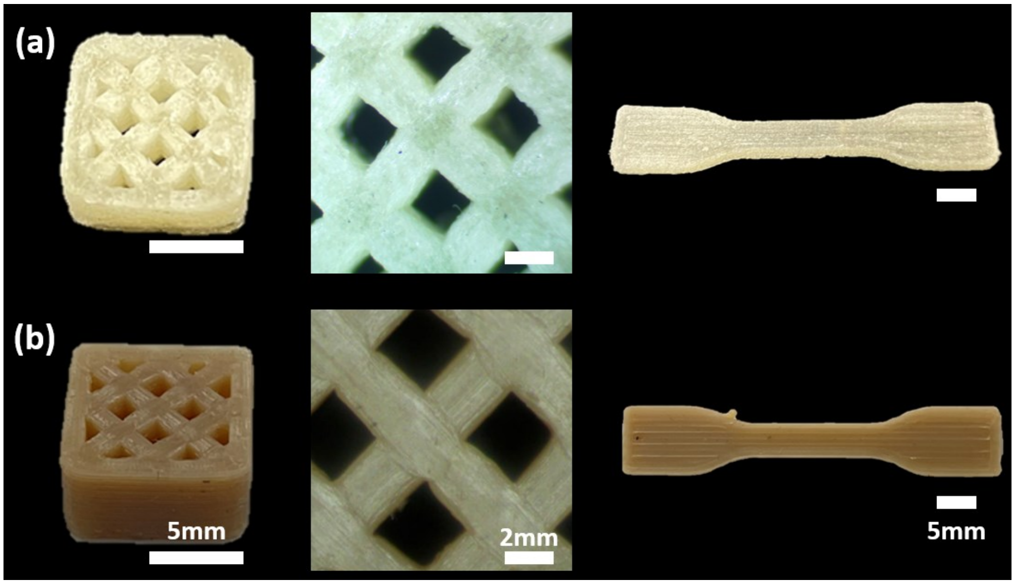

Figure 21: (a) 3D printed objects made from H-PIB-PU and photo under microscope. (b) 3D printed objects made from L-PIB-PU/hPU blend and photo under microscope.

The printing quality was further assessed in greater detail by examining the cross-sectional areas of the 3D-printed samples at higher magnification using scanning electron microscopy, which was expected to provide complementary internal structure information in addition to the surface-level observations obtained from optical microscopy. SEM analysis was conducted on hybrid L-PIB-PU/hPU blends containing 10–30 wt% hPU to determine whether the incorporation of hPU affected the quality of the printed objects. As shown in Figure 22a-c, no obvious interlayer boundaries were observed, indicating well and sufficient material fusion when the subsequent melt was deposited on the substrate layer. On the other hand, triangular internal void defects located at the same layer were presented for all three samples, this is induced by the intrinsic nature of the melt extrusion process during 3D printing. For the composite with the lowest hPU content (10wt%) (Figure 22c), the 3D-printed part exhibited the poorest cross-sectional quality, as evidenced by hair-like boundary defects observed in the inset SEM image. This outcome was anticipated, given that pristine L-PIB-PU was non-printable under the same conditions, and the minimal addition of hPU was insufficient to significantly improve in-layer fusion. Such hair-like defect was eliminated when the hPU content increased to 20wt% and 30wt%. However, it is important to note that the mechanical performance of the printed parts was not solely governed by cross-sectional morphology, whichwill be discussed in the subsequent section.

When comparing the cross-section quality of pristine H-PIB-PU and PIB-PU blend with a 90-10 (H/L) mass ratio, it was observed that the interlayer boundaries induced by the high melt viscosity and consequently restricted chain mobility presented in H-PIB-PU 3D printed sample were effectively eliminated upon the introduction of low molecular weight PIB-PU. It was proposed that the shorter chains can enhance the chain diffusion and entanglement across the interlayer boundaries. Similar results was reported in the work of Levenhagen et.al.[179]

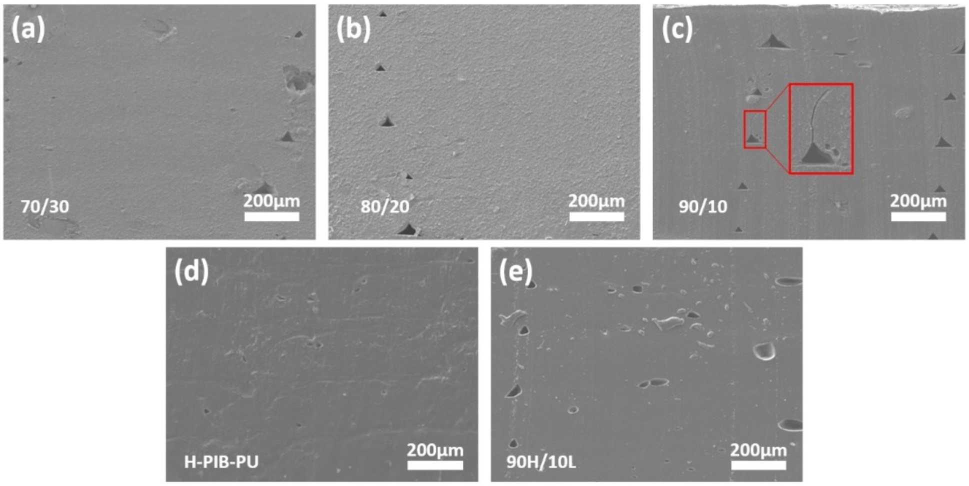

Figure 22: SEM images of cross-sections of the 3D printed structures made from L-PIB-PU/hPU blends at (a)(70/30), (b)(80/20), (c)(90/10) weight ratios, (d) H-PIB-PU, and (e) PIB-PUs blend at (90H/10L) weight ratio.

Effects of hPU and PIB-PU MW on Mechanical Properties: To study the mechanical properties of 3D printed PIB-PU based elastomers, dog bone shaped specimens were printed for tensile test. As shown in Figure 23, the incorporation of the hard polyurethane increased the composite's Young's modulus, but such modification also led to increased brittleness, making the material more prone to fracture during tensile testing. As a result, the toughness, tensile strength, and elongation at break decreased. This behavior became more pronounced with increasing hPU content (Table 3). For instance, the L-PIB-PU/hPU (90/10) exhibited 7.73MPa strength, 11.4MPa modulus and 215% elongation. L-PIB-PU/hPU (70/30) showed 6.63 MPa strength, 19.4MPa modulus and 62.3% elongation. This relationship between material composition and mechanical performance offered a means to tailor the mechanical properties of the composite according to specific application requirements. When considered alongside the cross-sectional quality analysis, it can be concluded that, although the incorporation of the hard polyurethane contributed to the elimination of interlayer defects, its inherent rigidity played a more dominant role in dictating the overall stress-strain behavior of the material.

Compared to 3D-printed parts composed solely of high molecular weight PIB-PU, the dog bone samples incorporating 10 wt% low molecular weight PIB-PU exhibited enhanced mechanical performance across all evaluated parameters. Specifically, the tensile strength increased from 4.33 MPa to 5.50 MPa, Young’s modulus improved from 4.65 MPa to 4.86 MPa, and the elongation at break rose from 332% to 348%. These improvements were attributed to enhanced interlayer chain diffusion and entanglement facilitated by the presence of L-PIB-PU. This hypothesis is further supported by the previously discussed cross-sectional analysis, which revealed less distinct interlayer boundaries following the incorporation of L-PIB-PU. However, the 80H/20L PIB-PU blend showed inferior mechanical performance (see in support information), indicating the importance of optimizing formulation design.

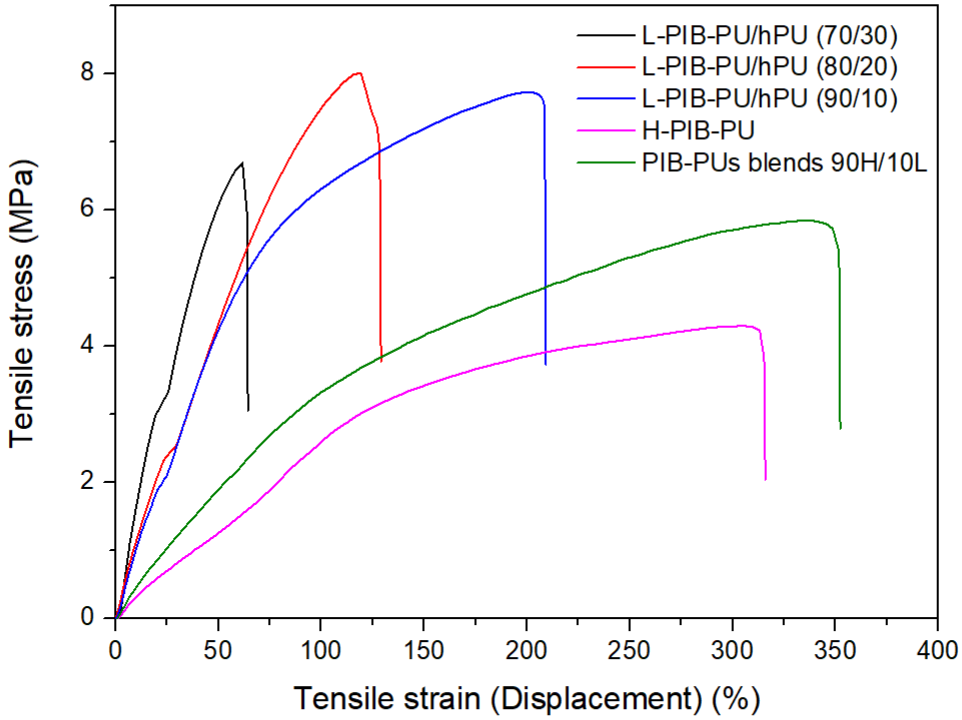

Figure 23: Representative stress-strain curves of 3D printed L-PIB-PU/hPU blends with different hPU loadings, H-PIB-PU, and PIB-PUs blend at (90H/10L) weight ratio.

Table 3: Stress-strain behavior summary for 3D printed PIB-PU based samples

Sample name	Tensile strength (Mpa)	Elongation at break (%)	Young's modulus (MPa)
L-PIB-PU/hPU (70/30)	6.23±0.41	62.3±2.4	19.4±3.7
L-PIB-PU/hPU (80/20)	7.32±0.12	113.3±12.3	11.77±0.75
L-PIB-PU/hPU (90/10)	7.73±0.09	215.7±8.7	11.4±0.44
H-PIB-PU	4.33±1.09	332±42	4.65±0.65
PIB-PUs (90H/10L)	5.50±0.11	348±23	4.86±0.20

Chemical stability test: To assess the materials' stability and integrity under highly corrosive environments, the weight changes of H-PIB-PU and L-PIB-PU/hPU (80/20) composites were recorded after immersing the 3D-printed specimens in 3.95 M and 7.9 M nitric acid solutions sequentially at 65 °C for 1 hour. A commercial thermoplastic polyurethane was used as a control sample and subjected to the same acid treatment conditions. Its flexible filament was 3D printed into identical geometries using the same printing parameters to ensure a consistent basis for comparison with the PIB-PU based materials. As shown in Figure 24b, there was no visual sign of degradation or color change of our 3D printed PIB-PU based objects after the initial 1-hour hot nitric acid immersion. In contrast, the commercial TPU sample underwent a pronounced color transition from white to bright orange, which was a clear indication of oxidative reaction occurrence[180]. To further evaluate their chemical resistance, all three samples were subsequently exposed to more aggressive conditions by doubling nitric acid concentration to 7.9M. In Figure 24c, complete decomposition of the 3D-printed commercial TPU sample was clearly observed under the harsher testing conditions, confirming its poor resistance to strong oxidative environments. In contrast, the 3D-printed parts made from both H-PIB-PU and L-PIB-PU/hPU (80/20) retained their shape fidelity with no visible degradation. In good agreement with our hypothesis, subsequent weight measurements showed minimal deviation from the original mass, further indicating that the barrier properties of the chemically inert PIB phase were preserved post-printing. These results demonstrated the superior chemical resistance of our PIB-PU based materials compared to the commercial TPU filament.

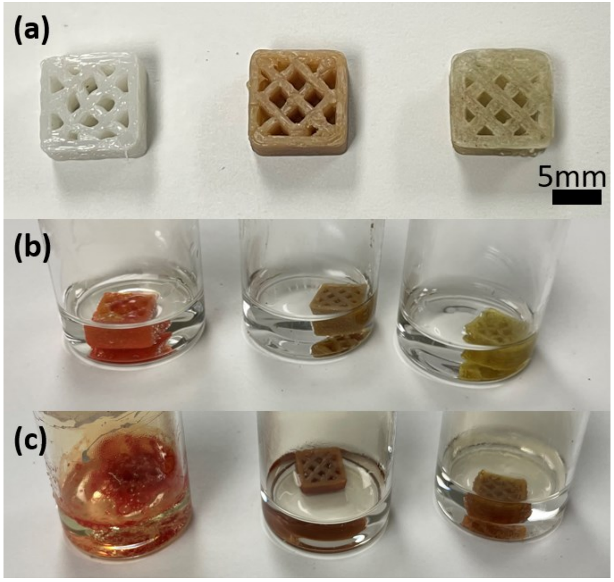

Figure 24: (a) 3D printed objects made from commercial TPU, L-PIB-PU/hPU (80/20), and H-PIB-PU before acid immersion test. (b) samples after 1 hour nitric acid (3.95M) immersion at 65℃. (c) samples after 7.9M nitric acid immersion (1hour, 65℃)

Table 4: Summary of weight change of 3D printed PIB-PU based samples before and after acid treatment

Sample name	TPU	L-PIB-PU/hPU	H-PIB-PU
Initial weight(g)	0.476	0.42	0.345
Final weight(g)	none	0.422	0.348

3.4 Conclusions

In this study, we demonstrated, for the first time, the successful 3D printing of flexible PIB-PU–based elastomers. The effectiveness of our previously proposed approach was further validated by demonstrating that the incorporation of a compatible rigid thermoplastic phase enabled flexible elastomers to be processed via melt-extrusion process during 3D printing. While neither L-PIB-PU nor hPU alone was printable under the given conditions, their combination resulted in a hybrid L-PIB-PU/hPU material that was successfully 3D printed The requirement for achieving sufficient material hardness to enable filament-based printing can be met through either the incorporation of an hard polyurethane (hPU) or by utilizing high molecular weight PIB-PU.

Each approach offered distinct advantages. hPU simplified the synthesis of PIB-PU and allowed for tunable mechanical properties through straightforward compositional adjustments. In contrast, high molecular weight PIB-PU can be directly 3D printed without the need for additional modifiers. Furthermore, incorporating 10 wt% low molecular weight PIB-PU into the high molecular weight matrix significantly improved interlayer adhesion. This enhancement was attributed to increased chain diffusion and entanglement across layer boundaries, resulting in improved mechanical performance, including higher Young’s modulus, tensile strength, and elongation at break.

Subsequent chemical resistance testing revealed that the inert PIB phase retained its barrier properties post-printing. Both pristine H-PIB-PU and L-PIB-PU/hPU (80/20) composites exhibited superior chemical stability compared to commercial TPU, which underwent visible degradation and oxidative discoloration. These findings underscore the potential of PIB-PU–based elastomers as high-performance, chemically resistant materials for advanced 3D-printed applications.

CHAPTER IV

DESIGNED POLYMER LIGANDS FOR PEROVSKITE QUANTUM DOTS AND THEIR BLOCK COPOLYMER NANOCOMPOSITES

Reproduced in parts from:

Tsai, C. H., Shen, N., Mi, C., Bu, J., Dong, Y., & Xu, W. (2024). Designed Polymer Ligands for Perovskite Quantum Dots and Their Block Copolymer Nanocomposites. *Advanced Optical Materials*, *12*(13), 2302731. https://doi.org/10.1002/adom.202302731

Abstract

Perovskite quantum dots (QDs) have efficient optical absorption and emission in the visible range, and show a strong quantum confinement effect and high external quantum efficiency. They have been at the forefront of next-generation photovoltaics and optoelectronics applications. However, two major challenges associated with perovskites and their nanomaterials are poor stability (such as against moisture and polar solvents), as well as the lack of efficient nanopatterning methods. In this work, we provide a promising approach to address both of those major challenges by molecular engineering and integration of QDs with block copolymers (BCP). The BCP thermoplastic elastomers not only substantially improve the stability of perovskite QDs by encapsulating them in a highly stable and soft matrix, but also enable molecular-level control of the alignment and assembly of perovskite QDs in the microphase-separated BCP matrix. We demonstrated

that designing and synthesis of compatible polymer ligands for perovskite QDs is key to enabling their selective and strong interaction with the BCP matrix. The structure and molecular weight of the BCP also play an important role in the interfacial structure and optical properties of the QDs-BCP nanocomposites. Such soft and flexible optical nanocomposites have potential applications in flexible optoelectronics, optical storage, and displays.

4.1 Introduction

Perovskites, or more specifically, metal halide perovskites (MHPs), are a class of semiconducting materials with unique optical and electronic properties.[62,63,181] They have been at the forefront of next-generation photovoltaics and optoelectronics due to their efficient optical absorption and emission in the visible range.[64,65,68] Besides being used in macroscopic or bulk states, perovskites can also be synthesized in solution in the form of colloidal quantum dots (QDs). Such perovskite QDs show a strong quantum confinement effect and can make devices with high external quantum efficiency.[182–184]

However, one of the major challenges for perovskites and their nanomaterials is limited stability.[78] They are vulnerable to many environmental factors, including moisture, certain solvents, oxygen, and heat.[79,80] Perovskite QDs with high surface areas are more susceptible to the effects of the environment. Several approaches are being explored to overcome this stability issue, including chemical methods such as capping agents, stabilizers, and physical methods such as device encapsulation;[132,185,186] but many of those methods have limited improvement or require complicated chemical modifications.

On the other hand, the lack of efficient nanopatterning methods for perovskites is another major challenge that prevents their further development and applications.[82] Directly patterning solid perovskite materials with photolithography-based techniques is not feasible due to the poor stability of perovskite under moisture, solvents, and dry etching.[81] Other nanopatterning techniques such as direct laser writing and focused ion beam milling have been used for nanopatterning of perovskite.[83,84] However, those methods are time-consuming, difficult to scale up, and costly. The high-energy beams cause severe structural damage to the perovskites and lead to the degradation of photophysical properties.

The integration of perovskite nanostructures with block copolymers (BCPs) provides a very promising approach to address those two challenges.[85–87] BCPs can self-assemble into various morphologies (including body-centered cubic spheres, hexagonally packed cylinders, bicontinuous gyroids, and lamellae) by controlling the molecular weights, block ratios, processing conditions, and substrates.[187,188] The BCPs can not only improve the stability of perovskite nanostructures by encapsulating them in a highly stable and soft matrix, but also enable molecular-level control of the alignment and assembly of perovskite nanostructures in the microphase-separated BCP matrix.[89–91]

There are two main approaches for the integration of BCPs with perovskite nanostructures.[97,189,190] The first one is based on introducing BCPs to perovskite precursors during nanoparticle synthesis, the BCPs act as polymer ligands or molecular templates for the synthesized perovskite nanoparticles. For instance, polystyrene-*b*-poly(2-vinylpyridine) (PS-*b*-P2VP) has been directly mixed with $MAPbBr_3$ perovskite precursors to form hybrid structures after crystallization. The precursors preferentially coordinated with the P2VP domains, which yields ordered perovskite nanostructures with controlled size.[92,93] The hybrid BCP-perovskite structures also exhibit enhanced photoluminescence with high resistance to both humidity and heat.[126] In another report, PS-*b*-P2VP was used as the polymer ligand for the synthesis of $CsPbBr_3$ nanocrystals.[101] The confined growth of the perovskite nanocrystal within the copolymer micelle leads to hybrid core-shell nanostructures with enhanced colloidal stability. Amphiphilic PS-*b*-P4VP (P4VP: poly(4-vinylpyridine)) block copolymers have been used to modify the surface of $CsPbBr_3$ nanowires,[117] which leads to enhanced colloidal stability and photoluminescent emission. PS-*b*-PEO was grafted on the surface of $MAPbBr_3$ quantum dots, which enables its good dispersity in water.[115] High photoluminescence quantum yield and low cytotoxicity were also demonstrated.

The second approach is based on directly mixing and co-assembling BCPs and perovskite nanostructures. For instance, $CsPbX_3$ (X=Cl, Br, or I) nanowires were incorporated in a polystyrene-*b*-polyisoprene-*b*-polystyrene (SIS) matrix, and the hybrid material was also used for direct ink writing 3D printing.[100] The nanowire could be aligned by the printing path, which resulted in hybrid structures with highly polarized absorption and emission. Nanocomposite based on PS-*b*-PEO (PEO: polyethylene oxide) and $MAPbBr_3$ QDs has also been studied,[191] and the hybrid structure was used as a photoactive floating gate for non-volatile flash photomemory application. It was found that the $MAPbBr_3$ QDs mainly located in the PEO domains in the microphase-separated structure. Block copolymer-derived inorganic nanoporous structures have also been used to direct the crystallization of metal halide perovskites,[135] and the formed interconnected perovskite structures are useful to enhance perovskite solar cell performance.

From those representative recent reports on the integration of perovskite nanostructures with BCPs, it can be seen that most of them are limited to either PS-*b*-PVP or PS-*b*-PEO as the polymer matrix. The preferential interaction between the perovskites or their precursors to the PVP or PEO block is related to Lewis acid-base interaction. For instance, the pyridine group is a Lewis base, and the uncoordinated cations in perovskites (such as Pb^{2+}) are soft Lewis acids. However, the PS-*b*-PVP copolymer is glassy, and the PS-*b*-PEO is a semicrystalline copolymer,[192,193] therefore, neither of them is suitable for providing good mechanical properties, especially in terms of softness and stretchability to the hybrid materials. Moreover, the hydrophilic blocks in them (PEO or PVP) have a high affinity to water and polar solvents; therefore, they have limited contribution to improving the stability of perovskite nanostructures embedded in them. To address those limitations, we focus on the molecular engineering of perovskite QDs and their interactions and controlled assembly with functional BCP thermoplastic elastomers.

In this study, polystyrene-*b*-polyisobutylene-*b*-polystyrene (SIBS) is used as the soft and flexible BCP matrix for $CsPbBr_3$ QDs to create functional nanocomposites. To enable the strong and selective interaction between the $CsPbBr_3$ QDs and SIBS matrix, customized polyisobutylene (PIB)-based polymer ligands were synthesized and used to replace the original short ligands on the QDs surface. The molecular structure and morphology of such nanocomposites were systematically studied with atomic force microscope (AFM), transmission electron microscope (TEM), and X-ray scattering. The optical properties and stability were studied with steady-state and time-resolved photoluminescence. The mechanical strength, flexibility, and stretchability of the SIBS-QDs nanocomposites were demonstrated. The polymer ligands on QDs, the molecular structure of the SIBS, and the loading of perovskites QDs were found to play significant roles in the hybrid structure and optical properties of the nanocomposites.

4.2 Materials and experimental section

Materials. Highly reactive polyisobutylene (Glissopal V1500 Mn = 2300) was obtained from BASF. Benzoyl peroxide (BPO), 1,4-dioxane, N,N-Dimethylformamide (DMF), tetrahydrofuran (THF), and methanol were purchased from Sigma Aldrich. 3-Dimethylaminoproplyamine, 1,3-propanesultone, triethylamine, chloroform, acetone, ethyl acetate, sodium sulfate, diethyl ether, methylene chloride, 4M hydrogen chloride in 1,4-dioxane, maleic anhydride, and anhydrous toluene were purchased from Fisher Scientific. Di-tert-butyl decarbonate ($(Boc)_2O$) was purchased from TCI chemicals. Poly(styrene-*b*-isobutylene-*b*-styrene) (SIBS 073T, and SIBS 062T) was provided by Kaneka corporation. Those chemicals were used as received.

$CsPbBr_3$ QDs synthesis. $CsPbBr_3$ QDs were synthesized using the hot-injection method as described in our previous reports.[194,195] Briefly, a precursor of Cs-oleate was made by dissolving Cs_2CO_3 in a mixture of oleic acid (OA) and 1-octadecene (ODE) at 150 °C. The temperature of the Cs-oleate solution was kept above 100 °C. To make a precursor solution for Pb and Br, $PbBr_2$ and $ZnBr_2$ were dissolved in a mixture of ODE, OA, and oleylamine (OAm) at 120 °C. The Cs precursor solution was added to the precursor solution of Pb and Br to initiate the reaction. Once the reaction was cooled down, the $CsPbBr_3$ QDs were purified with several washing steps.

It is noted that although $ZnBr_2$ was used during the synthesis, elemental analysis demonstrated that Zn^{2+} ions incorporation in the perovskite QDs is negligible. The main purpose of introducing $ZnBr_2$ during the QDs synthesis is to obtain a very rich Br^- environment by increasing the Br to Pb ratio to 10~25 to achieve good size control (below 7 nm) and strong quantum confinement of the QDs. Both inductively coupled plasma–mass spectrometry and energy-dispersive X-ray spectroscopy (EDS) are used to determine the concentration of Zn^{2+} ions in nanocrystal lattices.[56] The results indicated no sign of the incorporation of Zn^{2+} beyond the detection limit of the measurement ($Zn/Pb < 1 \times 10^{-3}$), setting an upper limit of <1 Zn^{2+} ion per QD. In hot injection synthesis, incorporating alien cations is usually difficult due to the self-purification of nanocrystals. Also, we didn't observe dimensional transformation of the $CsPbBr_3$ QDs in our system related to the use of $ZnBr_2$ during synthesis.

PIB-based polymer ligand synthesis. The chemical synthesis of the $ZW\text{-}NH_2$ molecules is a multi-step process, and the detailed procedure is described in the supporting information. Briefly, in the first step, free radical graft copolymerization of maleic anhydride onto highly reactive low Mw PIB will be conducted to generate PIBSA.[196] Then, the PIBSA was chemically modified with sulfobetaine zwitterion molecules. The mechanism is a ring-opening reaction between the amine-modified sulfobetaine zwitterion and the succinic anhydride groups on PIBSA.[47] The synthesis of amine-modified sulfobetaine zwitterion molecules is a three-step process starting with N, N-dimethylaminoproylamine, and the details can be found in the SI.

The synthesized PIB-based zwitterion ligands were then used for ligand exchange reaction of the pristine perovskite QDs in anhydrous toluene at room temperature. The sulfobetaine zwitterionic groups of the polymer ligands will strongly coordinate on the surface of perovskite QDs and replace the OA/OAm molecules.

Preparation of SIBS/p-QDs nanocomposites. SIBS copolymer was dissolved in anhydrous toluene and then mixed with polymer ligands modified $CsPbBr_3$ QDs suspension in toluene. The molar ratio of the SIBS chains and number of p-QDs (or QDs) was calculated and controlled. The final concentration of SIBS in the mixed solution was kept at 1.2 wt%. The ratio of the number of the QDs to SIBS chains was set at 2:100 or 0.8:100. For instance, to prepare 10 g of the SIBS-30/QDs solution with ratio of 2:100, the number of moles for SIBS is 10g x 1.2wt.%/ 75500 g/mol or 1.59×10^{-6} mol. The concentration of the original QDs solution (mole of QDs per liter) was measured to be 1×10^{-4} mol/L based on the optical absorbance and molar extinction coefficient,[197] so that the corresponding volume of QDs solution needed is 1.59×10^{-6} x 0.02 mol / 1×10^{-4} mol/L or 0.318 mL.

To fabricate the nanocomposite thin films, the mixed solution was spin-coated on a thin glass slide (thickness: 0.15 mm) at 6000 rpm for 30 seconds. The as-prepared films were further dried in ambient conditions without thermal annealing or solvent annealing. The preparation of nanocomposites composed of SIBS and pristine p-QDs was conducted using a similar procedure.

Characterization. An NMR spectrometer (Mercury-300, Varian Oxford) was used to record the ^1H NMR spectra. The FTIR spectra in attenuated total reflectance mode were recorded using an FTIR spectrometer (Nicolet iS50, Thermo Scientific). A UV-Vis spectrophotometer (8453, Agilent Technologies) was used to record the UV-Vis absorption spectra. The steady-state PL spectra of QDs and p-QDs solution, and SIBS/QDs and SIBS/p-QDs hybrid films were recorded using PL spectrophotometer (Cary Eclipse, Aglient Technologies). Time-resolved PL measurements were conducted with a customized wide-field/confocal epi-illuminating fluorescence microscope with 405 nm laser excitation. The second-order correlation measurements were conducted using the Hanbury Brown and Twiss interferometer. Excitation was performed via a 405 nm pulsed laser with a 4 MHz repetition rate, and average pulsed laser power of 1.1 nW.

4.3 Results and discussion

In our study, we chose BCP thermoplastic elastomer (TPE) as the soft matrix, which is a class of copolymers with a thermoplastic block and a rubbery block, they combine the good processability of thermoplastic and the high elasticity of elastomers. Specifically, SIBS copolymers with PIB as the soft block and polystyrene as the hard block were used in our study. The main reason for selecting SIBS is that it has excellent chemical, oxidative, and biostability, extremely low permeability, as well as high strength and elongation at break (> 600%).[145,146] Those advantages make it a perfect soft material to be assembled with perovskite QDs to create soft, stretchable, stable hybrid materials with molecular-level control of the interfacial and internal structure.

Pristine $CsPbBr_3$ QDs have oleic acid/oleylamine (OA/OAm) ligands on the surface, which do not have selective or preferential interactions with either block in the copolymer matrix. In order to address this challenge and achieve selective interaction between the QDs and copolymer matrix, we have designed polymer ligands with zwitterionic end groups to replace the original short ligands (Figure 25a). It is expected that the PIB-based ligands functionalized $CsPbBr_3$ QDs (p-QDs) will have strong and selective interactions with the PIB block in SIBS copolymer matrix.

The BCP matrix has a well-defined microphase-separated morphology which can be tuned by varying the length ratio of the two blocks. The SIBS copolymer with 30 wt% PS used in our study primarily has a hexagonal cylindrical structure as shown in Figure 25b. When the p-QDs are integrated into the SIBS matrix, strong and selective interaction between the polymer ligands and PIB block is expected to enable precise control of their spatial distribution as well as enhanced stability due to the excellent barrier properties of PIB (Figure 25b).

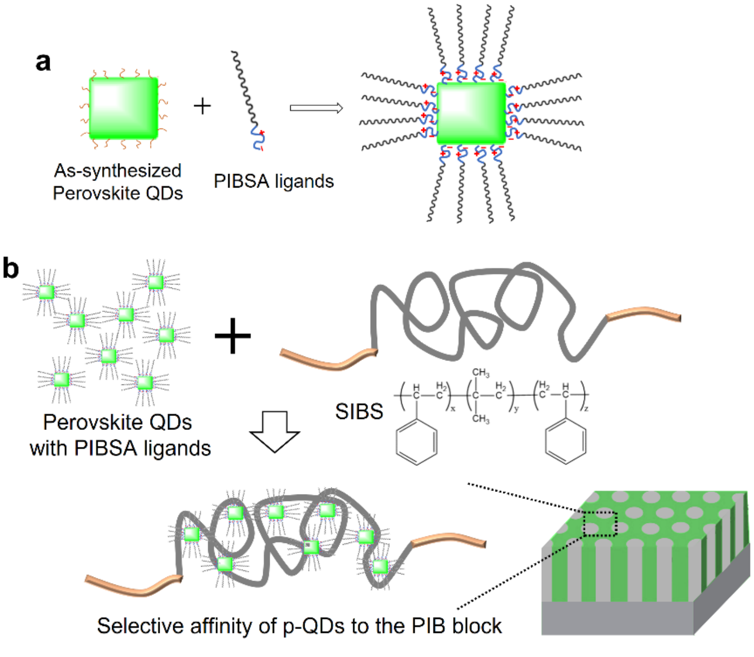

Figure 25: Schematics of ligand exchange and nanocomposite structure. (a) Schematic of the designed polymer ligands to replace original small molecule ligands on perovskite QDs. (b) The integration of p-QDs with copolymer TPEs to create functional optical nanocomposites.

Design and synthesis of polymer ligands: The design and synthesis of the PIB-based polymer ligand are shown in Figure 26a-b. In the first place, α-olefin-terminated PIB or highly reaction PIB (HR-PIB) reacts with maleic anhydride to form PIB chain terminated with succinic anhydride (PIBSA) (Figure 26a). This is archived *via* Alder-ene reaction at a high temperature (140 °C). FTIR of the HR-PIB (Figure 26d) shows peaks at 1388 and 1364 cm^{-1}, which correspond to the C-H stretching vibrations of the methyl groups ($-(CH_2-C(CH_3)_2)_n-$) in the main chain. The peak at 893 cm^{-1} corresponds to the out-of-plane deformation of vinyl groups in the HR-PIB chain.[198] After the reaction with maleic anhydride, PIBSA has three new peaks: the peaks at 1860 cm^{-1} and 1780 cm^{-1} correspond to the C=O stretching of the anhydride rings in succinic anhydride,[199] and the peak at 1076 cm^{-1} corresponds to the stretching of the =C-O-C= group in succinic anhydride.[200]

The PIB-based ligands need to have charged groups, preferably zwitterionic end groups, to enable strong interaction with $CsPbBr_3$ QDs. Such zwitterions combine Lewis acid and Lewis base moieties in their motifs, so that they can simultaneously interact with anions and cations on the perovskite QDs.[201] Therefore, a zwitterionic molecule with amine end group ($ZW-NH_2$) was synthesized to react with PIBSA. Details of the synthesis of the $ZW-NH_2$ molecules are described in appendix B (Figure B1). The NMR spectrum for the $ZW-NH_2$ molecule is shown in Figure 26c (see also Figure B2). Those characterizations confirm the structure and purity of the $ZW-NH_2$ molecules.

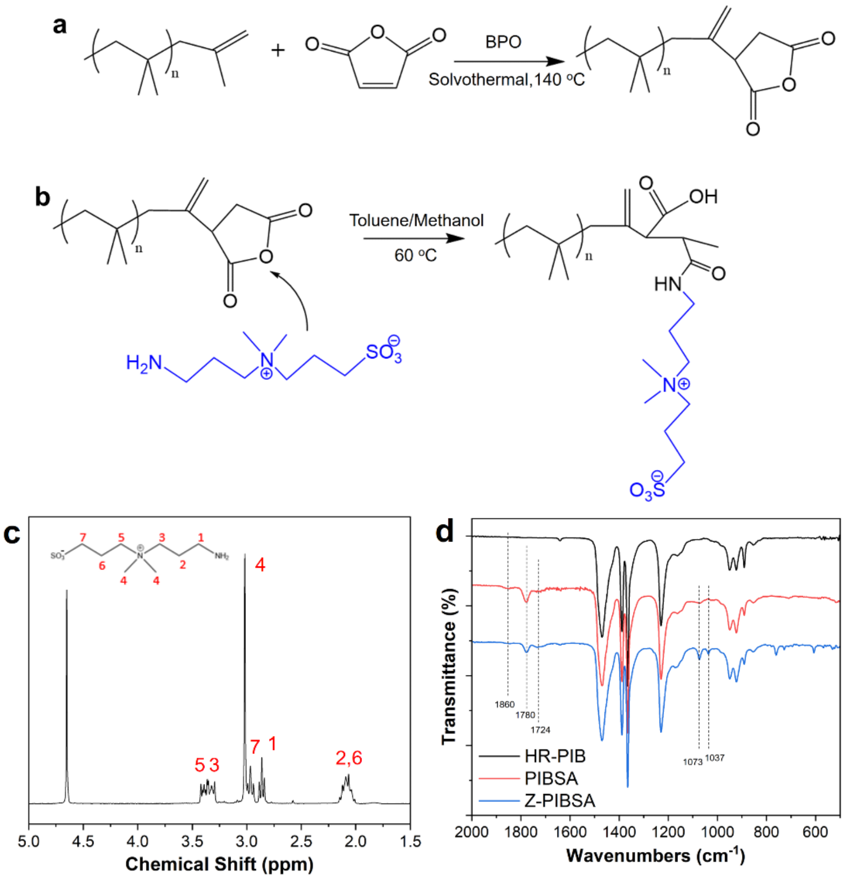

Figure 26: Synthesis of the PIB-based zwitterionic polymer ligands. (a) Reaction of highly reactive PIB and MA to form PIBSA. (b) The reaction of PIBSA with amine-modified sulfobetaine zwitterion to form the polymer ligand. (c) NMR of the amine-modified sulfobetaine zwitterion. (d) FTIR spectra of HR-PIB, PIBSA, and zwitterionic PIBSA.

Finally, the ZW-NH$_2$ and PIBSA react *via* a ring-opening process to form the polymer ligands (Figure 2b). The chemical structure and its changes were confirmed with FTIR (Figure 2d) and NMR characterization (Figure B3). It is observed that a new peak emerges at 1073 cm^{-1} after the reaction, which corresponds to the S=O stretching of the sulfoxide group present in ZW-NH$_2$. The two peaks at 1388 and 1364 cm^{-1}, which correspond to HR-PIB remain unchanged. These results suggest that the chemically modified PIBSA ligand was successfully synthesized.

Comparative study of pristine QDs and p-QDs: The photoluminescence (PL) emission peak for pristine QDs is at 478 nm, which slightly shifted to 476 nm for the p-QDs (Figure 27a). The UV absorption peak for pristine QDs is at 470 nm, which slightly shifts to 467 nm for the p-QDs. The small peak shift is related to the surface reconstruction during the ligand exchange process. TEM images (Figure 27a-b) show the $CsPbBr_3$ QDs have a near-cubic shape with an average size of 4.5 nm. After ligand exchange, the p-QDs still maintain the size and shape of the $CsPbBr_3$ QDs (Figure 27c). Due to the presence of long polymer ligands, the p-QDs are more dispersed or separated from each other compared with the dense assembly of pristine QDs.

The PL stability of the QDs and p-QDs suspension in toluene over time at ambient conditions (25 ^{o}C and 70% humidity) was studied (Figure 27d-f). The PL intensity of p-QDs is about 10% higher than pristine QDs at the same concentration and condition throughout the testing. Also, the PL intensity of pristine $CsPbBr_3$ QDs after 7 days is 81.7% of its initial intensity, and for p-QDs, this value increases to 85.8%. This shows that the PIB-based polymer ligands can enhance the stability of perovskite QDs in solution.

Importantly, p-QDs show significantly enhanced stability than pristine QDs when exposed to polar solvents such as ethanol (Figure 27g-i). The PL intensity of pristine QDs drops dramatically to almost zero after 10 mins of exposure to ethanol/toluene mixture containing 5 vol% ethanol. In addition, with the disappearance of the original PL peak, there is a weak redshifted peak at around 510 nm. This is probably due to the fusion/growth of the QDs after their surface is etched by polar solvent and loss of native ligands.

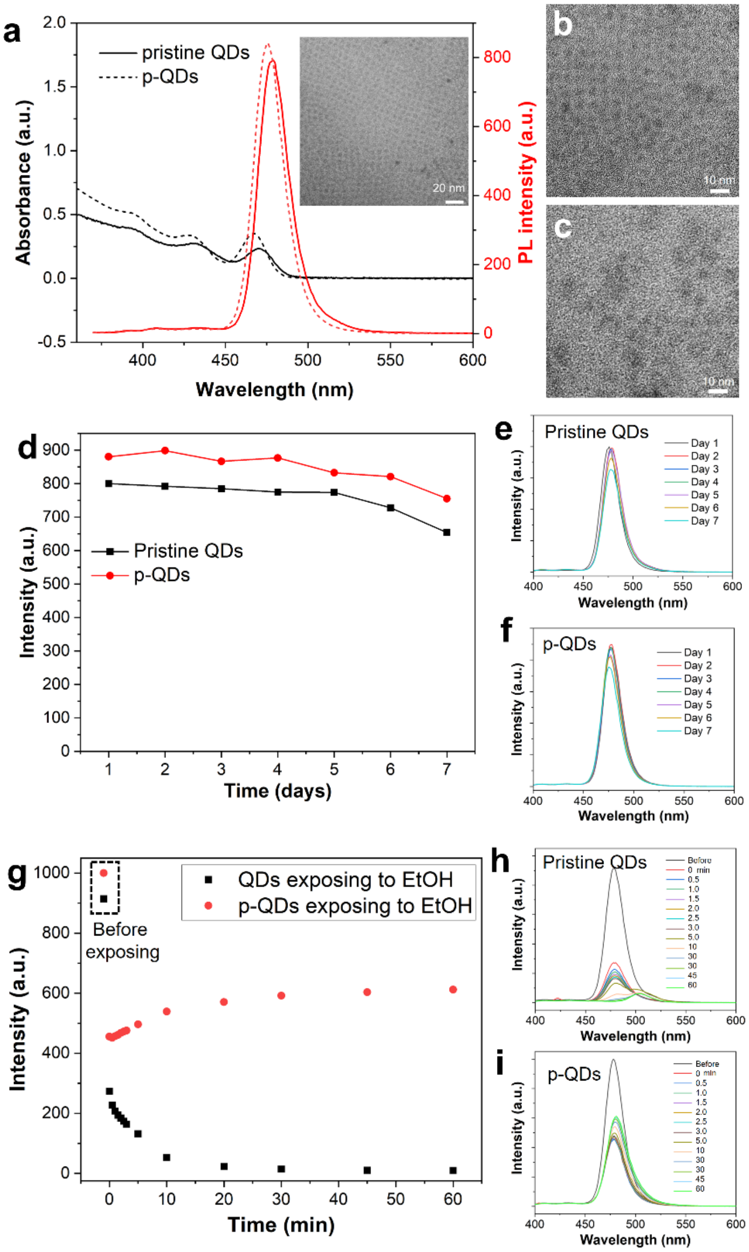

Figure 27: Optical properties and structure of pristine QDs and p-QDs. (a) PL and UV spectra of $CsPbBr_3$ QDs and the ligand-exchanged p-QDs. (b-c) TEM images of the $CsPbBr_3$ QDs. (d) PL intensity vs time for the pristine QDs and p-QDs in toluene, (e-f) PL spectra at different days for the pristine QDs and p-QDs in toluene. (g) PL intensity vs time for the pristine QDs and p-QDs in toluene/ethanol mixture, (h-i) PL spectra at different days for the pristine QDs and p-QDs in toluene/ethanol mixed solvent.

The p-QDs, on the other hand, maintain 60% of the PL intensity after hours of exposure to the same toluene/ethanol mixture with minimum peak shift. The significantly enhanced stability of p-QDs in polar solvents can be explained by the high hydrophobicity and impermeability of PIB-based ligands, which can largely reduce the contact between polar solvent molecules such as ethanol with perovskite QDs.

Structural study of SIBS/p-QDs nanocomposites: The introduction of perovskite QDs will have both entropic and enthalpic effects on the block copolymer matrix,[99,202] which is represented in this equation $\Delta G = (\Delta H_{NP/poly} + \Delta H_{surf}) - T\ (\Delta S_{conf} + \Delta S_{trans})$,[203,204] where ΔG is the overall free energy of the system, ΔH_{surf} and $\Delta H_{NP/poly}$are the surface energy variation and enthalpic energy difference between the perovskite NPs and polymer block, respectively. ΔS_{conf} and ΔS_{trans} are the changes in the conformational entropy of the polymer chains and the translational entropy of the introduced perovskite QDs, respectively. To achieve well-ordered structure of perovskite NPs in the TPE matrix without large-scale phase segregation, it is critical to control the enthalpic and entropic contributions of the perovskite QDs through ligand surface engineering.[119,205] In our system, the PIB-based polymer ligands on p-QDs are expected to lead to strong and selective interaction with the SIBS copolymer through the PIB block. Such preferred interaction provides favorable enthalpic interaction to overcome the inherent entropy penalties due to polymer chain stretching upon the sequestration of p-QDs.

The SIBS/p-QDs nanocomposite films were prepared by solution blending followed by spin coating into thin films. The mixed solution has a polymer concentration of 1.2 wt.%, and the final film thickness after spin coating and drying is about 50 nm (Figure B4). Two different types of SIBS were studied as the soft matrix for such nanocomposites, the first type has an overall Mw of 75,500 g/mol and PS block weight fraction of 30%, which is named SIBS-30. The second type of SIBS has a lower molecular weight (60,000 g/mol) and a slightly lower PS weight fraction (23%), which is named SIBS-23. We mixed p-QDs or pristine QDs with SIBS matrix with the mole ratio of QD particles to SIBS chains to be 2:100 or 0.8:100, and such samples are named as SIBS/p-QDs-2, or SIBS/p-QDs-0.8, respectively.

Before investigating the properties of SBIS/p-QDs nanocomposite films, we studied the effect of blending SIBS with p-QDs on its optical properties and stability in solution. For instance, the PL of p-QDs in toluene, and a mixture of p-QDs and SIBS-30 (mole ratio of p-QD particles to SIBS-30 chains is 2:100) in toluene with the exact same concentration of p-QDs were measured. The PL spectra and peak intensity over 7 days were compared (Figure B5). The results show that the incorporation of SIBS to p-QDs solution increases both the PL intensity and the long-term stability of the p-QDs. The PL intensity of p-QDs after 7 days is 85.8% of its initial intensity, and for SIBS-30/p-QDs, this value increases to 93.3%.

The morphology of SBIS/p-QDs nanocomposite films was studied with AFM. It is noted that the SIBS copolymer as well as the nanocomposite films were characterized in their as-prepared state without thermal or solvent annealing. The main reason is that the as-prepared SIBS has very similar morphology compared with the thermally annealed one (Figure B6), and thermal annealing has adverse effects on the optical properties of perovskite QDs. As a control sample, pristine SIBS-30 (Figure 28a-b) shows a microphase-separated morphology with PS cylindrical domains in the PIB matrix, and most of the PS cylinders are vertically aligned with some in the horizontal plane. Such morphology is typical for ABA-type block copolymers with similar composition and consistent with previous reports.[145,206]

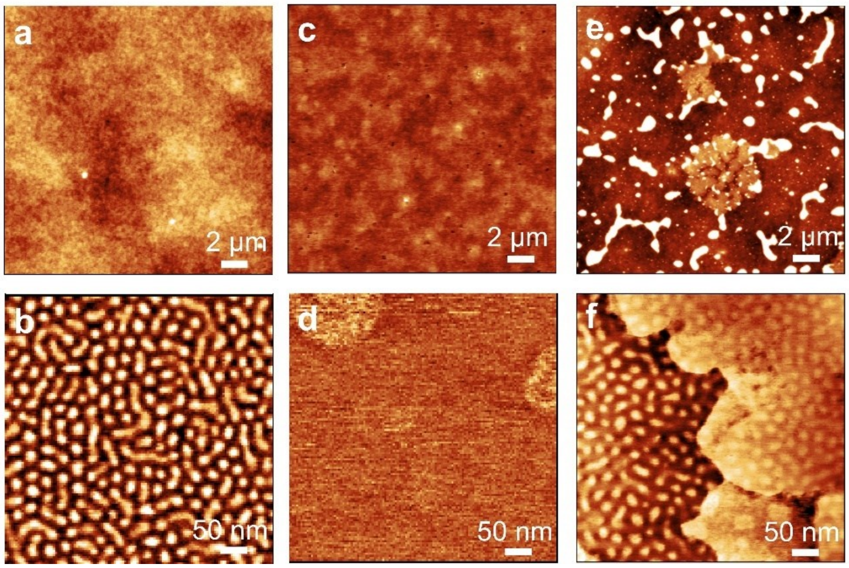

Figure 28: Morphology of the SIBS-30/p-QDs nanocomposites. (a-b) AFM images of SIBS-30 at two different magnifications. (c-d) AFM images of SIBS-30/p-QDs-2 composite at two different magnifications. (e-f) AFM images of SIBS-30/QDs-2 composite at two different magnifications. The top row are topography images, and the bottom row are phase images

AFM images of the SIBS-30/p-QDs-2 nanocomposite (Figure 28c-d) show a homogenous morphology without any aggregation of p-QDs. The high-resolution phase image does not show distinct microphase separation morphology compared with pristine SIBS-30, and the probable reason is that the PIB-based ligands on p-QDs have strong and preferential interaction with the soft PIB block, which reduces the contrast between the PS and PIB domains (stiffness/modulus) in AFM phase imaging.

In contrast, the nanocomposite composed of SIBS-30 and pristine QDs at the same ratio, which is named SIBS-30/QDs-2, shows a high extent of local aggregation of QDs (white domains in Figure 28e). From the higher magnification phase image (Figure 28f), it can be seen that some areas have microphase separated morphology similar to pristine SIBS, while other areas show aggregation of nanostructures. Such morphology is mainly due to the weak and nonspecific interaction between pristine QDs and the SIBS matrix, which can lead to uncontrolled aggregation of QDs.

The strong and preferential interaction between p-QDs with PIB block in SIBS is also confirmed with a control study. In this experiment, we blended p-QDs with the homopolymer of PIB and PS, respectively, in solution. The molar ratio of p-QDs to polymer was set to be 0.8:100 in both samples. The morphology of PIB/p-QDs and PS/p-QDs nanocomposites was studied by AFM (Figure B7). The results show that p-QDs form severe and large aggregates in PS matrix, which indicates the lack of strong and specific interaction between them. On the other hand, the PIB/p-QDs nanocomposite has very smooth surface and homogenous morphology which confirms the strong interaction between PIB-based ligands with PIB polymer.

TEM characterization was conducted on the SIBS-30/p-QDs nanocomposites (Figure 29). Pristine SIBS shows random-oriented PS cylinder structures in PIB matrix (Figure 29a). SIBS-30/p-QDs-0.8 shows hexagonal cylinder structure of the SIBS with vertically aligned PS cylinders in the PIB matrix (Figure 29b). Importantly, it also shows that the p-QDs (representatives are marked with red circles) are mostly located at PIB blocks, which are in between the PS cylindrical domains (representatives are marked with white circles). SIBS-30/p-QDs-2 nanocomposite shows a similar morphology but with a higher density of the p-QDs in the copolymer matrix (Figure 29c).

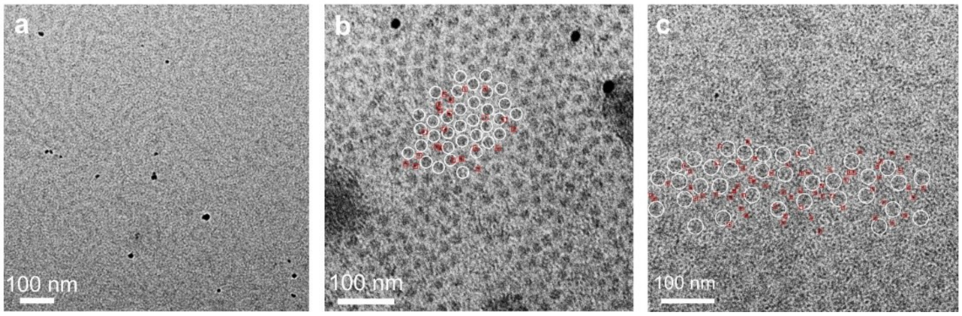

Figure 29: TEM images of (a) pristine SIBS, (b) SIBS-30/p-QDs-0.8 composite, and (c) SIBS-30/p-QDs-2 composite. The white circles correspond to representative PS domains in SIBS, and the red circles correspond to representative p-QDs in the composite.

We also studied the effect of block copolymer structure on the structure and properties of the SIBS/p-QDs and SIBS/QDs nanocomposites by comparing SIBS-30 and SIBS-23 as the soft matrix. AFM of SIBS-23 (Figure 30a-b) shows a similar microphase-separated morphology but with smaller domain sizes compared with SIBS-30 due to lower molecular weight and block length. The SIBS-23/p-QDs-2 nanocomposite has a small extent of local aggregation of p-QDs (Figure 30c-d), and the microphase-separated morphology in phase image is much less pronounced than pristine SIBS-23. On the other hand, the SIBS-23/QDs-2 nanocomposite (Figure 30e-f) shows a higher extent of QDs aggregation and the polymer matrix still shows high contrast between the PS and PIB domains in the phase image.

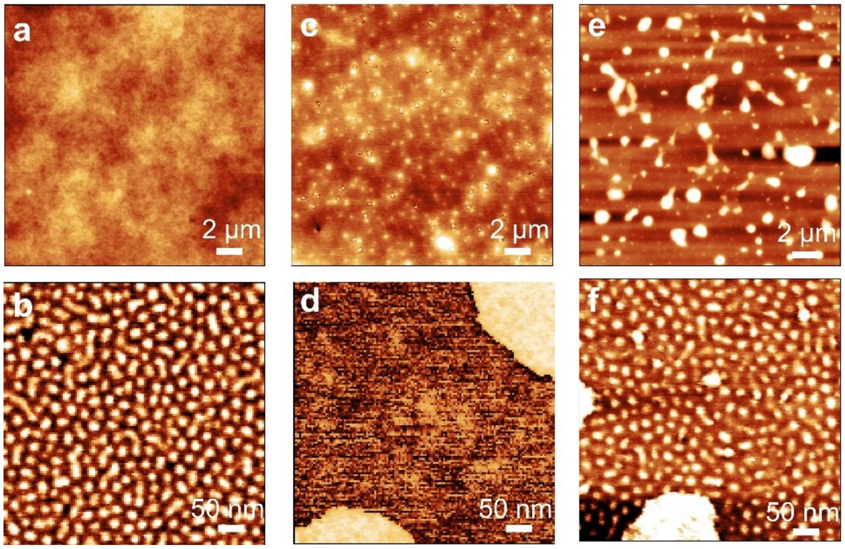

Figure 30: Morphology of the SIBS-23/p-QDs nanocomposites. (a-b) AFM images of SIBS-23 at two different magnifications. (c-d) AFM images of SIBS-23/p-QDs-2 composite at two different magnifications. (e-f) AFM images of SIBS-23/QDs-2 composite at two different magnifications. The top row are topography images, and the bottom row are phase images.

The main reason for such differences in morphology between SIBS-30/p-QDs and SIBS-23/p-QDs nanocomposites is that although SIBS-23 still has selective and preferential interaction with p-QDs through its PIB block, due to the shorter PIB block (PIB block Mw of 46,200 g/mol in SIBS-23, and PIB block Mw of 52,850 g/mol in SIBS-30) or smaller domain size, it is not as effective in accommodating or protecting the p-QDs, especially at high p-QDs loading. Thus, some extent of p-QDs aggregation occurs, but it is still less pronounced compared with SIBS-23/QDs nanocomposites.

Moreover, we also investigated the effect of p-QDs (or QDs) loading on the structure of the nanocomposites. To this purpose, we varied the molar ratio of p-QDs (or QDs) to SIBS from 2:100 to 0.8:100. For the SIBS-30/p-QDs-0.8 and SIBS-30/QDs-0.8 nanocomposites, AFM images (Figure B8) show that the morphological differences between those two samples are less pronounced due to lower QDs loading, and both show microphase-separated block copolymer morphology without obvious QDs or p-QDs aggregation on the surface. On the other hand, the morphology (Figure B9) of SIBS-23/p-QDs-0.8 and SIBS-23/QDs-0.8 are closer to pristine SIBS-23 due to lower QDs loading, with SIBS-23/QDs-0.8 having a higher density of aggregated domains.

The internal structures of the SIBS/QDs nanocomposites were also characterized by GISAXS (Figure B10). Pristine SIBS-30 copolymer shows a main peak (q*) at 0.023 $Å^{-1}$, which corresponds to an interdomain spacing (d) of 27.3 nm. Another peak at $\sqrt{3}q^*$ is also observed, which indicates a hexagonal-packed cylinder structure, and this result is consistent with our previous study.[43] After blending with $CsPbBr_3$ QDs, new peaks at lower q values (0.0053 and 0.0063 $Å^{-1}$) can be observed for SIBS-30/QDs-0.8 composite, which indicates the appearance of aggregates with size around 100 nm. Similarly, the pristine SIBS-23 copolymer shows q* at 0.025 $Å^{-1}$ and $\sqrt{3}q^*$ peak at 0.044 $Å^{-1}$, which corresponds to a smaller domain spacing of 24.9 nm due to the lower molecular weight. The SIBS-23/QDs-0.8 nanocomposite shows additional peaks at lower q range, which indicates the appearance of aggregates with size in the range of 41.0 to 66.1 nm. A more systematic investigation on the thermodynamics and structure of the SIBS/QDs nanocomposites by X-ray scattering and multiscale modeling will be conducted in the near future.

Optical properties and stability of SIBS/p-QDs nanocomposites: The optical properties of the SIBS/p-QDs nanocomposites were systematically investigated and correlated to their molecular-level structures. The SIBS-30/p-QDs-2 composite film has three times higher PL intensity than that of SIBS-30/QDs-2 at the same QD loading and conditions (Figure 31a-c). This can be related to the morphological study which shows that SIBS-30/p-QDs-2 has homogenous distribution of p-QDs, while SIBS-30/QDs-2 has substantial local aggregation of QDs. Moreover, the SIBS-30/QDs-2 nanocomposite can maintain a much higher (4 times) PL intensity after 7 days in ambient conditions (25ºC and 70% humidity). Similar results can be observed for SIBS-30/p-QDs-0.8 and SIBS-30/QDs-0.8 nanocomposites (Figure B11), but the differences are less pronounced. Such substantially enhanced photoluminescence and stability can be ascribed to the selective and strong interaction between the PIB ligands on p-QDs and PIB blocks in SIBS, which leads to better encapsulation and protection of the p-QDs.

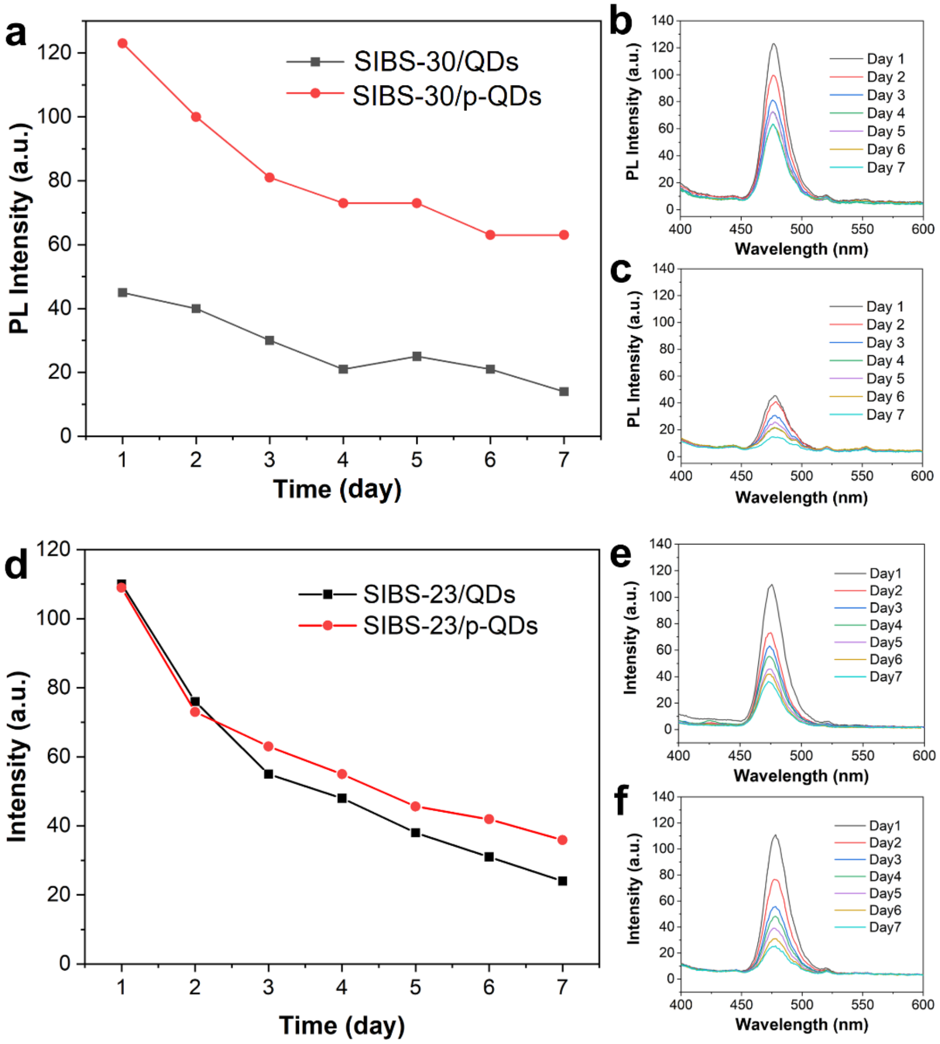

Figure 31: Optical properties and stability of the SIBS/p-QDs and SIBS-QDs nanocomposites. (a) PL peak intensity changes with time in ambient conditions for SIBS-30/QDs-2 and SIBS-30/p-QDs-2 composites. (b-c) PL spectra at different time for (b) SIBS-30/p-QDs-2 and (c) SIBS-30/QDs-2 composites, respectively. (d) PL peak intensity changes with time in ambient conditions for SIBS-23/QDs-2 and SIBS-23/p-QDs-2 composites. (e-f) PL spectra at different time for (e) SIBS-23/p-QDs-2 and (f) SIBS-23/QDs-2 composites, respectively.

Moreover, we found that the molecular structure of SIBS has substantial effects on the optical properties and stability of SIBS/p-QDs nanocomposites. When SIBS-23 was used as the soft matrix for p-QDs, the PL intensity and its change with time of SIBS-23/p-QDs and SIBS-23/QDs have a much smaller difference (Figure 31d-f, see also Figure B12).

The main reason for this can also be related to the morphological study that p-QDs already show some degree of aggregation in SIBS-23/p-QDs-2 nanocomposite due to the shorter PIB block length and smaller domain size. Therefore, the encapsulation and protection of the QDs by PIB blocks are less effective.

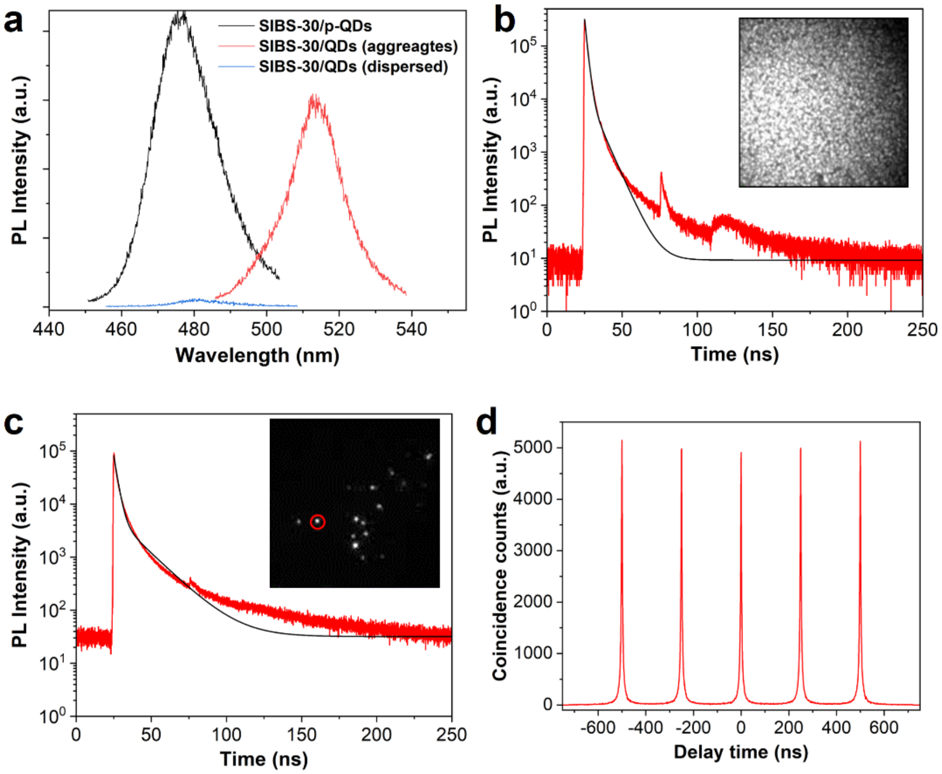

Figure 32: Time-resolve PL characterization of the SIBS/p-QDs nanocomposites. (a) PL spectra from localized regions of the nanocomposites collected by a confocal fluorescent microscope. (b) TRPL decay curves with data fitting (black curve) of SIBS-30/p-QDs-2 nanocomposite. Inset is the wide-field fluorescent image of the measured sample. (c) TRPL decay curves with data fitting (black curve) of SIBS-30/QDs-2 nanocomposite (measured from circled bright aggregate). Inset is the confocal fluorescent image of the measured sample. (d) Second-order correlation function measured from the bright aggregates shown in panel c inset.

Time-resolved PL measurement was conducted to further study the optical properties of the SIBS/p-QDs and SIBS-QDs nanocomposites. When comparing the confocal fluorescent images of SIBS-30/p-QDs-2 and SIBS-30/QDs-2 composites (Figure

32b-c insets), it is obvious that SIBS-30/p-QDs-2 has a uniform and much higher PL intensity across the entire sample, while SIBS-30/QDs-2 has some local aggregates with high PL intensity and the rest area has a much lower PL intensity. This is consistent with the morphological study by AFM discussed above.

PL spectra were collected from various locations on the nanocomposite films (Figure 32a). SIBS-30/p-QDs-2 composite showed consistent PL spectra throughout the sample with an emission peak at 478 nm. The SIBS-30/QDs-2 composite, on the other hand, showed significant differences between the aggregated domains and dispersed areas. The PL peak for the QDs aggregates in SIBS-30/QDs-2 composite has a significant red shift to 513 nm, and the dispersed areas have a much lower peak intensity but without an obvious peak shift. The large red shift in PL of the bright domains in SIBS-30/QDs-2 can be ascribed to the formation of QDs aggregates or superlattices inside the SIBS matrix.[207]

The PL decay curves for SIBS-30/p-QDs-2 and SIBS-30/QDs-2 composites are shown in Figure 32b-c. From the biexponential fitting of the curves, the short-lived PL lifetime (τ_1) and long-lived PL lifetime (τ_2) can be obtained. The τ_1 and τ_2 for SIBS-30/p-QDs-2 are 1.7 and 7.4 ns, respectively. The τ_1 and τ_2 for SIBS-30/QDs-2 in aggregated QDs domains are 2.3 and 15.9 ns, respectively. The observation of aggregated QDs domains in SIBS-30/QDs-2 composite is further confirmed with the second-order correlation function measurements under pulse-laser excitation. Fitting of the curve gives the second-order correlation at zero delay g2(0) of 1.0, which proves the presence of QDs aggregated or superlattice in those bright domains.

Last but not least, the other important advantage of using SIBS as the block copolymer matrix for perovskite QDs is its excellent mechanical flexibility and stretchability. We demonstrated this by deforming a rectangle-shaped SIBS/QDs nanocomposite membrane. The membrane shows strong fluorescence under UV illumination. It can be easily bent and twisted and then recovered without breaking or permanent deformation (Figure 33a-b). We also conducted tensile testing on a dogbone-shaped SIBS/QDs nanocomposite (Figure 33c-d). The results show that the nanocomposite has a Young's modulus of 3.9 MPa, and an elongation at break of 750%, which proves the excellent flexibility and stretchability of the SIBS/QDs nanocomposites. Such flexible SIBS/QDs nanocomposite membrane can maintain its strong photoluminescence after being immersed in water for months (Figure B13).

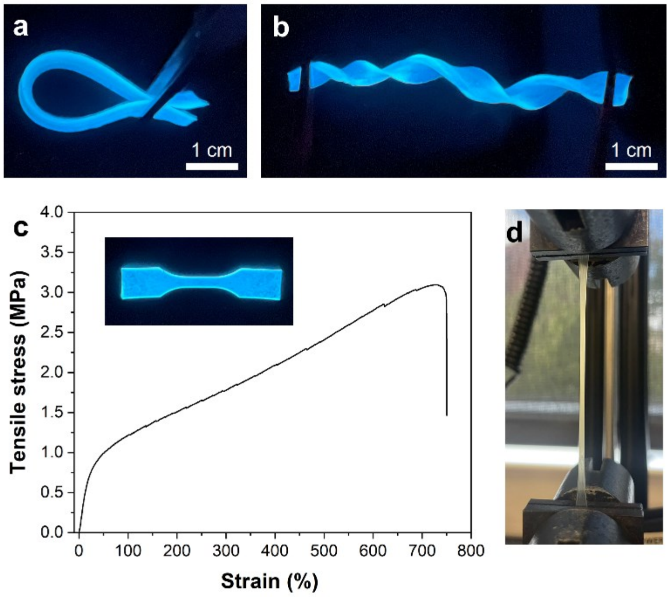

Figure 33: (a-b) Photos of a rectangle-shaped SIBS/QDs nanocomposite membrane during bending and twisting under UV illumination. (c) Stress-strain curve for the SIBS/QDs nanocomposite, inset shows the tensile testing sample under UV illumination. (d) Photo of the SIBS/QDs nanocomposite during stretching

4.4 Conclusions

In summary, we have designed and synthesized PIB-based polymer ligands for perovskite QDs and based on the strong and selective interactions between the polymer ligands and SIBS TPE copolymer, a series of functional nanocomposites were prepared and their structure-property relationship was elucidated. We discovered that the chemical compatibility of the polymer ligands and copolymer matrix is the key to achieve precise control of the distribution of perovskite QDs inside the soft matrix and prevent aggregation. Moreover, the PIB-based ligands on perovskite QDs and the incorporation of p-QDs inside the PIB domain of SIBS copolymer can substantially enhance the PL stability due to the high impermeability and chemical stability of PIB. Our approach to creating soft nanocomposites by molecular engineering and integration of perovskite QDs and TPE copolymers is of high importance to flexible optoelectronics, optical storage, and displays.

Our SIBS/QDs nanocomposites have unique advantages compared with previous reports on hybrid materials composed of perovskite nanostructures and BCPs. Most of those studies utilize PS-*b*-PVP or PS-*b*-PEO BCPs, which are neither flexible nor stretchable.[31–33] Our system has significantly higher flexibility and stretchability due to the SIBS matrix. Moreover, the hydrophilic PVP or PEO blocks in those BCPs are not desirable to protect the perovskite QDs from moisture, water, or polar solvents. The SIBS copolymer used in our study has superior impermeability to gas, water, and moisture, and provides better protection to the embedded perovskite QDs. Last but not least, SIBS has also been demonstrated to have excellent biocompatibility and biostability, which can lead to the future development of such SIBS/QDs nanocomposites in biomedical and bioelectronics applications.

CHAPTER V

INTEGRATION OF SULFONATED SIBS COPOLYMER WITH PEROVSKITE QDS FOR SOFT OPTICAL MATERIALS WITH ENHANCED STABILITY

Abstract

Metal halide perovskite (MHP) represents a cutting-edge material in the advancement of next-generation optoelectronic applications, owing to its exceptional attributes such as heightened light absorption efficiency, tolerance to bandgap defects, and superior color purity compared to conventional semiconductors. However, its commercial viability remains a formidable challenge due to its inherently dynamic ionic nature, rendering MHP susceptible to degradation upon exposure to polar solvents, moisture, and oxygen. This study proposed a novel approach to mitigate such environmental instability by integrating partially sulfonated block copolymer poly(styrene-b-isobutylene-b-styrene) (s-SIBS) with perovskite quantum dots (QDs). Herein, s-SIBS functioned as a protective matrix shielding QDs from ambient environment. The sulfonic acid groups within the s-SIBS matrix were observed to attract perovskite QDs through Lewis acid-base interactions, thereby providing additional functionality by enabling preferential QDs distribution. A systematic investigation encompassing sulfonation degree, BCP-QDs ratio, and the influence of SIBS molecular weight was undertaken to optimize the nanocomposite's fluorescence stability under ambient conditions.

5.1 Introduction

Lead halide perovskite quantum dot is a novel type of colloidal semiconductor nanocrystal material intermediating between the solid state and the molecular state. Typically, the stoichiometry for a metal halide perovskite is ABX_3[208] where the crystal lattice of perovskite consists of corner sharing octahedra $[BX_6]^{4-}$ with A^+ cations occupying the central voids. (A, B, X sites correspond to monovalent cation, divalent cation and halide anion, respectively). Within the nanoscale 3D structure, the restricted electron motion of QDs results in atom-like electronic states so the emission linewidth of monodispersed QDs is narrow and thus lead to a high color purity[68]. And by changing the crystal size or halide composition, QDs can vary the effective bandgap[209] so a wide color gamut can be achieved. Besides, the photoluminescence quantum yield(PLQY) of perovskite QDs can reach near unity values with red[210], green[211] or blue[212] color emission, which stands for high brightness. The abovementioned three unique features of perovskite QDs (high color purity, brightness, and wide tunable color gamut) make it a promising candidate for display applications.

Compared with conventional semiconductors, MHP shows improved defect tolerance where defect-induced trap states lie within the valance band and conduction band (shallow traps) that doesn’t dramatically alter the electronic structure of MHP[213]. Such phenomenon is attributed to the fact that the upper boundary (CBM) and lower boundary(VBM) of the bandgap are both formed by antibonding orbitals[214] so there is no mid-gap states formation for MHP. But the stability and performances of perovskite QDs, due to its highly dynamic nature as well as high surface-to-volume ratio, are still significantly influenced by external factors such as moisture, oxygen, or polar solvent[215]. Isolating perovskite QDs from ambient environment by embedding it in polymer matrix with hydrophobic nature is one of the major directions in enhancing the perovskite QDs device lifetime. For instance, PCL[216] and PS[217] based matrixes were incorporated with QDs and fabricated into textiles by electrospinning. Both paper-like textiles showed outstanding environmental resistance but the mechanical properties, especially the stretchability, were not discussed in detail. Other encapsulating polymers such as PS-P2VP[218], and PS-PEO[219] also did not exhibit elasticity due to their glassy or semicrystalline nature.

To fabricate a polymer-QDs composite with flexible and stretchable nature, we developed a strategy using a chemical stable block copolymer poly(styrene-b-isobutylene-b-styrene) (SIBS) with excellent barrier properties[49,220].SIBS is a type of thermoplastic elastomer consisting of two immiscible, polyisobutylene and polystyrene, phases with different glass transition temperatures[221]. The microphase separation of the glassy (PS) and soft (PIB) segments results in a physically entangled network which enables SIBS with combined advantages of thermosets and thermoplastics, namely rubber-like mechanical performance while maintaining the processability similar to conventional thermoplastics. In our previous work[98], PIB-based zwitterionic ligands were exchanged onto the QDs surface so the compatibility between the SIBS matrix and QDs can be improved. Due to the backbone structure and fully saturated nature of PIB soft phase, the composite exhibited strong luminescence even after one month immersion in water. The SIBS-QDs composite can also be bent, twisted and stretched to over 750% elongation. In this work, we instead perform sulfonation functionalization on the PS segments from SIBS to achieve the compatibility and selective affinity between the QDs and polymer matrix.

Sulfonate group can donate one electron by Lewis acid-base interaction to uncoordinated lead ions on the perovskite lattice surface. Yang[222] demonstrated that the addition of 4-dodecylbenzenesulfonic acid (DBSA) improved the QDs integrity as well as its solvent stability after washing cycles. Such behavior was attributed to the similar electronic features between sulfonate ions and Br^- ions so that the delocalization of the Pb electron cloud can be eliminated and inherently suppress the nonradiative recombination of photo-induced excitons. The DBSA-QD thin film as the proof of concept showed enhanced stability where 89% of the PL intensity was preserved after being heated at 60°C for 150 hours. Similarly, Fang[223] investigated the influence of the incorporation of the same benzenesulfonic acid in the precursor solution and reported that the halide interstitial and vacancy defects were simultaneously suppressed by coordination between the lead ion and the ionic sulfonate head of DBSA. In this work, SIBS undergoes sulfonation functionalization reaction was selected by taking advantages of the intrinsic PIB inertness, the lead ion affinity and the passivation effect of the sulfonated PS phase.

To evaluate the fluorescent performances of s-SIBS/QDs nanocomposites, steady state PL stability tests, TRPL tests were conducted to a series of s-SIBS/QDs spin-coated thin films to investigate the effects of QDs loading, sulfonation degree, and SIBS composition. AFM, TEM, and SAXS were used in morphological study to elucidate the nanocomposites' structure-property relationship. The tensile test and flexibility demonstration of s-SIBS/QDs nanocomposite indicated its robust and elastic feature. In summary, the sulfonation functionalization will have compound beneficial effects on fabricating a more PL stable material due to the ionic interaction between QDs and s-SIBS and the approach.

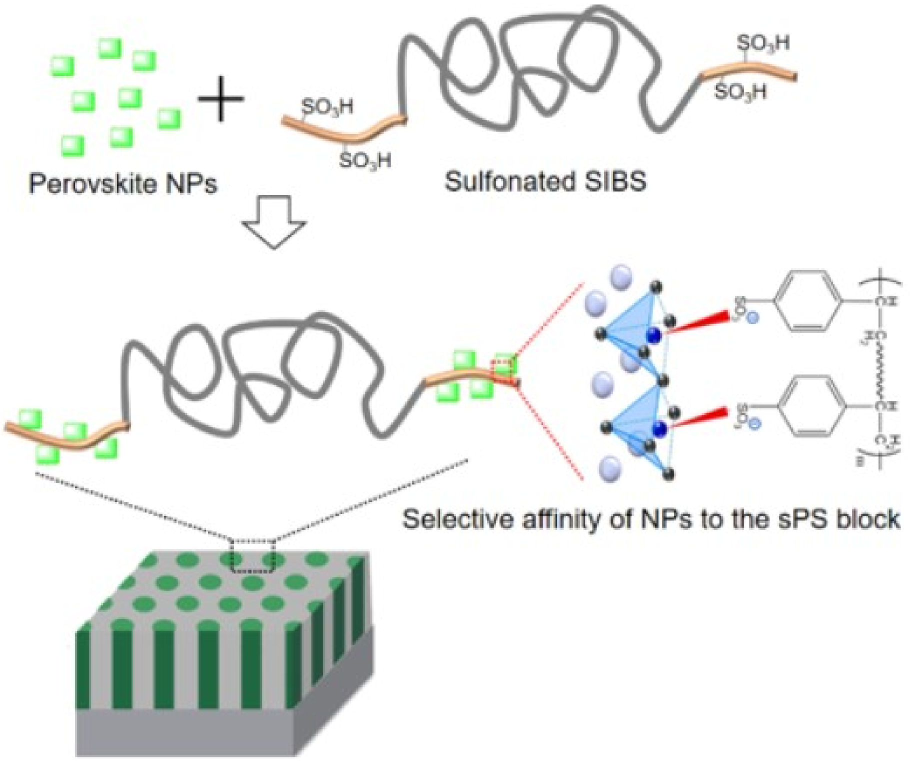

Figure 34: Schematic of electrostatic interaction between the metal ions on QD surface and sulfonate groups in the polymer matrix.

5.2 Materials and experimental section

Materials: Poly(styrene-b-isobutylene-b-styrene) (SIBS 073T, and SIBS 062T) were provided by Kaneka corporation. Sulfuric acid, acetic anhydride were purchased from Fisher Scientific. Toluene, methanol, isopropanol, dichloroethane, and dichloromethane were purchased from Sigma Aldrich. All chemicals were used as received.

Sulfonating agent preparation: Acetyl sulfate as the sulfonating agent was freshly synthesized before use. Acetic anhydride was dispersed in dichloromethane at 1:2 volume ratio after the moisture in the solvent was removed by nitrogen purging. Sulfuric acid was added dropwise into the acetic anhydride solution which was ice bathed to 0°C. The solution was kept stirring at 0°C for 10mins before SIBS sulfonation experiment.

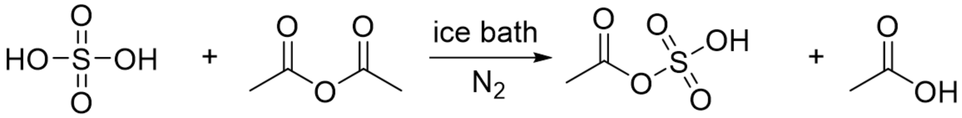

Figure 35: Synthesis of acetyl sulfate as the sulfonating agent.

Sulfonation of SIBS: SIBS was added in dichloroethane at 10%(w/v) concentration at 40℃ under 450 rpm stirring condition. After SIBS was fully dissolved, freshly prepared acetyl sulfate solution was added into SIBS solution slowly by a syringe to begin the sulfonation reaction. By varying the reaction time, the sulfonation degree of SIBS can be controlled. The reaction was terminated by isopropanol addition.

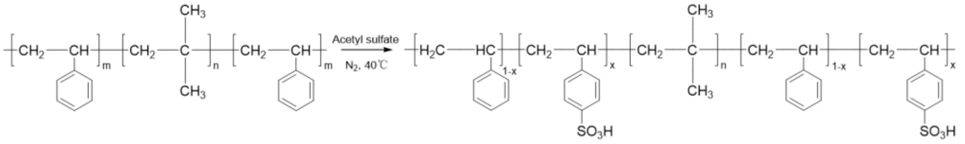

Figure 36: Reaction conditions for SIBS sulfonation.

s-SIBS collection and purification: s-SIBS was precipitated by adding the solution obtained from the sulfonation reaction into methanol at 1:40 volume ratio under stirring. The solid was collected and dialyzed in DI water till neutral PH value was achieved. The s-SIBS was ready for use after freeze-drying and stored in a desiccator.

$CsPbBr_3$ quantum dots synthesis: Hot-injection method was used in this study to synthesize perovskite QDs following the procedure reported in previous work[194]. Briefly, a hot Cs-oleate precursor solution was first prepared by dissolving Cs_2CO_3 in oleic acid (OA)/1-octadecene (ODE) mixture under N_2 atmosphere, during the process the solution temperature was kept at 150°C. The other precursor solution containing Pb and Br was prepared in a similar manner where $PbBr_2$ and $ZnBr_2$ were added into the mixed solution of OA, ODE, and oleylamine (OAm) at 120°C in N_2 atmosphere which was subsequently injected into the Cs-oleate to initiate the reaction. The synthesized $CsPbBr_3$ then purified by centrifuge and antisolvent washing and redispersed in hexane. According to our previous work[98], the $ZnBr_2$ addition during the synthesis process led to Br^- rich environment for enhanced size control and there was no sign of Zn^{2+} incorporation or dimensional transformation of the CsPbBr3 QDs.

s-SIBS/QDs thin film fabrication: In a glovebox, s-SIBS was measured according to the s-SIBS/QDs molar ratio and fully dissolved in anhydrous toluene. Measured perovskite QDs solution was added into s-SIBS and the resulting solution with 3wt% polymer final concentration was spin-coated on cover glass to fabricate s-SIBS/QDs nanocomposite thin films for subsequent characterizations.

Characterization: FTIR spectrometer in attenuated total reflectance mode (, Perkin Elmer) was used to confirm the sulfonation functionalization. A UV-Vis spectrophotometer (8453, Agilent Technologies) was used to record the absorption spectra. The steady-state PL spectra of QDs solution and BCP-QDs thin film samples were recorded using PL spectrophotometer (Cary Eclipse, Aglient Technologies). X-ray photoelectron spectroscopy (XPS) was performed using PHI 5000 Versaprobe II system., Atomic force microscope (AFM) was conducted with NT-MDT AFM with a SMENA scanning head, and with a Bruker Dimension Icon AFM. Images were acquired in tapping mode using Si cantilevers with 300 kHz resonance frequency, the scan rate was 0.5 Hz. Transmission electron microscopy (TEM) was performed using Tecnai G2 F20, small angle X-ray scattering (SAXS) was performed using Xenocs Xeuss 3.0. TRPL was conducted using a customized wide-field/confocal epi-illuminating fluorescence microscope with 405 nm laser excitation. Tensile test was performed using Instron 5567 according to ASTM D412 standard.

5.3 Results and discussion

In this study, the PS phase of SIBS was partially sulfonated with sulfonation degrees ranging from 8%~22%. It was expected that the grafted sulfonic acid groups can attract and passivate perovskite QDs through Lewis acid-base interaction since sulfonate ion shares similar electron features of Br^- ion[222]. And following experiments validated that all s-SIBS utilized in this investigation were fully soluble in non-polar toluene, thereby establishing compatibility with perovskite QDs for nanocomposite fabrication. Figure 37a showed the FTIR spectra of pristine SIBS and s-SIBS exhibiting four new peaks associated with sulfonation reaction at $1126cm^{-1}$, $1031cm^{-1}$, $1006cm^{-1}$, and $835cm^{-1}$ which are in agreement with other literatures[224,225]. Specifically, the peaks at $1126cm^{-1}$ and $1006cm^{-1}$ are the characteristics peaks of out-of-plane vibration of SO_3H group substituted aromatic ring. The peak at $1031cm^{-1}$ corresponds to the symmetric stretching vibration of SO_3H groups. The peak at $835cm^{-1}$ is considered as the out of plane deformation band assigned to substituted aromatic ring. Furthermore, the ratio of peak intensity between $1006cm^{-1}$ peak and the reference peak at $1365cm^{-1}$, respectively representing the amount of grafted sulfonic acid groups and CH_3 groups in PIB phase, was reported to have linear relationship with sulfonation degree[225]. Consequently, the sulfonation degrees of synthesized s-SIBSs shown in Figure 37a were then calculated as 8% and 18% respectively.

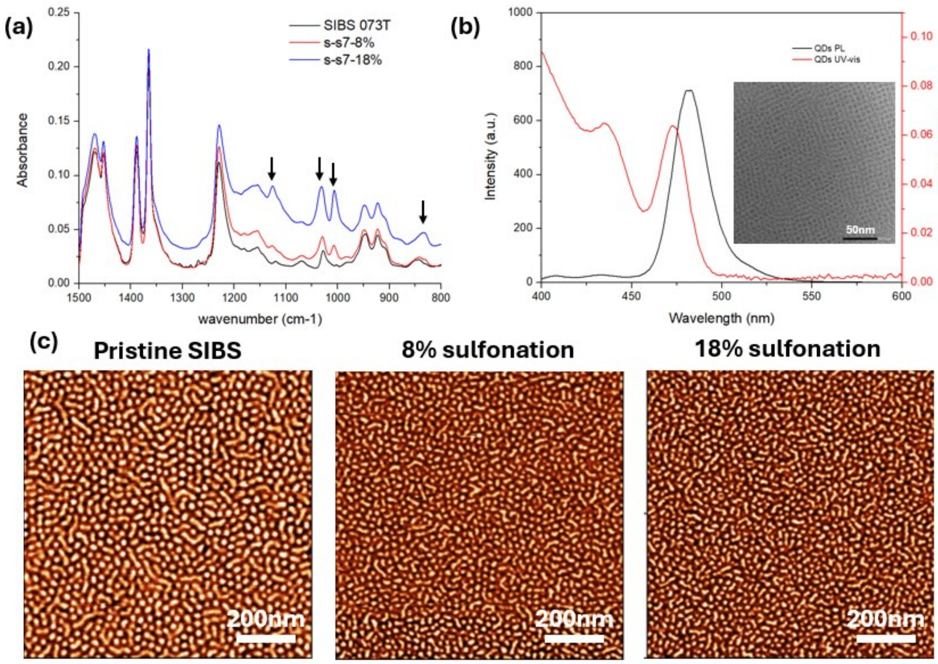

Figure 37: (a) FT-IR of partially sulfonated SIBS with 0%, 8%, 18% sulfonation degree. (b) PL and UV-vis of pristine QDs, inset is the corresponding TEM image. (c) 1x1 um AFM phase images of s-SIBS at 0%, 8%, and 18% SD, respectively

As shown in Figure 37b, the UV absorption peak and PL emission peak for $CsPbBr_3$ QDs were measured as 470nm and 478nm, respectively. The TEM inset image clearly showed $CsPbBr_3$ QDs were in cubic α phase with a characteristic length of 4.5nm. The AFM images in Figure 37c showed that partially sulfonated SIBS still maintained its distinct microphase separated morphology inherited from pristine SIBS where PS cylinders are hexagonally packed within PIB matrix. A reduction in the polystyrene domain size was observed following partial sulfonation of the PS phase. This phenomenon was further corroborated by SAXS analysis (provided in the Supporting Information), which revealed a decrease in interdomain spacing from 26.7 nm ($q = 0.023$ Å^{-1}) in pristine SIBS to 24.2

nm ($q = 0.026$ Å^{-1}) in the sulfonated derivative s-SIBS-8%. Similar trends have been reported in previous studies. In R.A. Weiss' work[226], the scattering peak of sulfonated SEBS copolymer transited to higher wavevector region, indicating smaller and less homogeneous phase morphology. Furthermore, Mani et al.[227] proposed that the development of microphase separation transition for BCP ionomer is a more kinetically influenced procedure where the ionic associations in PS phase decreased the molecular mobility and consequently hindered the self-assembly of microphases. So, a smaller domain size was expected for sulfonated SIBS.

The effect of perovskite QDs loading: For the composites containing pristine SIBS 073T and perovskite QDs, the corresponding AFM images revealed a progressive reduction in phase contrast with increasing QD loading. This decrease in phase contrast is attributed to the absence of selective interactions between the pristine SIBS matrix and the QDs. It was proposed that the introduced QDs were randomly dispersed throughout the polymer matrix, irrespective of the rubbery PIB or glassy PS phases, resulting in a more mechanically homogeneous composite. And as the perovskite QDs content increased, the influence of this random distribution became more pronounced (Figure 38). On the other hand, AFM images of the pristine SIBS-QD composites revealed a markedly different morphology compared to that of the neat SIBS. The characteristic hexagonally close-packed (hcp) morphology of the block copolymer was no longer evident; instead, the composite morphology transited into irregular, enlarged domains. This morphological evolution suggested that the incorporated QDs did not selectively associate with either the PIB or PS domains, but formed large, randomly distributed aggregates throughout the polymer matrix.

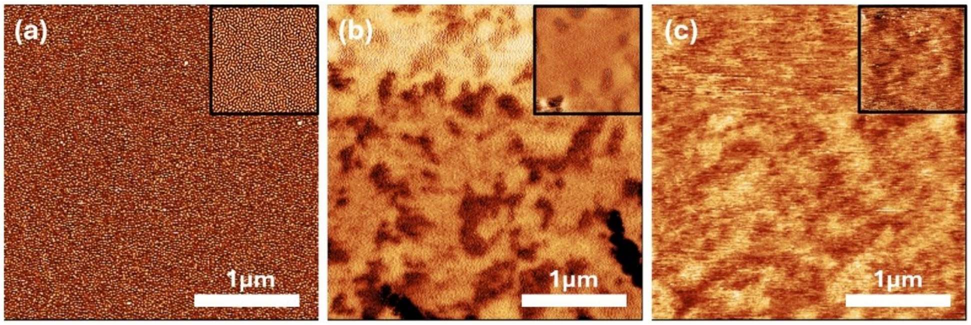

Figure 38: AFM phase images of (a) pristine SIBS, (b) 100:4 pristine SIBS-QDs composite, and (c) 100:6 pristine SIBS-QDs composite at 3x3μm scale. Insets are 1x1μm AFM phase images.

Figure 39 summarized the PL stability performance over 8 days for s-s7-8%+QDs composites with different QDs loadings (100:4 and 100:6 in terms of molar ratio between polymer and perovskite QDs). It was observed that when an equivalent amount of perovskite QDs was incorporated into BCP matrix (Figure 39a), the photoluminescence intensity of s-SIBS-%+QDs composite was significantly higher than that of pristine SIBS+QDs composite throughout the entire 8-day stability test conducted under ambient conditions. Such increase in PL intensity clearly evidenced the radiative recombination of the embedded perovskite QDs was promoted, which was attributed to the passivating effect of sulfonate groups and the Lewis's acid-base interactions between s-SIBS and the ionic surface of perovskite QDs. Figure 39d showed that beyond the expected increase in PL intensity resulting from the higher concentration of perovskite QDs, the s-SIBS+QDs composite continued to exhibit an additional enhancement in photoluminescence when the molar ratio increased to 100:6, resulting in a higher final retention of 75.6% compared to that of 65.5% for control sample without sulfonation. The variation in perovskite QD loading, along with the corresponding stability test results, indicated that s-SIBS was more effective in QD encapsulation and defect passivation. These findings confirmed that sulfonation of the SIBS matrix played a beneficial role in the fabrication of perovskite QD nanocomposites with enhanced environmental stability.

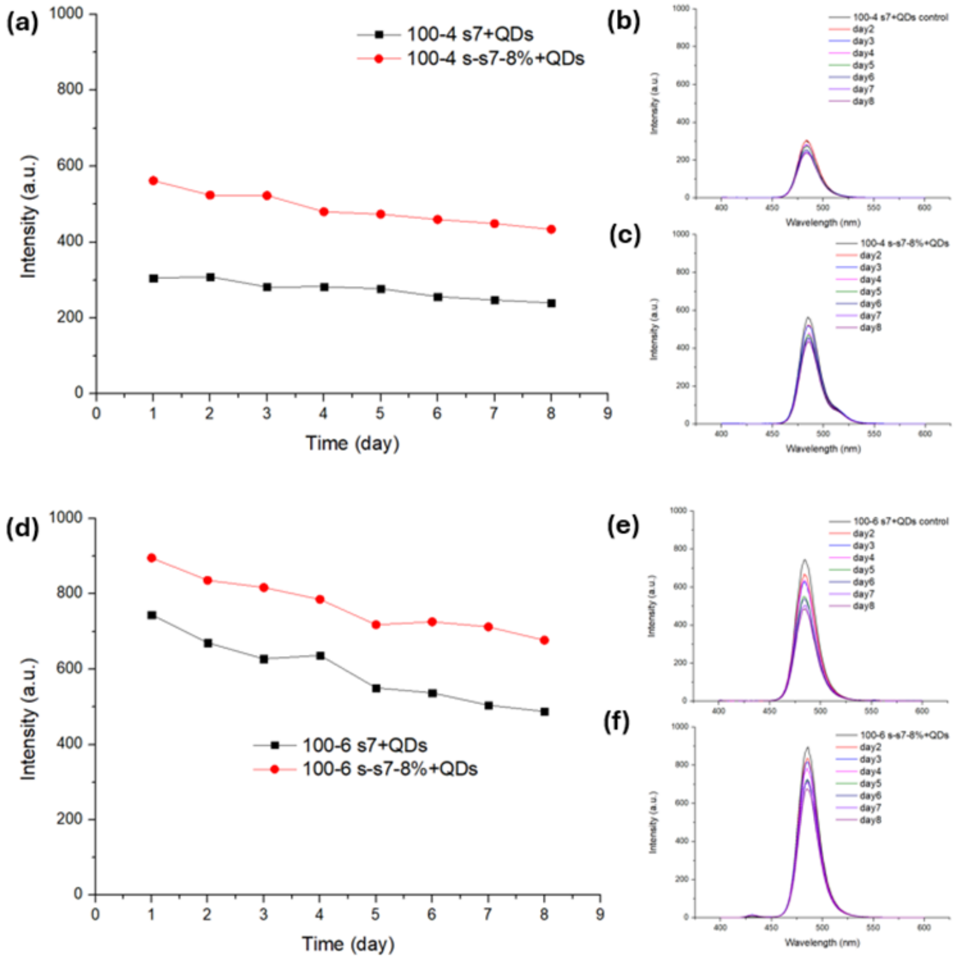

Figure 39: PL stability test showing the effect of QDs loading. (a) and (d) are the maximum PL intensity summary for 100:4 and 100:6 ratio composites. (b), (c) are the corresponding emission spectrum summary for s-s7-8%+QDs composite and its control sample at 100:4 molar ratio. (e), (f) are the PL summary for s-s7-8%+QDs composite and it control sample at 100:6 molar ratio.

Figure 40 revealed the morphological evolution of nanocomposites when different amounts of perovskite QDs were incorporated into s-SIBS matrix. Similar to the previously discussed morphology evolution of pristine SIBS+QDs composite, the introduction of perovskite QDs disturbed the microphase separated morphology of s-SIBS, leading to the formation of perovskite-rich regions with irregular boundaries (Figure 40b) at micrometer scale which was also reflected in TEM characterization. When the s-SIBS+QDs composite was subjected to higher QDs loading, an increase in QDs-rich area dimension was expected. But due to the additional electrostatic interaction between s-SIBS matrix and perovskite QDs, the random distribution of QDs was hindered so relatively distinct region boundaries remained (Figure 40c).

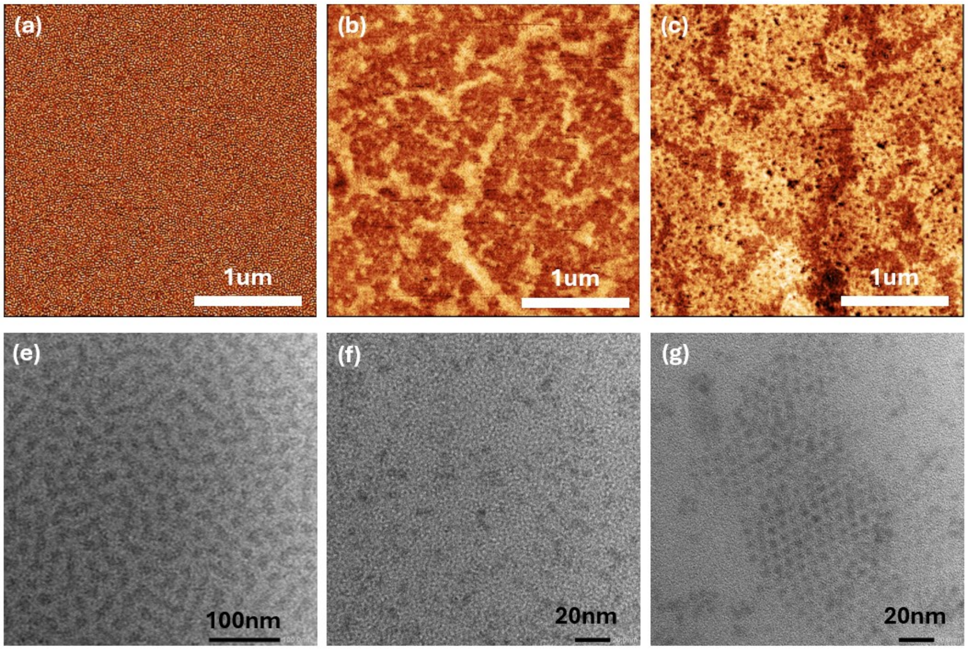

Figure 40: (a)-(c) are the 3x3um AFM scanning images for SIBS073T, 100-4 s-s7-8+QDs, and 100-6 s-s7-8+QDs. (e)-(f) are the corresponding TEM images for SIBS073T, 100-4 s-s7-8+QDs, and 100-6 s-s7-8+QDs

Effect of sulfonation degree: With equivalent perovskite QDs loading, when the sulfonation degree of the composite sample increased from 8% to 18%, the PL stability test of the nanocomposite showed an unexpected drop of initial PL intensity compared with control sample, accompanied by an unexpected increasing trend. Specifically, its corresponding PL intensity kept increasing when stored in ambient condition during the 12-day stability experiment and exceeded control sample's PL intensity value at day 7. The final PL intensity at day12 was 274.9% of the first day value, while the control sample showed a final retention of 58% initial intensity. Uddin et al.[228] previously reported an increasing trend in which the PL intensity of QDs was recorded for 10 days. According to their proposed mechanism, the lower initial PL intensity can be attributed to a similar ligand exchange process between sulfonated SIBS and QDs where the deprotonation of sulfonic acid group leads to the protonation of OA- capping ligand. As the result, the perovskite QD surface was temporarily unpassivated and its exciton radiative recombination was suppressed because of less ligand coverage. During the 12-day PL stability test, s-SIBS polymers containing the sulfonate ions were expected to bind onto the perovskite surface gradually through lewis acid-base interaction, so the s-SIBS/QDs thin film showed increasing PL intensity due to the passivation effect of sulfonate groups.

Such an increasing trend was also present for 100:6 molar ratio case. At 8% SD, the PL intensity versus time of s-s7-8%/QDs composite showed a slow decay pattern with a final retention of 75.6% as mentioned in previous discussion. On the other hand, the s-SIBS/QDs at 18% SD possessed an additional growth in PL intensity at the early stage. Specifically, its PL intensity value gradually shifted upwards and showed a 20% increase at day3(from 808.5 a.u. to 969.4 a.u.) then followed a decay pattern for the rest of the stability test. It was noted that even the PL decay slope for 18% SD composite was smaller than that of 8% composite. Such alleviated decay behavior and the two-stage PL intensity-time pattern originated from the increased QDs loading. An excessive fraction of QDs cannot be bonded with sulfonic acid groups so the nanocomposite did not exhibit a keep increasing PL behavior as of 100:4 case. The other fraction of interacted QDs compensated for some PL intensity loss and accounted for the slower decay pattern. The 20% growth of PL intensity due to s-SIBS passivation effect brought a higher final PL retention of 114.9%, indicating s-s7-18% a better candidate material for QDs encapsulation and passivation, evidencing the positive effect of increased sulfonation degree.

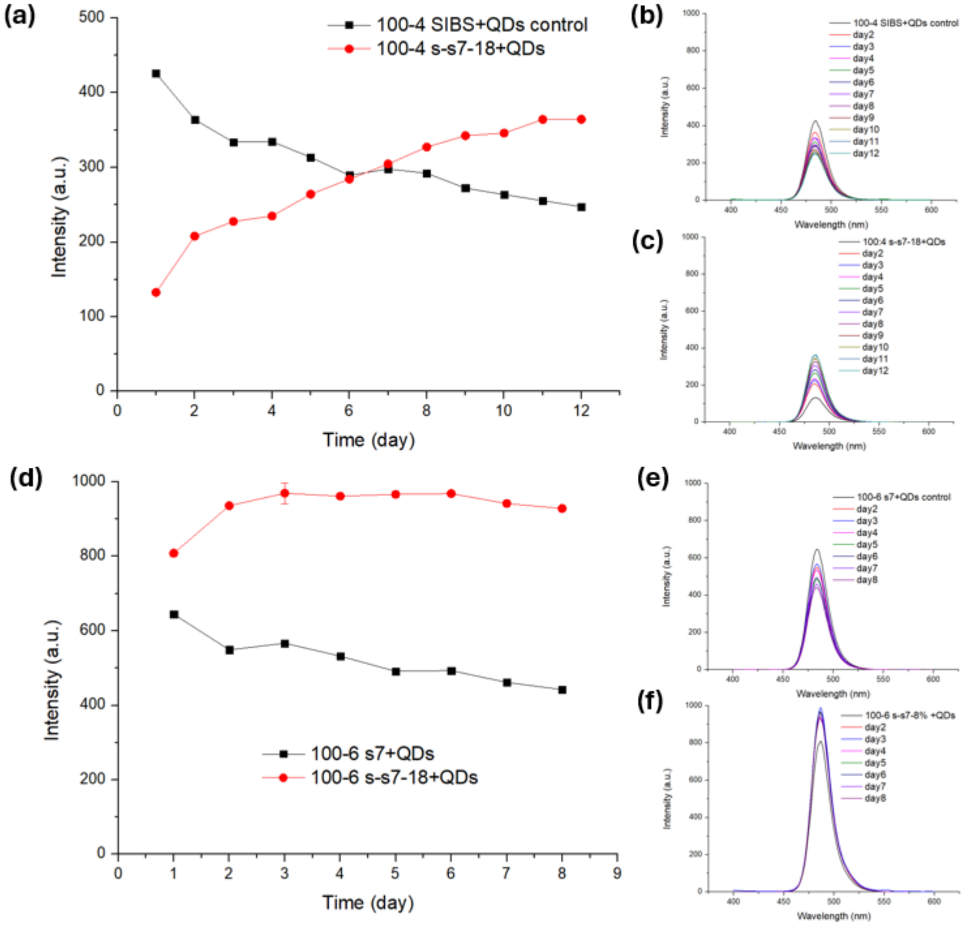

Figure 41: PL stability test showing the effect of sulfonation degree. (a) and (d) are the maximum PL intensity summary for 100-4 and 100-6 polymer/QDs composites. (b), (c) are PL test results of 100-4 polymer/QDs composites for 12days. (e), (f) are PL test results of 100-6 polymer/QDs composites for 8days

The morphological evolution of nanocomposites with different sulfonation degrees were exhibited in Figure 42. It was obvious that the sulfonation modification significantly altered the local distribution of perovskite QDs within the SIBS matrix. As shown in Figure 42a-c, the introduction of sulfonate groups led to the division of QD-rich regions, with higher degrees of sulfonation resulting in increasingly smaller and more dispersed QDs-rich domains. This trend was further evidenced by the corresponding TEM images (Figure 42d-f). The observed reduction in QDs aggregation was attributed to the increased number of sulfonate groups, which acted as anchoring sites throughout the polymer matrix, thereby promoting a more uniform distribution of QDs and effectively mitigating their tendency from clustering. Furthermore, this more uniform distribution of nanocrystal fillers was expected to influence the composite's mechanical properties (in "Tensile and flexibility test" section).

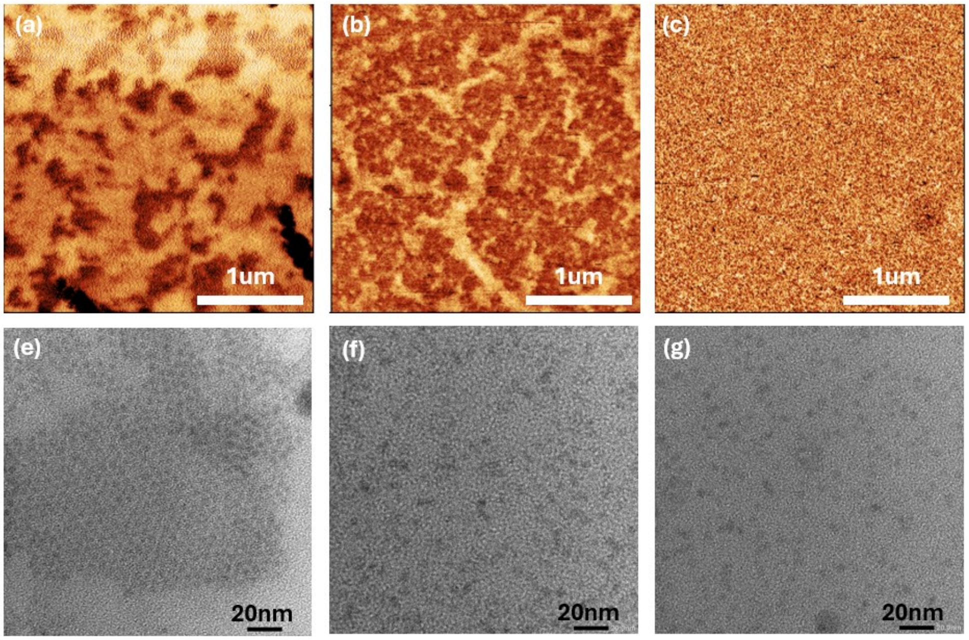

Figure 42: (a)-(c) are the 3x3um AFM scanning images for 100:4 pristine SIBS+QDs composite, 100:4 s-s7-8+QDs composite, and 100:4 s-s7-18+QDs composite. (e)-(f) are the corresponding TEM images for pristine SIBS+QDs, s-s7-8+QDs, and s-s7-18+QDs composites at 100:4 molar ratio, respectively.

Effect of block copolymer matrix composition: SIBS 062T exhibited a different PL stability behavior. Specifically, its composite with QDs also showed a significant drop of PL intensity compared with pristine SIBS062T/QDs. But the increasing trend was not as prominent as that of s-s7-18%, the s-s6-22%/QDs composite's final PL intensity at day 8 did not surpass the value of control sample (213.7a.u., 547.2a.u.), and the final retention was lower than that of s-s7-18% composite (120.8%, 247% at day8) as well. It can also be observed from its corresponding AFM images that large aggregation of QDs were not incorporated into the polymer matrix. All those experimental results evidenced that 100-6 s-s7-18+QDs composition is the better candidate based on its better encapsulation performance of QDs.

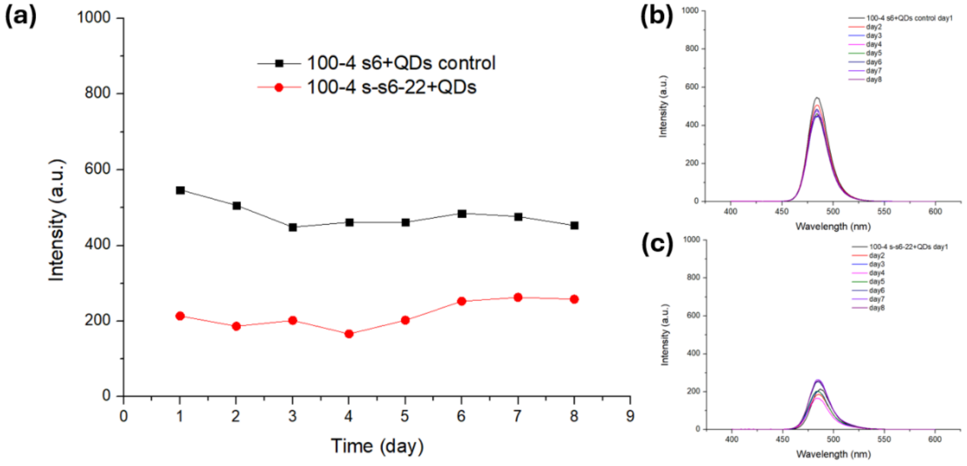

Figure 43: PL stability test to investigate the effect of SIBS composition. (a) is the maximum PL intensity summary for s-s6-10 and s-s6-22 polymer/QDs samples. (b), (c) are PL test results of 100-4 s-s6-22/QDs composites and its control sample for 8days

Time resolved photoluminescence (TRPL) study: The PL decay curves of pristine SIBS 073T, 8%, and 18% sulfonated SIBS 073T mixed with QDs at the same SIBS/QDs molar ratio were investigated and shown in Figure. Through biexponential fitting, shorter lifetime τ_1 and longer lifetime τ_2 were calculated and listed along with TRPL curves. Based on the $\tau_2$value, the level of perovskite QDs' radiative recombination can be evaluated. It can be concluded from the decay fitting curves that after SIBS matrix was sulfonated, longer lifetime τ_2 of the s-SIBS/QDs composite exhibited an increase from 8.4ns to 15.4ns at 8% sulfonation degree, and 14ns at 18% sulfonation degree, respectively. The differences of long-live lifetime were further evidenced by the local PL spectra shown in Figure. In Figure 44e, all three TRPL curves were summarized and s-s7-18%/QDs composite showed the most stable decay pattern. Although 18% SD composite did not possess the largest τ_2, but the contribution of radiative recombination was the largest (11%) compared to pristine SIBS (6%) and 8% SD composite (2%). Based on the experimental results of TRPL summary and previously discussed PL stability test, it can be concluded that for SIBS 073T, the increase of SD can suppress the non-radiative recombination of perovskite QDs and enhance the fluorescence stability of the s-SIBS/QDs nanocomposite.

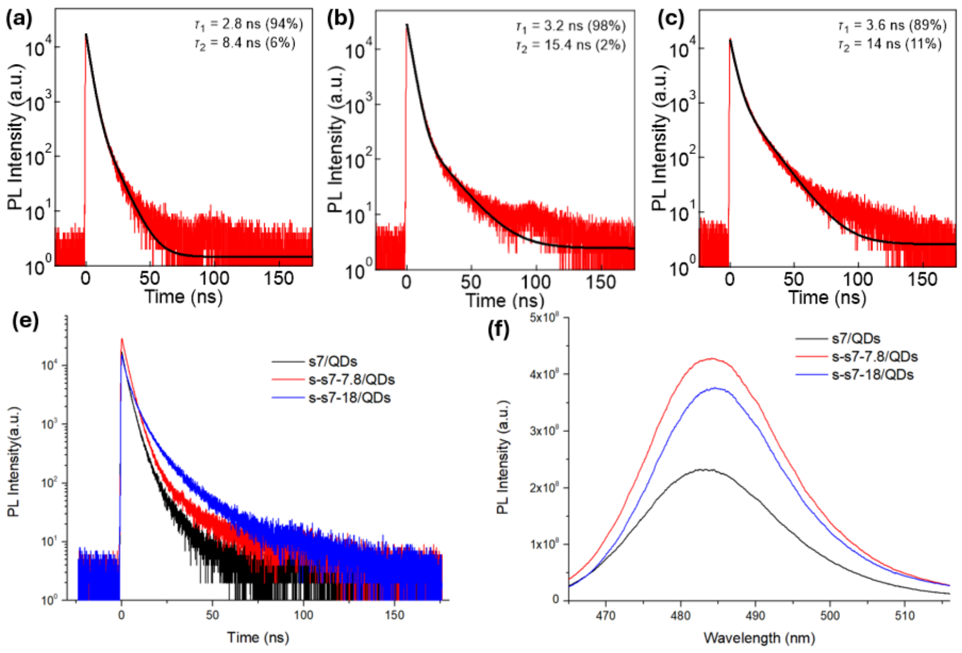

Figure 44: (a) TRPL data and corresponding fitting for 100:4 SIBS073T+QDs composite where τ_1=2.8ns, τ_2=8.4ns. (b) TRPL and fitting for 100:4 s-s7-8+QDs composite where τ_1=3.2ns, τ_2=15.4ns. (c) TRPL and fitting for 100:4 s-s7-18+QDs composite where τ_1=3.6ns, τ_2=14ns. (e) Summary of TRPL curves for pristine SIBS+QDs, s-s7-8+QDs, and s-s7-18+QDs composites at 100:4 ratio. (f) Radiative recombination property comparison for s7/QDs, s-s7-8/QDs, and s-s7-18/QDs composites.

Tensile and flexibility test: One of the advantages of incorporating QDs in SIBS BCP matrix is that the fabricated composite can be subjected to a wide range of mechanical deformation without breaking the QDs encapsulation. In figure, s-s7-8%/QDs film was cut into rectangular shape for flexibility demonstration including bending, twisting, and stretching. The cut sample showed strong fluorescence under UV irradiation and can be easily recovered to previous state without permanent damage. Tensile tests were also conducted to evaluate the mechanical performance of SIBS/QDs nanocomposite. The stress-strain curve showed that if the polymer matrix went through sulfonation reaction, the elasticity of the composite will be significantly enhanced elongation from 352% to 741%. And due to additional matrix-filler interaction, the s-SIBS/QDs composite also exhibited 7.5% larger modulus, and 146% higher tensile strength compared to pristine SIBS/QDs composite. The enhanced mechanical performance was attributed to the alleviation of QDs aggregation which caused a more uniform QDs distribution in the polymer matrix and the increased connection between BCP and QDs filler thanks to the presence of sulfonic acid groups that can interact with CsPbBr3 QDs. The flexibility and tensile tests demonstrated that the sulfonated SIBS can not only improve the photoluminescence properties of perovskite QDs through better encapsulation and passivation, but also lead to more robust and elastic

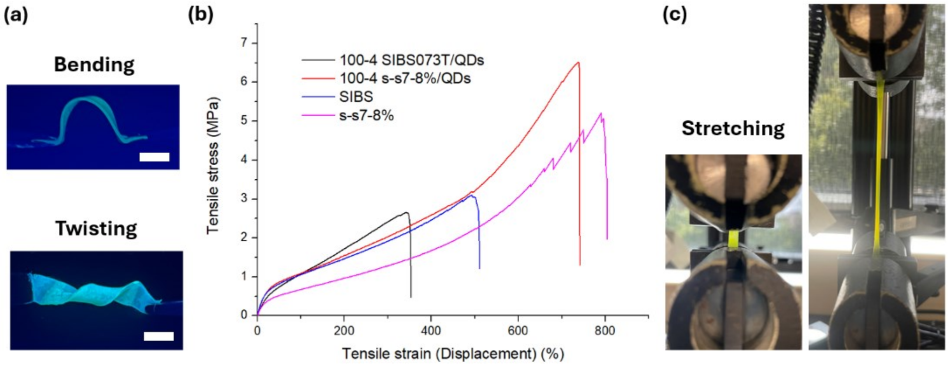

Figure 45: (a) Photos of UV illuminated s-s7-8%/QDs rectangular stripe being bended and twisted for flexibility demonstration. (b) Stress-strain curves of s-s7-8%/QDs and corresponding control sample of pristine SIBS. (c) Stretchability demonstration of s-s7-8%/QDs nanocomposite. Scale bar length is 5mm.

5.4 Conclusions

In this work, we demonstrated successful synthesis of partially sulfonated SIBS with variable sulfonation degree. s-SIBS was selected as the protective material for QDs nanocomposite fabrication due to expected Lewis's acid-base interaction between sulfonic acid groups anchored in PS phase and Pb ions on the perovskite surface.

We spin-coated a series of s-SIBS/QDs nanocomposite thin films to systematically investigate the effect of QDs loading, sulfonation degree, and BCP composition to obtain optimized processing parameters. PL stability test under ambient condition, morphological study, TRPL, and tensile test were conducted to evaluate the performance of fabricated s-SIBS/QDs nanocomposites. It was proposed that the ionic interactions brought by sulfonation functionalization had several beneficial effects on nanocomposite's PL and mechanical performances. Compared with pristine SIBS, s-SIBS exhibited better encapsulation property supported by its higher final PL retention value. The passivation effect of s-SIBS was confirmed by its higher PL intensity and longer exciton lifetime. By combining the mentioned two effects, s-SIBS/QDs exhibited more pronounced photoluminescence as well as improved stability against external factors such as oxygen and moisture. Especially for 100:6 s-s7-18%/QDs composite, it showed 114.8% PL retention after an 8-day long stability test. s-SIBS 073T also alleviated QDs aggregation and caused a more uniform QDs distribution across the matrix. Along with the effect of matrix-filler interaction, s-SIBS/QDs composite showed improved mechanical elastic and robust features including higher value of elongation, tensile strength, and Young's modulus.

In summary, we demonstrated the incorporation of molecularly engineered TPE block copolymer with QDs to fabricate deformable nanocomposite with enhanced optical and mechanical properties, which is of great potential for flexible optoelectronic and display applications.

CHAPTER VI

SUMMARY

6.1 Summary of major results

In this study, advanced functional elastomers leveraging the distinctive properties of polyisobutylene (PIB) were successfully synthesized, expanding their potential applications in rapid prototyping, tissue engineering, and soft optical materials.

Our initial investigation focused on synthesizing PIB-based thermoplastic polyurethanes using both low (50 kDa) and high (100 kDa) molecular weight variants. These materials were demonstrated for novel 3D printing capabilities via FDM method. The critical hardness requirement for high printing quality, in L-PIB-PU case, was met by introducing compatible hard polyurethane synthesized by random copolymerization of MDI and chain extender BDO which were presented in PIB-PU. This approach significantly reduced the necessary molecular weight of PIB-PU, thus providing an alternative formulation with simplified operation procedures. The hybrid's mechanical performance can be easily tailored by adjusting hPU content. Furthermore, the mechanical performance of 3D printed objects made from H-PIB-PU was enhanced by promoting interlayer adhesion through the incorporation of low molecular weight PIB-PU.

In our second study, we developed a zwitterionic PIB-based ligand for the effective encapsulation and environmental isolation of unprotected perovskite quantum dots (QDs).

This was followed by the fabrication of flexible nanocomposites composed of poly(styrene-isobutylene-styrene) (SIBS) and perovskite QDs, targeting applications in soft optical materials. The inherent compatibility between the PIB-based capping ligand on the perovskite QDs and the PIB phase within the SIBS matrix played a critical role in both preventing QDs aggregation and promoting their preferential distribution throughout the elastomeric matrix. The corresponding nanocomposite showed excellent elasticity and PL stability evidenced by 750% elongation and long-term water immersion test, respectively.

In our third study, we introduced an alternative strategy for the fabrication of soft optical materials exhibiting enhanced photoluminescence stability and selective QDs distribution. This approach involved the grafting of sulfonic acid groups onto the polystyrene phase to enable surface encapsulation and defect passivation of QDs via Lewis acid-based interactions. Partially sulfonated SIBS can be processed by non-polar solvent and also alleviate the QDs aggregation, indicating the effectiveness and simplicity of this proposed approach. Following formulation optimization, a flexible nanocomposite was successfully fabricated, demonstrating not only sustained PL stability but also an initial increase in PL intensity during the early stages of the stability assessment.

6.2 Future work

Future work stemming from the first study will focus on further evaluating the biocompatibility of 3D-printed PIB-PU materials through *in vitro* studies. Additionally, the potential application of these materials in wearable devices with complex geometries will be explored, leveraging the processability and tunable mechanical properties demonstrated in the current work.

For the second and third study, future research will aim to develop effective strategies to achieve long-range, ordered, phase-separated morphologies within the nanocomposites. This structural control is anticipated to enable precise patterning or alignment of quantum dots, further enhancing their optical performance and expanding their functionality in advanced soft material systems.

REFERENCES

(1) Jung, Y. S.; Chang, J. B.; Verploegen, E.; Berggren, K. K.; Ross, C. A. A Path to Ultranarrow Patterns Using Self-Assembled Lithography. *Nano Lett.* **2010**, *10* (3), 1000–1005. https://doi.org/10.1021/nl904141r.

(2) Leibler, L. Theory of Microphase Separation in Block Copolymers. *Macromolecules* **1980**, *13* (6), 1602–1617. https://doi.org/10.1021/ma60078a047.

(3) Bates, F. S.; Fredrickson, G. H. Block Copolymer Thermodynamics: Theory and Experiment. *Annu. Rev. Phys. Chem.* **1990**, *41* (1), 525–557. https://doi.org/10.1146/annurev.pc.41.100190.002521.

(4) Carrick, B. R.; Weigand, S.; Seitzinger, C. L.; Lodge, T. P. Concentration and Temperature Dependence of the Interaction Parameter and Correlation Length for Poly(Benzyl Methacrylate) in Ionic Liquids. *Macromolecules* **2022**, *55* (19), 8899–8908. https://doi.org/10.1021/acs.macromol.2c01365.

(5) Matsen, M. W.; Schick, M. Stable and Unstable Phases of a Diblock Copolymer Melt. *Phys. Rev. Lett.* **1994**, *72* (16), 2660–2663. https://doi.org/10.1103/PhysRevLett.72.2660.

(6) Vavasour, J. D.; Whitmore, M. D. Self-Consistent Mean Field Theory of the Microphases of Diblock Copolymers. *Macromolecules* **1992**, *25* (20), 5477–5486. https://doi.org/10.1021/ma00046a055.

(7) Vavasour, J. D.; Whitmore, M. D. Self-Consistent Field Theory of Block Copolymers with Conformational Asymmetry. *Macromolecules* **1993**, *26* (25), 7070–7075. https://doi.org/10.1021/ma00077a054.

(8) Khandpur, A. K.; Foerster, S.; Bates, F. S.; Hamley, I. W.; Ryan, A. J.; Bras, W.; Almdal, K.; Mortensen, K. Polyisoprene-Polystyrene Diblock Copolymer Phase Diagram near the Order-Disorder Transition. *Macromolecules* **1995**, *28* (26), 8796–8806. https://doi.org/10.1021/ma00130a012.

(9) Bates, F. S.; Fredrickson, G. H. Block Copolymers—Designer Soft Materials. *Physics Today* **1999**, *52* (2), 32–38. https://doi.org/10.1063/1.882522.

(10) Qi, S.; Wang, Z.-G. On the Nature of the Perforated Layer Phase in Undiluted Diblock Copolymers. *Macromolecules* **1997**, *30* (15), 4491–4497. https://doi.org/10.1021/ma970206t.

(11) Gillard, T. M.; Lee, S.; Bates, F. S. Dodecagonal Quasicrystalline Order in a Diblock Copolymer Melt. *Proc. Natl. Acad. Sci. U.S.A.* **2016**, *113* (19), 5167–5172. https://doi.org/10.1073/pnas.1601692113.

(12) Lee, S.; Bluemle, M. J.; Bates, F. S. Discovery of a Frank-Kasper σ Phase in Sphere-Forming Block Copolymer Melts. *Science* **2010**, *330* (6002), 349–353. https://doi.org/10.1126/science.1195552.

(13) Xiao, L.-L.; Zhou, X.; Yue, K.; Guo, Z.-H. Synthesis and Self-Assembly of Conjugated Block Copolymers. *Polymers* **2020**, *13* (1), 110. https://doi.org/10.3390/polym13010110.

(14) Li, S.; Jiang, Y.; Chen, J. Z. Y. Morphologies and Phase Diagrams of ABC Star Triblock Copolymers Confined in a Spherical Cavity. *Soft Matter* **2013**, *9* (19), 4843. https://doi.org/10.1039/c3sm27770d.

(15) Mai, S.-M.; Mingvanish, W.; Turner, S. C.; Chaibundit, C.; Fairclough, J. P. A.; Heatley, F.; Matsen, M. W.; Ryan, A. J.; Booth, C. Microphase-Separation Behavior of Triblock Copolymer Melts. Comparison with Diblock Copolymer Melts. *Macromolecules* **2000**, *33* (14), 5124–5130. https://doi.org/10.1021/ma000154z.

(16) Nakazawa, H.; Ohta, T. Microphase Separation of ABC-Type Triblock Copolymers. *Macromolecules* **1993**, *26* (20), 5503–5511. https://doi.org/10.1021/ma00072a031.

(17) Zheng, W.; Wang, Z.-G. Morphology of ABC Triblock Copolymers. *Macromolecules* **1995**, *28* (21), 7215–7223. https://doi.org/10.1021/ma00125a026.

(18) Auschra, C.; Stadler, R. New Ordered Morphologies in ABC Triblock Copolymers. *Macromolecules* **1993**, *26* (9), 2171–2174. https://doi.org/10.1021/ma00061a005.

(19) Stadler, R.; Auschra, C.; Beckmann, J.; Krappe, U.; Voight-Martin, I.; Leibler, L. Morphology and Thermodynamics of Symmetric Poly(A-Block-B-Block-C) Triblock Copolymers. *Macromolecules* **1995**, *28* (9), 3080–3097. https://doi.org/10.1021/ma00113a010.

(20) Tang, P.; Qiu, F.; Zhang, H.; Yang, Y. Morphology and Phase Diagram of Complex Block Copolymers: ABC Linear Triblock Copolymers. *Phys. Rev. E* **2004**, *69* (3), 031803. https://doi.org/10.1103/PhysRevE.69.031803.

(21) Zhang, X.; Berry, B. C.; Yager, K. G.; Kim, S.; Jones, R. L.; Satija, S.; Pickel, D. L.; Douglas, J. F.; Karim, A. Surface Morphology Diagram for Cylinder-Forming Block Copolymer Thin Films. *ACS Nano* **2008**, *2* (11), 2331–2341. https://doi.org/10.1021/nn800643x.

(22) Mishra, V.; Fredrickson, G. H.; Kramer, E. J. Effect of Film Thickness and Domain Spacing on Defect Densities in Directed Self-Assembly of Cylindrical Morphology Block Copolymers. *ACS Nano* **2012**, *6* (3), 2629–2641. https://doi.org/10.1021/nn205120j.

(23) Limary, R.; Green, P. F. Hierarchical Pattern Formation in Thin Film Diblock Copolymers above the Order−Disorder Transition Temperature. *Macromolecules* **1999**, *32* (24), 8167–8172. https://doi.org/10.1021/ma9906074.

(24) Jiang, Y.; Yan, C.; Shi, D.; Liu, Z.; Yang, M. Enhanced Rheological Properties of PLLA with a Purpose-Designed PDLA-b-PEG-b-PDLA Triblock Copolymer and the Application in the Film Blowing Process to Acquire Biodegradable PLLA Films. *ACS Omega* **2019**, *4* (8), 13295–13302. https://doi.org/10.1021/acsomega.9b01470.

(25) Hashimoto, T.; Bodycomb, J.; Funaki, Y.; Kimishima, K. The Effect of Temperature

Gradient on the Microdomain Orientation of Diblock Copolymers Undergoing an Order−Disorder Transition. *Macromolecules* **1999**, *32* (3), 952–954. https://doi.org/10.1021/ma981249s.

(26) Bodycomb, J.; Funaki, Y.; Kimishima, K.; Hashimoto, T. Single-Grain Lamellar Microdomain from a Diblock Copolymer. *Macromolecules* **1999**, *32* (6), 2075–2077. https://doi.org/10.1021/ma981538g.

(27) Mita, K.; Tanaka, H.; Saijo, K.; Takenaka, M.; Hashimoto, T. Ordering of Cylindrical Domains of Block Copolymers under Moving Temperature Gradient: Separation of ∇ T - Induced Ordering from Surface-Induced Ordering. *Macromolecules* **2008**, *41* (18), 6787–6792. https://doi.org/10.1021/ma800361d.

(28) Gotrik, K. W.; Hannon, A. F.; Son, J. G.; Keller, B.; Alexander-Katz, A.; Ross, C. A. Morphology Control in Block Copolymer Films Using Mixed Solvent Vapors. *ACS Nano* **2012**, *6* (9), 8052–8059. https://doi.org/10.1021/nn302641z.

(29) Kim, S. H.; Misner, M. J.; Xu, T.; Kimura, M.; Russell, T. P. Highly Oriented and Ordered Arrays from Block Copolymers via Solvent Evaporation. *Advanced Materials* **2004**, *16* (3), 226–231. https://doi.org/10.1002/adma.200304906.

(30) Peng, J.; Kim, D. H.; Knoll, W.; Xuan, Y.; Li, B.; Han, Y. Morphologies in Solvent-Annealed Thin Films of Symmetric Diblock Copolymer. *The Journal of Chemical Physics* **2006**, *125* (6), 064702. https://doi.org/10.1063/1.2219446.

(31) Hur, S.-M.; Khaira, G. S.; Ramírez-Hernández, A.; Müller, M.; Nealey, P. F.; De Pablo, J. J. Simulation of Defect Reduction in Block Copolymer Thin Films by Solvent Annealing. *ACS Macro Lett.* **2015**, *4* (1), 11–15. https://doi.org/10.1021/mz500705q.

(32) Chavis, M. A.; Smilgies, D.; Wiesner, U. B.; Ober, C. K. Widely Tunable Morphologies in Block Copolymer Thin Films Through Solvent Vapor Annealing Using Mixtures of Selective Solvents. *Adv Funct Materials* **2015**, *25* (20), 3057–3065. https://doi.org/10.1002/adfm.201404053.

(33) Kang, H.; Kim, K.; Sohn, B.-H. Shearing with Solvent Vapor Annealing on Block Copolymer Thin Films for Templates with Macroscopically Aligned Nanodomains. *Nanotechnology* **2020**, *31* (45), 455302. https://doi.org/10.1088/1361-6528/aba8bf.

(34) Singh, M.; Agrawal, A.; Wu, W.; Masud, A.; Armijo, E.; Gonzalez, D.; Zhou, S.; Terlier, T.; Zhu, C.; Strzalka, J.; Matyjaszewski, K.; Bockstaller, M.; Douglas, J. F.; Karim, A. Soft-Shear-Aligned Vertically Oriented Lamellar Block Copolymers for Template-Free Sub-10 Nm Patterning and Hybrid Nanostructures. *ACS Appl. Mater. Interfaces* **2022**, *14* (10), 12824–12835. https://doi.org/10.1021/acsami.1c23865.

(35) Blanazs, A.; Armes, S. P.; Ryan, A. J. Self-Assembled Block Copolymer Aggregates: From Micelles to Vesicles and Their Biological Applications. *Macromol. Rapid Commun.* **2009**, *30* (4–5), 267–277. https://doi.org/10.1002/marc.200800713.

(36) Li, S.; Byrne, B.; Welsh, J.; Palmer, A. F. Self-Assembled Poly(Butadiene)- *b* - poly(Ethylene Oxide) Polymersomes as Paclitaxel Carriers. *Biotechnology Progress* **2007**, *23* (1), 278–285. https://doi.org/10.1021/bp060208.

(37) Lomas, H.; Canton, I.; MacNeil, S.; Du, J.; Armes, S. P.; Ryan, A. J.; Lewis, A. L.; Battaglia, G. Biomimetic pH Sensitive Polymersomes for Efficient DNA Encapsulation and Delivery. *Advanced Materials* **2007**, *19* (23), 4238–4243. https://doi.org/10.1002/adma.200700941.

(38) Ranquin, A.; Versées, W.; Meier, W.; Steyaert, J.; Van Gelder, P. Therapeutic Nanoreactors: Combining Chemistry and Biology in a Novel Triblock Copolymer Drug Delivery System. *Nano Lett.* **2005**, *5* (11), 2220–2224. https://doi.org/10.1021/nl051523d.

(39) Christian, N. A.; Milone, M. C.; Ranka, S. S.; Li, G.; Frail, P. R.; Davis, K. P.; Bates, F. S.; Therien, M. J.; Ghoroghchian, P. P.; June, C. H.; Hammer, D. A. Tat-Functionalized Near-Infrared Emissive Polymersomes for Dendritic Cell Labeling. *Bioconjugate Chem.* **2007**, *18* (1), 31–40. https://doi.org/10.1021/bc0601267.

(40) Bakshi, M. S. Colloidal Micelles of Block Copolymers as Nanoreactors, Templates for Gold Nanoparticles, and Vehicles for Biomedical Applications. *Advances in Colloid and Interface Science* **2014**, *213*, 1–20. https://doi.org/10.1016/j.cis.2014.08.001.

(41) Jiang, X.; Luo, S.; Armes, S. P.; Shi, W.; Liu, S. UV Irradiation-Induced Shell Cross-Linked Micelles with pH-Responsive Cores Using ABC Triblock Copolymers. *Macromolecules* **2006**, *39* (18), 5987–5994. https://doi.org/10.1021/ma061386m.

(42) Du, J.; Armes, S. P. pH-Responsive Vesicles Based on a Hydrolytically Self-Cross-Linkable Copolymer. *J. Am. Chem. Soc.* **2005**, *127* (37), 12800–12801. https://doi.org/10.1021/ja054755n.

(43) Wang, W.; Lu, W.; Goodwin, A.; Wang, H.; Yin, P.; Kang, N.-G.; Hong, K.; Mays, J. W. Recent Advances in Thermoplastic Elastomers from Living Polymerizations: Macromolecular Architectures and Supramolecular Chemistry. *Progress in Polymer Science* **2019**, *95*, 1–31. https://doi.org/10.1016/j.progpolymsci.2019.04.002.

(44) Hadjichristidis, N.; Pitsikalis, M.; Pispas, S.; Iatrou, H. Polymers with Complex Architecture by Living Anionic Polymerization. *Chem. Rev.* **2001**, *101* (12), 3747–3792. https://doi.org/10.1021/cr9901337.

(45) Maji, P.; Naskar, K. Styrenic Block Copolymer-based Thermoplastic Elastomers in Smart Applications: Advances in Synthesis, Microstructure, and Structure–Property Relationships—A Review. *J of Applied Polymer Sci* **2022**, *139* (39), e52942. https://doi.org/10.1002/app.52942.

(46) Gopalan, A. M.; Naskar, K. Ultra-high Molecular Weight Styrenic Block Copolymer/TPU Blends for Automotive Applications: Influence of Various Compatibilizers. *Polymers for Advanced Techs* **2019**, *30* (3), 608–619. https://doi.org/10.1002/pat.4497.

(47) St. Clair, D. J. Rubber-Styrene Block Copolymers in Adhesives. *Rubber Chemistry and Technology* **1982**, *55* (1), 208–218. https://doi.org/10.5254/1.3535868.

(48) Ouyang, C.; Wang, S.; Zhang, Y.; Zhang, Y. Improving the Aging Resistance of Styrene–Butadiene–Styrene Tri-Block Copolymer Modified Asphalt by Addition of Antioxidants. *Polymer Degradation and Stability* **2006**, *91* (4), 795–804. https://doi.org/10.1016/j.polymdegradstab.2005.06.009.

(49) Pinchuk, L.; Wilson, G. J.; Barry, J. J.; Schoephoerster, R. T.; Parel, J.-M.; Kennedy, J. P. Medical Applications of Poly(Styrene-Block-Isobutylene-Block-Styrene) ("SIBS"). *Biomaterials* **2008**, *29* (4), 448–460. https://doi.org/10.1016/j.biomaterials.2007.09.041.

(50) Costa, P.; Gonçalves, S.; Mora, H.; Carabineiro, S. A. C.; Viana, J. C.; Lanceros-Mendez, S. Highly Sensitive Piezoresistive Graphene-Based Stretchable Composites for Sensing Applications. *ACS Appl. Mater. Interfaces* **2019**, *11* (49), 46286–46295. https://doi.org/10.1021/acsami.9b19294.

(51) Lin, B.; Xu, F.; Su, Y.; Zhu, Z.; Ren, Y.; Ding, J.; Yuan, N. Facile Preparation of Anion-Exchange Membrane Based on Polystyrene- *b* -Polybutadiene- *b* -Polystyrene for the Application of Alkaline Fuel Cells. *Ind. Eng. Chem. Res.* **2019**, *58* (49), 22299–22305. https://doi.org/10.1021/acs.iecr.9b05314.

(52) Tan, J.; Mei Ding, Y.; Tao He, X.; Liu, Y.; An, Y.; Min Yang, W. Abrasion Resistance of Thermoplastic Polyurethane Materials Blended with Ethylene–Propylene–Diene Monomer Rubber. *J of Applied Polymer Sci* **2008**, *110* (3), 1851–1857. https://doi.org/10.1002/app.28756.

(53) Cozzens, D.; Ojha, U.; Kulkarni, P.; Faust, R.; Desai, S. Long Term *in Vitro* Biostability of Segmented Polyisobutylene-based Thermoplastic Polyurethanes. *J Biomedical Materials Res* **2010**, *95A* (3), 774–782. https://doi.org/10.1002/jbm.a.32897.

(54) Chen, Z.; Li, Z.; Li, J.; Liu, C.; Lao, C.; Fu, Y.; Liu, C.; Li, Y.; Wang, P.; He, Y. 3D Printing of Ceramics: A Review. *Journal of the European Ceramic Society* **2019**, *39* (4), 661–687. https://doi.org/10.1016/j.jeurceramsoc.2018.11.013.

(55) Tan, X. P.; Tan, Y. J.; Chow, C. S. L.; Tor, S. B.; Yeong, W. Y. Metallic Powder-Bed Based 3D Printing of Cellular Scaffolds for Orthopaedic Implants: A State-of-the-Art Review on Manufacturing, Topological Design, Mechanical Properties and Biocompatibility. *Materials Science and Engineering: C* **2017**, *76*, 1328–1343. https://doi.org/10.1016/j.msec.2017.02.094.

(56) Wang, X.; Jiang, M.; Zhou, Z.; Gou, J.; Hui, D. 3D Printing of Polymer Matrix Composites: A Review and Prospective. *Composites Part B: Engineering* **2017**, *110*, 442–458. https://doi.org/10.1016/j.compositesb.2016.11.034.

(57) Li, F.; Macdonald, N. P.; Guijt, R. M.; Breadmore, M. C. Increasing the Functionalities of 3D Printed Microchemical Devices by Single Material, Multimaterial, and Print-Pause-Print 3D Printing. *Lab Chip* **2019**, *19* (1), 35–49. https://doi.org/10.1039/C8LC00826D.

(58) Zhou, L.-Y.; Fu, J.; He, Y. A Review of 3D Printing Technologies for Soft Polymer Materials. *Advanced Functional Materials* **2020**, *30* (28), 2000187. https://doi.org/10.1002/adfm.202000187.

(59) Cheng, C.-Y.; Xie, H.; Xu, Z.; Li, L.; Jiang, M.-N.; Tang, L.; Yang, K.-K.; Wang, Y.-Z. 4D Printing of Shape Memory Aliphatic Copolyester via UV-Assisted FDM Strategy for Medical Protective Devices. *Chemical Engineering Journal* **2020**, *396*, 125242. https://doi.org/10.1016/j.cej.2020.125242.

(60) Regehly, M.; Garmshausen, Y.; Reuter, M.; König, N. F.; Israel, E.; Kelly, D. P.; Chou, C.-Y.; Koch, K.; Asfari, B.; Hecht, S. Xolography for Linear Volumetric 3D Printing.

Nature **2020**, *588* (7839), 620–624. https://doi.org/10.1038/s41586-020-3029-7.

(61) Zhang, W.; Eperon, G. E.; Snaith, H. J. Metal Halide Perovskites for Energy Applications. *Nature Energy* **2016**, *1* (6), 1–8.

(62) Ning, Z.; Gong, X.; Comin, R.; Walters, G.; Fan, F.; Voznyy, O.; Yassitepe, E.; Buin, A.; Hoogland, S.; Sargent, E. H. Quantum-Dot-in-Perovskite Solids. *Nature* **2015**, *523* (7560), 324–328. https://doi.org/10.1038/nature14563.

(63) Ning, C.-Z.; Dou, L.; Yang, P. Bandgap Engineering in Semiconductor Alloy Nanomaterials with Widely Tunable Compositions. *Nat Rev Mater* **2017**, *2* (12), 17070. https://doi.org/10.1038/natrevmats.2017.70.

(64) Gao, L.; Quan, L. N.; García De Arquer, F. P.; Zhao, Y.; Munir, R.; Proppe, A.; Quintero-Bermudez, R.; Zou, C.; Yang, Z.; Saidaminov, M. I.; Voznyy, O.; Kinge, S.; Lu, Z.; Kelley, S. O.; Amassian, A.; Tang, J.; Sargent, E. H. Efficient Near-Infrared Light-Emitting Diodes Based on Quantum Dots in Layered Perovskite. *Nat. Photonics* **2020**, *14* (4), 227–233. https://doi.org/10.1038/s41566-019-0577-1.

(65) Jiang, Y.; Sun, C.; Xu, J.; Li, S.; Cui, M.; Fu, X.; Liu, Y.; Liu, Y.; Wan, H.; Wei, K.; Zhou, T.; Zhang, W.; Yang, Y.; Yang, J.; Qin, C.; Gao, S.; Pan, J.; Liu, Y.; Hoogland, S.; Sargent, E. H.; Chen, J.; Yuan, M. Synthesis-on-Substrate of Quantum Dot Solids. *Nature* **2022**, *612* (7941), 679–684. https://doi.org/10.1038/s41586-022-05486-3.

(66) Kang, J.; Wang, L.-W. High Defect Tolerance in Lead Halide Perovskite CsPbBr3. *J. Phys. Chem. Lett.* **2017**, *8* (2), 489–493. https://doi.org/10.1021/acs.jpclett.6b02800.

(67) Brandt, R. E.; Poindexter, J. R.; Gorai, P.; Kurchin, R. C.; Hoye, R. L. Z.; Nienhaus, L.; Wilson, M. W. B.; Polizzotti, J. A.; Sereika, R.; Žaltauskas, R.; Lee, L. C.; MacManus-Driscoll, J. L.; Bawendi, M.; Stevanović, V.; Buonassisi, T. Searching for "Defect-Tolerant" Photovoltaic Materials: Combined Theoretical and Experimental Screening. *Chem. Mater.* **2017**, *29* (11), 4667–4674. https://doi.org/10.1021/acs.chemmater.6b05496.

(68) García de Arquer, F. P.; Talapin, D. V.; Klimov, V. I.; Arakawa, Y.; Bayer, M.; Sargent, E. H. Semiconductor Quantum Dots: Technological Progress and Future Challenges. *Science* **2021**, *373* (6555), eaaz8541. https://doi.org/10.1126/science.aaz8541.

(69) Zhao, Q.; Wang, S.; Kim, Y.-H.; Mondal, S.; Miao, Q.; Li, S.; Liu, D.; Wang, M.; Zhai, Y.; Gao, J.; Hazarika, A.; Li, G.-R. Advantageous Properties of Halide Perovskite Quantum Dots towards Energy-Efficient Sustainable Applications. *Green Energy & Environment* **2024**, *9* (6), 949–965. https://doi.org/10.1016/j.gee.2023.04.001.

(70) Zhou, X.; Zhang, J.; Tong, X.; Sun, Y.; Zhang, H.; Min, Y.; Qian, Y. Near-Unity Quantum Yield and Superior Stable Indium-Doped CsPbBrI3− Perovskite Quantum Dots for Pure Red Light-Emitting Diodes. *Advanced Optical Materials* **2022**, *10* (2), 2101517. https://doi.org/10.1002/adom.202101517.

(71) Zhu, C.; Jin, J.; Wang, Z.; Xu, Z.; Folgueras, M. C.; Jiang, Y.; Uzundal, C. B.; Le, H. K. D.; Wang, F.; Zheng, X. (Rayne); Yang, P. Supramolecular Assembly of Blue and Green Halide Perovskites with Near-Unity Photoluminescence. *Science* **2024**, *383* (6678), 86–93. https://doi.org/10.1126/science.adi4196.

(72) Ashjari, T.; Arabpour Roghabadi, F.; Ahmadi, V. Facile Synthesis of Durable Perovskite Quantum Dots Film with near Unity Photoluminescence Quantum Yield for Efficient Perovskite Light Emitting Diode. *Applied Surface Science* **2020**, *510*, 145513. https://doi.org/10.1016/j.apsusc.2020.145513.

(73) Konstantakou, M.; Perganti, D.; Falaras, P.; Stergiopoulos, T. Anti-Solvent Crystallization Strategies for Highly Efficient Perovskite Solar Cells. *Crystals* **2017**, *7* (10), 291. https://doi.org/10.3390/cryst7100291.

(74) Lee, J.-W.; Kim, H.-S.; Park, N.-G. Lewis Acid–Base Adduct Approach for High Efficiency Perovskite Solar Cells. *Acc. Chem. Res.* **2016**, *49* (2), 311–319. https://doi.org/10.1021/acs.accounts.5b00440.

(75) Protesescu, L.; Yakunin, S.; Bodnarchuk, M. I.; Krieg, F.; Caputo, R.; Hendon, C. H.; Yang, R. X.; Walsh, A.; Kovalenko, M. V. Nanocrystals of Cesium Lead Halide Perovskites (CsPbX3, X = Cl, Br, and I): Novel Optoelectronic Materials Showing Bright Emission with Wide Color Gamut. *Nano Lett.* **2015**, *15* (6), 3692–3696. https://doi.org/10.1021/nl5048779.

(76) Zhang, F.; Zhong, H.; Chen, C.; Wu, X.; Hu, X.; Huang, H.; Han, J.; Zou, B.; Dong, Y. Brightly Luminescent and Color-Tunable Colloidal CH3NH3PbX3 (X = Br, I, Cl) Quantum Dots: Potential Alternatives for Display Technology. *ACS Nano* **2015**, *9* (4), 4533–4542. https://doi.org/10.1021/acsnano.5b01154.

(77) Pradhan, N. Alkylammonium Halides for Facet Reconstruction and Shape Modulation in Lead Halide Perovskite Nanocrystals. *Acc. Chem. Res.* **2021**, *54* (5), 1200–1208. https://doi.org/10.1021/acs.accounts.0c00708.

(78) Steele, J. A.; Lai, M.; Zhang, Y.; Lin, Z.; Hofkens, J.; Roeffaers, M. B. J.; Yang, P. Phase Transitions and Anion Exchange in All-Inorganic Halide Perovskites. *Acc. Mater. Res.* **2020**, *1* (1), 3–15. https://doi.org/10.1021/accountsmr.0c00009.

(79) Wang, D.; Wright, M.; Elumalai, N. K.; Uddin, A. Stability of Perovskite Solar Cells. *Solar Energy Materials and Solar Cells* **2016**, *147*, 255–275. https://doi.org/10.1016/j.solmat.2015.12.025.

(80) Zhang, H.; Ren, X.; Chen, X.; Mao, J.; Cheng, J.; Zhao, Y.; Liu, Y.; Milic, J.; Yin, W.-J.; Grätzel, M.; Choy, W. C. H. Improving the Stability and Performance of Perovskite Solar Cells *via* off-the-Shelf Post-Device Ligand Treatment. *Energy Environ. Sci.* **2018**, *11* (8), 2253–2262. https://doi.org/10.1039/C8EE00580J.

(81) Mao, J.; Sha, W. E. I.; Zhang, H.; Ren, X.; Zhuang, J.; Roy, V. A. L.; Wong, K. S.; Choy, W. C. H. Novel Direct Nanopatterning Approach to Fabricate Periodically Nanostructured Perovskite for Optoelectronic Applications. *Adv. Funct. Mater.* **2017**, *27* (10), 1606525. https://doi.org/10.1002/adfm.201606525.

(82) Jeong, B.; Han, H.; Park, C. Micro- and Nanopatterning of Halide Perovskites Where Crystal Engineering for Emerging Photoelectronics Meets Integrated Device Array Technology. *Advanced Materials* **2020**, *32* (30), 2000597. https://doi.org/10.1002/adma.202000597.

(83) Gholipour, B.; Adamo, G.; Cortecchia, D.; Krishnamoorthy, H. N. S.; Birowosuto,

Muhammad. D.; Zheludev, N. I.; Soci, C. Organometallic Perovskite Metasurfaces. *Adv. Mater.* **2017**, *29* (9), 1604268. https://doi.org/10.1002/adma.201604268.

(84) Wang, Z.; Yang, T.; Zhang, Y.; Ou, Q.; Lin, H.; Zhang, Q.; Chen, H.; Hoh, H. Y.; Jia, B.; Bao, Q. Flat Lenses Based on 2D Perovskite Nanosheets. *Adv. Mater.* **2020**, *32* (30), 2001388. https://doi.org/10.1002/adma.202001388.

(85) Raja, S. N.; Bekenstein, Y.; Koc, M. A.; Fischer, S.; Zhang, D.; Lin, L.; Ritchie, R. O.; Yang, P.; Alivisatos, A. P. Encapsulation of Perovskite Nanocrystals into Macroscale Polymer Matrices: Enhanced Stability and Polarization. *ACS Appl. Mater. Interfaces* **2016**, *8* (51), 35523–35533. https://doi.org/10.1021/acsami.6b09443.

(86) Benas, J.-S.; Liang, F.-C.; Chen, W.-C.; Hung, C.-W.; Chen, J.-Y.; Zhou, Y.; Han, S.-T.; Borsali, R.; Kuo, C.-C. Lewis Adduct Approach for Self-Assembled Block Copolymer Perovskite Quantum Dots Composite toward Optoelectronic Application: Challenges and Prospects. *Chemical Engineering Journal* **2022**, *431*, 133701. https://doi.org/10.1016/j.cej.2021.133701.

(87) Kim, S.; Lee, H.; Han, H.; Park, Y.; Lee, K.; Kim, Y.; Zan, G.; Lee, J.; Kim, D.; Kim, J.; Jeong, B.; Kim, J.-H.; Park, C. Phase-Purified Ruddlesden–Popper Perovskites Vertically Oriented in Block Copolymer Nanostructures for Environmentally Stable Light Conversion and Charge Trapping. *Advanced Optical Materials* **2023**, *11* (16), 2300053. https://doi.org/10.1002/adom.202300053.

(88) Mathur, A.; Khamgaonkar, S.; Maheshwari, V. Copolymer Mediated Engineering of Halide Perovskites and Associated Devices: Current State and Future. *Advanced Physics Research* **2023**, *2* (5), 2200088. https://doi.org/10.1002/apxr.202200088.

(89) Li, Y.; Lv, Y.; Guo, Z.; Dong, L.; Zheng, J.; Chai, C.; Chen, N.; Lu, Y.; Chen, C. One-Step Preparation of Long-Term Stable and Flexible $CsPbBr_3$ Perovskite Quantum Dots/Ethylene Vinyl Acetate Copolymer Composite Films for White Light-Emitting Diodes. *ACS Appl. Mater. Interfaces* **2018**, *10* (18), 15888–15894. https://doi.org/10.1021/acsami.8b02857.

(90) Hung, C.-C.; Lin, Y.-C.; Chuang, T.-H.; Chiang, Y.-C.; Chiu, Y.-C.; Mumtaz, M.; Borsali, R.; Chen, W.-C. Harnessing of Spatially Confined Perovskite Nanocrystals Using Polysaccharide-Based Block Copolymer Systems. *ACS Appl. Mater. Interfaces* **2022**, *14* (26), 30279–30289. https://doi.org/10.1021/acsami.2c09296.

(91) Yang, W.; Fei, L.; Gao, F.; Liu, W.; Xu, H.; Yang, L.; Liu, Y. Thermal Polymerization Synthesis of CsPbBr3 Perovskite-Quantum-Dots@copolymer Composite: Towards Long-Term Stability and Optical Phosphor Application. *Chemical Engineering Journal* **2020**, *387*, 124180. https://doi.org/10.1016/j.cej.2020.124180.

(92) Han, H.; Jeong, B.; Park, T. H.; Cha, W.; Cho, S. M.; Kim, Y.; Kim, H. H.; Kim, D.; Ryu, D. Y.; Choi, W. K.; Park, C. Highly Photoluminescent and Environmentally Stable Perovskite Nanocrystals Templated in Thin Self-Assembled Block Copolymer Films. *Advanced Functional Materials* **2019**, *29* (26), 1808193. https://doi.org/10.1002/adfm.201808193.

(93) Lee, K.; Han, H.; Kim, Y.; Park, J.; Jang, S.; Lee, H.; Lee, S. W.; Kim, H.; Kim, Y.;

Kim, T.; Kim, D.; Wang, G.; Park, C. Retina-Inspired Structurally Tunable Synaptic Perovskite Nanocones. *Adv Funct Materials* **2021**, *31* (52), 2105596. https://doi.org/10.1002/adfm.202105596.

(94) Park, Y.; Han, H.; Lee, H.; Kim, S.; Park, T. H.; Jang, J.; Kim, G.; Park, Y.; Lee, J.; Kim, D.; Kim, J.; Jung, Y. S.; Jeong, B.; Park, C. Sub-30 Nm 2D Perovskites Patterns via Block Copolymer Guided Self-Assembly for Color Conversion Optical Polarizer. *Small* **2023**, *19* (47), 2300568. https://doi.org/10.1002/smll.202300568.

(95) Chao, Y.; Chen, J.; Yang, D.; Tseng, Y.; Hsu, C.; Chen, J. High-Performance Non-Volatile Flash Photomemory via Highly Oriented Quasi-2D Perovskite. *Adv Funct Materials* **2022**, *32* (19), 2112521. https://doi.org/10.1002/adfm.202112521.

(96) Han, H.; Oh, J. W.; Lee, H.; Lee, S.; Mun, S.; Jeon, S.; Kim, D.; Jang, J.; Jiang, W.; Kim, T.; Jeong, B.; Kim, J.; Ryu, D. Y.; Park, C. Rewritable Photoluminescence and Structural Color Display for Dual-Responsive Optical Encryption. *Advanced Materials* **2024**, *36* (14), 2310130. https://doi.org/10.1002/adma.202310130.

(97) Han, H.; Oh, J. W.; Park, J.; Lee, H.; Park, C.; Lee, S. W.; Lee, K.; Jeon, S.; Kim, S.; Park, Y.; Jeong, B.; Ryu, D. Y.; Park, C. Hierarchically Ordered Perovskites with High Photo-Electronic and Environmental Stability via Nanoimprinting Guided Block Copolymer Self-Assembly. *Adv Materials Inter* **2022**, *9* (16), 2200082. https://doi.org/10.1002/admi.202200082.

(98) Tsai, C.-H.; Shen, N.; Mi, C.; Bu, J.; Dong, Y.; Xu, W. Designed Polymer Ligands for Perovskite Quantum Dots and Their Block Copolymer Nanocomposites. *Advanced Optical Materials n/a* (n/a), 2302731. https://doi.org/10.1002/adom.202302731.

(99) Chen, W.-C.; Lin, Y.-C.; Hung, C.-C.; Hsu, L.-C.; Wu, Y.-S.; Liu, C.-L.; Kuo, C.-C.; Chen, W.-C. Stretchable Photosynaptic Transistor with an Ultralow Energy Consumption Conferred Using Conjugated Block Copolymers/Perovskite Quantum Dots Nanocomposites. *Materials Today* **2023**, *70*, 57–70. https://doi.org/10.1016/j.mattod.2023.10.010.

(100) Zhou, N.; Bekenstein, Y.; Eisler, C. N.; Zhang, D.; Schwartzberg, A. M.; Yang, P.; Alivisatos, A. P.; Lewis, J. A. Perovskite Nanowire–Block Copolymer Composites with Digitally Programmable Polarization Anisotropy. *Science Advances* **2019**, *5* (5), eaav8141. https://doi.org/10.1126/sciadv.aav8141.

(101) Hou, S.; Guo, Y.; Tang, Y.; Quan, Q. Synthesis and Stabilization of Colloidal Perovskite Nanocrystals by Multidentate Polymer Micelles. *ACS Appl. Mater. Interfaces* **2017**, *9* (22), 18417–18422. https://doi.org/10.1021/acsami.7b03445.

(102) Hintermayr, V. A.; Lampe, C.; Löw, M.; Roemer, J.; Vanderlinden, W.; Gramlich, M.; Böhm, A. X.; Sattler, C.; Nickel, B.; Lohmüller, T.; Urban, A. S. Polymer Nanoreactors Shield Perovskite Nanocrystals from Degradation. *Nano Lett.* **2019**, *19* (8), 4928–4933. https://doi.org/10.1021/acs.nanolett.9b00982.

(103) Greiner, M. G.; Singldinger, A.; Henke, N. A.; Lampe, C.; Leo, U.; Gramlich, M.; Urban, A. S. Energy Transfer in Stability-Optimized Perovskite Nanocrystals. *Nano Lett.* **2022**, *22* (16), 6709–6715. https://doi.org/10.1021/acs.nanolett.2c02108.

(104) Xue, Q.; Lampe, C.; Naujoks, T.; Frank, K.; Gramlich, M.; Schoger, M.; Vanderlinden, W.; Reisbeck, P.; Nickel, B.; Brütting, W.; Urban, A. S. Doubly Stabilized Perovskite Nanocrystal Luminescence Downconverters. *Advanced Optical Materials* **2022**, *10* (14), 2102791. https://doi.org/10.1002/adom.202102791.

(105) Kim, M.; Kim, J.; Bang, J.; Jang, Y. J.; Park, J.; Kim, D. H. Simultaneously Achieving Room-Temperature Circularly Polarized Luminescence and High Stability in Chiral Perovskite Nanocrystals *via* Block Copolymer Micellar Nanoreactors. *J. Mater. Chem. A* **2023**, *11* (24), 12876–12884. https://doi.org/10.1039/D2TA06996B.

(106) He, Y.; Yoon, Y. J.; Harn, Y. W.; Biesold-McGee, G. V.; Liang, S.; Lin, C. H.; Tsukruk, V. V.; Thadhani, N.; Kang, Z.; Lin, Z. Unconventional Route to Dual-Shelled Organolead Halide Perovskite Nanocrystals with Controlled Dimensions, Surface Chemistry, and Stabilities. *Sci. Adv.* **2019**, *5* (11), eaax4424. https://doi.org/10.1126/sciadv.aax4424.

(107) Pan, A.; Yan, L.; Ma, X.; Wu, Y.; Zhang, Y.; Zhou, G.; He, L. Strongly Luminescent and Highly Stable Core-Shell Suprastructures from in-Situ Growth of CsPbBr3 Perovskite Nanocrystals in Multidentate Copolymer Micelles. *Journal of Alloys and Compounds* **2020**, *844*, 156102. https://doi.org/10.1016/j.jallcom.2020.156102.

(108) Nah, Y.; Jang, D.; Kim, D. H. Block Copolymer Micelles Enable Facile Synthesis of Organic–Inorganic Perovskite Nanostructures with Tailored Architecture. *Chem. Commun.* **2021**, *57* (15), 1879–1882. https://doi.org/10.1039/D0CC06935C.

(109) Imran, M.; Mai, B. T.; Goldoni, L.; Cirignano, M.; Jalali, H. B.; Di Stasio, F.; Pellegrino, T.; Manna, L. Switchable Anion Exchange in Polymer-Encapsulated $APbX_3$ Nanocrystals Delivers Stable All-Perovskite White Emitters. *ACS Energy Lett.* **2021**, *6* (8), 2844–2853. https://doi.org/10.1021/acsenergylett.1c01232.

(110) Yoon, Y. J.; Chang, Y.; Zhang, S.; Zhang, M.; Pan, S.; He, Y.; Lin, C. H.; Yu, S.; Chen, Y.; Wang, Z.; Ding, Y.; Jung, J.; Thadhani, N.; Tsukruk, V. V.; Kang, Z.; Lin, Z. Enabling Tailorable Optical Properties and Markedly Enhanced Stability of Perovskite Quantum Dots by Permanently Ligating with Polymer Hairs. *Advanced Materials* **2019**, *31* (32), 1901602. https://doi.org/10.1002/adma.201901602.

(111) Pan, S.; Chen, Y.; Wang, Z.; Harn, Y.-W.; Yu, J.; Wang, A.; Smith, M. J.; Li, Z.; Tsukruk, V. V.; Peng, J.; Lin, Z. Strongly-Ligated Perovskite Quantum Dots with Precisely Controlled Dimensions and Architectures for White Light-Emitting Diodes. *Nano Energy* **2020**, *77*, 105043. https://doi.org/10.1016/j.nanoen.2020.105043.

(112) Liang, S.; He, S.; Zhang, M.; Yan, Y.; Jin, T.; Lian, T.; Lin, Z. Tailoring Charge Separation at Meticulously Engineered Conjugated Polymer/Perovskite Quantum Dot Interface for Photocatalyzing Atom Transfer Radical Polymerization. *J. Am. Chem. Soc.* **2022**, *144* (28), 12901–12914. https://doi.org/10.1021/jacs.2c04680.

(113) Liu, Y.; Wang, Z.; Liang, S.; Li, Z.; Zhang, M.; Li, H.; Lin, Z. Polar Organic Solvent-Tolerant Perovskite Nanocrystals Permanently Ligated with Polymer Hairs via Star-like Molecular Bottlebrush Trilobe Nanoreactors. *Nano Lett.* **2019**, *19* (12), 9019–9028. https://doi.org/10.1021/acs.nanolett.9b04047.

(114) Shen, J.; Meng, N.; Chen, J.; Zhu, Y.; Yang, X.; Jia, Y.; Li, C. Polyacrylic Acid- *b* -Polystyrene-Passivated $CsPbBr_3$ Perovskite Quantum Dots with High Photoluminescence Quantum Yield for Light-Emitting Diodes. *Chem. Commun.* **2022**, *58* (26), 4235–4238. https://doi.org/10.1039/D2CC00051B.

(115) Yang, S.; Zhang, F.; Tai, J.; Li, Y.; Yang, Y.; Wang, H.; Zhang, J.; Xie, Z.; Xu, B.; Zhong, H.; Liu, K.; Yang, B. A Detour Strategy for Colloidally Stable Block-Copolymer Grafted $MAPbBr_3$ Quantum Dots in Water with Long Photoluminescence Lifetime. *Nanoscale* **2018**, *10* (13), 5820–5826. https://doi.org/10.1039/C8NR01493K.

(116) Cueto, C.; Donoghue, C.; Bolduc, K.; Emrick, T. Zwitterionic Block Copolymers for the Synthesis and Stabilization of Perovskite Nanocrystals. *Chemistry A European J* **2022**, *28* (30), e202200409. https://doi.org/10.1002/chem.202200409.

(117) Liu, H.; Siron, M.; Gao, M.; Lu, D.; Bekenstein, Y.; Zhang, D.; Dou, L.; Alivisatos, A. P.; Yang, P. Lead Halide Perovskite Nanowires Stabilized by Block Copolymers for Langmuir-Blodgett Assembly. *Nano Res.* **2020**, *13* (5), 1453–1458. https://doi.org/10.1007/s12274-020-2717-9.

(118) He, Y.; Liang, Y.; Liang, S.; Harn, Y.-W.; Li, Z.; Zhang, M.; Shen, D.; Li, Z.; Yan, Y.; Pang, X.; Lin, Z. Dual-Protected Metal Halide Perovskite Nanosheets with an Enhanced Set of Stabilities. *Angewandte Chemie International Edition* **2021**, *60* (13), 7259–7266. https://doi.org/10.1002/anie.202014983.

(119) Avugadda, S. K.; Castelli, A.; Dhanabalan, B.; Fernandez, T.; Silvestri, N.; Collantes, C.; Baranov, D.; Imran, M.; Manna, L.; Pellegrino, T.; Arciniegas, M. P. Highly Emitting Perovskite Nanocrystals with 2-Year Stability in Water through an Automated Polymer Encapsulation for Bioimaging. *ACS Nano* **2022**, *16* (9), 13657–13666. https://doi.org/10.1021/acsnano.2c01556.

(120) Shi, B.; Hu, W.; Li, S.; Xia, Z.; Lü, C. Perovskite Photoinitiated RAFT-Mediated Polymerization-Induced Self-Assembly for Organic–Inorganic Hybrid Nanomaterials. *Inorg. Chem. Front.* **2024**, *11* (8), 2471–2478. https://doi.org/10.1039/D4QI00233D.

(121) Luo, F.; Li, S.; Cui, L.; Zu, Y.; Chen, Y.; Huang, D.; Weng, Z.; Lin, Z. Biocompatible Perovskite Quantum Dots with Superior Water Resistance Enable Long-Term Monitoring of the H_2 S Level *in Vivo*. *Nanoscale* **2021**, *13* (34), 14297–14303. https://doi.org/10.1039/D1NR02248B.

(122) Lee, S. M.; Jung, H.; Park, W. I.; Lee, Y.; Koo, E.; Bang, J. Preparation of Water-Soluble CsPbBr3 Perovskite Quantum Dot Nanocomposites via Encapsulation into Amphiphilic Copolymers. *ChemistrySelect* **2018**, *3* (40), 11320–11325. https://doi.org/10.1002/slct.201802237.

(123) Sun, J.; Li, B.; Hu, L.; Guo, J.; Ling, X.; Zhang, X.; Zhang, C.; Wu, X.; Huang, H.; Han, C.; Liu, X.; Li, Y.; Huang, S.; Wu, T.; Yuan, J.; Ma, W. Hybrid Block Copolymer/Perovskite Heterointerfaces for Efficient Solar Cells. *Advanced Materials* **2023**, *35* (1), 2206047. https://doi.org/10.1002/adma.202206047.

(124) Zong, Y.; Zhou, Y.; Zhang, Y.; Li, Z.; Zhang, L.; Ju, M.-G.; Chen, M.; Pang, S.; Zeng, X. C.; Padture, N. P. Continuous Grain-Boundary Functionalization for High-

Efficiency Perovskite Solar Cells with Exceptional Stability. *Chem* **2018**, *4* (6), 1404–1415. https://doi.org/10.1016/j.chempr.2018.03.005.

(125) Wang, C.; Song, Z.; Zhao, D.; Awni, R. A.; Li, C.; Shrestha, N.; Chen, C.; Yin, X.; Li, D.; Ellingson, R. J.; Zhao, X.; Li, X.; Yan, Y. Improving Performance and Stability of Planar Perovskite Solar Cells through Grain Boundary Passivation with Block Copolymers. *Solar RRL* **2019**, *3* (9), 1900078. https://doi.org/10.1002/solr.201900078.

(126) Li, C.; Chen, Y.; Liu, F.; Liu, K.; Li, X.; Zhang, X.; Zhang, H.; Shi, Z.; Chen, W.; Ahmed, I.; Arshid, N.; Wang, J.; Sun, Z.; Xiong, S.; Zhan, Y. Highly Luminescent and Patternable Block Copolymer Templated 3D Perovskite Films. *Advanced Materials Technologies* **2021**, *6* (7), 2001209. https://doi.org/10.1002/admt.202001209.

(127) Han, T.; Zhao, Y.; Yoon, J.; Woo, J. Y.; Cho, E.; Kim, W. D.; Lee, C.; Lee, J.; Choi, J.; Han, J.; Nam, J.; Wang, K.; Priya, S.; Balaban, M.; Jeon, I.; Yang, Y. Spontaneous Hybrid Cross-Linked Network Induced by Multifunctional Copolymer toward Mechanically Resilient Perovskite Solar Cells. *Adv Funct Materials* **2022**, *32* (40), 2207142. https://doi.org/10.1002/adfm.202207142.

(128) Cheon, J.; Park, J.-M.; Son, J.; Lee, M.; Lee, S.; Park, C.; Kim, H. J.; Kim, J.-H.; Park, J. S.; Jeong, B. Stretchable Metal Halide Perovskite Color Conversion Layers with Block Copolymer Dispersant. *Advanced Optical Materials* **2024**, *12* (20), 2400407. https://doi.org/10.1002/adom.202400407.

(129) Jiang, D.-H.; Kobayashi, S.; Jao, C.-C.; Mato, Y.; Isono, T.; Fang, Y.-H.; Lin, C.-C.; Satoh, T.; Tung, S.-H.; Kuo, C.-C. Light Down-Converter Based on Luminescent Nanofibers from the Blending of Conjugated Rod-Coil Block Copolymers and Perovskite through Electrospinning. *Polymers* **2020**, *12* (1), 84. https://doi.org/10.3390/polym12010084.

(130) Wang, Q.; Chen, B.; Liu, Y.; Deng, Y.; Bai, Y.; Dong, Q.; Huang, J. Scaling Behavior of Moisture-Induced Grain Degradation in Polycrystalline Hybrid Perovskite Thin Films. *Energy & Environmental Science* **2017**, *10* (2), 516–522. https://doi.org/10.1039/C6EE02941H.

(131) Wang, K.; Yang, D.; Wu, C.; Sanghadasa, M.; Priya, S. Recent Progress in Fundamental Understanding of Halide Perovskite Semiconductors. *Progress in Materials Science* **2019**, *106*, 100580. https://doi.org/10.1016/j.pmatsci.2019.100580.

(132) Xiang, W.; Shengzhong (Frank) Liu; Tress, W. A Review on the Stability of Inorganic Metal Halide Perovskites: Challenges and Opportunities for Stable Solar Cells. *Energy & Environmental Science* **2021**, *14* (4), 2090–2113. https://doi.org/10.1039/D1EE00157D.

(133) Castro-Méndez, A.-F.; Hidalgo, J.; Correa-Baena, J.-P. The Role of Grain Boundaries in Perovskite Solar Cells. *Advanced Energy Materials* **2019**, *9* (38), 1901489. https://doi.org/10.1002/aenm.201901489.

(134) Scharber, M. C.; Sariciftci, N. S. Efficiency of Bulk-Heterojunction Organic Solar Cells. *Progress in Polymer Science* **2013**, *38* (12), 1929–1940. https://doi.org/10.1016/j.progpolymsci.2013.05.001.

(135) Tan, K. W.; Moore, D. T.; Saliba, M.; Sai, H.; Estroff, L. A.; Hanrath, T.; Snaith, H. J.; Wiesner, U. Thermally Induced Structural Evolution and Performance of Mesoporous Block Copolymer-Directed Alumina Perovskite Solar Cells. *ACS Nano* **2014**, *8* (5), 4730–4739. https://doi.org/10.1021/nn500526t.

(136) Tan, Z.-K.; Moghaddam, R. S.; Lai, M. L.; Docampo, P.; Higler, R.; Deschler, F.; Price, M.; Sadhanala, A.; Pazos, L. M.; Credgington, D. Bright Light-Emitting Diodes Based on Organometal Halide Perovskite. *Nature nanotechnology* **2014**, *9* (9), 687–692.

(137) Li, M.; Yang, Y.; Kuang, Z.; Hao, C.; Wang, S.; Lu, F.; Liu, Z.; Liu, J.; Zeng, L.; Cai, Y.; Mao, Y.; Guo, J.; Tian, H.; Xing, G.; Cao, Y.; Ma, C.; Wang, N.; Peng, Q.; Zhu, L.; Huang, W.; Wang, J. Acceleration of Radiative Recombination for Efficient Perovskite LEDs. *Nature* **2024**, *630* (8017), 631–635. https://doi.org/10.1038/s41586-024-07460-7.

(138) Veldhuis, S. A.; Boix, P. P.; Yantara, N.; Li, M.; Sum, T. C.; Mathews, N.; Mhaisalkar, S. G. Perovskite Materials for Light-Emitting Diodes and Lasers. *Advanced Materials* **2016**, *28* (32), 6804–6834. https://doi.org/10.1002/adma.201600669.

(139) Li, Y.; Zhang, X.; Huang, H.; Kershaw, S. V.; Rogach, A. L. Advances in Metal Halide Perovskite Nanocrystals: Synthetic Strategies, Growth Mechanisms, and Optoelectronic Applications. *Materials Today* **2020**, *32*, 204–221. https://doi.org/10.1016/j.mattod.2019.06.007.

(140) Yang, Y.; Lee, J. T.; Liyanage, T.; Sardar, R. Flexible Polymer-Assisted Mesoscale Self-Assembly of Colloidal $CsPbBr_3$ Perovskite Nanocrystals into Higher Order Superstructures with Strong Inter-Nanocrystal Electronic Coupling. *J. Am. Chem. Soc.* **2019**, *141* (4), 1526–1536. https://doi.org/10.1021/jacs.8b10083.

(141) Zhang, M.; Lu, Q.; Wang, C.; Dai, H.; He, J.; Mohamed, Z.; Chen, X.; Ge, B. High-Performance and Stability Bifacial Flexible Self-Powered Perovskite Photodetector by Surface Plasmon Resonance and Hydrophobic Treatments. *Organic Electronics* **2021**, *99*, 106330. https://doi.org/10.1016/j.orgel.2021.106330.

(142) An, J.; Chen, M.; Liu, G.; Hu, Y.; Chen, R.; Lyu, Y.; Sharma, S.; Liu, Y. Water-Stable Perovskite-on-Polymer Fluorescent Microspheres for Simultaneous Monitoring of pH, Urea, and Urease. *Anal Bioanal Chem* **2021**, *413* (6), 1739–1747. https://doi.org/10.1007/s00216-020-03144-z.

(143) Cinquino, M.; Prontera, C. T.; Giuri, A.; Pugliese, M.; Giannuzzi, R.; Maggiore, A.; Altamura, D.; Mariano, F.; Gigli, G.; Esposito Corcione, C.; Giannini, C.; Rizzo, A.; De Marco, L.; Maiorano, V. Thermochromic Printable and Multicolor Polymeric Composite Based on Hybrid Organic–Inorganic Perovskite. *Advanced Materials* **2024**, *36* (2), 2307564. https://doi.org/10.1002/adma.202307564.

(144) Li, J.; Cao, H.-L.; Jiao, W.-B.; Wang, Q.; Wei, M.; Cantone, I.; Lü, J.; Abate, A. Biological Impact of Lead from Halide Perovskites Reveals the Risk of Introducing a Safe Threshold. *Nat Commun* **2020**, *11* (1), 310. https://doi.org/10.1038/s41467-019-13910-y.

(145) Shen, N.; Liu, S.; Kasbe, P.; Khabaz, F.; Kennedy, J. P.; Xu, W. Macromolecular Engineering and Additive Manufacturing of Poly(Styrene- *b* -Isobutylene- *b* -Styrene). *ACS Appl. Polym. Mater.* **2021**, *3* (9), 4554–4562. https://doi.org/10.1021/acsapm.1c00616.

(146) Shen, N.; Bu, J.; Prévôt, M. E.; Hegmann, T.; Kennedy, J. P.; Xu, W. Macromolecular Engineering and Additive Manufacturing of Polyisobutylene-Based Thermoplastic Elastomers. II. The Poly(Styrene- *b* -isobutylene- *b* -styrene)/Poly(Phenylene Oxide) System. *Macromol. Rapid Commun.* **2023**, *44* (1), 2200109. https://doi.org/10.1002/marc.202200109.

(147) Golling, F. E.; Pires, R.; Hecking, A.; Weikard, J.; Richter, F.; Danielmeier, K.; Dijkstra, D. Polyurethanes for Coatings and Adhesives – Chemistry and Applications. *Polymer International* **2019**, *68* (5), 848–855. https://doi.org/10.1002/pi.5665.

(148) Lamba, N. K. *Polyurethanes in Biomedical Applications*; Routledge: New York, 2017. https://doi.org/10.1201/9780203742785.

(149) Mattia, J.; Painter, P. A Comparison of Hydrogen Bonding and Order in a Polyurethane and Poly(Urethane−urea) and Their Blends with Poly(Ethylene Glycol). *Macromolecules* **2007**, *40* (5), 1546–1554. https://doi.org/10.1021/ma0626362.

(150) Chattopadhyay, D. K.; Webster, D. C. Thermal Stability and Flame Retardancy of Polyurethanes. *Progress in Polymer Science* **2009**, *34* (10), 1068–1133. https://doi.org/10.1016/j.progpolymsci.2009.06.002.

(151) Zdrahala, R. J.; Gerkin, R. M.; Hager, S. L.; Critchfield, F. E. Polyether-based Thermoplastic Polyurethanes. I. Effect of the Hard-segment Content. *J of Applied Polymer Sci* **1979**, *24* (9), 2041–2050. https://doi.org/10.1002/app.1979.070240912.

(152) Zdrahala, R. J.; Hager, S. L.; Gerkin, R. M.; Critchfield, F. E. Polyether Based Thermoplastic Polyurethanes Effect of the Soft Segment Molecular Weight. *Journal of Elastomers & Plastics* **1980**, *12* (4), 225–244. https://doi.org/10.1177/009524438001200404.

(153) Kay, M. J.; McCabe, R. W.; Morton, L. H. G. Chemical and Physical Changes Occurring in Polyester Polyurethane during Biodegradation. *International Biodeterioration & Biodegradation* **1993**, *31* (3), 209–225. https://doi.org/10.1016/0964-8305(93)90006-N.

(154) Umare, S. S.; Chandure, A. S. Synthesis, Characterization and Biodegradation Studies of Poly(Ester Urethane)s. *Chemical Engineering Journal* **2008**, *142* (1), 65–77. https://doi.org/10.1016/j.cej.2007.11.017.

(155) Szelest-Lewandowska, A.; Masiulanis, B.; Szymonowicz, M.; Pielka, S.; Paluch, D. Modified Polycarbonate Urethane: Synthesis, Properties and Biological Investigation *in Vitro*. *J Biomedical Materials Res* **2007**, *82A* (2), 509–520. https://doi.org/10.1002/jbm.a.31357.

(156) Khan, I.; Smith, N.; Jones, E.; Finch, D. S.; Cameron, R. E. Analysis and Evaluation of a Biomedical Polycarbonate Urethane Tested in an in Vitro Study and an Ovine Arthroplasty Model. Part I: Materials Selection and Evaluation. *Biomaterials* **2005**, *26* (6), 621–631. https://doi.org/10.1016/j.biomaterials.2004.02.065.

(157) Santerre, J. P.; Woodhouse, K.; Laroche, G.; Labow, R. S. Understanding the Biodegradation of Polyurethanes: From Classical Implants to Tissue Engineering Materials. *Biomaterials* **2005**, *26* (35), 7457–7470.

https://doi.org/10.1016/j.biomaterials.2005.05.079.

(158) Christenson, E. M.; Dadsetan, M.; Wiggins, M.; Anderson, J. M.; Hiltner, A. Poly(Carbonate Urethane) and Poly(Ether Urethane) Biodegradation: In Vivo Studies. *Journal of Biomedical Materials Research Part A* **2004**, *69A* (3), 407–416. https://doi.org/10.1002/jbm.a.30002.

(159) Christenson, E. M.; Anderson, J. M.; Hiltner, A. Oxidative Mechanisms of Poly(Carbonate Urethane) and Poly(Ether Urethane) Biodegradation: In Vivo and in Vitro Correlations. *Journal of Biomedical Materials Research Part A* **2004**, *70A* (2), 245–255. https://doi.org/10.1002/jbm.a.30067.

(160) Brown, D. W.; Lowry, R. E.; Smith, L. E. Kinetics of Hydrolytic Aging of Polyester Urethane Elastomers. *Macromolecules* **1980**, *13* (2), 248–252.

(161) Wu, Y.; Sellitti, C.; Anderson, J. M.; Hiltner, A.; Lodoen, G. A.; Payet, C. R. An FTIR–ATR Investigation of in Vivo Poly(Ether Urethane) Degradation. *Journal of Applied Polymer Science* **1992**, *46* (2), 201–211. https://doi.org/10.1002/app.1992.070460202.

(162) Zur, G.; Linder-Ganz, E.; Elsner, J. J.; Shani, J.; Brenner, O.; Agar, G.; Hershman, E. B.; Arnoczky, S. P.; Guilak, F.; Shterling, A. Chondroprotective Effects of a Polycarbonate-Urethane Meniscal Implant: Histopathological Results in a Sheep Model. *Knee Surg Sports Traumatol Arthrosc* **2011**, *19* (2), 255–263. https://doi.org/10.1007/s00167-010-1210-5.

(163) Solouk, A.; Cousins, B. G.; Mirzadeh, H.; Seifalian, A. M. Application of Plasma Surface Modification Techniques to Improve Hemocompatibility of Vascular Grafts: A Review. *Biotech and App Biochem* **2011**, *58* (5), 311–327. https://doi.org/10.1002/bab.50.

(164) Pinchuk, L. Crack Prevention of Implanted Prostheses. US4851009A, July 25, 1989. https://patents.google.com/patent/US4851009/en (accessed 2023-08-31).

(165) Simmons, A.; Hyvarinen, J.; Odell, R. A.; Martin, D. J.; Gunatillake, P. A.; Noble, K. R.; Poole-Warren, L. A. Long-Term in Vivo Biostability of Poly(Dimethylsiloxane)/Poly(Hexamethylene Oxide) Mixed Macrodiol-Based Polyurethane Elastomers. *Biomaterials* **2004**, *25* (20), 4887–4900. https://doi.org/10.1016/j.biomaterials.2004.01.004.

(166) Kang, J.; Erdodi, G.; Brendel, C. M.; Ely, D.; Kennedy, J. P. Polyisobutylene-Based Polyurethanes. V. Oxidative-Hydrolytic Stability and Biocompatibility. *Journal of Polymer Science Part A: Polymer Chemistry* **2010**, *48* (10), 2194–2203. https://doi.org/10.1002/pola.23989.

(167) Puskas, J. E.; Kaszas, G. Polyisobutylene-Based Thermoplastic Elastomers: A Review. *Rubber Chemistry and Technology* **1996**, *69* (3), 462–475. https://doi.org/10.5254/1.3538381.

(168) Jia, J.; Lin, P.; Liu, Q. Morphology and Properties of High Molecular Weight Polyisobutylene and Thermoplastic Polyurethane Elastomer. *Journal of Applied Polymer Science* **2022**, *139* (2), 51466. https://doi.org/10.1002/app.51466.

(169) Kennedy, J. P. From Thermoplastic Elastomers to Designed Biomaterials. *Journal*

of Polymer Science Part A: Polymer Chemistry **2005**, *43* (14), 2951–2963. https://doi.org/10.1002/pola.20844.

(170) Ranade, S. V.; Miller, K. M.; Richard, R. E.; Chan, A. K.; Allen, M. J.; Helmus, M. N. Physical Characterization of Controlled Release of Paclitaxel from the TAXUS$^{\text{TM}}$ Express2$^{\text{TM}}$ Drug-Eluting Stent. *Journal of Biomedical Materials Research Part A* **2004**, *71A* (4), 625–634. https://doi.org/10.1002/jbm.a.30188.

(171) Kekec, N. C.; Akolpoglu, M. B.; Bozuyuk, U.; Kizilel, S.; Nugay, N.; Nugay, T.; Kennedy, J. P. Calcification Resistance of Polyisobutylene and Polyisobutylene-Based Materials. *Polymers for Advanced Technologies* **2019**, *30* (7), 1836–1846. https://doi.org/10.1002/pat.4616.

(172) Deodhar, T.; Nugay, N.; Nugay, T.; Patel, R.; Moggridge, G.; Kennedy, J. P. Synthesis of High-Molecular-Weight and Strength Polyisobutylene-Based Polyurethane and Its Use for the Development of a Synthetic Heart Valve. *Macromolecular Rapid Communications* **2023**, *44* (1), 2200147. https://doi.org/10.1002/marc.202200147.

(173) Valino, A. D.; Dizon, J. R. C.; Espera, A. H.; Chen, Q.; Messman, J.; Advincula, R. C. Advances in 3D Printing of Thermoplastic Polymer Composites and Nanocomposites. *Progress in Polymer Science* **2019**, *98*, 101162. https://doi.org/10.1016/j.progpolymsci.2019.101162.

(174) Meththananda, I. M.; Parker, S.; Patel, M. P.; Braden, M. The Relationship between Shore Hardness of Elastomeric Dental Materials and Young's Modulus. *Dental Materials* **2009**, *25* (8), 956–959. https://doi.org/10.1016/j.dental.2009.02.001.

(175) Lee, J. H.; Gwon, S.; Shin, M. Effect of Filler Particle Characteristics on Yield Stress and Viscosity of Fresh Sulfur Composites. *Journal of Materials Research and Technology* **2021**, *12*, 2138–2152. https://doi.org/10.1016/j.jmrt.2021.03.116.

(176) Kulkarni, P.; Ojha, U.; Wei, X.; Gurung, N.; Seethamraju, K.; Faust, R. Thermal and Mechanical Properties of Polyisobutylene-based Thermoplastic Polyurethanes. *J of Applied Polymer Sci* **2013**, *130* (2), 891–897. https://doi.org/10.1002/app.39236.

(177) Karatasos, K.; Ryckaert, J.-P. Local Dynamics of Polyisobutylene Revisited. *Macromolecules* **2001**, *34* (21), 7232–7235. https://doi.org/10.1021/ma010869h.

(178) Wei, X.; Bagdi, K.; Ren, L.; Shah, P.; Seethamraju, K.; Faust, R. Polyisobutylene-Based Thermoplastic Polyurethanes Exhibit Significant Phase Mixing. *Polymer* **2013**, *54* (6), 1647–1655. https://doi.org/10.1016/j.polymer.2013.01.029.

(179) Levenhagen, N. P.; Dadmun, M. D. Bimodal Molecular Weight Samples Improve the Isotropy of 3D Printed Polymeric Samples. *Polymer* **2017**, *122*, 232–241. https://doi.org/10.1016/j.polymer.2017.06.057.

(180) Wegener, G.; Brandt, M.; Duda, L.; Hofmann, J.; Klesczewski, B.; Koch, D.; Kumpf, R.-J.; Orzesek, H.; Pirkl, H.-G.; Six, C.; Steinlein, C.; Weisbeck, M. Trends in Industrial Catalysis in the Polyurethane Industry. *Applied Catalysis A: General* **2001**, *221* (1–2), 303–335. https://doi.org/10.1016/S0926-860X(01)00910-3.

(181) Zhang, Y.; Fang, H.; Zhang, X.; Wang, S.; Xing, G. 8-(4-aminophenyl)BODIPYs

as Fluorescent pH Probes: Facile Synthesis, Computational Study and Lysosome Imaging. *ChemistrySelect* **2016**, *1* (1), 1–6. https://doi.org/10.1002/slct.201500016.

(182) Ha, S.-T.; Su, R.; Xing, J.; Zhang, Q.; Xiong, Q. Metal Halide Perovskite Nanomaterials: Synthesis and Applications. *Chemical Science* **2017**, *8* (4), 2522–2536. https://doi.org/10.1039/C6SC04474C.

(183) Dong, Y.; Wang, Y.-K.; Yuan, F.; Johnston, A.; Liu, Y.; Ma, D.; Choi, M.-J.; Chen, B.; Chekini, M.; Baek, S.-W.; Sagar, L. K.; Fan, J.; Hou, Y.; Wu, M.; Lee, S.; Sun, B.; Hoogland, S.; Quintero-Bermudez, R.; Ebe, H.; Todorovic, P.; Dinic, F.; Li, P.; Kung, H. T.; Saidaminov, M. I.; Kumacheva, E.; Spiecker, E.; Liao, L.-S.; Voznyy, O.; Lu, Z.-H.; Sargent, E. H. Bipolar-Shell Resurfacing for Blue LEDs Based on Strongly Confined Perovskite Quantum Dots. *Nat. Nanotechnol.* **2020**, *15* (8), 668–674. https://doi.org/10.1038/s41565-020-0714-5.

(184) Xue, C.-X.; Chiu, Y.-C.; Liu, T.-W.; Huang, T.-Y.; Liu, J.-S.; Chang, T.-W.; Kao, H.-Y.; Wang, J.-H.; Wei, S.-Y.; Lee, C.-Y.; Huang, S.-P.; Hung, J.-M.; Teng, S.-H.; Wei, W.-C.; Chen, Y.-R.; Hsu, T.-H.; Chen, Y.-K.; Lo, Y.-C.; Wen, T.-H.; Lo, C.-C.; Liu, R.-S.; Hsieh, C.-C.; Tang, K.-T.; Ho, M.-S.; Su, C.-Y.; Chou, C.-C.; Chih, Y.-D.; Chang, M.-F. A CMOS-Integrated Compute-in-Memory Macro Based on Resistive Random-Access Memory for AI Edge Devices. *Nat Electron* **2020**, *4* (1), 81–90. https://doi.org/10.1038/s41928-020-00505-5.

(185) Jeong, M.; Choi, I. W.; Go, E. M.; Cho, Y.; Kim, M.; Lee, B.; Jeong, S.; Jo, Y.; Choi, H. W.; Lee, J.; Bae, J.-H.; Kwak, S. K.; Kim, D. S.; Yang, C. Stable Perovskite Solar Cells with Efficiency Exceeding 24.8% and 0.3-V Voltage Loss. *Science* **2020**, *369* (6511), 1615–1620. https://doi.org/10.1126/science.abb7167.

(186) Li, M.; Li, H.; Fu, J.; Liang, T.; Ma, W. Recent Progress on the Stability of Perovskite Solar Cells in a Humid Environment. *J. Phys. Chem. C* **2020**, *124* (50), 27251–27266. https://doi.org/10.1021/acs.jpcc.0c08019.

(187) Liao, Y.; Chen, W.; Borsali, R. Carbohydrate-Based Block Copolymer Thin Films: Ultrafast Nano-Organization with 7 Nm Resolution Using Microwave Energy. *Advanced Materials* **2017**, *29* (35), 1701645. https://doi.org/10.1002/adma.201701645.

(188) Mai, Y.; Eisenberg, A. Self-Assembly of Block Copolymers. *Chem. Soc. Rev.* **2012**, *41* (18), 5969. https://doi.org/10.1039/c2cs35115c.

(189) Li, C.; Rafique, S.; Zhan, Y. Synergy of Block Copolymers and Perovskites: Template Growth through Self-Assembly. *J. Phys. Chem. Lett.* **2022**, *13* (50), 11610–11621. https://doi.org/10.1021/acs.jpclett.2c02983.

(190) Mathur, A.; Li, A.; Maheshwari, V. Hydrophobic–Hydrophilic Block Copolymer Mediated Tuning of Halide Perovskite Photosensitive Device Stability and Efficiency. *ACS Appl. Mater. Interfaces* **2023**, *15* (21), 25932–25941. https://doi.org/10.1021/acsami.3c02748.

(191) Chang, Y.-H.; Ku, C.-W.; Zhang, Y.-H.; Wang, H.-C.; Chen, J.-Y. Ultrafast Responsive Non-Volatile Flash Photomemory via Spatially Addressable Perovskite/Block Copolymer Composite Film. *Advanced Functional Materials* **2020**, *30* (21), 2000764.

https://doi.org/10.1002/adfm.202000764.

(192) Rejek, T.; Schweizer, P.; Joch, D.; Portilla, L.; Spiecker, E.; Halik, M. Buried Microphase Separation by Dynamic Interplay of Crystallization and Microphase Separation in Semicrystalline PEO-Rich PS- *b* -PEO Block Copolymer Thin Films. *Macromolecules* **2020**, *53* (13), 5604–5613. https://doi.org/10.1021/acs.macromol.9b02760.

(193) Lee, J.-Y.; Crosby, A. J. Crazing in Glassy Block Copolymer Thin Films. *Macromolecules* **2005**, *38* (23), 9711–9717. https://doi.org/10.1021/ma051716n.

(194) Dong, Y.; Qiao, T.; Kim, D.; Parobek, D.; Rossi, D.; Son, D. H. Precise Control of Quantum Confinement in Cesium Lead Halide Perovskite Quantum Dots via Thermodynamic Equilibrium. *Nano Lett.* **2018**, *18* (6), 3716–3722. https://doi.org/10.1021/acs.nanolett.8b00861.

(195) Mi, C.; Atteberry, M. L.; Mapara, V.; Hidayatova, L.; Gee, G. C.; Furis, M.; Yip, W. T.; Weng, B.; Dong, Y. Biexciton-like Auger Blinking in Strongly Confined $CsPbBr_3$ Perovskite Quantum Dots. *J. Phys. Chem. Lett.* **2023**, *14* (23), 5466–5474. https://doi.org/10.1021/acs.jpclett.3c01145.

(196) Gong, W.; Qi, R. Graft Copolymerization of Maleic Anhydride onto Low-molecular-weight Polyisobutylene through Solvothermal Method. *J of Applied Polymer Sci* **2009**, *113* (3), 1520–1528. https://doi.org/10.1002/app.30020.

(197) Puthenpurayil, J.; Cheng, O. H.-C.; Qiao, T.; Rossi, D.; Son, D. H. On the Determination of Absorption Cross Section of Colloidal Lead Halide Perovskite Quantum Dots. *The Journal of Chemical Physics* **2019**, *151* (15), 154706. https://doi.org/10.1063/1.5126039.

(198) Sclavons, M.; Franquinet, P.; Carlier, V.; Verfaillie, G.; Fallais, I.; Legras, R.; Laurent, M.; Thyrion, F. C. Quantification of the Maleic Anhydride Grafted onto Polypropylene by Chemical and Viscosimetric Titrations, and FTIR Spectroscopy. *Polymer* **2000**, *41* (6), 1989–1999. https://doi.org/10.1016/S0032-3861(99)00377-8.

(199) Nakason, C.; Kaesaman, A.; Supasanthitikul, P. The Grafting of Maleic Anhydride onto Natural Rubber. *Polymer Testing* **2004**, *23* (1), 35–41. https://doi.org/10.1016/S0142-9418(03)00059-X.

(200) Shen, Y.; Qi, R.; Liu, Q.; Zhou, C. Solvothermal Preparation and Characterization of Maleic Anhydride Grafting High Density Polyethylene Copolymer. *J of Applied Polymer Sci* **2007**, *104* (5), 3443–3452. https://doi.org/10.1002/app.26033.

(201) Wang, S.; Du, L.; Jin, Z.; Xin, Y.; Mattoussi, H. Enhanced Stabilization and Easy Phase Transfer of $CsPbBr_3$ Perovskite Quantum Dots Promoted by High-Affinity Polyzwitterionic Ligands. *J. Am. Chem. Soc.* **2020**, *142* (29), 12669–12680. https://doi.org/10.1021/jacs.0c03682.

(202) Yi, C.; Yang, Y.; Liu, B.; He, J.; Nie, Z. Polymer-Guided Assembly of Inorganic Nanoparticles. *Chem. Soc. Rev.* **2020**, *49* (2), 465–508. https://doi.org/10.1039/C9CS00725C.

(203) Gai, Y.; Lin, Y.; Song, D.-P.; Yavitt, B. M.; Watkins, J. J. Strong Ligand–Block Copolymer Interactions for Incorporation of Relatively Large Nanoparticles in Ordered Composites. *Macromolecules* **2016**, *49* (9), 3352–3360. https://doi.org/10.1021/acs.macromol.5b02609.

(204) Yan, N.; Zhang, Y.; He, Y.; Zhu, Y.; Jiang, W. Controllable Location of Inorganic Nanoparticles on Block Copolymer Self-Assembled Scaffolds by Tailoring the Entropy and Enthalpy Contributions. *Macromolecules* **2017**, *50* (17), 6771–6778. https://doi.org/10.1021/acs.macromol.7b01076.

(205) Liang, F.; Jhuang, F.; Fang, Y.; Benas, J.; Chen, W.; Yan, Z.; Lin, W.; Su, C.; Sato, Y.; Chiba, T.; Kido, J.; Kuo, C. Synergistic Effect of Cation Composition Engineering of Hybrid $Cs_{1-x}FA_xPbBr_3$ Nanocrystals for Self-Healing Electronics Application. *Advanced Materials* **2023**, *35* (9), 2207617. https://doi.org/10.1002/adma.202207617.

(206) Posocco, P.; Fermeglia, M.; Pricl, S. Morphology Prediction of Block Copolymers for Drug Delivery by Mesoscale Simulations. *J. Mater. Chem.* **2010**, *20* (36), 7742. https://doi.org/10.1039/c0jm01301c.

(207) Baranov, D.; Toso, S.; Imran, M.; Manna, L. Investigation into the Photoluminescence Red Shift in Cesium Lead Bromide Nanocrystal Superlattices. *J. Phys. Chem. Lett.* **2019**, *10* (3), 655–660. https://doi.org/10.1021/acs.jpclett.9b00178.

(208) Swarnkar, A.; Ravi, V. K.; Nag, A. Beyond Colloidal Cesium Lead Halide Perovskite Nanocrystals: Analogous Metal Halides and Doping. *ACS Energy Lett.* **2017**, *2* (5), 1089–1098. https://doi.org/10.1021/acsenergylett.7b00191.

(209) Kovalenko, M. V.; Protesescu, L.; Bodnarchuk, M. I. Properties and Potential Optoelectronic Applications of Lead Halide Perovskite Nanocrystals. *Science* **2017**, *358* (6364), 745–750. https://doi.org/10.1126/science.aam7093.

(210) Hassan, Y.; Park, J. H.; Crawford, M. L.; Sadhanala, A.; Lee, J.; Sadighian, J. C.; Mosconi, E.; Shivanna, R.; Radicchi, E.; Jeong, M.; Yang, C.; Choi, H.; Park, S. H.; Song, M. H.; De Angelis, F.; Wong, C. Y.; Friend, R. H.; Lee, B. R.; Snaith, H. J. Ligand-Engineered Bandgap Stability in Mixed-Halide Perovskite LEDs. *Nature* **2021**, *591* (7848), 72–77. https://doi.org/10.1038/s41586-021-03217-8.

(211) Tao, Y.; Zhang, M.; Li, D.; Liu, K.; Xu, J.; Wei, L.; Zhang, K.; Wang, Y.; Dai, F.; Teng, L.; Wang, L.; Wu, Z.; Xing, J. Near-Unity Quantum Yield and Long-Term Emission Stability in Halide Perovskite Nanocrystal Glass Composite. *Spectrochimica Acta Part A: Molecular and Biomolecular Spectroscopy* **2024**, *316*, 124379. https://doi.org/10.1016/j.saa.2024.124379.

(212) Liu, A.; Bi, C.; Li, J.; Zhang, M.; Cheng, C.; Binks, D.; Tian, J. High Color-Purity and Efficient Pure-Blue Perovskite Light-Emitting Diodes Based on Strongly Confined Monodispersed Quantum Dots. *Nano Lett.* **2023**, *23* (6), 2405–2411. https://doi.org/10.1021/acs.nanolett.3c00548.

(213) Bai, Y.; Hao, M.; Ding, S.; Chen, P.; Wang, L. Surface Chemistry Engineering of Perovskite Quantum Dots: Strategies, Applications, and Perspectives. *Advanced Materials* **2022**, *34* (4), 2105958. https://doi.org/10.1002/adma.202105958.

(214) Tao, S.; Schmidt, I.; Brocks, G.; Jiang, J.; Tranca, I.; Meerholz, K.; Olthof, S. Absolute Energy Level Positions in Tin- and Lead-Based Halide Perovskites. *Nat Commun* **2019**, *10* (1), 2560. https://doi.org/10.1038/s41467-019-10468-7.

(215) Chi, W.; Banerjee, S. K. Achieving Resistance against Moisture and Oxygen for Perovskite Solar Cells with High Efficiency and Stability. *Chem. Mater.* **2021**, *33* (12), 4269–4303. https://doi.org/10.1021/acs.chemmater.1c00773.

(216) Patel, M.; Patel, R.; Park, C.; Cho, K.; Kumar, P.; Park, C.; Koh, W.-G. Water-Stable, Biocompatible, and Highly Luminescent Perovskite Nanocrystals-Embedded Fiber-Based Paper for Anti-Counterfeiting Applications. *Nano Convergence* **2023**, *10* (1), 21. https://doi.org/10.1186/s40580-023-00366-6.

(217) Tian, T.; Yang, M.; Fang, Y.; Zhang, S.; Chen, Y.; Wang, L.; Wu, W.-Q. Large-Area Waterproof and Durable Perovskite Luminescent Textiles. *Nat Commun* **2023**, *14* (1), 234. https://doi.org/10.1038/s41467-023-35830-8.

(218) Han, H.; Oh, J. W.; Park, J.; Lee, H.; Park, C.; Lee, S. W.; Lee, K.; Jeon, S.; Kim, S.; Park, Y.; Jeong, B.; Ryu, D. Y.; Park, C. Hierarchically Ordered Perovskites with High Photo-Electronic and Environmental Stability via Nanoimprinting Guided Block Copolymer Self-Assembly. *Advanced Materials Interfaces* **2022**, *9* (16), 2200082. https://doi.org/10.1002/admi.202200082.

(219) *Ultrafast Responsive Non-Volatile Flash Photomemory via Spatially Addressable Perovskite/Block Copolymer Composite Film - Chang - 2020 - Advanced Functional Materials - Wiley Online Library.* https://onlinelibrary.wiley.com/doi/full/10.1002/adfm.202000764 (accessed 2024-05-06).

(220) Shen, N.; Bu, J.; Prévôt, M. E.; Hegmann, T.; Kennedy, J. P.; Xu, W. Macromolecular Engineering and Additive Manufacturing of Polyisobutylene-Based Thermoplastic Elastomers. II. The Poly(Styrene-b-Isobutylene-b-Styrene)/Poly(Phenylene Oxide) System. *Macromolecular Rapid Communications* **2023**, *44* (1), 2200109. https://doi.org/10.1002/marc.202200109.

(221) Shen, N.; Liu, S.; Kasbe, P.; Khabaz, F.; Kennedy, J. P.; Xu, W. Macromolecular Engineering and Additive Manufacturing of Poly(Styrene-b-Isobutylene-b-Styrene). *ACS Appl. Polym. Mater.* **2021**, *3* (9), 4554–4562. https://doi.org/10.1021/acsapm.1c00616.

(222) Yang, D.; Li, X.; Zhou, W.; Zhang, S.; Meng, C.; Wu, Y.; Wang, Y.; Zeng, H. CsPbBr3 Quantum Dots 2.0: Benzenesulfonic Acid Equivalent Ligand Awakens Complete Purification. *Advanced Materials* **2019**, *31* (30), 1900767. https://doi.org/10.1002/adma.201900767.

(223) Fang, T.; Yuan, S.; Li, X.; Shan, Q.; Zhou, Y.; Xu, B.; Liu, G.; Zhang, S.; Li, X.; Li, W.; Fan, Z.; Zeng, H. Sulfonate Additive Simultaneously Suppresses Interstitials and Vacancies Toward Efficient and Stable Perovskite Quantum Dot LEDs. *Advanced Optical Materials* **2024**, *12* (10), 2302253. https://doi.org/10.1002/adom.202302253.

(224) Martins, C. R.; Ruggeri, G.; De Paoli, M.-A. Synthesis in Pilot Plant Scale and Physical Properties of Sulfonated Polystyrene. *J. Braz. Chem. Soc.* **2003**, *14* (5), 797–802. https://doi.org/10.1590/S0103-50532003000500015.

(225) Elabd, Y. A.; Napadensky, E. Sulfonation and Characterization of Poly(Styrene-Isobutylene-Styrene) Triblock Copolymers at High Ion-Exchange Capacities. *Polymer* **2004**, *45* (9), 3037–3043. https://doi.org/10.1016/j.polymer.2004.02.061.

(226) Weiss, R. A.; Sen, A.; Pottick, L. A.; Willis, C. L. Block Copolymer Ionomers: 2. Viscoelastic and Mechanical Properties of Sulphonated Poly(Styrene-Ethylene/Butylene-Styrene). *Polymer* **1991**, *32* (15), 2785–2792. https://doi.org/10.1016/0032-3861(91)90109-v.

(227) Mani, S.; Weiss, R. A.; Williams, C. E.; Hahn, S. F. Microstructure of Ionomers Based on Sulfonated Block Copolymers of Polystyrene and Poly(Ethylene-*Alt*-Propylene). *Macromolecules* **1999**, *32* (11), 3663–3670. https://doi.org/10.1021/ma9900986.

(228) Uddin, M. A.; Mobley, J. K.; Masud, A. A.; Liu, T.; Calabro, R. L.; Kim, D.-Y.; Richards, C. I.; Graham, K. R. Mechanistic Exploration of Dodecanethiol-Treated Colloidal CsPbBr3 Nanocrystals with Photoluminescence Quantum Yields Reaching Near 100%. *J. Phys. Chem. C* **2019**, *123* (29), 18103–18112. https://doi.org/10.1021/acs.jpcc.9b05612.

APPENDICES

APPENDIX A:

SUPPORT INFORMATION FOR ADDITIVE MANUFACTURING OF PIB-BASED POLYURETHANE AND ITS COMPOSITE WITH HARD POLYURETHANE

Polyisobutylene-polyurethane synthesis and characterizations:

Chemicals: All chemicals were used as received from the vendor unless specified that they were purified. Methanol (MeOH), n-hexanes, hydrochloric acid (HCl, 37% aqueous solution), sodium bicarbonate ($NaHCO_3$), sodium sulfate (Na_2SO_4), sodium chloride (NaCl) were purchased from Fisher Scientific. Sulfuric acid, (H_2SO_4, 98% *conc.*), dichloromethane (CH_2Cl_2), diethyl ether (Et_2O), methyl magnesium bromide (CH_3MgBr, 3 M in Et_2O), N,N,N',N'-tetramethyl ethylenediamine (TMEDA), 1,4-butanediol (BDO), methylene diphenyl diisocyanate (MDI), titanium tetrachloride ($TiCl_4$, ReagentPlus grade), 9-borabicyclo 3.3.1 nonane (9-BBN, 0.5 M in THF), potassium hydroxide (KOH), calcium chloride ($CaCl_2$), calcium hydride (CaH_2), dibutyltin dilaurate (DBTDL) were purchased from Sigma-Aldrich. Allyl trimethyl silane (ATMS) was purchased from TCI and hydrogen peroxide (H_2O_2, 35% solution in water) was purchased from Merck. Isobutylene (IB, 99% pure) monomer was supplied by ExxonMobil in a high-pressure stainless-steel cylinder. n-Hexanes and CH_2Cl_2 were dried using CaH_2 and freshly distilled before use for polymerization of isobutylene. THF was dried using Na–Benzophenone and freshly distilled before use in the synthesis of initiator, hydroboration of allyl end-groups, and synthesis of polyurethanes. MDI was freshly distilled and stored at – 12 °C in a vessel with

N_2 headspace. The distillation was caried out under a vacuum, with pressure maintained around 30 mTorr and pitching flask heated at 130 °C. The removal of oligomeric species from the MDI monomer was confirmed by ^1H NMR analysis. BDO was freshly distilled and stored under an N_2 atmosphere with activated molecular sieves. The initiator 5-tert-butyl-1,3-bis(2-chloro-2-propyl)benzene was prepared from 5-(tert-Butyl)isophthalic acid purchased from TCI, as described below.

Synthesis of dimethyl-5-(*tert*-butyl)isophthalate:

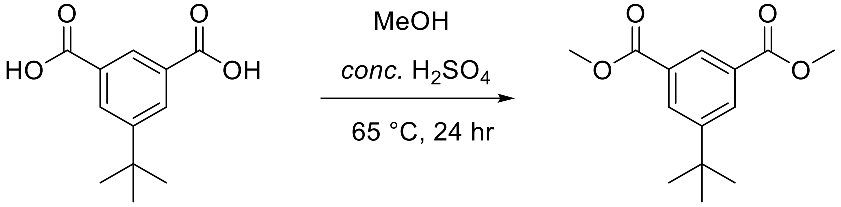

In a 1000 mL round bottom flask with a magnetic stir bar, 5-(tert-Butyl)isophthalic acid (25 g, 0.113 mol, 1 eq.) was dissolved in MeOH (500 mL, 12.8 mol, 110 eq.) and 98% *conc*. H_2SO_4 (50 mL, 0.94 mol, 8.4 eq) was added slowly and stirred overnight at 65 °C. After 24 hr, TLC analysis with a 7% MeOH in CH_2Cl_2 solution was used to check for conversion (R_f= 0.6). After full conversion was observed, the reaction solution was cooled to 25 °C, and then stored in at 5 °C to precipitate the solids from the solution. After 24 hr, a white precipitate was seen at the bottom of the flask and the solution was decanted. The precipitate was filtered and washed with DI water (3 x 20 mL). The washed precipitate was dissolved in 300 mL of Et_2O to obtain a clear solution. Using a separatory funnel, the ether solution was washed with aqueous saturated $NaHCO_3$ (80 mL), brine (40 mL) and then dried over Na_2SO_4. The solution was filtered and then dried using a rotary evaporator to afford a white solid powder which was further dried overnight under a high vacuum at

25 °C. The final yield was 25.1 g (90% yield) of dimethyl-5-(*tert*-butyl)isophthalate. ^{1}H NMR (400 MHz, $CDCl_3$-*d*) δ ppm 1.39 (s, 10 H), 1.55 (s, 2 H), 3.96 (s, 6 H), 8.28 (s, 2 H), 8.51 (s, 1 H).

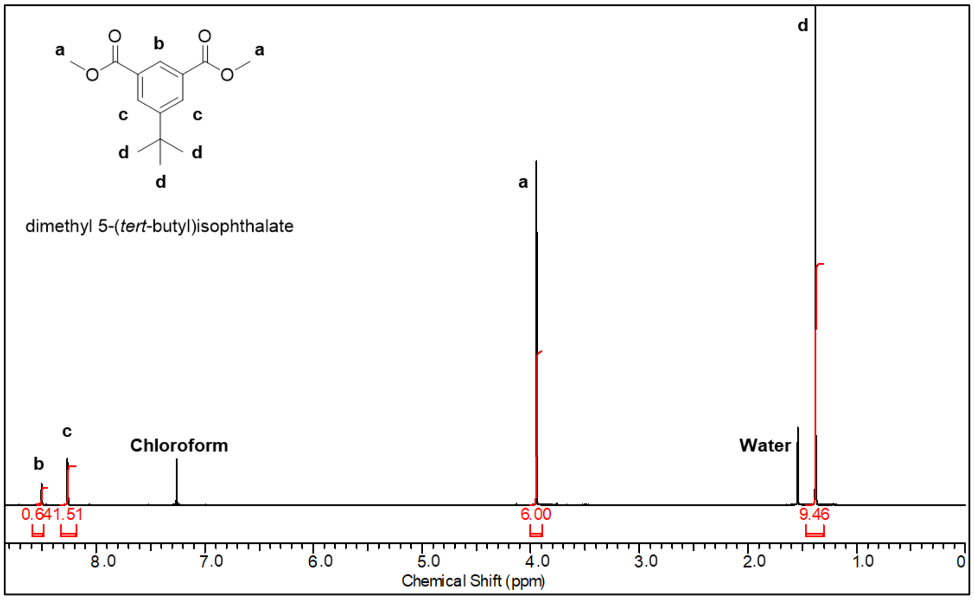

Figure A1: ^{1}H NMR spectrum of dimethyl-5-(*tert*-butyl)isophthalate

Synthesis of 2,2'-(5-(tert-butyl)-1,3-phenylene)bis(propan-2-ol):

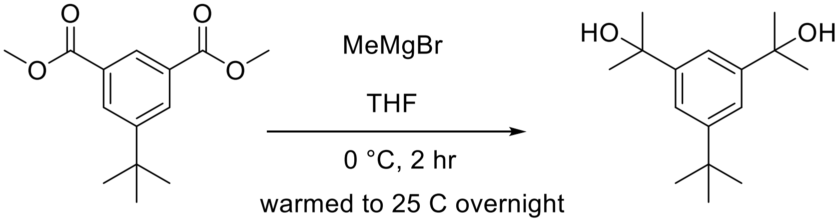

In a 1000 mL round bottom flask with a magnetic stir bar, dimethyl-5-(*tert*-butyl)isophthalate (20 g, 80 mmol, 1 eq.) was loaded. Freshly distilled THF (360 mL) was added to obtain a clear solution at 25 °C under stirring. The flask was cooled using an ice bath, maintained at 0 °C, and equipped with an addition funnel with a pressure-regulating side arm and sealed at the top with a rubber septum. The setup was evacuated and backfilled with dry N_2 three times to maintain an inert atmosphere for the Grignard reagent addition step. CH_3MgBr (140 mL, 399 mmol, 5 eq.) was charged into the addition funnel under N_2 circulation. The CH_3MgBr solution was added dropwise to the flask solution under constant stirring, and the reaction solution slowly changed color. After complete addition (120 minutes), the setup was transferred to a water bath and allowed to gradually warm up to 25 °C overnight. Using a rotary evaporator, the THF was evaporated from the reaction solution to obtain a crude white solid. The solids were dissolved using an aqueous 1M HCl solution until all the solids were dissolved, with a final pH of 5 – 6 which is necessary to quench the excess CH_3MgBr. The solution was then washed with 300 mL of Et_2O (2 x 150 mL) and the aqueous layer was separated. The organic layer was collected, washed with brine (40 mL), dried over Na_2SO_4, and filtered to obtain a clear solution. The solution was dried using a rotary evaporator to yield a white solid crystalline powder and dried further under high vacuum overnight. The final yield was 18 g of 2,2'-(5-(tert-butyl)-1,3-phenylene)bis(propan-2-ol). ^{1}H NMR (400 MHz, DMSO-*d*$_6$) δ ppm 1.29 (s, 9 H), 1.41 (s, 12 H), 4.86 (s, 2 H), 7.22 - 7.43 (m, 3 H)

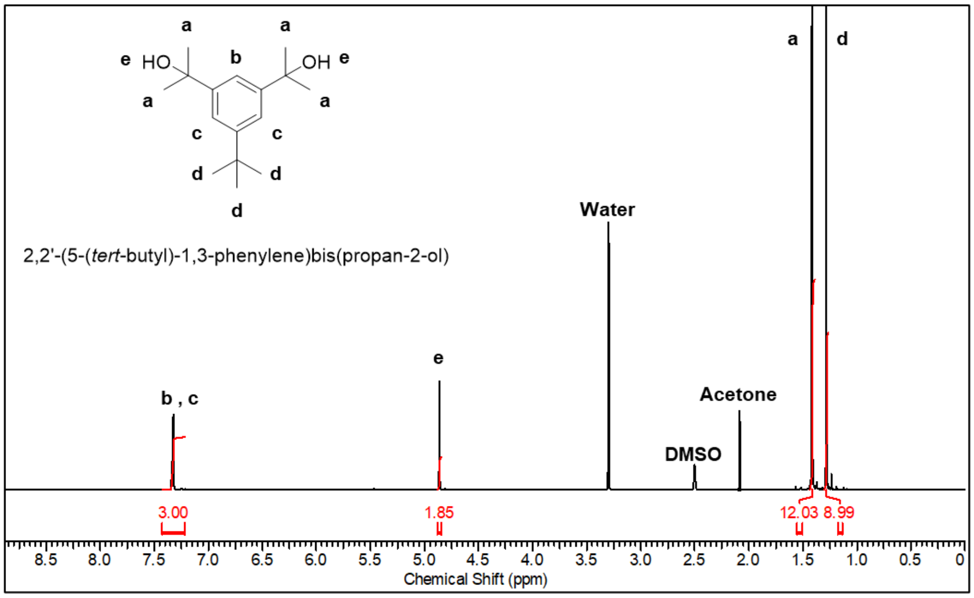

Figure A2: ^{1}H NMR spectrum of 2,2'-(5-(tert-butyl)-1,3-phenylene)bis(propan-2-ol)

Synthesis of 5-tert-butyl-1,3-bis(2-chloro-2-propyl)benzene:

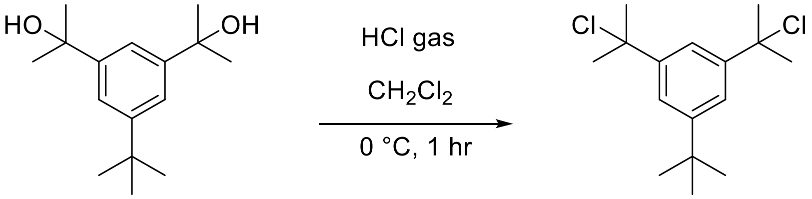

In a flame-dried 250 mL single-necked round bottom flask with a magnetic stir bar, 2,2'-(5-(tert-butyl)-1,3-phenylene)bis(propan-2-ol) (17.7 g, 70.8 mmol, 1 eq.) and $CaCl_2$ (15.7 g, 141.5 mmol, 2 eq.) was added and sealed with a rubber septum. 60 mL of dried CH_2Cl_2 was added to the flask under an N_2 atmosphere along with constant stirring to obtain a slurry at 25 °C. The slurry was then cooled using salt in an ice water bath for 30 mins and maintained at – 10 °C. Once cooled, HCl gas was bubbled through the slurry with magnetic stirring. The conversion was quantitatively tracked using a ^{1}H NMR analysis every 15 mins, and as conversion increased, the solubility of the solids in the slurry improved. After 60 mins, a yellow solution of $CaCl_2$ and product in CH_2Cl_2 was obtained, and the flask was removed from the cooling bath and allowed to warm up to 25 °C. Using a cotton plug, $CaCl_2$ was separated, the clear yellow solution was dried using a rotary evaporator, and the crude solid was dried further under high vacuum on a Schlenk line. The product was purified by recrystallization in anhydrous n-hexanes at 30 °C under constant stirring to obtain a clear solution. The solution was then placed in a refrigerator at 4 °C and left undisturbed for the pure crystals to grow. After 1 day the solution was decanted, the crystals were quickly filtered and washed with chilled n-hexanes, dried under high vacuum at 25 °C on a Schlenk line for 1 hr using an aluminum foil covered round bottom flask. The initiator gradually decomposes at room temperature and effort should be made to keep at low temperature under nitrogen. Pure, transparent needle-shaped crystals of 5-tert-butyl-1,3-bis(2-chloro-2-propyl)benzene were obtained with a yield of 10 g (56.7 %). ^{1}H NMR (500 MHz, DMSO-d_6) δ ppm 1.29 - 1.33 (m, 9 H) 1.99 (s, 12 H) 7.52 - 7.55 (m, 2 H) 7.61 (t, J=1.96 Hz, 1 H).

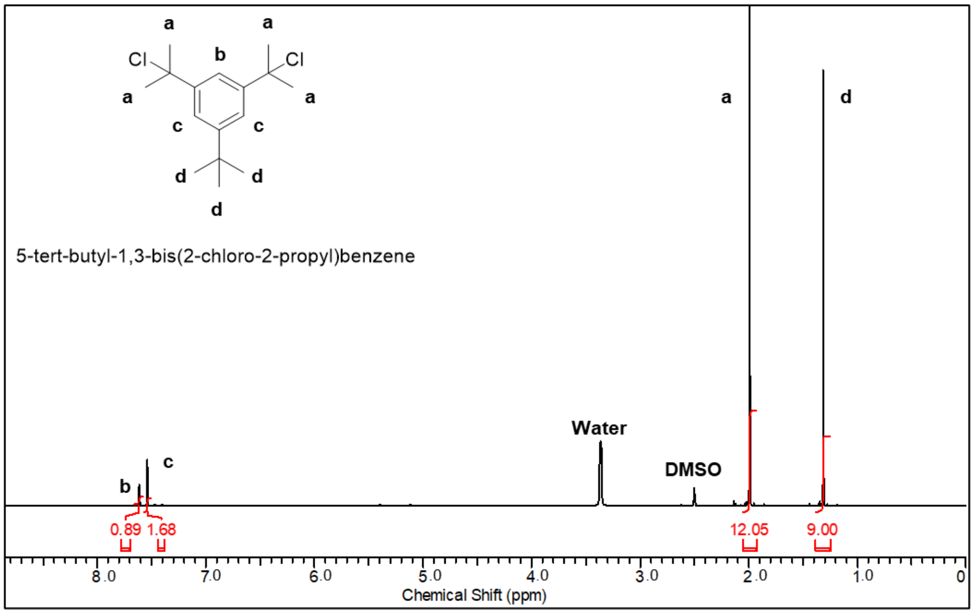

Figure A3: ^{1}H NMR spectrum of initiator 5-tert-butyl-1,3-bis(2-chloro-2-propyl)benzene

Synthesis of allyl end-functional polyisobutylene:

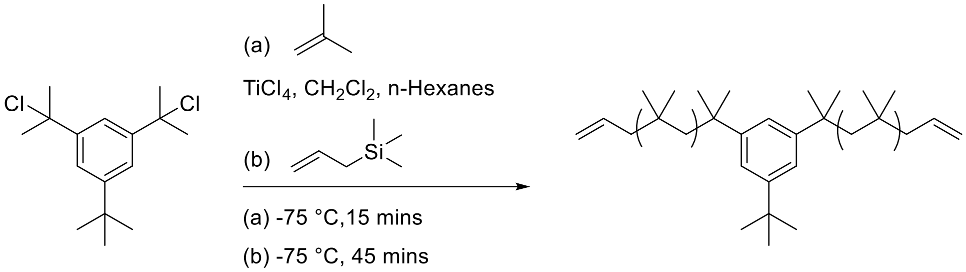

A flame-dried 15000 mL 3-necked round bottom flask was vacuum evacuated, backfilled with dry N_2, and equipped with a Teflon mechanical stir rod and overhead motor. Freshly distilled n-hexanes (2000 mL) and CH_2Cl_2 (1300 mL) were added under N_2 to the flask, along with the recrystallized initiator 5-tert-butyl-1,3-bis(2-chloro-2-propyl)benzene

(9.58 g, 33.3 mmol, 1 eq.) and TMEDA (10 mL, 66. 7 mmol, 2 eq.) at 25 °C. The solution was briefly stirred for 5 mins and then cooled using a dry ice-isopropanol cooling bath to −75 °C with continuous stirring. Once the temperature stabilized, liquid isobutylene (159 mL, 1785.7 mmol, 53.6 eq.) was transferred under an N_2 atmosphere to the reaction solution under stirring. The polymerization was initiated by adding a solution of $TiCl_4$ in CH_2Cl_2 (58.5 mL, 533.4 mmol, 16 eq.) under an N_2 atmosphere to the stirred reaction solution which changes from colorless to a bright orange color. After 15 min, the polymer chains were end-capped by adding ATMS (53 mL, 333.4 mmol, 10 eq.) and the reaction solution was stirred for 45 mins. The polymerization was quenched using MeOH (480 mL) and stirred for 15 mins to quench the excess $TiCl_4$, and then removed from the cooling bath and allowed to warm to 25 °C. The flask was then opened to air, and an aqueous solution of $NaHCO_3$ (60 g in 600 mL of water) was slowly added to the light-yellow colored reaction solution with a final pH of 5 – 6. The stirring was stopped to allow the aqueous and organic layers to separate, and the organic layer was transferred to a separatory funnel. The solution was washed with aqueous saturated $NaHCO_3$ (450 mL, 3 x 150 mL) to neutralize the acid and obtain a clear organic layer with a final pH between 7 – 8. The polyisobutylene, PiB, was precipitated in excess neutral MeOH under constant stirring in a large beaker. The stirring was stopped and PiB layer was allowed to settle, and the solvent was decanted to separate the solvent from the polymer. The PiB layer was redissolved in n-Hexanes and transferred to a round bottom flask. The solution was dried on a rotary evaporator to obtain a clear and viscous product. The polymer was further dried in a heated flask at 60 °C overnight under constant stirring, on a high vacuum Schlenk line to obtain PiB diallyl which was tacky and optically clear. The target batch size was 100 g of polymer molecular weight for the reaction was M_n= 3000 g/mol. The final molecular weight was confirmed using both GPC and ^{1}H NMR analysis. From GPC, M_n = 2812 g/mol, M_w = 3050 g/mol, $Đ$ = 1.1; ^{1}H NMR, molecular weight= 2883 g/mol. Allyl functionality was calculated using ^{1}H NMR peak integrals with the initiator peak as the internal reference. Allyl functionality= (3.94/ 4.00) x 100= 98.5 % and batch yield was 98.1 g (98 %).

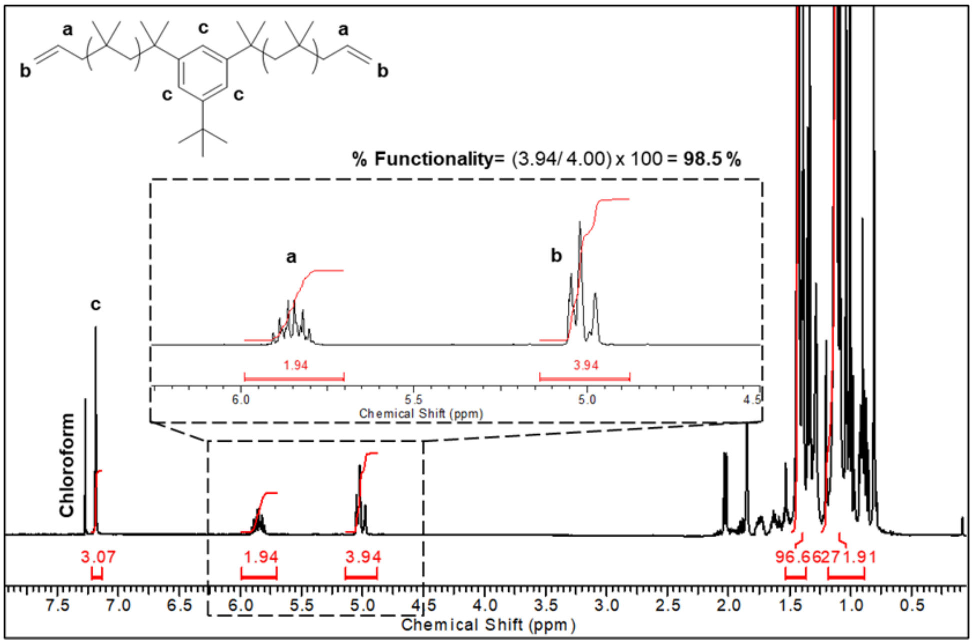

Figure A4: ^{1}H NMR spectrum of PiB end-functionalized with allyl groups

Synthesis of hydroxyl end-functional polyisobutylene:

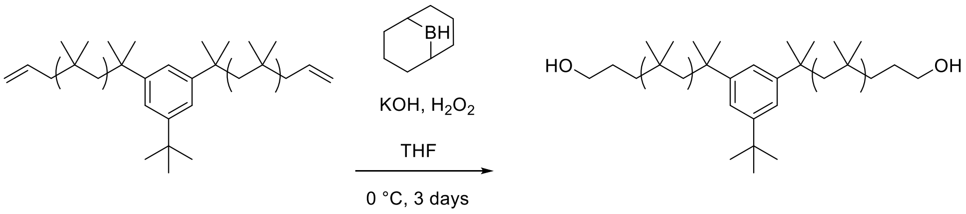

A flame-dried 2-necked round bottom flask was vacuum evacuated, backfilled with dry N_2, and equipped with a Teflon mechanical stir rod and overhead motor. Freshly distilled THF (900 mL) was used to dissolve the dried PiB diallyl (98 g, 33.7 mmol, 1 eq.) to obtain a clear solution. The solution was transferred to the 2-necked flask, and an addition funnel was attached to the flask and sealed at the top with a rubber septum. The headspace in the reactor setup was quickly evacuated and backfilled with N_2 three times to maintain an inert atmosphere inside. The flask was cooled using an ice-water bath with salt and the temperature was maintained at 0 °C. The 9-BBN (404.4 mL, 202.2 mmol, 6 eq.) solution was loaded into the funnel and added dropwise to the PiB solution. After the complete addition of the 9-BBN, the setup was allowed to gradually warm up to 25 °C overnight under an N_2 atmosphere. On the second day, the flask was cooled down and maintained at 0 °C for the oxidation step. A freshly prepared solution of KOH (63.6 g, 1078.4 mmol, 32 eq.) in MeOH (300 mL) was loaded into the addition funnel and added dropwise to the PiB solution. After the complete addition of KOH, an H_2O_2 (35 % aqueous solution, 81.1 mL, 943.6 mmol, 28 eq.) was added dropwise to the reaction solution. The flask was removed from the cooling bath and was allowed to gradually warm up to 25 °C overnight. On the third day, n-hexanes (320 mL) was added to the flask under stirring to help extract the PiB polymer from the THF reaction solution. The contents of the flask were transferred to a beaker and a freshly prepared solution of $KHCO_3$ (32.4g, 323.5 mmol, 9.6 eq.) in water (320 mL) was added to the reaction solution, stirred for 1 hr and the pH was recorded (pH should be between 7 and 8 before the starting to work up the PiB diol). HCl solution (37% solution, 7 mL) was added to neutralize any excess base and reach the desired pH range for work up. The contents of the beaker were emptied into a separatory funnel to allow the layers to separate, and the bottom aqueous layer was collected and kept aside. The turbid top layer in the funnel was washed with n-hexanes (3 x 100 mL) to separate out any leftover water and a clear organic solution with a pH of 7 was obtained. The PiB diol in the organic solution was precipitated in excess neutral MeOH under constant stirring in a beaker. The precipitated PiB diol was allowed to settle, MeOH was decanted, and n-hexanes (300 mL) was added to redissolve the PiB diol. The solution was dried using a rotary evaporator to obtain a viscous product, which was further dried overnight on a high vacuum Schlenk line at 60 °C under constant stirring. A final yield of 95 g PiB diol (96.9 % yield) was recorded which was tacky and optically clear. The % conversion of allyl groups was confirmed using ^{1}H NMR; Diol functionality= (3.95/4.00) x 0.985 x 100= 97 %).

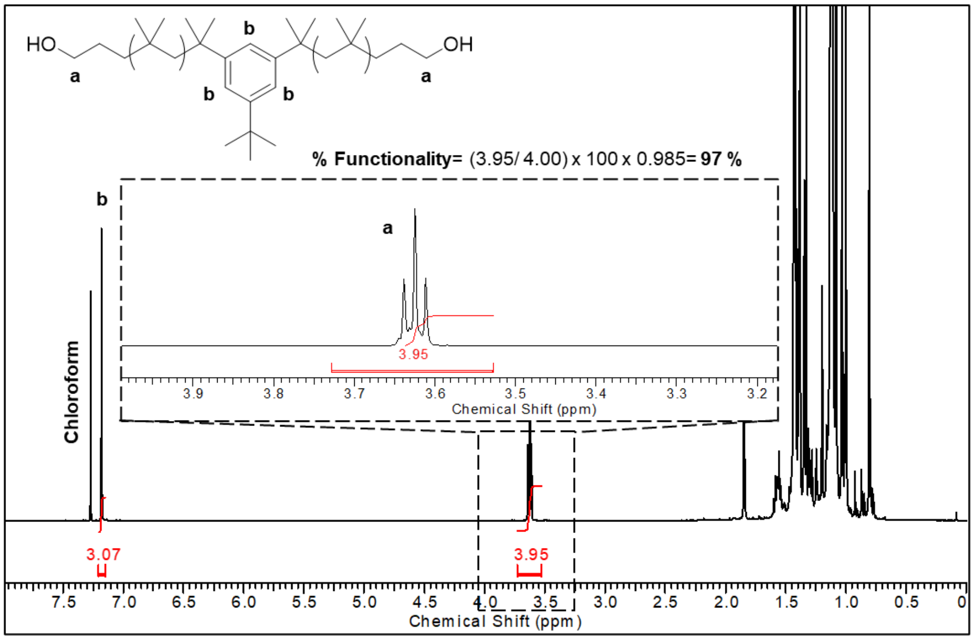

Figure A5: ^{1}H NMR spectrum of PiB end-functionalized with hydroxyl groups

Synthesis of polyisobutylene-polyurethanes (PIB-PU):

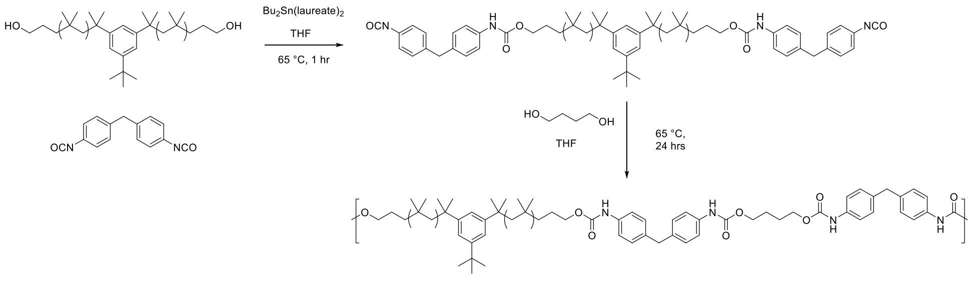

The target molecular weight for the PiB-PU is 100,000 g/ mol with a soft to hard block ratio of 70:30. For calculations, molecular weight= 2,883 g/ mol was used from ^{1}H NMR analysis for PiB diol. A flame-dried 2-necked round bottom flask was vacuum evacuated, backfilled with dry N_2, and equipped with a Teflon mechanical stir rod and overhead motor. Freshly distilled THF (325 mL) was used to dissolve the dried PiB diol (96 g, 33.0 mmol, 1 eq.) to obtain a clear solution. The solution was transferred to the 2-necked flask, distilled MDI (33.4 g, 133.5 mmol, 4 eq.) was added as a coarse powder and the side neck was sealed with a rubber septum. The headspace in the reactor setup was quickly evacuated and backfilled with dry N_2 3 times to maintain an inert moisture-free atmosphere inside. The catalyst solution of $Bu_2Sn(laureate)_2$ (78.9 mg, 0.13 mmol) in 10 mL of freshly distilled THF was added and the reaction solution was stirred at 65 °C for 1 hr under an N_2 atmosphere to form the prepolymer. After 1 hr, the chain extender 1,4-butanediol (8.95 g, 99.3 mmol, 3 eq.) was slowly added to the prepolymer solution to prevent any sudden changes in the viscosity of the solution and achieve full conversion of the isocyanate functionality. The reaction solution was stirred overnight at 65 °C under an N_2 atmosphere to reach the target molecular weight. An aliquot from the reaction flask was taken the next day to check the molecular weight via GPC and –NCO conversion using FT-

IR after 24 hrs. When the peak from free NCO groups (2280 cm^{-1}) disappeared in the FT-IR, the target molecular weight was achieved, the system was cooled to 25 °C and the tin catalyst was quenched using H_2O (3 mL) in 10 mL of distilled THF. The reaction solution was diluted further with distilled THF (325 mL), stirred for 30 mins and cast into films using PTFE molds. The wet films were air dried overnight using a fume hood followed by drying in a vacuum oven at 60 °C for 24 hours. The dried transparent films were weighed to record a yield of 135 g of PiB-PU (97.6 %). The PiB-PU was characterized by ^{1}H NMR, DSC, FT-IR and tested for mechanical properties according to the ASTM D638 (Type V) standard.

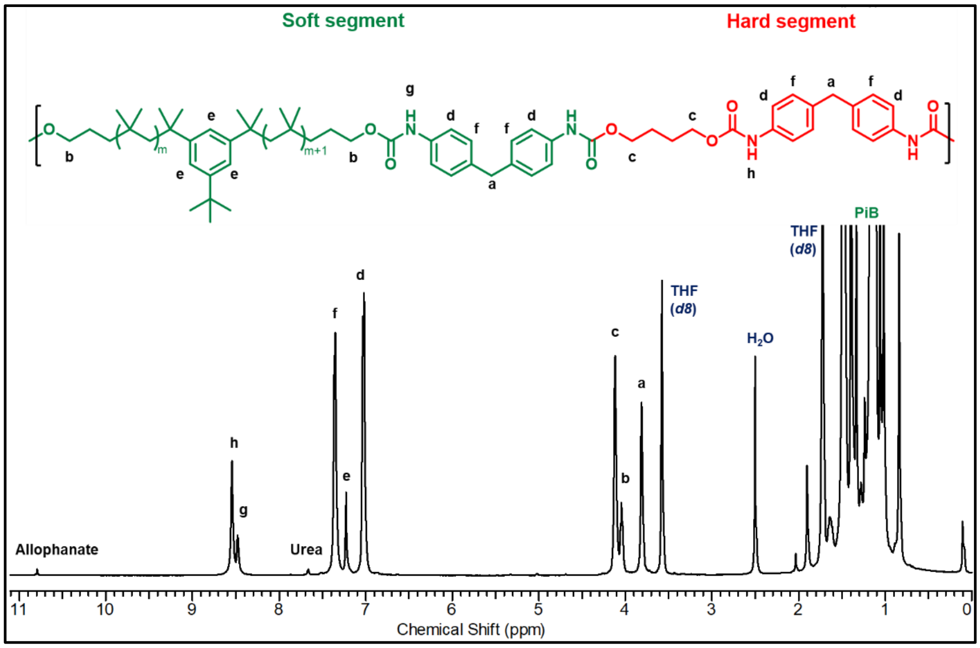

Figure A6: ^{1}H NMR spectrum of PiB-PU taken in THF (d8)

Supporting Information:

GPC: Molecular Weight analysis was carried out using the TOSOH EcoSec GPC 8320 system equipped with a Quad detector with two 17393 TSKgel columns (7.8 mm ID x 30 cm, 13 µm) and one 17367-TSKgel Guard Column (7.5 mm ID x 7.5 cm, 13 µm). Inhibitor-free HPLC grade Tetrahydrofuran (THF) was used as the eluent at a flow rate of 1 mL/min at 40 °C. Data were measured relative to polystyrene standards ($Đ < 1.05$). 5 mg of sample was weighed in a glass GPC vial with a stir bar and 2 mL of HPLC grade THF was added to it. The vial was sealed with a PTFE cap and the contents were stirred at 25 °C until the PIB-PU sample dissolved in THF to yield a homogeneous solution and the stir bar was removed. The solution was filtered using a PET filter loaded on a 5 mL syringe, and the filtered solution was collected in a 2 mL glass GPC vial and then sealed with a cap. The samples were analyzed to give retention times which were processed to calculate values of number average molecular weight (M_n), weight average molecular weight (M_w), and dispersity index ($Đ$).

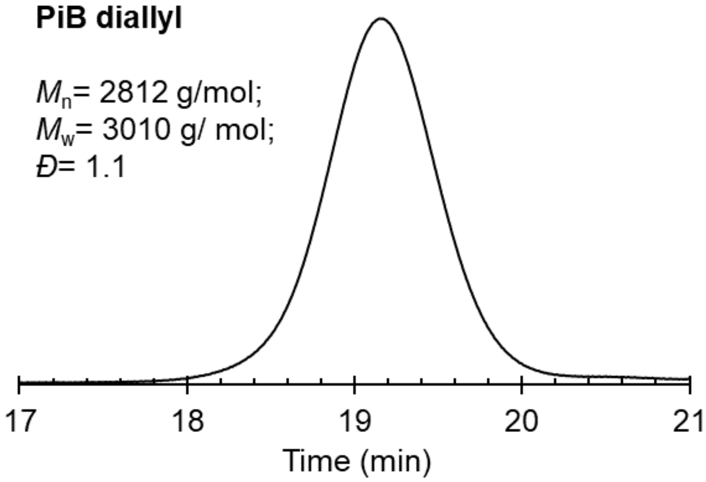

Figure A7: GPC chromatogram for PiB diallyl synthesized using cationic polymerization

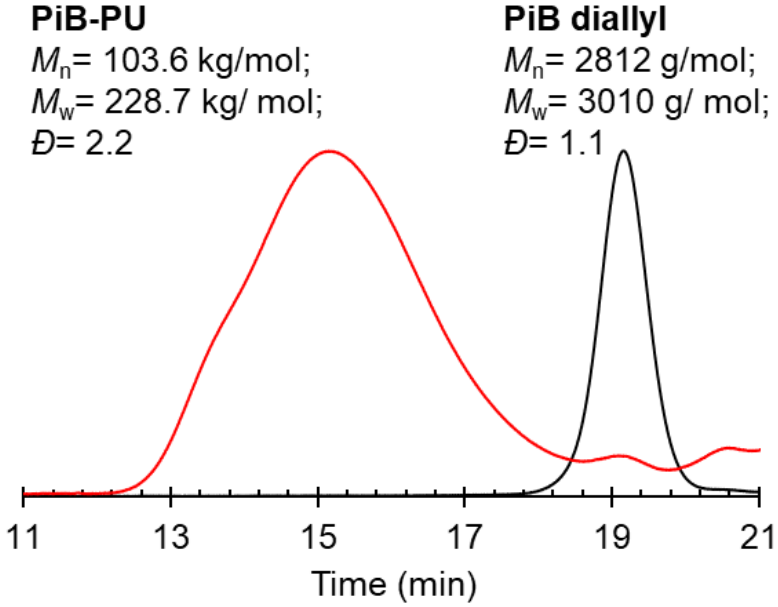

Figure A8: GPC chromatogram for PiB-PU and compared to the PiB diallyl starting material

NMR: Polyurethane samples were analyzed at 30 °C in Tetrahydrofuran-*d8* using the Agilent 500 MHz instrument for ^{1}H analysis equipped with an N_2 gas pneumatic supply. Spectra were processed using the ACD LABS 12.0 software. 60 mg of sample was weighed in a scintillation vial and 0.9 mL of THF-*d8* was added to it. The vial was sealed with a PTFE cap and stirred until all solids dissolved completely to yield a homogeneous solution. The entire solution was transferred to a 5 mm glass NMR tube to ensure a fill level of at least 5 cm and then sealed with a PTFE cap. Standard ^{1}H analyses were run at a 90° pulse angle with (a) 128 scans, 10 sec relaxation delay for the PIB samples, and (b) 64 scans, 1 sec relaxation delay for the initiator synthesis products.

DSC: Differential Scanning Calorimetry (DSC) was carried out using the TA instruments DSC250 instrument equipped with an autosampler, RCS 90 cooler and an N_2 gas supply. 5 mg of sample was weighed in a standard DSC aluminum pan and sealed with an aluminum lid using the provided press to ensure no gaps or openings. The sample pans were analyzed for heat flow (Watts/ gram) against an empty reference pan between -90 °C and 200 °C using a standard Heat-Cool-Heat test with a ramp rate of 10 °C/ min for the heating and cooling cycles. Data was processed using the TA instruments TRIOS software to report the melting temperature (T_m) and glass transition temperature (T_g) for the final PIB-PU sample

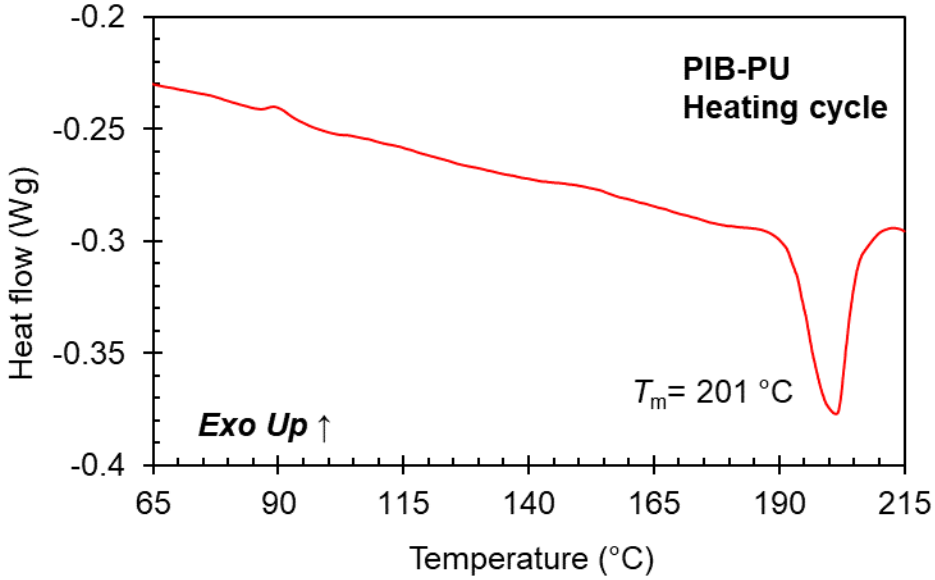

Figure A9: Differential scanning calorimetry of PiB-PU; a melting point of 201 °C is observed.

FT-IR: Dried PIB-PU thin films were analyzed using the PerkinElmer Frontier FT-

IR Spectrometer instrument with Universal Attenuated Total Reflection (UATR) equipped with a Diamond/ ZnSe crystal. A typical scan was run for 32 scans between 600 and 4000 cm^{-1} with a resolution of cm^{-1} and an accumulation number of 20 secs. A background scan was run before the samples to establish a reference that will be used to compare the samples. FT-IR analysis was used to track the progress of the reaction to complement the GPC data, by checking for free isocyanate functionality (–NCO) in the reaction solution. Once the total required BDO was added and the desired M_w was achieved, the peak corresponding to free–NCO was absent indicating that the reaction was complete. FT-IR analysis was utilized to check for the presence of any urea linkages in the final dried films, which may have resulted from the side reaction of –NCO with trace moisture in the reaction solution.

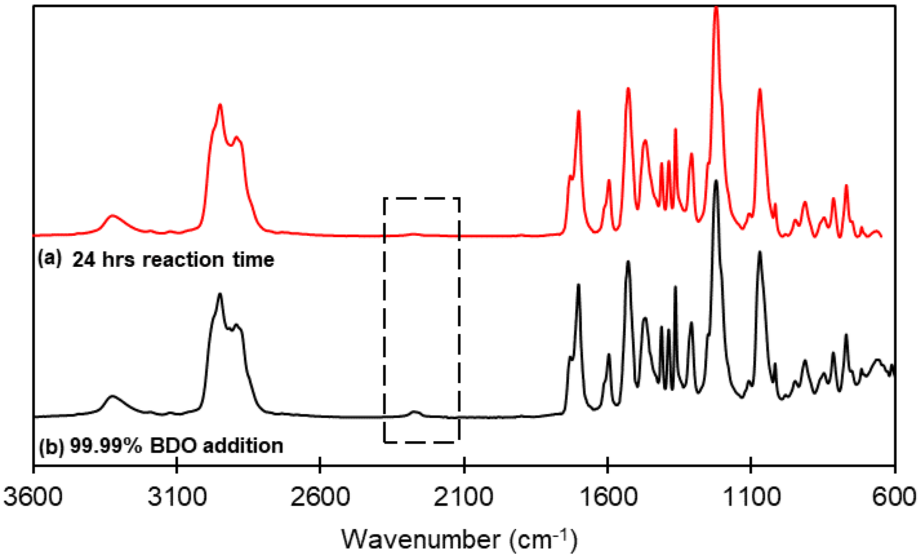

Figure A10: FT-IR of PiB-PU (a) during synthesis after 99.99% addition of BDO chain extender; (b) after 24 hr of reaction time just before quenching and casting films

Tensile Testing: PIB-PU samples were tested on the Universal Testing Machine from Instron (5567) equipped with a 1 kN load cell and pneumatic gas clamps. The samples were tested until failure with a rate of 100% elongation per minute. Samples were shaped according to the ASTM D638 (Type V) standard from fully dried, solvent cast PIB-PU films. 5 samples for every batch were tested to report the tensile stress at 100% elongation, tensile stress, and elongation at break.

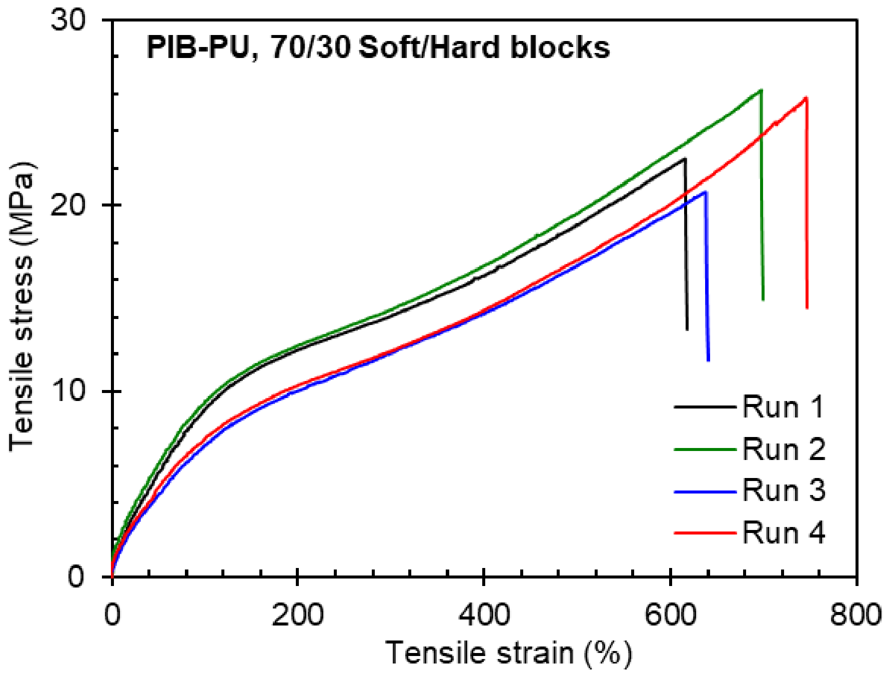

Figure A11: Tensile studies of casted PIB-PU tested according to ASTM-D638 (type V) standard; Maximum stress at break= 24.5 ± 4.1MPa, maximum strain at break= 677.5 ± 62.4 %

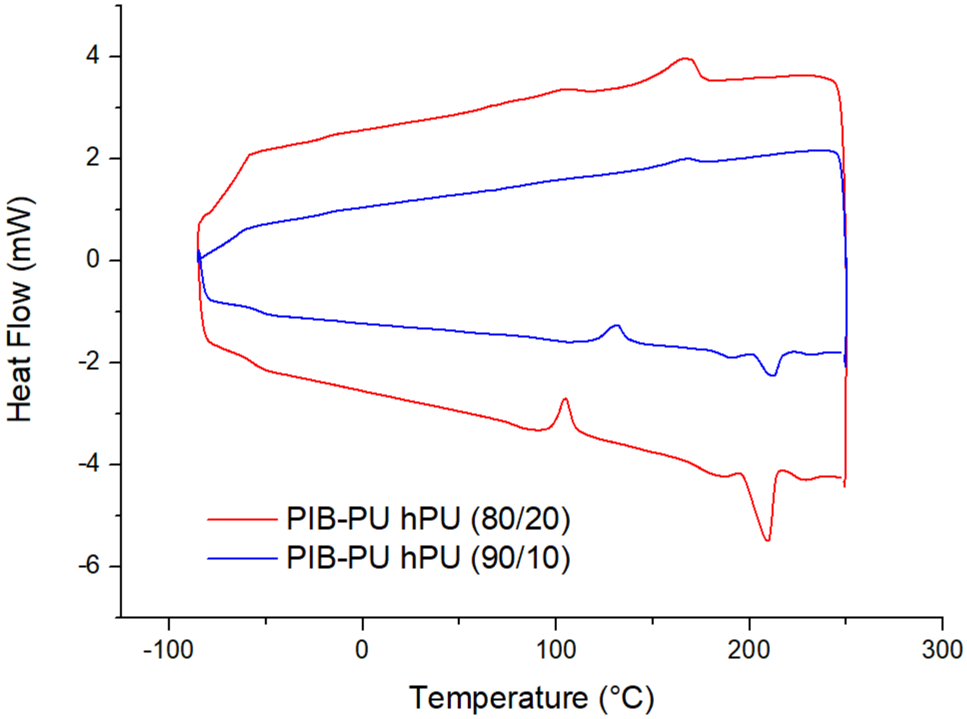

Figure A12: DSC data for L-PIB-PU/hPU composites with 10wt% and 20wt% hPU content.

APPENDIX B:

SUPPORT INFORMATION FOR DESIGNED POLYMER LIGANDS FOR PEROVSKITE QUANTUM DOTS AND THEIR BLOCK COPOLYMER NANOCOMPOSITES

1. PIBSA synthesis by the solvothermal method

Free radical graft copolymerization of maleic anhydride (MA) onto highly reactive low Mw PIB was conducted to generate PIB chain terminated with succinic anhydride (PIBSA). Specifically, 0.136 g (0.56 mmol) BPO, 1.950 g (20 mmol) MA, 15.63 g (6.8 mmol) HR-PIB, and 15 mL chloroform were sealed into an autoclave. The vessel was heated to 110˚C under vacuum for 3 h and cooled to room temperature. The transparent viscous product was washed with acetone for 10 min at least three times to remove the excess MA. The purified product was dried under vacuum at 60˚C overnight. The final product was a viscous liquid at room temperature.

2. Amine-modified sulfobetaine zwitterion synthesis

All the chemicals involved with amine-modified sulfobetaine zwitterion (NH_2-ZW) synthesis and $CsPbBr_3$ QDs solution were handled in the glove box, and all the chemical reactions were taken placed in the fume hood and connected to the Schlenk line.

Step 1. 2 mL (0.016 mol) of N, N-dimethylaminoproylamine was added to 17 mL 1,4-dioxane, then 5.47 mL (0.024 mol) of Di-tert-butyl decarbonate (Boc) was added dropwise to the mixed solution at 0˚C with stirring for 2 h and purged with N_2. The mixed solution was then warmed up to room temperature and kept stirring for one day. The solvent was evaporated and the compound was dissolved in 50 mL of DI water and was extracted by ethyl acetate. It was extracted at least three times. Na_2SO_4 was added to the solution to remove water. After ethyl acetate was evaporated, the yellowish oil-like product was obtained, which was subsequently utilized in the next step without undergoing any additional purification.

Step 2. 1.825 g (9 mmol) of the compound obtained from step 1 was dissolved in 7.5 mL DMF, then 1.17 mL (13.3 mmol) of 1,3-propane sultone was added to the mixed solution. The solution was stirred at room temperature for two days and purged with nitrogen. DMF was evaporated, and the yellow viscous compound was dispersed with 15 mL of diethyl ether and stirred for 10 min. The solvent with residual 1,3 propane sultone was decanted. The product was dried under vacuum in a vacuum oven at room temperature. 4.13 g (12.7 mmol) yellow paste product was obtained.

Step 3. 2.86 g (9 mmol) of the compound obtained from step 2 was dissolved in 60 mL of methylene chloride at 0°C, then 6 mL of 4M HCl in 1,4-dioxane was added dropwise into the mixed solution, and stirred for 30 min. The solution was discarded, and excess triethylamine was added to remove residual HCl. White solid salts were formed then 3 mL of chloroform was added to remove the salt. The supernatant was discarded. The viscous product was recrystallized in methylene chloride/methanol. The final product was collected and dried under vacuum at 40 °C overnight.

3. PIB-based zwitterionic ligands Synthesis

Briefly, 2 g (0.46 mmol) PIMA polymer was dissolved in 10 mL of toluene. 0.746

g (3.33 mmol) of NH_2-ZW was dissolved in 17 mL of methanol. The 17 mL of NH_2-ZW solution was added dropwise to the polymer solution and left stirring overnight at 55°C. The supernatant was decanted, then toluene was added to dissolve the product. The ligand solution was added dropwise into large excess methanol under vigorous stirring. The polymer ligand was precipitated, collected, and subsequently dried under vacuum at 40°C overnight. The white viscous product was obtained.

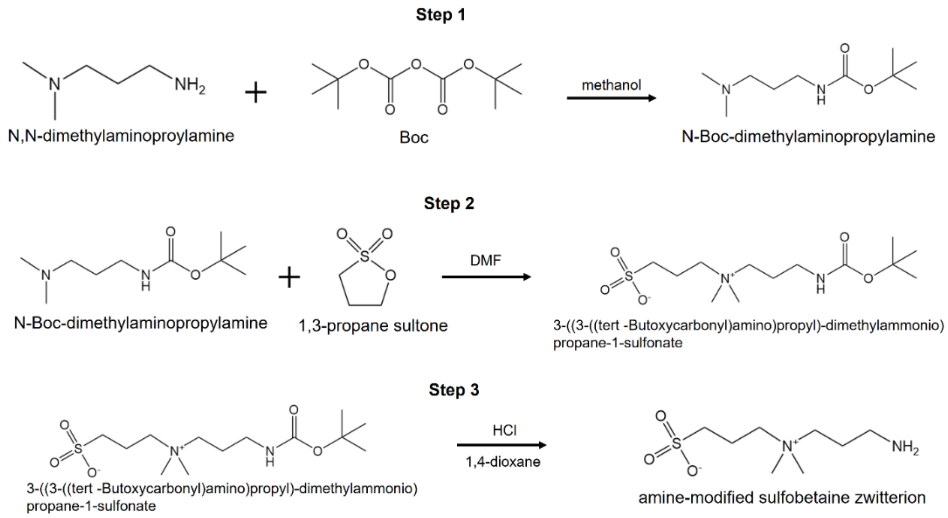

Figure B1. The three-step chemical reaction to synthesize the amine-modified sulfobetaine zwitterionic molecules.

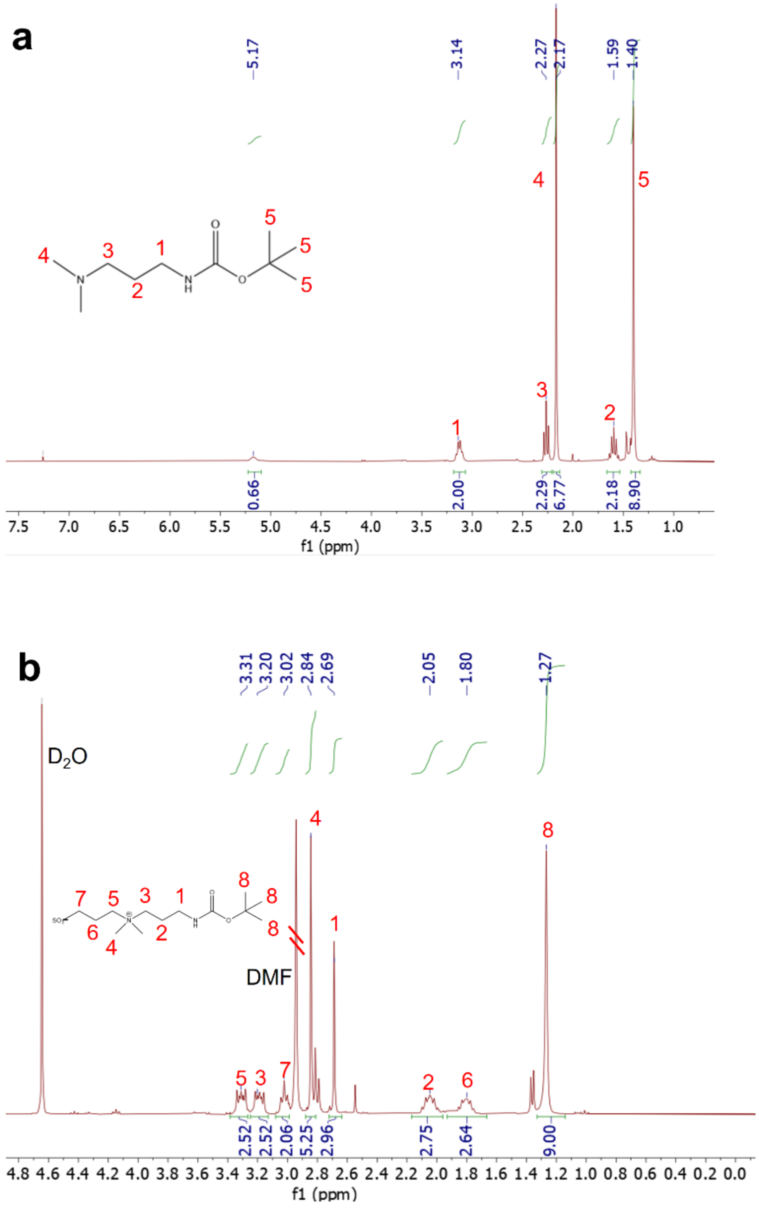

Figure B2. NMR spectra of the two precursor molecules during the three-step synthesis of amine-modified sulfobetaine zwitterion.

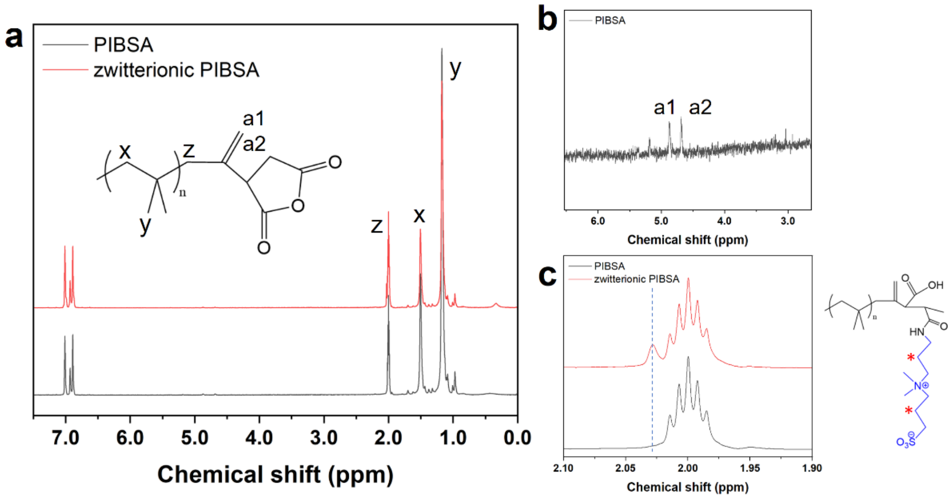

Figure B3. (a) 1H NMR spectra of PIBSA and zwitterionic PIBSA. (b) Highlight of the region between 3.0 and 6.0 ppm of NMR spectrum of PIBSA. (c) Highlight of the NMR between 1.9 and 2.1 ppm of the two samples.

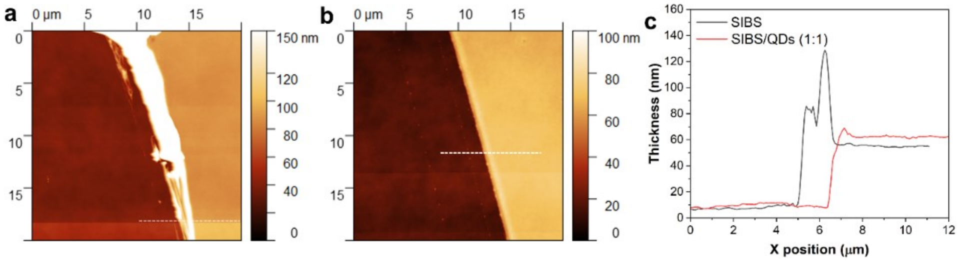

Figure B4. AFM image of the edge of (a) SIBS thin film and (b) SIBS/QDs-2 nanocomposite film. (c) Thickness measurements of the two samples from AFM cross-section analysis.

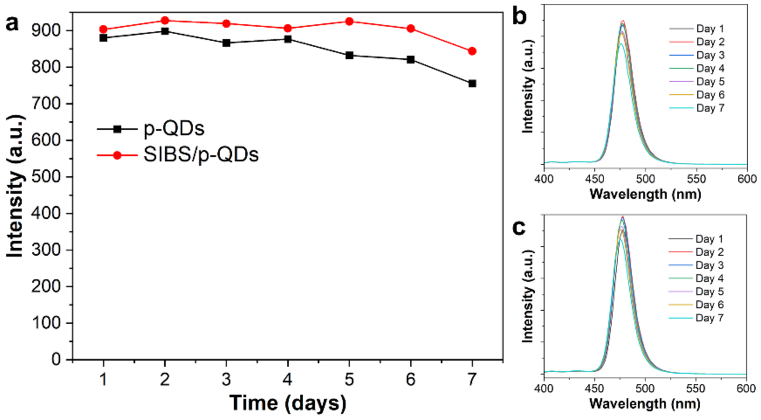

Figure B5. (a) PL intensity vs time for the p-QDs and SIBS/p-QDs in toluene, (e-f) PL spectra at different days for the p-QDs and SIBS/p-QDs in toluene.

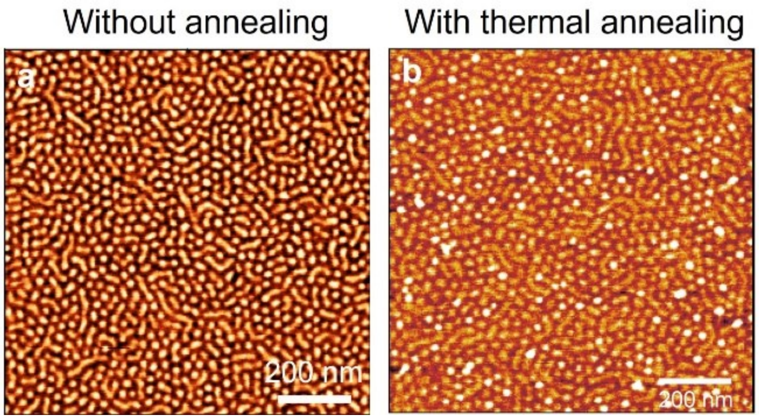

Figure B6. AFM phase images of SIBS-30 thin film (~ 100 nm thickness) without annealing (a) and after thermal annealing at 115 ºC for 12 hours.

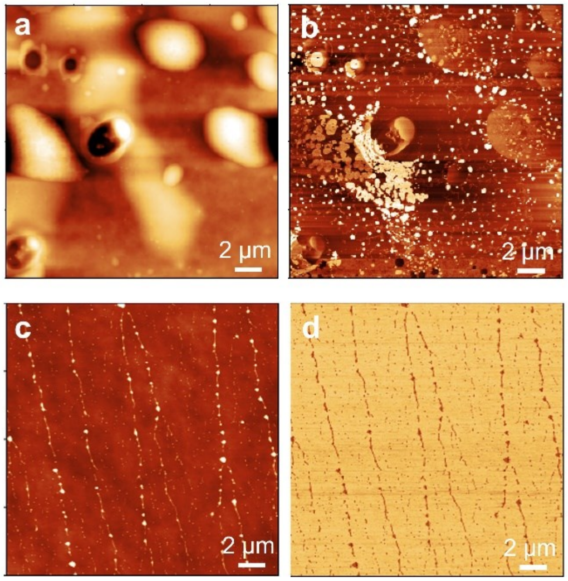

Figure B7. (a-b) AFM topography (a) and phase (b) images of the PS/p-QDs nanocomposite film, which shows severe aggregation. (c-d) AFM topography (c) and phase (d) images of the PIB/p-QDs nanocomposite film, which shows smooth and homogeneous morphology.

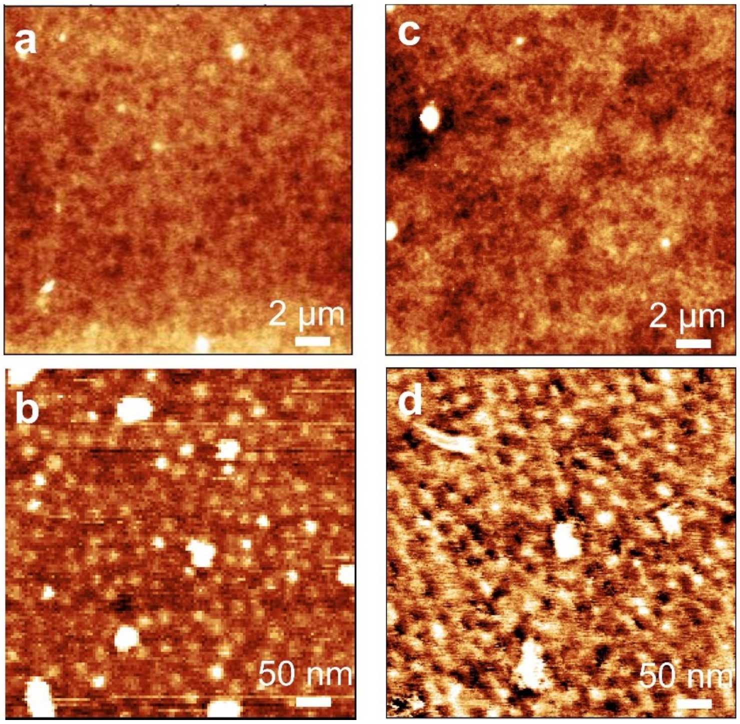

Figure B8. (a-b) AFM images of SIBS-30/p-QDs-0.8 composite at two different magnifications. (c-d) AFM images of SIBS-30/QDs-0.8 composite at two different magnifications. The top row are topography images, and the bottom row are phase images.

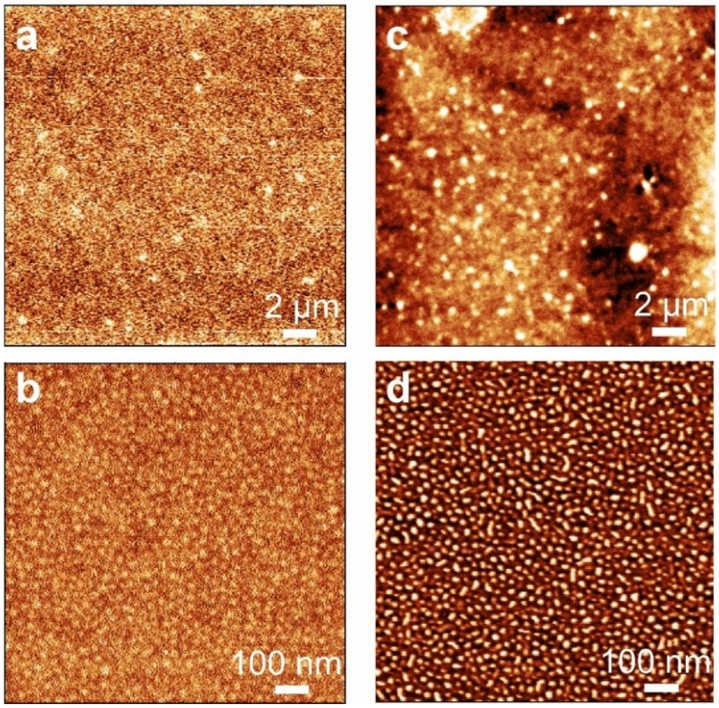

Figure B9. (a-b) AFM images of SIBS-23/p-QDs-0.8 composite at two different magnifications. (c-d) AFM images of SIBS-23/QDs-0.8 composite at two different magnifications. The top row are topography images, and the bottom row are phase images.

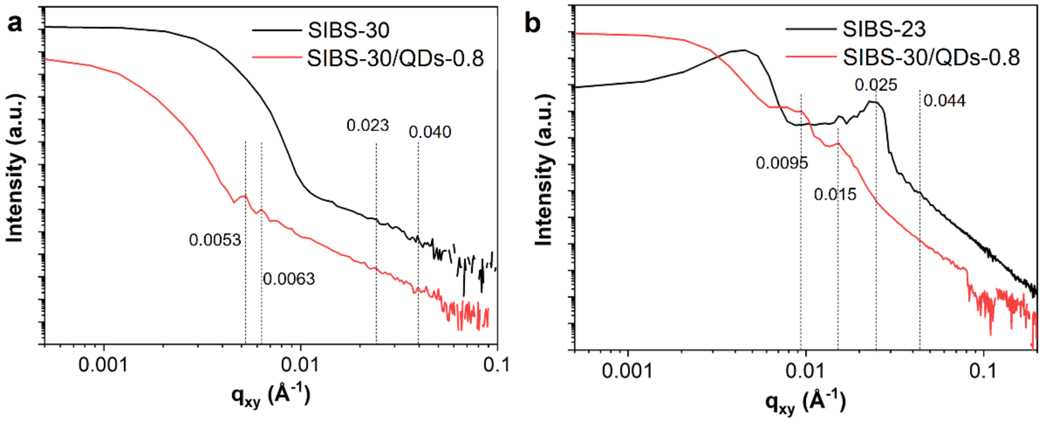

Figure B10. (a) GISAXS curves for SIBS-30 and SIBS-30/QDs-0.8 nanocomposite. (b) GISAXS curves for SIBS-23 and SIBS-23/QDs-0.8 nanocomposite

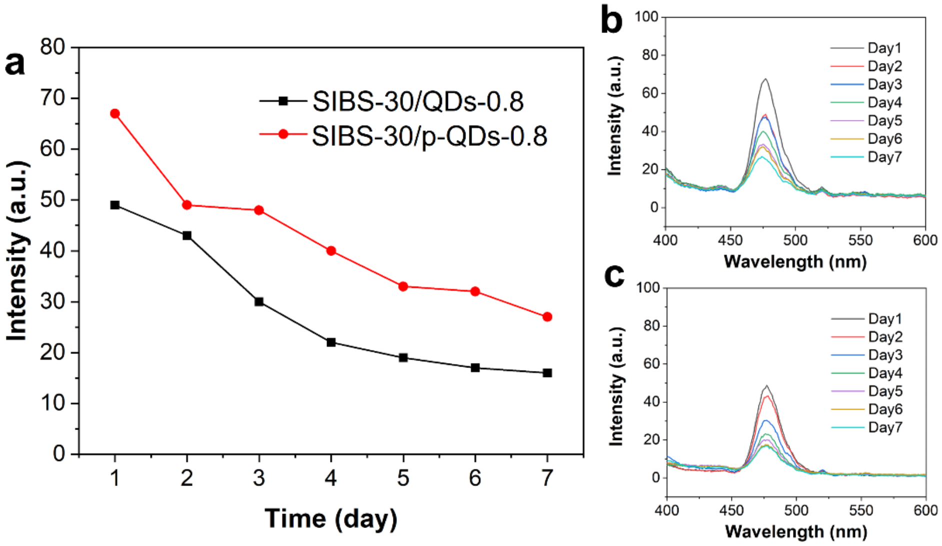

Figure B11. (a) Photoluminescence (PL peak intensity) decay with time in ambient condition for SIBS-30/QDs-0.8 and SIBS-30/p-QDs-0.8 composites. (b-c) PL spectra at different time for (b) SIBS-30/p-QDs-0.8 and (c) SIBS-30/QDs-0.8 composites, respectively.

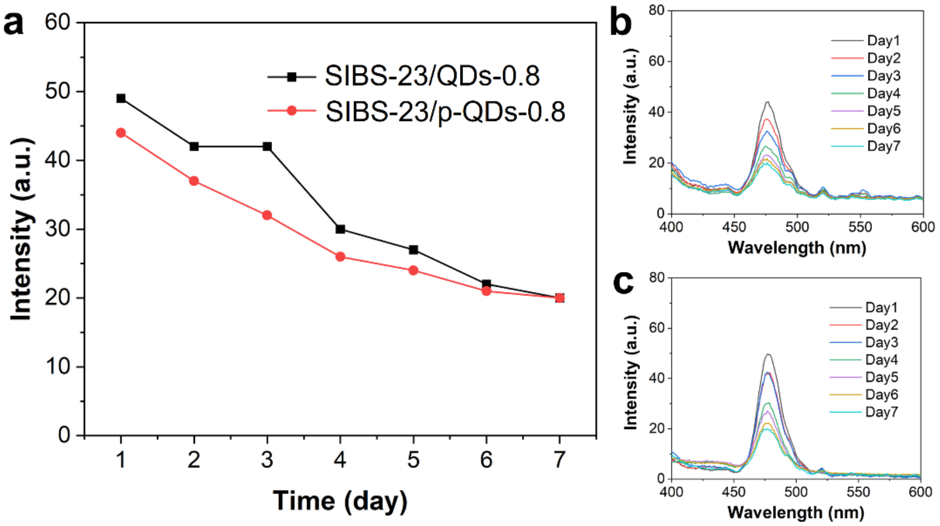

Figure B12. (a) Photoluminescence (PL peak intensity) decay with time in ambient condition for SIBS-23/QDs-0.8 and SIBS-23/p-QDs-0.8 composites. (b-c) PL spectra at different time for (b) SIBS-23/p-QDs-0.8 and (c) SIBS-23/QDs-0.8 composites, respectively.

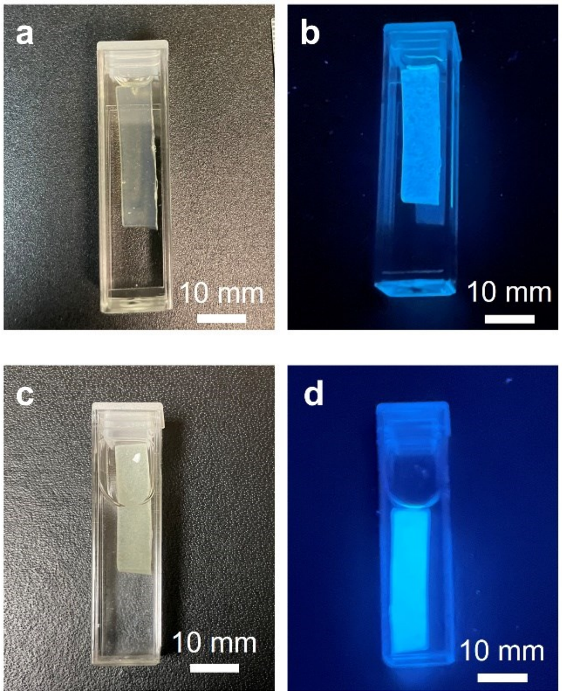

Figure B13. (a-b) Photos of an as-prepared SIBS/QDs nanocomposite membrane under normal light and UV irradiation. (c-d) Photos of the same sample after one month immersion in water under normal light and UV irradiation.

APPENDIX C:

SUPPORT INFORMATION FOR PARTIALLY SULFONATED POLY(STYRENE-B-ISOBUTYLENE-B-STYRENE) INCORPORATED WITH PEROVSKITE QUANTUM DOTS TOWARDS STABILIZED SOFT OPTICAL MATERIAL

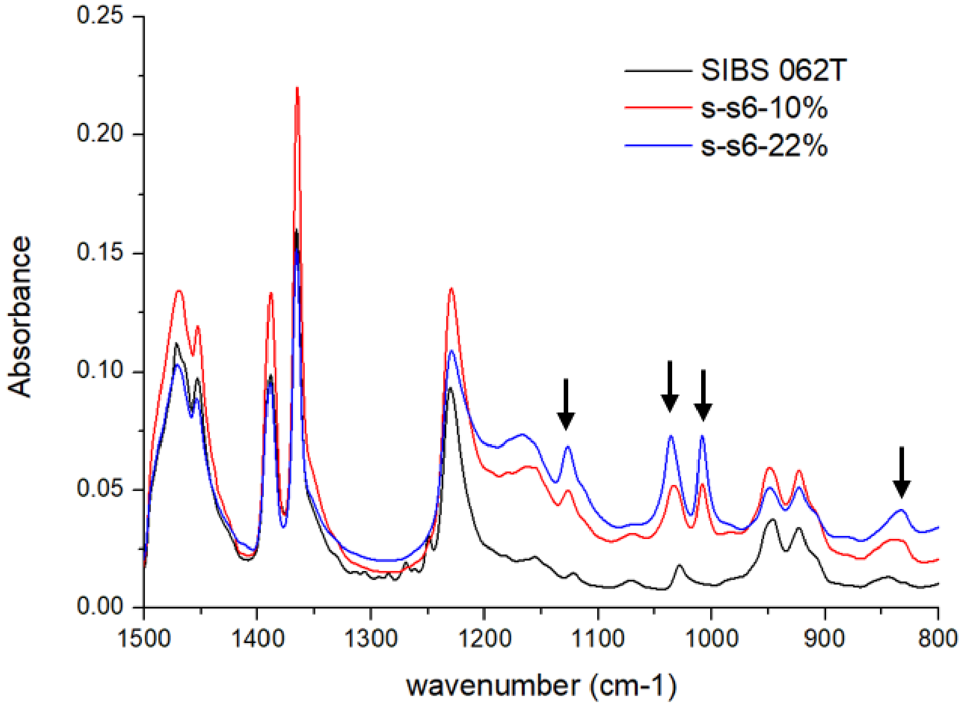

Figure C1: The summary of partially sulfonated SIBS 062T with calculated 10% and 22% sulfonation degrees.

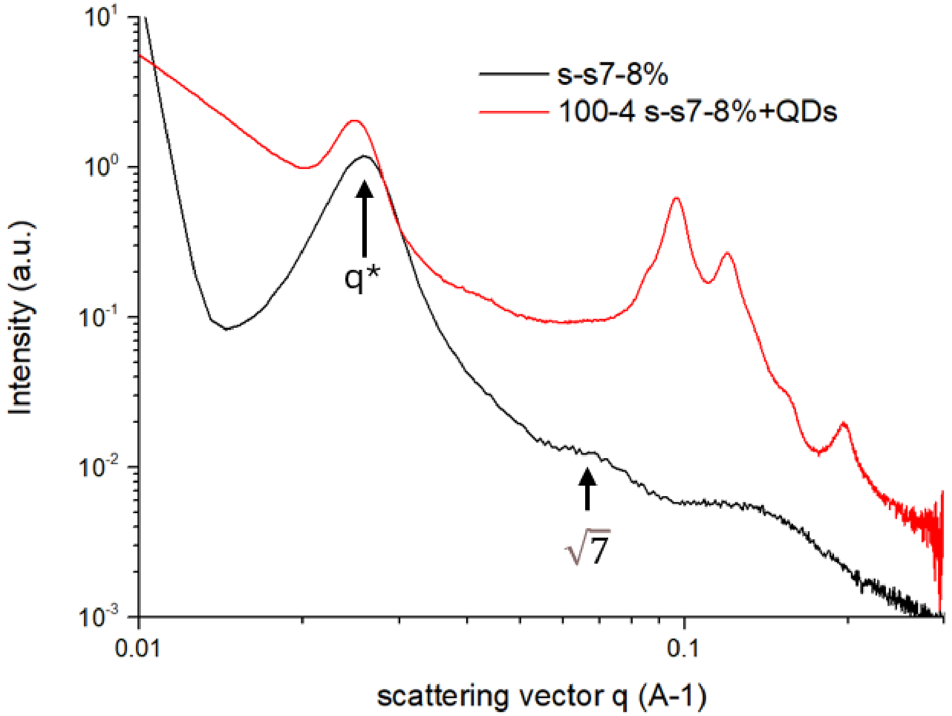

Figure C2: SAXS data for 8% SD s-SIBS 073T and its control sample. The peaks in the higher q region corresponding to the interparticle spacing of perovskite QDs.

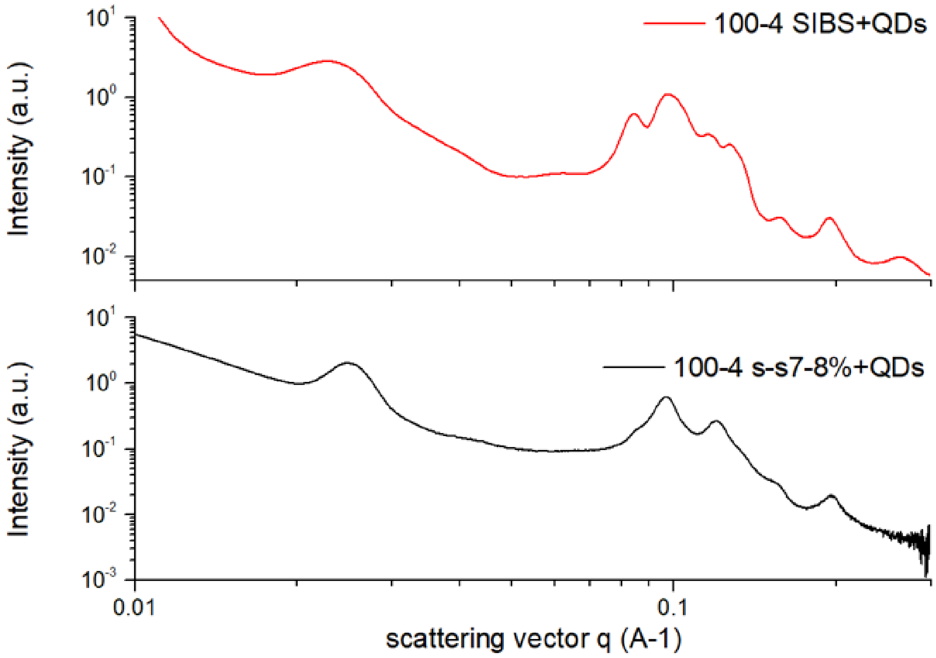

Figure C3: SAXS comparison to study the effect of sulfonic acid groups.

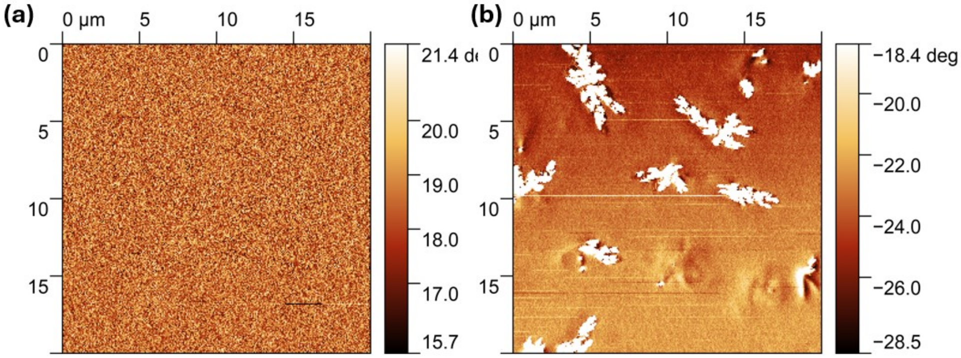

Figure C4: AFM phase images for (a) s-s6-22 as the control sample and (b) s-s6-22+QDs. The irregular large crystals were induced by QDs aggregation.

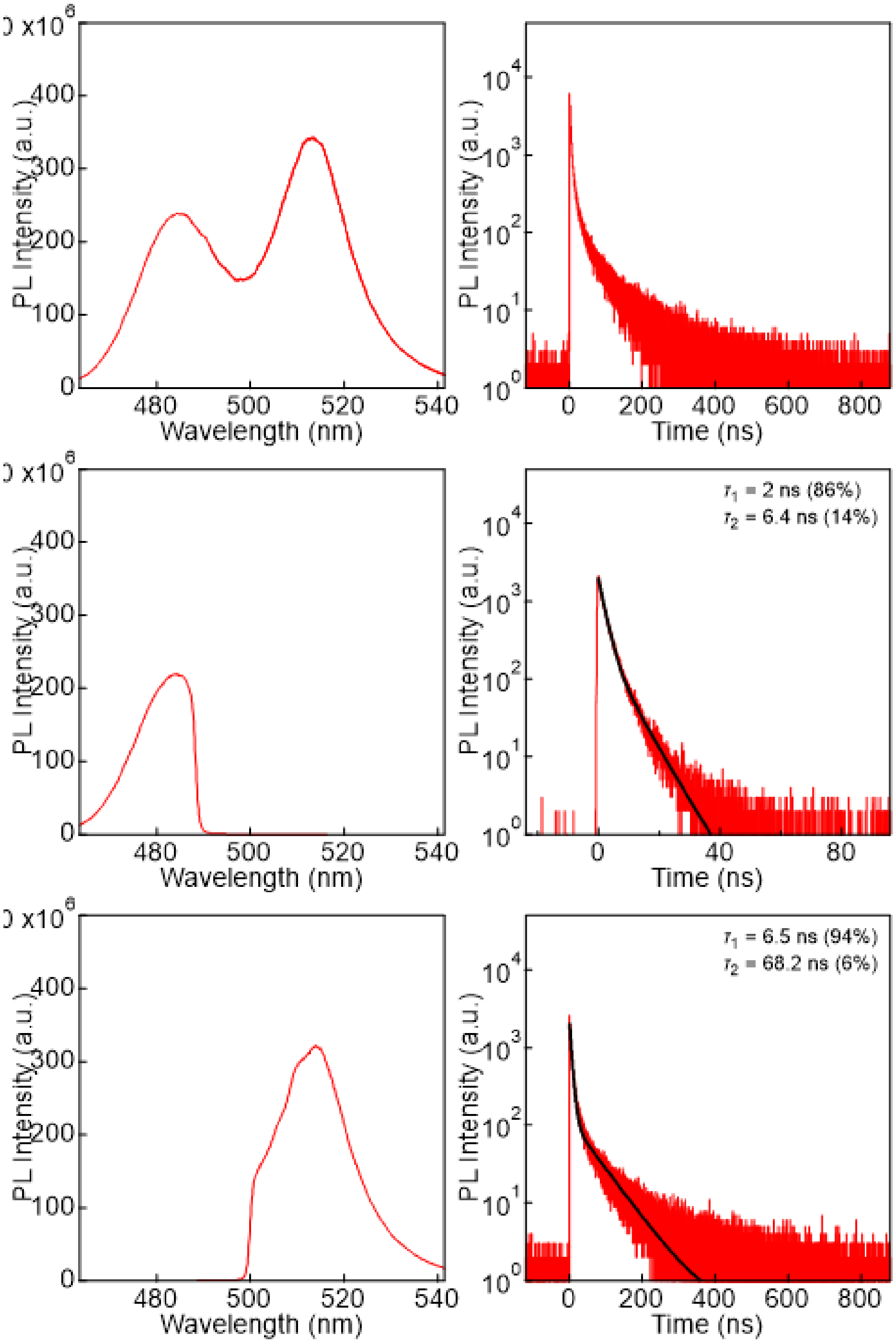

Figure C5: TRPL results for s-s6-22+QDs sample and corresponding lifetime of each band selectively using bandpass filters. The additional peak at higher wavelength region was induced by the large crystal presented in the AFM image.

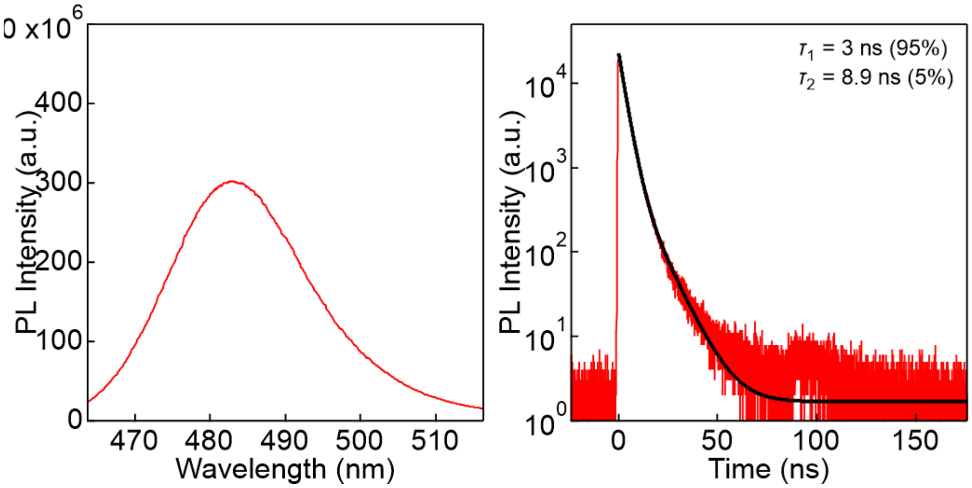

Figure C6: TRPL result for pristine SIBS 062T+QDs control sample.

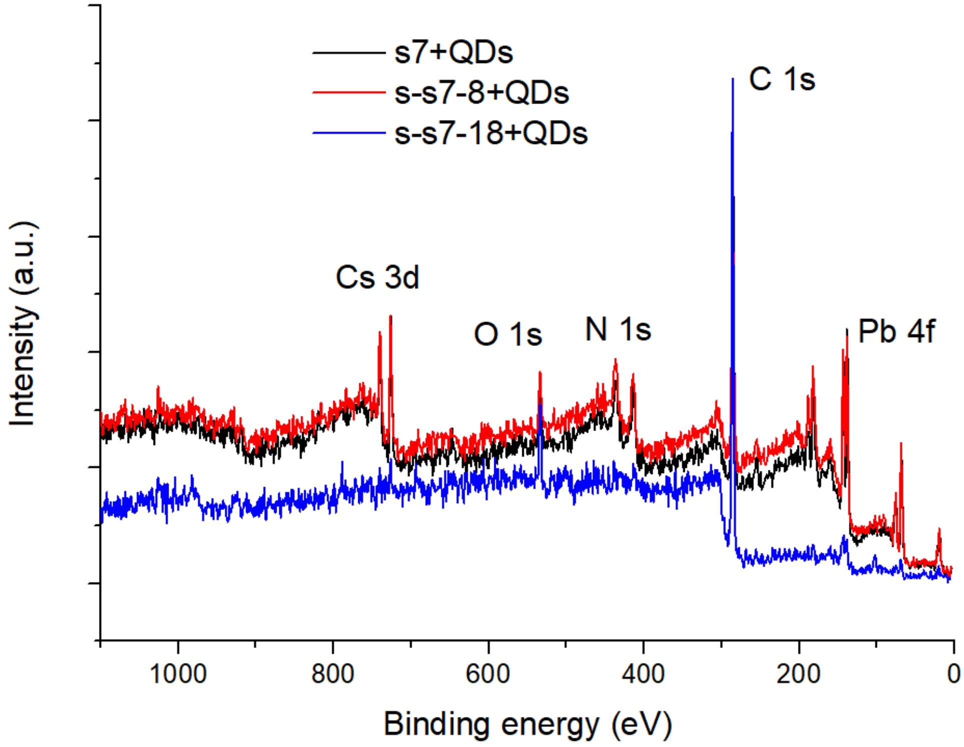

Figure C7: XPS results for partially sulfonated SIBS 073T with 8% and 18% sulfonation degrees and corresponding control sample without sulfonating treatment. Labelled peaks evidenced the presence of perovskite QDs.